

**Electromechanical Systems to Enhance the  
Usability and Diagnostic Capabilities of  
Ultrasound Imaging**

by  
Matthew Wright Gilbertson

B.S., Massachusetts Institute of Technology (2008)  
S.M., Massachusetts Institute of Technology (2010)

Submitted to the Department of Mechanical Engineering  
in partial fulfillment of the requirements for the degree of  
Doctor of Philosophy in Mechanical Engineering

at the  
MASSACHUSETTS INSTITUTE OF TECHNOLOGY

June 2014

© Massachusetts Institute of Technology 2014. All rights reserved.

**Signature redacted**

Author .....  
.....

Department of Mechanical Engineering

May 9, 2014

Certified by .....

**Signature redacted**

Dr. Brian Anthony

Principal Research Scientist, Dept. of Mechanical Engineering

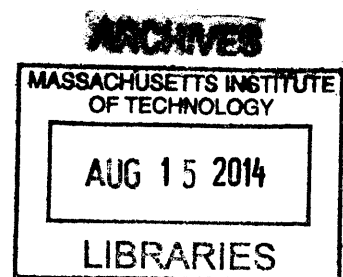
Thesis Supervisor

**Signature redacted**

Accepted by .....

Prof. David Hardt

Chairman, Department Committee on Graduate Theses





# **Electromechanical Systems to Enhance the Usability and Diagnostic Capabilities of Ultrasound Imaging**

by

Matthew Wright Gilbertson

Submitted to the Department of Mechanical Engineering  
on May 9, 2014, in partial fulfillment of the  
requirements for the degree of  
Doctor of Philosophy in Mechanical Engineering

## **Abstract**

Ultrasound is used extensively in medicine to non-invasively examine soft tissues. Compared to computed-tomography (CT) scanning or X-ray imaging, ultrasound is lower-cost, more portable, real time, and subjects neither the caregiver nor the patient to potentially harmful ionizing radiation, which makes it the imaging modality of choice for many medical applications. Common uses include fetal, vascular, and musculoskeletal imaging, as well as biopsy needle insertion guidance. With 165 million ultrasound exams conducted in the United States annually, and an annual US market of \$1.3 billion, improvements to the usability and diagnostic capabilities of ultrasound imaging could lead to significant improvements in medical care.

Ultrasound is unique because it generally requires significant contact force with the patient. This has a number of important consequences. The contact forces exerted by the ultrasound probe are generally not known, resulting in images that are acquired at non-repeatable levels of compression, which makes sequentially-acquired ultrasound images difficult to compare and reproduce. Contact force has also been implicated as a major risk factor in work-related musculoskeletal disease (WRMSD) amongst ultrasonographers; currently, clinical reports indicate that nearly 90% of sonographers scan in pain.

This thesis explores the mechanical design and experimental evaluation of three novel electro-mechanical systems that could be used to enhance the usability and diagnostic capabilities of ultrasound by measuring and/or controlling probe acquisition state (i.e., contact forces, torques, and angles of orientation). The first system, a hand-held servo-driven ball screw stage, improves image repeatability by applying a constant, programmable contact force between the probe and the patient, and attenuates hand tremors by a factor of 10. The second system, a force/torque-measuring ultrasound probe, was used in the first rigorous clinical study to characterize contact forces and torques applied during abdominal scanning. The third device, driven by a voice coil motor, enables high-bandwidth constant force scanning, and was used to measure the elastic modulus of tissue—an indicator of tissue health—at repeatable pre-load forces.

All three systems, each of which was built and refined with two or more prototypes, were evaluated through in-vivo and/or clinical studies at Boston Children's and Massachusetts General Hospitals. The results of these studies, as well as modeling and simulations, are presented in this thesis.

Thesis Supervisor: Dr. Brian Anthony

Title: Principal Research Scientist, Dept. of Mechanical Engineering

## Acknowledgments

First, I would like thank my advisor, Dr. Brian Anthony. Brian's diverse set of skills enabled him to assist me in a wide range of subjects from mechanical design to controls to general project strategizing. Brian always found a way to make time for me when I had questions or needed advice. He gave me the flexibility and freedom to explore promising new routes. I have thoroughly enjoyed learning from and collaborating with Brian throughout the last six years on this project.

I would also like to thank my colleagues and friends in our lab group. Combining forces with their wide spectrum of skills has enabled this project to soar. I would like to thank Shih-Yu Sun, for his extensive help with Matlab; Javier Ramos, for his creativity in the early design of one of the prototypes; Lauren Chai, for her pioneering work in phantom making; Dr. Bill Vannah, for his valuable insights and help with several of the experiments; Sisir Koppaka, for his work in explaining and interpreting gigabytes worth of data; John Lee, for setting up the ultrasound system and assisting me with many of the experiments; Aaron Zakrzewski for his tutelage in the art of phantom making; as well as my other colleagues in the lab: Dr. Kai Thomenius, Dr. Xian Du, Shawn Zhang, Ina Kundu, Nigel Kojimoto, and Javier Gonzalez. I am glad that we are all on the same team.

Third, I would like to thank my family. My wife Amanda, for her limitless encouragement and support of me, as well as her clinical insights and suggestions for the project; my brother Eric, for helping me troubleshoot problems, often as we ran along the Charles; and the rest of my family and friends, for supporting me throughout the last ten years at MIT.



# Contents

<b>1</b>	<b>Introduction</b>	<b>29</b>
1.1	Medical Ultrasound Imaging . . . . .	30
1.2	The sonographer-probe-patient system . . . . .	31
1.2.1	Augmented control of the acquisition state . . . . .	32
1.3	Prior Art: Systems to Control Ultrasound Acquisition State . . . . .	34
1.3.1	Structural Loop . . . . .	37
1.3.2	Discussion of the Prior Art . . . . .	39
1.4	The Importance of Contact Force . . . . .	42
1.4.1	Contact Force and Tissue Deformation . . . . .	44
1.4.2	Contact Force and Sonographer Fatigue & Injury . . . . .	45
1.4.3	Contact Force and Mechanical Properties Estimation . . . . .	45
1.5	Thesis Scope . . . . .	46
<b>2</b>	<b>“Meta” Design</b>	<b>49</b>
2.0.1	Range of Ultrasound Exams . . . . .	54
2.0.2	Range of Sonographers . . . . .	54
2.0.3	Range of Patients . . . . .	57
2.1	Most Critical Functional Requirements . . . . .	57
2.2	Range of Motion vs. Characteristic Scan Length . . . . .	59
2.2.1	Influence of Patient Cooperativeness and User Training & Feed-back . . . . .	64
2.3	Power requirements . . . . .	66
2.3.1	Summary . . . . .	68

<b>3 The Force-Measuring Ultrasound Probe</b>	<b>71</b>
3.1 Summary . . . . .	71
3.2 Introduction . . . . .	72
3.3 Series 1 Force-Measuring Probe: Design Process . . . . .	75
3.3.1 Design Parameters: Component Selection . . . . .	77
3.3.2 3D Laser Scanning the Ultrasound Probes . . . . .	80
3.4 System Description . . . . .	80
3.5 Gravity Compensation . . . . .	86
3.6 Measurement Accuracy and Precision . . . . .	87
3.6.1 Inertial Forces Induced by Involuntary Hand Tremors . . . . .	88
3.6.2 Accelerations Induced by Involuntary Hand Tremors . . . . .	89
3.6.3 Noise From Cable Pull Force . . . . .	89
3.6.4 Noise Sources . . . . .	89
3.7 Sonographer Studies . . . . .	91
3.7.1 Correlations with BMI and Sonographer Experience . . . . .	95
3.8 Force-Measuring Probe - Series 1: Conclusions . . . . .	99
<b>4 Force-Measuring Probe: Series 2</b>	<b>103</b>
4.1 Introduction . . . . .	103
4.2 Objectives . . . . .	103
4.3 Mechanical Design . . . . .	105
4.4 System components: Series 2 . . . . .	114
4.5 Comparison: Series 1 vs. Series 2 . . . . .	119
4.6 Conclusions . . . . .	120
<b>5 The Force-Controlled Ultrasound Probe</b>	<b>123</b>
5.1 Summary . . . . .	123
5.2 Related Work: Hand Tremor Suppression Systems . . . . .	125
5.3 Force-controlled probe: design process . . . . .	129
5.3.1 Functional Requirements . . . . .	130
5.3.2 Design Parameters . . . . .	133

5.3.3	Voice coil vs. Ball screw + servo motor: Power requirements . . . . .	139
5.3.4	Component Selection & Layout . . . . .	140
5.4	Force-controlled probe prototype 2: Mechanical components . . . . .	141
5.4.1	Angle Measurement and Gravity Compensation with the Accelerometer . . . . .	143
5.4.2	Electronics and Software . . . . .	146
5.4.3	Selecting the Appropriate Contact Force . . . . .	149
5.5	Control System Overview . . . . .	150
5.6	System Modeling and Experimental Testing . . . . .	152
5.6.1	System Model . . . . .	153
5.6.2	Model Parameters - Interface A . . . . .	155
5.6.3	Model Parameters - Interface B . . . . .	156
5.6.4	Model Parameters - Friction . . . . .	157
5.6.5	Hand Tremors . . . . .	158
5.6.6	Simplified Model . . . . .	159
5.6.7	Experimental Evaluation: Frequency Response . . . . .	159
5.6.8	Equations of motion . . . . .	160
5.6.9	Hand Phantom Stage . . . . .	163
5.7	Experimental Data . . . . .	165
5.7.1	Frequency Response: Model vs. Data . . . . .	165
5.7.2	Frequency Response: Discussion . . . . .	165
5.7.3	Experimental Evaluation: Image Stabilization . . . . .	168
5.7.4	User Studies to Evaluate Force Control . . . . .	172
5.8	Tissue Dynamic Viscosity Measurements . . . . .	178
5.9	Workflow Enhancements: Endpoint Avoidance and Contact State Change	180
5.9.1	“Soft” Limits . . . . .	180
5.9.2	Varying the target force . . . . .	183
5.10	Changes in Contact State: Making and Breaking Contact . . . . .	186
5.10.1	Making contact . . . . .	186
5.10.2	Breaking Contact . . . . .	187

5.10.3	Contact with hard surfaces . . . . .	187
5.11	Summary . . . . .	189
<b>6</b>	<b>Ergonomics Considerations - Enabling Clinical Studies and Use</b>	<b>191</b>
6.1	Duchenne Muscular Dystrophy Study . . . . .	191
6.1.1	Third prototype: objectives . . . . .	193
6.1.2	Third Prototype: Design Parameters . . . . .	194
6.1.3	Design Considerations: Motor Wire Strain Relief . . . . .	197
6.2	Three Prototypes: Comparison . . . . .	202
6.3	Results . . . . .	204
6.3.1	DMD Study: Early Results . . . . .	204
6.4	User Feedback: Prototype 3 . . . . .	209
6.5	Conclusions . . . . .	211
6.6	Suggested Future Work . . . . .	213
<b>7</b>	<b>The High-Speed Dynamic Imaging Probe</b>	<b>215</b>
7.1	Summary . . . . .	215
7.2	Introduction . . . . .	215
7.2.1	Tissue non-linearity . . . . .	217
7.3	Elastography . . . . .	220
7.3.1	Strain-Based Elastography . . . . .	220
7.3.2	Shear Wave-Based Elastography . . . . .	221
7.4	High-speed dynamic imaging probe: mechanical design . . . . .	224
7.4.1	Design parameters: component selection . . . . .	227
7.5	Dynamic imaging probe: Versions 1 and 2 . . . . .	229
7.5.1	Version 1 . . . . .	229
7.5.2	Version 2 . . . . .	232
7.6	Dynamic imaging probe: control and modeling . . . . .	235
7.6.1	Control . . . . .	236
7.7	Modeling and Simulation . . . . .	238
7.7.1	Mechanical model . . . . .	238

7.7.2	Electrical model . . . . .	240
7.7.3	Modeling the closed loop system . . . . .	241
7.8	High speed imaging . . . . .	243
7.8.1	Pixel column synchronization . . . . .	247
7.8.2	Limitations of pixel column synchronization . . . . .	249
7.9	Single-element ultrasound transducer . . . . .	250
7.9.1	Imaging shear wave propagation with the single-element transducer . . . . .	252
7.10	Dynamic Imaging Probe: Summary . . . . .	260
7.11	Discussion . . . . .	261
<b>8</b>	<b>Design for All Exams</b>	<b>263</b>
8.1	Mapping the Design Space . . . . .	263
8.2	Conclusion . . . . .	267
<b>9</b>	<b>Contributions and Suggestions for Future Work</b>	<b>269</b>
9.1	Conclusion . . . . .	269
9.2	Workflow Enhancements and Suggested Use . . . . .	270
9.2.1	Uses: Current Prototypes . . . . .	270
9.2.2	Uses: Ideal Realizations . . . . .	271
9.3	Contributions . . . . .	273
9.4	Suggestions for Future Work . . . . .	276
9.4.1	Force-Controlled Probe: . . . . .	276
9.4.2	Force-Measuring Probe: . . . . .	279
9.4.3	High-Speed Dynamic Imaging Probe: . . . . .	280



# List of Figures

1-1	Diagram of the image control system consisting of the sonographer, ultrasound probe, and patient. Black lines indicate control signals, blue lines indicate feedback paths. $G(s)$ represents the sonographer's mental controller. . . . .	33
1-2	Block diagram of the sonographer-probe-patient image control system. $X(s)$ represents the acquisition state of the probe (i.e., force, torques, orientation, and position). . . . .	34
1-3	Diagram of the augmented control framework. The devices described in the thesis, which contribute the items outlined in red, provide either actuation or sensing between the sonographer's hand and the ultrasound probe, as well as audio and additional visual feedback, enabling tighter control of the acquisition state. $X_{ref}(s)$ refers to the desired acquisition state. . . . .	35
1-4	Systems from the literature that measure and/or control ultrasound probe acquisition state, grouped by number of degrees of freedom and form factor (i.e., Earth-grounded, patient-grounded, or hand-held). References are listed in Table 1.1. . . . .	36
1-5	Left: the structural loop for a machine tool, which is the force path through the machine from the tool to the workpiece. Right: the force path for ultrasound imaging, in which the "tool" is the ultrasound probe and the "workpiece" is the patient. Images reproduced from FUNdaMENTALS of Design, page 3-24, by Slocum [99], and from <a href="https://www.osha.gov/SLTC/etools/hospital/sonography/images">https://www.osha.gov/SLTC/etools/hospital/sonography/images</a> . . .	37

1-6	Illustrations of the structural loop—i.e., the force path through the device (or sonographer’s arm) from the ultrasound probe to the patient. As discussed in Section 2.2, the hand-held configuration can be considered either earth-grounded or patient-grounded, based upon whether the sonographer rests his/her arm or hand upon the patient. . . . .	38
1-7	The basilic vein imaged at three different contact forces. “N” refers to Newtons of force. The images are difficult to compare due to the different levels of compression. . . . .	44
1-8	Elastograms of the quadriceps at 1N, 9N, and 18N preload forces. The colored region indicates the elastic modulus of the tissue; the colormap scale, which is the same for all three images, is depicted in the lower right of the 18N image. The elastic modulus estimates, expressed in kPa, are calculated for the region of interest highlighted by the white circle. It is evident in these images that variations in preload force result in different estimates of elastic modulus. . . . .	46
1-9	The hierarchy of the systems and studies presented in this thesis. . . .	48
2-1	Overview of the design process. The input is the intended use, typical range of sonographers and patients, and the outputs are the device functional requirements and suggested design parameters. . . . .	50
2-2	A sampling of ten of the most common types of ultrasound exams, along with the parameters associated with each exam. . . . .	55
2-3	A Pareto Chart showing the distribution of five most commonly performed ultrasound exam types. Data are from the GAO Analysis of Medicare Part B claims for 2005, so it therefore represents exams for patients >65 years [78]. . . . .	56
2-4	Hand tremor power spectrum, from MacLachlan [62]. A majority of the tremor characteristics lie below 10 Hz. . . . .	57

2-5	To test the effect of scan length upon necessary device range of motion, a human volunteer moved an infrared marker with different scan lengths $L_{scan}$ above a tracking system, which measured height $Z(t)$ . . . . .	60
2-6	Three most common structural loop configurations encountered during hand-held ultrasound scanning. A: seated, elbow supported. B: seated, elbow not supported. C: standing, elbow not supported. . . . .	61
2-7	Example $Z(t)$ versus time plots for seated, elbow resting (left) and seated, elbow not supported (right). . . . .	61
2-8	Z-motion range versus scan length for the different structural loop scenarios shown in Fig. 2-6. Runs are slightly horizontally offset for clarity. Vertical bars span $\pm 1\sigma$ , while the middle of the bars is the average. Black line represents linear fit. . . . .	62
2-9	Zoomed-in version of Fig. 2-8, with characteristic scan lengths for different types of ultrasound exams displayed. The devices presented in this thesis are shown on the Y-axis; the corresponding stroke lengths are noted. . . . .	63
2-10	Minimum necessary device stroke length versus scan length, with uncooperative patient motion and user training & feedback. . . . .	65
3-1	Devices from the literature to measure probe contact force. References are listed in Table 3.1. . . . .	73
3-2	Attaching the ultrasound probe to the device with the locking 3D printed clamp. . . . .	79
3-3	Mating the top shell with the bottom shell. The shells are held together by magnets. . . . .	80
3-4	SolidWorks rendering of the force-measuring probe, Series 1. . . . .	81
3-5	Front, side, and back views of the six-axis force/torque-measuring ultrasound probe. Depicted with a 3D-printed ultrasound probe mock-up.	82
3-6	3D laser scanning the GE C1-5D transducer with the NextEngine scanner. . . . .	83

3-7	Solid models of the seven ultrasound probes associated with this thesis research, obtained by 3D laser scanning the ultrasound probes. . . . .	83
3-8	Exploded view of the device. . . . .	84
3-9	Left: probe-tip coordinate system. It is hypothesized that $F_y$ is greatest during scanning. . . . .	85
3-10	Projections of the gravitational acceleration vector onto the X, Y, and Z planes. Pitch angle $\theta$ is the angle between vertical and the Z-plane; roll angle $\alpha$ is the angle between vertical and the X-plane. Yaw angle cannot be accurately measured with an accelerometer alone. . . . .	86
3-11	System model. Stiffness $k$ and damping $b$ are present in the load cell-to-probe connection. . . . .	88
3-12	Photograph of the complete system. The ultrasound probe cable 1 is Velcro-strapped 2 to the device cable to provide strain relief. A steel enclosure 4 houses the electronic components while the laptop 5 displays and records the probe contact state. . . . .	90
3-13	Contributions from each noise source to noise in $F_y$ and $\tau_x$ . $F_x$ and $F_z$ (not shown) are similar to $F_y$ ; $\tau_y$ and $\tau_z$ are similar to $\tau_x$ . The non-repeatable tug of the cable comprises the majority of total signal noise, followed by the load cell sensor noise. . . . .	90
3-14	An example plot of axial force, $F_y$ , versus time for Run 479. Yellow regions indicate time during which the probe was not in contact. Text annotations at the top denote the organ or tissue that was investigated, while vertical blue lines demarcate different organs. . . . .	92
3-15	One of the 53 ultrasound exams conducted at MGH - Boston. The device was approved for use by the MGH Internal Review Board. . . .	92

3-16 Box and whisker plot of the forces (top) and torques (bottom) for Runs 1 - 9. Solid horizontal black line within each box indicates median value; boxes enclose 50% of the data. Whiskers extend $\pm 2.7\sigma$ from the median value; assuming a normal distribution, 99.3% of the data fall within the whisker bounds. A noise-measurement run is shown on the right. . . . .	93
3-17 Forces and torques from all 53 runs. . . . .	94
3-18 Histogram of the axial force $F_y$ for all of the 53 exams. X-axis indicates force range; Y-axis is the number of times that force range was recorded. 96	
3-19 Mean axial force versus volunteer BMI. Each unique icon represents a unique sonographer. In the plot, we observe a wide spread in contact forces from 5 N to 14 N. Certain sonographers (e.g., pink star) apply consistently lower force, while other sonographers (e.g., blue star and pink triangle) apply consistently higher forces. The data were split into two groups with a BMI = 25 cutoff, and it was found that a statistically significantly higher maximum force was applied to higher BMI subjects. 97	
3-20 Mean axial force versus volunteer BMI, averaged for each volunteer. Blue circles indicate average force, red line spans $\pm 1\sigma$ . . . . .	98
3-21 Mean contact force versus years of sonographer experience, with each icon colored with respect to patient BMI. As in Fig. 3-19, we observe a wide spread in the contact forces. No trend is clearly observable, indicating little to no correlation between contact force and the number of years of experience of the songrapher. . . . .	100
4-1 Side view of the ultrasound probe showing the application of force $F$ along the Y axis, which induces a bending moment $M$ about the load cell. Note: the X-axis is out of the page. . . . .	106

4-2	Image of the finite element analysis for the load cell with a worst case bending moment applied. Deformation is exaggerated by a factor of 7.2. The stress in load cell, which is indicated by the colormap, is highest in the regions with highest radius of curvature. The maximum stress of 264 GPa is less than the 325 GPa yield stress of the 2024 aluminum. This suggests that, even at the highest forces, the load cell is not expected to be damaged. . . . .	107
4-3	Design iterations for the force-measuring probe, Series 2. “P” denotes “plastic” and “LC” denotes “load cell.” The original 6-axis load cell design ① is shown on the left, final design ⑤ is shown on the right. . .	108
4-4	Linear bearing concept for Series 2 of the force-measuring probe. The linear bearing resists all bending moments and forces except for the contact force along the Y-axis, which is transmitted directly to the load cell. . . . .	109
4-5	Force-measuring probe concept ④, consisting of a 3D printed stainless steel probe clamp and a waterjetted/machined anchor bracket. . . .	110
4-6	Force-measuring probe, Series 2, concept ⑤, in which the load is sandwiched between aluminum mounting brackets, which are secured to the 3D printed plastic probe clamp and bottom shell. . . . .	112
4-7	Bottom views of the configurations tested. The configurations varied in terms of the material of the part mounted to each side of the load cell (3D printed plastic, aluminum, or steel) and whether the real load cell or mock-up load cell was used. Black arrows indicate chronological direction of development. . . . .	113
4-8	Prototypes of the Series 2 force-measuring probe. The prototypes differ in terms of part thickness, clearances, and cord grip. A major factor that necessitated a number of additional iterations was due to the kinematics of how the probe clamp fit around the probe. Black lines indicate the chronological progression of the various design iterations. . . . .	115
4-9	Force-measuring probe, Series 2: the complete system. . . . .	116

4-10 Photograph of the signal electronics box, which contains the Futek CSG110 signal amplifier and NI USB-6009 DAQ board. Wires are all strain-relieved with cord clamps. Components were laid out to minimize overall volume to maximize portability. . . . .	117
4-11 Screenshot of the graphical user interface (GUI) for the Series 2 force-measuring probe. The GUI displays the contact force as well as the pitch and roll angles of inclination of the probe. . . . .	117
4-12 Magnetically attaching the AC adapter to the black plastic holder. . .	118
4-13 The force-measuring ultrasound probe, Series 2, after clinical use at MGH. . . . .	118
4-14 Size comparison of the Series 1 and Series 2 force-measuring probes. .	119
4-15 Spider plot comparing the original functional requirements with the actual values for the force-measuring probes. ' $T_{a\&r}$ ' refers to the total time to attach and remove the probe. . . . .	121
5-1 The three force-controlled ultrasound probes that have been developed. Prototype 1 was the subject of the author's masters research [40]; Prototypes 2 and 3([15],[16],[17],[18],[41],[43]), which are discussed in this thesis, were developed during the author's PhD research. . . . .	124
5-2 Five hand tremor suppression devices from the literature. Labels are identified in Table 5.1. Note: the photos in a given row are for a particular device. . . . .	126
5-3 Solid model (L) & photo (R) of the force-controlled ultrasound probe, Prototype #2. The device is depicted without the protective plastic cover. . . . .	129
5-4 The five most critical components in the system, along with examples of each. . . . .	134
5-5 Pugh chart comparing the various linear actuation options to the baseline rotary motor + transmission option. . . . .	135

5-6 Candidate mechanisms for converting rotational motion into linear motion: ball screw, rack and pinion, belt drive, and cable drive. Clockwise, from top-left: ball screw, preloaded rack and pinion, cable drive, and belt drive. . . . .	136
5-7 Images of the force-controlled probe, Prototype 2. . . . .	142
5-8 Exploded view of the force-controlled ultrasound probe, Prototype 2. Labels are discussed in Table 5.3. . . . .	144
5-9 The device compensates for up to 5.0 cm of relative motion between the sonographer and patient. . . . .	146
5-10 The 3-layer, surface-mount PCB for Prototype 2. Routes signals between device, amplifier, DAQ board, and power supplies. Op amp performs gravity compensation with accelerometer and load cell voltages. . . . .	147
5-11 The electrical enclosure for prototype 2 (left), which contains the PCB (Fig. 5-10), amplifier, AC adapters, UMI-7744 screw terminal board, and Futek CSG110 signal amplifier. . . . .	147
5-12 The system, equipped for clinical use. . . . .	148
5-13 A block diagram of the control system, which consists of both a closed loop force controller and closed loop position controller. The signals are summed together via an analog operational amplifier circuit. Both loops can be independently enabled or disabled. . . . .	151
5-14 A block diagram showing the force controller only, which was used in the experiments in Section 5.7. . . . .	152
5-15 A model of the system while the device is grasped by the sonographer and placed in contact with the patient. . . . .	154
5-16 Model of the ultrasound probe gripped by the sonographer. . . . .	162
5-17 Diagrams of the hand phantom stage evaluating the frequency response of (A) the force-controlled ultrasound probe, and (B) the force-measuring ultrasound probe proxy . . . . .	164

5-18 Magnitude (top) and phase (bottom) response with moving hand phantom stage. Averaged experimental data are shown as dotted lines; simulated response is solid. Magnitude is expressed in N/mm as the relative amplitude between contact force and input motion. Data for the force-controlled ultrasound (FCUS) probe are shown in blue; data for the force-measuring proxy probe are red. . . . .	166
5-19 Illustration of vessel segmentation with Matlab for one run (run 3) with force control off (left) and force control on (right) for all frames. Best fit ellipses from each of the 193 frames are overlaid upon the first ultrasound image, which is also shown in the bottom right corner. . .	170
5-20 Inclusion centroid depth vs time for moving phantom. Centroid depth refers to the depth of the best-fit ellipse centroid for the vessel wall. Dashed line denotes force-control (FC) off; solid line denotes force-control on. The traces are vertically offset from each other for visual clarity; the mean value for all three traces was approximately 1.6 mm. . . . .	171
5-21 Contact force versus time for Subject 6 in each of the four scenarios. The operator held the probe stationary during the first ten seconds and conducted a sweeping motion for the subsequent twenty seconds. . . . .	173
5-22 Mean contact forces and standard deviations for all fifteen operators in the three scanning scenarios, with 3.0 N target force. Dots represent mean forces while the vertical bars extend $\pm$ one standard deviation from the mean. . . . .	174
5-23 Mean contact forces and standard deviations for all fifteen operators in the three scanning scenarios <u>for Prototype 1</u> , with 5.0 N target force, reproduced from [42]. Icons represent mean forces while the vertical bars extend $\pm$ one standard deviation from the mean. . . . .	175
5-24 Histograms of the forces applied by all fifteen operators in the three scenarios, with 3.0 N target force. . . . .	176
5-25 Tissue dynamic viscosity $\mu$ versus frequency: data with the force-controlled ultrasound probe compared with other studies. . . . .	179

5-26	The device's usable range of motion is 5.0 cm. 'SW' = 'switch.'	180
5-27	Absolute value of the position controller output signal versus position for three possible modes of operation. Due to the fixed PID-based controller, Mode 1 was exclusively implemented in the system.	182
5-28	Force versus time (top) and ultrasound probe position versus time (bottom) during a phantom scan for five endpoint avoidance strategies. "EA" refers to " <u>Endpoint Avoidance</u> ".	184
5-29	A flow chart of the complete control system, which includes endpoint avoidance and the ability to make and break probe/patient contact.	188
6-1	Ultrasound images of the quadriceps in a healthy patient (left) and in a patient with DMD (right). Image reproduced from Koppaka, et al [54].	192
6-2	Prototype 2 instrumented with the LED array, which displays the position of the actuator.	196
6-3	The digital display indicates the angle of inclination of the device from vertical. A green LED illuminates when the angle is negative.	196
6-4	Prototype #3. Labels: 1) servo motor, 2) LED bar graph actuator position indicator, 3) two-digit angle display, 4) ergonomic 3D-printed shell, and 5) 3D-printed probe clamp.	198
6-5	Exploded view of Prototype 3. Components are described in Table 6.1.	199
6-6	In the first design iteration of the motor shell, the motor wire lead was subject to repeated bending and unbending during operation, eventually leading to fatigue and loss of electrical continuity.	201
6-7	Redesigned 3-piece breakaway motor cover, which eliminates strain on the motor cable.	202
6-8	Spider plot comparing the functional requirements of Prototype 2 with the actual capabilities of each of the three prototypes.	204
6-9	Illustration of the extraction of a series of ultrasound images at specified forces from the force sweep.	206

6-10 Illustration of the image processing steps applied to the images, described in [54] and [55]. The input is a sequence of 19 images taken at known forces; output is a binary decision: DMD or healthy. . . . .	207
6-11 Classification accuracy for each of the muscle groups. Accuracy is measured in terms of the Adjusted Rand Index [87], in which higher values indicate higher classification accuracy. Plot borrowed from Koppaka et al [54]. . . . .	208
7-1 Non-linear force-displacement characteristics of human skin (left) [108] and the forearm of a human volunteer, as measured with the dynamic imaging probe (right). . . . .	218
7-2 Elastic modulus measurements of the quadriceps at different preload forces. Force was recorded with the force-measuring probe; elastic modulus was calculated with the Supersonic Imagine 15-4 probe. . . .	219
7-3 The Voigt body, consisting of a simple parallel mass spring system, is the simplest realistic tissue model. . . . .	222
7-4 Plot from Catheline et al (1999) [28]. Shear wave velocity measurements vs. frequency for beef muscle tissue, demonstrating that velocity levels out above about 60 Hz. . . . .	223
7-5 The dynamic imaging device, Version 1, which was designed to accommodate the Terason 7L3V linear array probe. Solid model (left) and photo (right). Due to spherical distortion of the camera lens, the photo (right) appears warped compared to the solid model. . . . .	230
7-6 Views of Version 1 from the front, sides, top, and bottom. . . . .	231
7-7 Solid model rendering (left) and photo (right) of the dynamic imaging probe, Version 2, designed to accommodate a single-element Olympus ultrasonic transducer, and to address the limitations of Version 1. . .	232
7-8 Views of Version 2 from the front, top, back, bottom, and sides. . . .	233
7-9 Exploded view of Version 2. Labels are discussed in the Table 7.3. . .	235

7-10 Block diagram of the control loop implemented for force and position control modes. In this figure, “X” can represent either position or force.	236
7-11 The addition of a reference voltage in the feedback path enables superior control over the target position/force and is used to measure the frequency response of the system. . . . .	238
7-12 Mechanical model of the dynamic imaging probe . . . . .	239
7-13 Electrical model of the voice coil [58], shown within dotted red line on the right. The Copley amplifier is depicted as the dependent current source on the left. . . . .	240
7-14 Bode magnitude (top) and phase (bottom) plots comparing the model (Equation 7.14) with the actual performance of the dynamic imaging probe, Version 2. The resonant peak occurs around 16.7 Hz. Gain is expressed as the ratio of the effective position commanded by $V_{ref}$ to the output position $x_3$ of the voice coil, in units of mm/mm. . . . .	242
7-15 Relative timing with 20 Hz indentation (red) and 25 Hz imaging frequency (black). . . . .	244
7-16 As a result, the 20 Hz indentation is sampled 5 times/cycle, for a rate of $f_3 = 5$ Hz. . . . .	245
7-17 An example of stacking together phase-synchronized pixel columns to reconstruct an image of a constant phase. . . . .	248
7-18 Left: example raw image of a flat plate beneath a homogeneous phantom, imaging frequency = 30 Hz, indentation frequency = 29 Hz. Right: image corrected by the pixel column synchronization method.	249
7-19 Images of a phantom containing a flat plate, reconstructed using pixel column synchronization. More blurring is present when the plate (ultrasound probe) is moving quickly (right). . . . .	250
7-20 Images of a phantom containing a large round inclusion, before and after reconstruction using pixel column synchronization. The presence a double-line artifact is visible, which blurs the image . . . . .	251

7-21 A comparison between the images obtained with a linear-array transducer and a single-element transducer. . . . .	253
7-22 Overview of the experiments to evaluate the elasticity of the tissue at different preload forces. . . . .	254
7-23 M-mode images of the 50 Hz indentation of the tissue at different preload forces. The ultrasound probe is at the top of the image; deeper tissue structures such as the ulna bone are at the bottom of the image. . . . .	255
7-24 Images of the tissue layers at each preload force with the motion of the ultrasound probe removed. . . . .	256
7-25 Example M-mode imaging of shear wave speed estimation from the Catheline et al [28]. Vertical displacement is exaggerated to enhance shear wave visualization. . . . .	257
7-26 Zoomed-in M-mode image of the compression of the tissue at 11 N preload force. The dotted line is drawn through corresponding peaks in the traces at each depth, and has a slope of 4.3 m/s. . . . .	258
7-27 Elastic modulus vs. preload force for the dynamic imaging probe and force-measuring Supersonic Imagine Probe from Fig. 7-2 (right), compared to the literature (left). . . . .	259
7-28 Spider plot comparing the functional requirements for the high-speed dynamic imaging probe (red) with the actual performance of Version 2 (blue). . . . .	261
8-1 Suggested design for a force-controlled or force-measuring ultrasound probe in each of the commonly-performed exams, along with the most important functional requirements. . . . .	264

8-2 Bandwidth versus range of motion of various systems in the literature, along with the devices presented in this thesis. The devices outlined in blue are all earth- or patient/grounded systems, while the rest are handheld. For clarity, two force-measuring devices from the literature are shown to the left of the force-measuring device in this thesis, all of which have zero range of motion. . . . .	266
9-1 A photograph of the force-controlled probe with the 6-DOF probe tracking system by Sun [107], [105], [106]. The device, which has not yet been used in studies, could be used to control the complete 6-DOF contact state of the probe. . . . .	278
9-2 Ultrasound imaging tasks that exacerbate musculoskeletal injury symptoms, from a study of 1621 sonographers, reproduced from [70]. . . .	281

# List of Tables

1.1	The references corresponding to the prior art images shown in Fig. 1-4. Note: the two-digit number after the author's name refers to the publication year. . . . .	35
2.1	Parameters associated with the sonographer. . . . .	56
2.2	Special design considerations for patients $\pm 2\sigma$ from the mean value of the given parameter. . . . .	58
2.3	Mappings between the input variables and the functional requirements. . . . .	59
3.1	References corresponding to the labels in Fig. 3-1. . . . .	72
3.2	Functional requirements for the force-measuring probe, Series 1. . . . .	77
3.3	Summary of force [N] and torque [mNm] data for the 53 runs. . . . .	95
3.4	Statistical correlations between contact force and subject BMI. . . . .	99
4.1	Functional requirements of the force-measuring probe: Series 2. . . . .	105
4.2	descriptions of each of the configurations, along with the measured torsional stiffness of each. . . . .	113
4.3	Comparison between the Series 1 and Series 2 force-measuring probes. . . . .	119
4.4	Comparison between functional requirements ( $FR_P$ ) and measured capabilities ( $D_P$ ) of the force-measuring probe, Series 1 and 2. . . . .	120
5.1	References corresponding to the prior art shown in Fig. 5-2. . . . .	125
5.2	Summary of the quantitative functional requirements for the force-controlled ultrasound probe, Prototype 2. . . . .	133
5.3	Descriptions of the components of Prototype 2 . . . . .	145

5.4	Mean value of the standard deviations $\bar{\sigma}$ in centroid and height for the three runs. . . . .	170
5.5	Measures of the mean contact force for all exams. “P1” denotes Prototype 1, while “P2” denotes Prototype 2. P1 data are reproduced from [42]. . . . .	177
6.1	Description of the components of Prototype 3 shown in Fig. 6-5. . . . .	200
6.2	Comparison between functional requirements of Prototype 2 ( $FR_P$ ) and measured capabilities ( $D_P$ ) of the three force-controlled probes, Prototypes 1-3. Although Prototype 1 was not designed with the same functional requirements as Prototypes 2 and 3, we include it in this table for comparison purposes. . . . .	203
7.1	Functional requirements for the dynamic imaging probe . . . . .	227
7.2	The most critical design parameters for the dynamic imaging probe. .	228
7.3	Descriptions of the components of Version 2 . . . . .	234
7.4	Comparison between functional requirements and measured capabilities of the dynamic imaging probe, Version 2. . . . .	260

# Chapter 1

## Introduction

This thesis explores the mechanical design, construction, and experimental evaluation of three novel, hand-held, electromechanical systems that measure and/or control the contact acquisition state of an ultrasound probe during medical ultrasound imaging. Conceptually motivated by the idea of how to improve the repeatability of ultrasound imaging, the three systems were designed to understand current ultrasound imaging practice, and then to enhance the diagnostic capabilities of ultrasound by improving the repeatability of the probe acquisition state (i.e., the relative contact forces, torques, position, and orientation of the probe with respect to the patient), as well as reduce the level of skill necessary to acquire diagnostic-quality images.

The first system described in this thesis attenuates involuntary hand motion, including tremors, to maintain a constant, programmable contact force between the ultrasound probe and the patient. The second system passively measures contact forces, torques, and orientation angles, and was used in the first study to rigorously quantify these parameters in abdominal scanning. The third system enables high-bandwidth constant-force scanning, as well as evaluation of tissue elasticity at different preload forces.

Each of the three systems was designed through a deterministic design process, and each was fabricated and refined through two or more prototypes. For each of the three systems, this thesis describes the design process, including functional requirement definition and component selection, mechanical fabrication, and the results of clinical

and/or *in vivo* studies.

## 1.1 Medical Ultrasound Imaging

Ultrasound is a widely-used modality to image soft, near-surface biological tissues. Unlike CT or X-ray imaging, ultrasound subjects neither the caregiver nor the patient to potentially harmful ionizing radiation, which makes it the imaging modality of choice for frequent imaging of soft tissues. Common applications include fetal imaging, cardiovascular assessment, tumor detection, biopsy needle insertion guidance, and musculoskeletal imaging. Variation in sonographer<sup>1</sup> technique and experience results in image and imaging-workflow variation. Improvements to the usability and diagnostic capabilities of ultrasound imaging could therefore lead to significant improvements in the quality of medical care.

In current sonographic practice, the acquisition state—i.e., the position, orientation, contact forces, and contact torques of the ultrasound probe—are implicitly controlled by the sonographer, based upon qualitative image appearance, and are not easily quantified. As a result, the acquisition state is not repeatable. Non-repeatability in the acquisition state variables, such as the contact force, can make dimensional measurements difficult to precisely reproduce at a later date [25].

For instance, within the context of longitudinal imaging, in which repeated images are acquired over periods of time, clinicians may not be able to determine whether a near-skin-surface tumor has changed dimensions over time, or if instead they are acquiring the image with increased pressure or at a different location. Sonographers performing an ultrasound-guided biopsy must insert the biopsy needle while watching the ultrasound image and maintaining the probe force—a difficult combination which can lead to inaccurate biopsy siting. Control of the ultrasound probe position, orientation, and contact force could thus lead to more consistent ultrasound images or reduced-complexity, safer medical procedures.

---

<sup>1</sup> “Sonographer” is the term used for a medical professional who performs diagnostic ultrasound, and is the term that is used in this thesis.

Any solid body has six independent degrees of freedom (DOFs): three translational DOFs (e.g., Cartesian X-Y-Z) and three rotational DOFs (e.g., Eulerian  $\phi$ - $\theta$ - $\psi$ ). An ultrasound probe, therefore, can be moved by the sonographer in six DOFs with respect to the patient's body. To achieve maximum image repeatability and resolution in longitudinal ultrasound imaging, the probe would need to be re-localized at the same X-Y-Z position and  $\phi$ - $\theta$ - $\psi$  orientation with respect to the patient's body. In our group, Sun [105], [106] presents a system that uses skin feature tracking to achieve 6-DOF probe re-localization.

## 1.2 The sonographer-probe-patient system

In conventional ultrasound imaging, the acquisition state of the ultrasound probe is controlled qualitatively by the sonographer's sensory control system, which consists of the sonographer's proprioception and eye-hand feedback loop. The sonographer grasps the probe and places it in contact with the patient at the area of interest. Cycling his/her gaze between the live ultrasound image on the computer screen and the ultrasound probe itself, the user manipulates the ultrasound probe until the desired image is attained.

During manipulation, the user varies the acquisition state of the probe. Proprioception tells the sonographer the relative and approximate position of his/her hand, arm, and joints, as well as the strength of effort being applied [45] and enables him/her to manipulate the probe while looking at the computer screen. Occasional glances at the probe are necessary for determining more accurately the position of the probe relative to the patient's body.

Consider, for example, a typical abdominal ultrasound scan. A patient complaining of abdominal pain sees a doctor. The doctor orders an abdominal ultrasound scan. The patient sees a sonographer, who performs the abdominal scan according to a standard protocol. The protocol for the procedure details which views should be obtained for which organs; for example, the long axis and transverse views of the liver, or the distal common bile duct in the region of the pancreatic head, are two of

the many images recommended by the American College of Radiology for abdominal scanning [4].

Thinking of the imaging scenario as a control system, the input into the control system is the sonographer's mental picture of the ultrasound image that he/she wishes to capture, based upon his/her prior experience and the protocol for the procedure, or may be an image from a previous exam on the computer screen. The sonographer's objective is to vary the acquisition state of the ultrasound probe in order to obtain the best clinically useful image, i.e., best match between the notional target image and the actual image. The sonographer's arm and hand act as the actuator, manipulating and varying the acquisition state of the probe. A combination of eye/hand feedback and proprioception help the sonographer to manipulate the probe. The output of the system is the ultrasound image. The sonographer sees the ultrasound image on the computer screen, mentally compares it with the target image he/she is seeking to capture, and varies the acquisition state of the ultrasound probe in order to attain that target image. Disturbance inputs into the system include patient motion and involuntary sonographer hand motion due to tremors. An illustration of the system is shown in Fig. 1-1.

Transforming this system into a more familiar block diagram format, the closed-loop image control system is illustrated in Fig. 1-2.

### 1.2.1 Augmented control of the acquisition state

The objective of the devices described in the thesis is to help the sonographer to explicitly or implicitly control the acquisition state variables for the purposes of increased image repeatability and decreased sonographer skill level. This is an "augmented" control system: the device is essentially an inner loop within the control system which either actively controls the contact state or informs the sonographer of the contact state so that he/she can control it more tightly. A block diagram of the augmented control framework is shown in Fig. 1-3.

## The sonographer-probe-patient control system

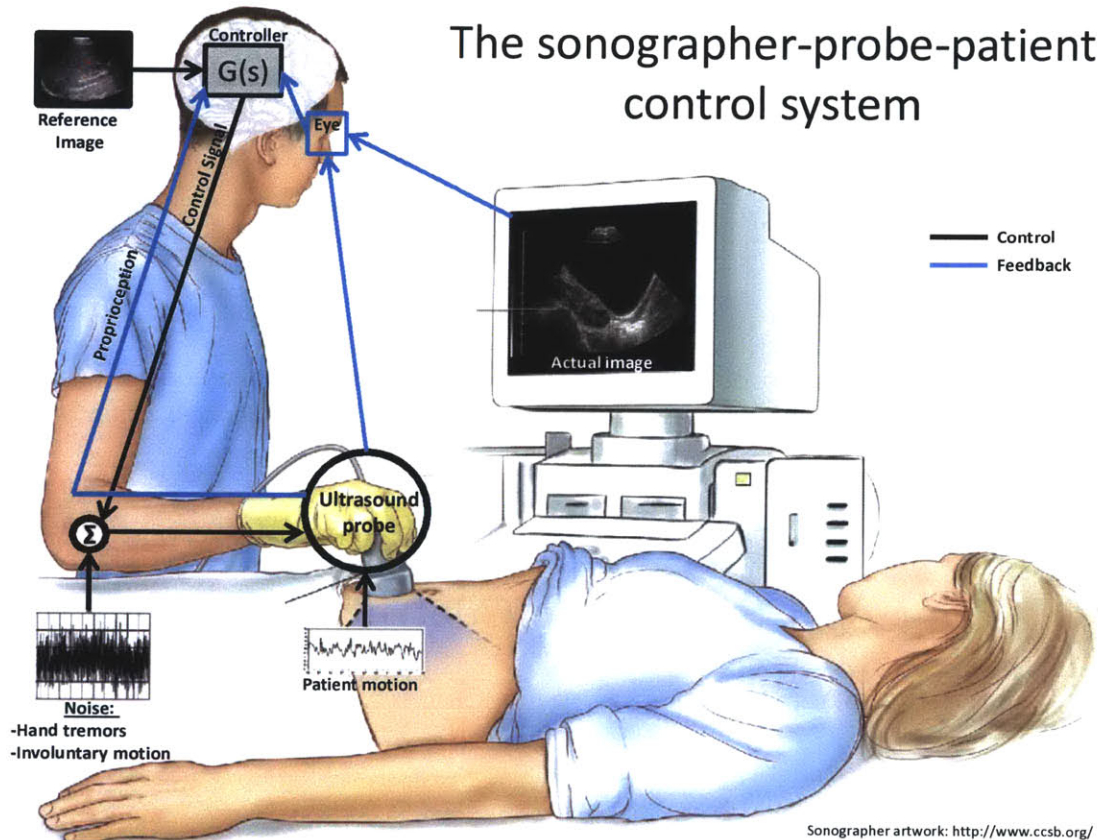


Figure 1-1: Diagram of the image control system consisting of the sonographer, ultrasound probe, and patient. Black lines indicate control signals, blue lines indicate feedback paths.  $G(s)$  represents the sonographer's mental controller.

# Conventional Ultrasound Imaging

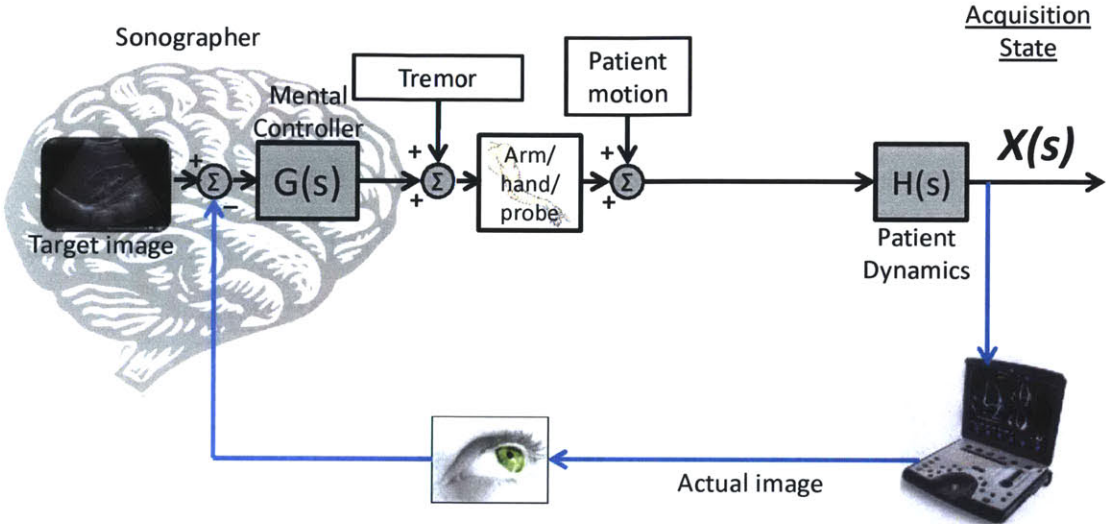


Figure 1-2: Block diagram of the sonographer-probe-patient image control system.  $X(s)$  represents the acquisition state of the probe (i.e., force, torques, orientation, and position).

## 1.3 Prior Art: Systems to Control Ultrasound Acquisition State

The literature is rich with systems that mechanically control or measure one or more of the ultrasound probe acquisition state variables. Many of the systems are complex and bulky. The systems can be grouped by various criterion; for example, the systems from the literature vary in terms of the number of degrees of freedom in which the ultrasound probe can be moved, ranging from 0 DOFs (unactuated force-measuring probes) to 6 DOFs, as well as several overactuated 6 DOF systems. The systems also differ in terms of form factor; i.e., hand-held, patient-grounded (mounted to patient), or Earth-grounded (mounted to the floor). A sampling of 33 systems from the literature is shown in Fig. 1-4; the corresponding references are listed in Table 1.1.

# Augmented Control of the Acquisition State

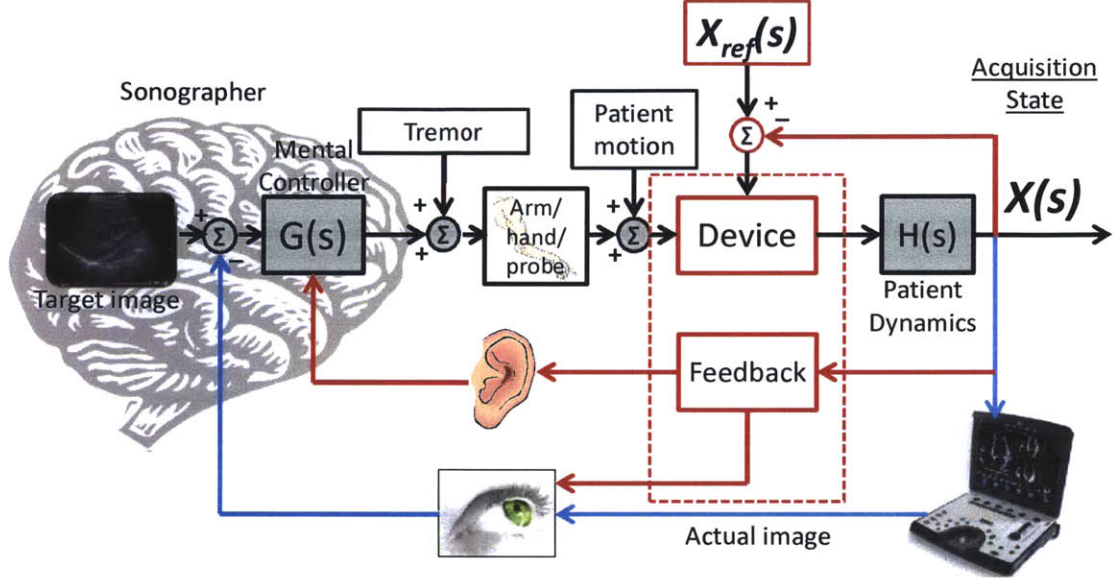
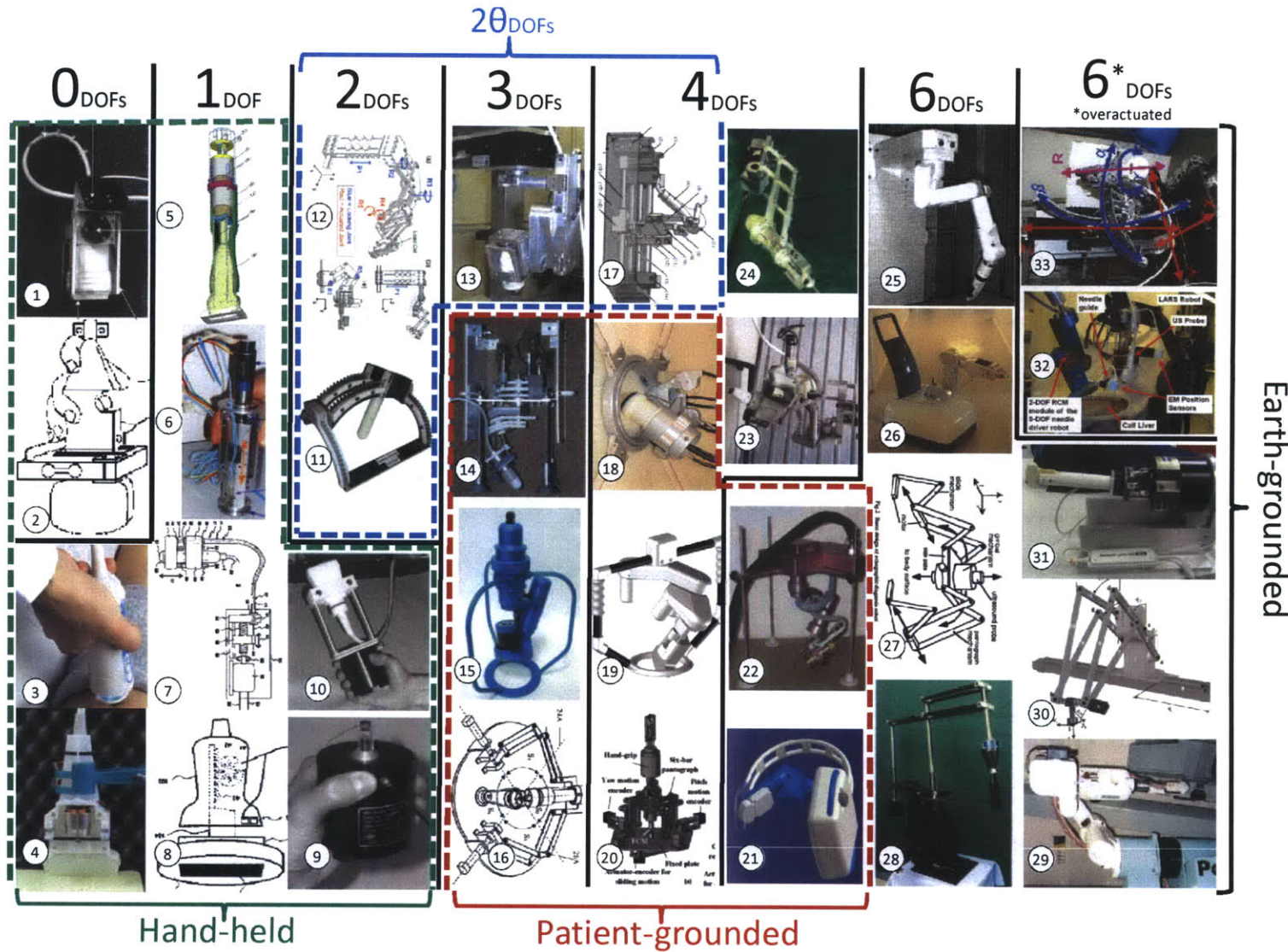


Figure 1-3: Diagram of the augmented control framework. The devices described in the thesis, which contribute the items outlined in red, provide either actuation or sensing between the sonographer's hand and the ultrasound probe, as well as audio and additional visual feedback, enabling tighter control of the acquisition state.  $X_{ref}(s)$  refers to the desired acquisition state.

Table 1.1: The references corresponding to the prior art images shown in Fig. 1-4.  
Note: the two-digit number after the author's name refers to the publication year.

Label	Reference	Label	Reference	Label	Reference
1	Burcher 05 [25]	12	Schlosser 10 [95]	23	Vilchis 07 [112]
2	Chadli 12 [29]	13	Goldberg 01 [46]	24	Davies 98 [33]
3	Echosens 24 [7]	14	Gourdon 99 [47]	25	Degou lange 98 [84]
4	Azar 12[20]	15	Courrèges 03 [32]	26	Mob. Robotics 04 [3]
5	Rivaz 07 [88]	16	Najafi 04 [71]	27	Masuda 01 [64]
6	Marchal 04 [63]	17	Gumprecht 13 [48]	28	Salcudean 99 [91]
7	Matsumura 09 [65]	18	Vilchis 03 [110]	29	De Cunha 98 [34]
8	Osaka 09 [81]	19	Robosoft 14 [8]	30	Lessard 07 [59]
9	Sandrin 02 [94]	20	Najafi 11 [72]	31	Ding 08 [97]
10	Bercoff 03 [21]	21	Al Bassit 04 [14]	32	Boctor 04 [23]
11	Gilbertson 10 [40]	22	Al Bassit 04 [14]	33	Mitsubishi 01 [68]

Figure 1-4: Systems from the literature that measure and/or control ultrasound probe acquisition state, grouped by number of degrees of freedom and form factor (i.e., Earth-grounded, patient-grounded, or hand-held). References are listed in Table 1.1.



### 1.3.1 Structural Loop

Before describing the prior art in detail<sup>2</sup>, we lay the groundwork for the discussion by presenting the concept of the *structural loop*. The classifications “patient-grounded” and “earth grounded” refer to the characteristics of the path the force takes through the device from the ultrasound probe and patient, known in the machine design vernacular as the “structural loop” [99], shown within the context of machining in Fig. 1-5.

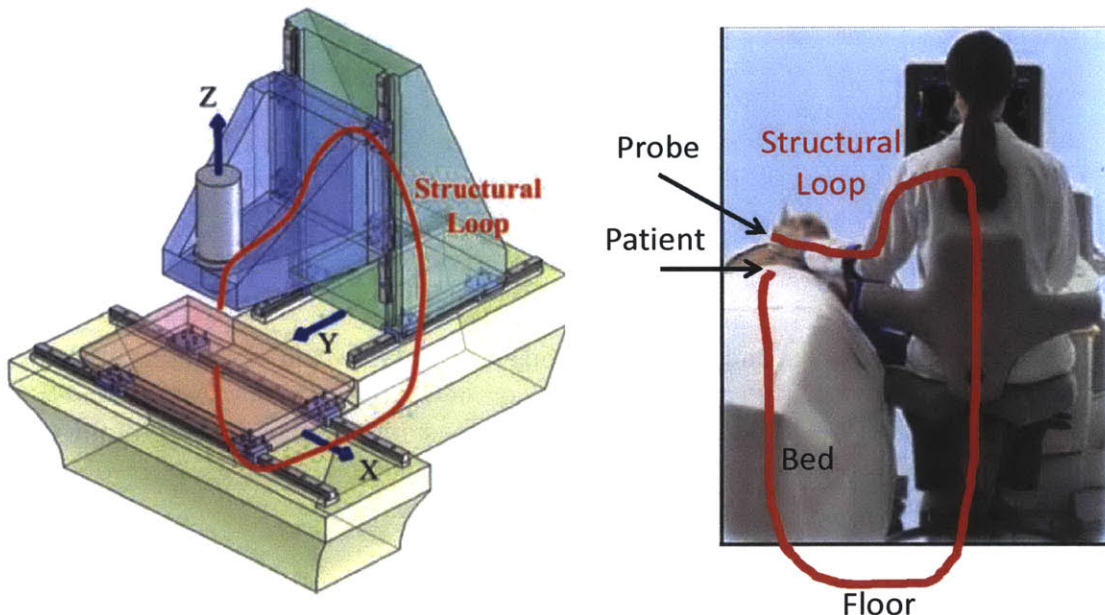


Figure 1-5: Left: the structural loop for a machine tool, which is the force path through the machine from the tool to the workpiece. Right: the force path for ultrasound imaging, in which the “tool” is the ultrasound probe and the “workpiece” is the patient. Images reproduced from FUNdaMENTALS of Design, page 3-24, by Slocum [99], and from <https://www.osha.gov/SLTC/etools/hospital/sonography/images>.

As discussed at length in Section 2.2, hand-held devices can be either patient-grounded or earth-grounded, depending upon whether the sonographer rests his/her hand or arm upon the patient. If, as illustrated<sup>3</sup> in Fig. 1-6 (left), the sonographer’s hand is outstretched, with no support on the patient, the configuration is categorized

<sup>2</sup>For an excellent discussion of several of these systems from a different perspective (and in French), see Al Bassit’s Ph.D. thesis [14].

<sup>3</sup>images are reproduced from (L-R): <http://www3.gehealthcare.com>, <http://www.robosoft.com/>, <http://www.ece.ubc.ca/tims>. Accessed April 2014.

as *earth-grounded* (right), because the force goes through the sonographer's arm, through his/her body into the floor, through the floor, up through the patient's bed, and through the patient back to the ultrasound probe. If the sonographer rests his/her arm or hand upon the patient, which is common in sonography, the configuration is *patient-grounded* (center), because the force goes through the sonographer's hand and directly into the patient—a much smaller structural loop.

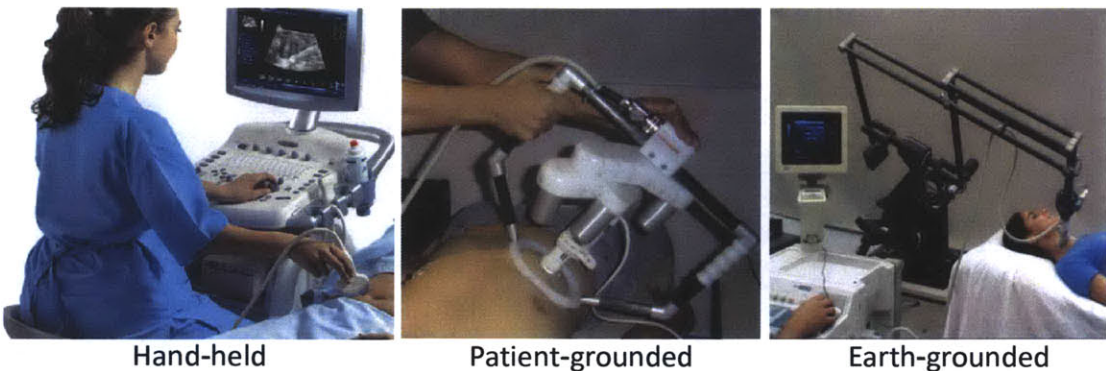


Figure 1-6: Illustrations of the structural loop—i.e., the force path through the device (or sonographer's arm) from the ultrasound probe to the patient. As discussed in Section 2.2, the hand-held configuration can be considered either earth-grounded or patient-grounded, based upon whether the sonographer rests his/her arm or hand upon the patient.

The configuration of the structural loop has a number of important implications. If the loop is patient-grounded, then the acquisition state will be measured with respect to the patient's own coordinate system. If the patient moves (e.g., due to respiration, heartbeat, or other voluntary/involuntary motion), then the device will move along with the patient, and accurate patient-referenced position measurement will be maintained. If the patient leaves and returns a period of time later, and the device is placed at the same location on the patient's body (based on anatomical features, for example), the images could be acquired at the same patient location. If, on the other hand, the device is earth-grounded, acquisition state will be measured with respect to the world. Patient motion will cause contact forces and torques to change because the device is fixed to the ground. If the patient leaves and returns at a later time, when the device is placed in contact with the patient at the same

anatomical location, the device joint angles will be at a different configuration.

In machine design, shorter, closed structural loops generally have higher stiffness and higher accuracy. This means that reducing the size of the structural loop reduces the constraints on stiffness and joint position sensor accuracy, allowing the device to be lighter and potentially cheaper. Therefore, when designing systems that control ultrasound probe acquisition state, we generally expect systems with smaller structural loops to be less expensive and have higher position accuracy.

### 1.3.2 Discussion of the Prior Art

#### Degrees of Freedom

In the discussion that follows, numbers in parentheses refer to the labels in Fig. 1-4. In Fig. 1-4, we see that the systems differ widely in terms of the number of DOFs. The zero- and one-DOF systems are all hand-held, while the two- and higher-DOF devices, which are all too large to be hand-held, are either patient-grounded or earth-grounded. Eleven of the 33 systems can control all of the probe's six DOFs. The Boctor (32) and Mitsuishi (33) systems are both over-actuated; the extra DOF can be used to allow the imaging target to be positioned in a more convenient or comfortable location. All of the six- and higher-DOF systems are earth-grounded. Because earth-grounded systems do not need to be comfortably-supported by the patient or held in the hand, there are fewer size and mass constraints, which means the systems can have more DOFs.

#### Hand-held systems

In Fig. 1-4, we see that 10 of the 33 systems presented are hand-held. With the exception of the passive force-measuring probes ((1) and (2)), all of the hand-held systems have one linear DOF, which is oriented along the axis of the probe. The devices by Sandrin (9), Bercoff (10), Echosens (3), Azar (4), and Rivaz (5) are all designed for vibro-elastography, in which the ultrasound probe is vibrated at high frequencies, launching shear waves into the tissue. Shear wave propagation speed is

measured with high-speed imaging in order to calculate the elastic modulus of the tissue. Shear wave imaging is discussed in detail in Section 7.3.2.

The devices by Marchal [63], Osaka [81], and Matsumura [65], have longer ranges of motion. Marchal [63] designs a one-DOF haptic device that uses a linear actuator to feedback to the sonographer the force encountered by the slave robot. Osaka [81] and Matsumura [65] present single-DOF handheld ultrasound imaging systems with varied actuation strategies. Osaka describes rack-and-pinion-driven and hydraulically-actuated devices, while Matsumura details a system driven by a remote linear actuator via a flexible cable, surrounded by a non-compressible housing. To our knowledge, there exists no physical implementation and no clinical studies have been performed with either the Matsumura or Osaka systems.

The instrumented, 0-DOF force-measuring ultrasound probes of Burcher [25], Chadli [29], Salcudean (not pictured)[91], and Han [49] (not pictured) measure one or more of the probe's three contact forces and three contact torques, in addition to one or more of the probe's three orientation angles  $\phi$ - $\theta$ - $\psi$ . Burcher [25] and Han [49] present a system that consists of a passive unactuated ultrasound probe equipped with a force sensor and a stereoscopic positioning system. The force and position are recorded each time an ultrasound image is gathered. The sonographer could use the real-time force, torque, or angle readouts from these systems to manually control the acquisition state of the probe.

There is also work to use the skin's natural features to encode the probe's position and orientation with respect to the patient's body. Sun [105], [106] uses a probe-mounted camera to record video of the skin surface during scanning. Using visual SLAM methods, the position and orientation of the probe is measured, and a real-time GUI helps the sonographer to place the probe at the target location.

### Patient-grounded systems

Eight of the 33 systems are patient-grounded. Vilchis (18)[110] presents a three-DOF device that is strapped to the patient by a series of belts, which are driven by motors secured to the examination bed. The Syrtech (14), Teresa (15), Estele (19), and

Otelo (21 & 22) systems are similar devices that control 3-6 of the ultrasound probe's DOFs. All five devices are held against the patient's body by a sonographer, while the ultrasound probe is moved. The two systems by Najafi (16 and 20) employ a novel linkage design to manipulate the ultrasound probe in 3 or 4 kinematically-decoupled degrees of freedom. The spring-counterbalanced system rotates the ultrasound probe around a remote center of motion.

### **Earth-grounded systems**

Fifteen of the 33 systems are earth-grounded. With the exception of #'s (11), (17), and (27), all of the earth-grounded systems generally consist of a long arm reaching over the patient with the ultrasound probe mounted at the endpoint. In these systems, the patient is moved into the workspace of the robot. Salcudean [91] creates a six-DOF teleoperated system that can be used to track the length of the carotid artery. The device is anchored to a table next to the patient and has a long arm with an ultrasound probe at the endpoint that reaches to the patient. Degoulange [84] presents a six-DOF robotic arm that can similarly be used to position an ultrasound probe at a desired contact force with respect to the patient. Vilchis-Gonzalez [112] developed a three-DOF dual remote-center robot that manipulates the probe to achieve two localized rotational- and one linear-DOF. The device is suspended over the patient by an external structure. These systems have a large workspace and can reach a wide area of the patient's body, although their size and level of complexity limit their portability and ease of use.

There are a number of systems that control exactly two of the probe's rotational DOFs. Schlosser [95] presents a tele-operated manipulator with two actuated rotational DOFs and three un-actuated, locking DOFs for ultrasound imaging during radiotherapy beam delivery. Goldberg [46] demonstrates a robotic ultrasound system that employs the Stoianovici 3-DOF arm [104] to rotate the probe in pitch and yaw with one translational DOF. Gumprecht [48] shows a 4-DOF system that can rotate the ultrasound probe in pitch and yaw DOFs (in addition to two translational DOFs), while the probe images through a water-filled bag. In the author's master

thesis [40], a device was presented that rotates the ultrasound probe in pitch and roll DOFs about a remote center of rotation.

### Tele-Echography

Many of these systems were developed for teleoperated ultrasound (also known as *tele-echography*) imaging, in which a sonographer manipulates a joystick or other hand-held device, the positions and orientations of which are measured, digitized, and transmitted electronically to a slave device, which manipulates the ultrasound probe according to the sonographer's gestures. This framework enables the sonographer to be in a different location than the patient and could be employed when a skilled sonographer is not available to conduct an exam (assuming that the device is available). The Syrtech (14), Teresa (15), Estele (19), Otelo (21 & 22), Mitsubishi (33), TER (18), Masuda (27), Najafi (16 & 20) robots were all developed for tele-echography applications.

## 1.4 The Importance of Contact Force

As discussed, the acquisition state can be characterized by a number of parameters, including the 3 Cartesian coordinates (X-Y-Z), 3 Eulerian angles ( $\phi$ - $\theta$ - $\psi$ ), their derivatives, as well as the 3 contact forces and 3 contact torques. The devices presented in this thesis all control or measure at least one of the acquisition state variables. In terms of image quality, sonographer level of experience and health, and diagnostic capabilities, contact force is one of the most important of these variables. The reasons why the contact force is important are discussed below:

1. *Tissue deformation*: Contact force deforms tissue.
2. *Sonographer fatigue & injury*: Contact force has been implicated as a risk factor in sonographer fatigue and musculoskeletal injury.
3. *Measure mechanical properties*: Varying the contact force while measuring tissue displacement can yield a measurement of tissue mechanical properties, which

correlate to health.

To better understand the importance of contact force, it is worthwhile to highlight some of the reasons why sonographers apply varying forces over the course of exams. From conversations with sonographers, as well as a search of relevant literature, the following (incomplete) list can be made of some of the reasons to apply high forces:

1. Deeper tissues are easier to see [10]. Ultrasound probes are typically depth-limited to 12 cm. Therefore, to see deeper structures, it is necessary to press with a high force in order to compress superficial tissue layers and bring the deeper layers within the field of view. For patients with thicker fat layers, the tissue of interest might be even deeper, and require even more force to bring it within the field of view.
2. Displace tissues for needle biopsy [10]. When performing biopsies, in which the needle must be inserted into the desired structure without perforating other structures, it is sometimes necessary to apply high amounts of force in order to push structures away from the needle's path.
3. Assess compressibility of veins in deep-vein thrombosis (DVT) exams. In DVT, a blood clot (thrombus) forms in a deep vein, impairing circulation. The thrombus can detach and travel to the lungs in a life-threatening complication called pulmonary embolism. To test for the presence of thrombus with ultrasound, the probe is placed in contact and the vein in question is imaged. Pressure is applied with the probe in an effort to collapse the vein. Because unobstructed veins typically collapse under sufficient force, the failure of the vein to collapse could indicate the presence of a thrombus ([9] is a video of the process).
4. Better acoustic coupling. A certain minimal amount of contact force is necessary in order to ensure that the entire face of the probe is in contact with the tissue; probe/skin contact area can be increased by pressing harder.
5. Displace bowel gas [12].

### 1.4.1 Contact Force and Tissue Deformation

One of the unique aspects of ultrasound imaging is that it requires physical contact with the patient. Variations in the contact force lead to variations in the ultrasound image due to tissue deformation, and make the images difficult to reproduce at a later date [25]. Fig. 1-7 illustrates that differences in probe contact force can lead to different ultrasound images of the same tissue even though the internal structure of the tissue has not changed. The left image of the basilic vein, acquired at 1 N of contact force using the force-controlled ultrasound probe discussed in Chapters 5 and 6, depicts the vein in a nearly circular shape. In the right image, as the force increases to 5 N (a typical force for vascular imaging [91]), the vein is almost completely collapsed. The images are difficult to directly compare; for instance, if the images were acquired at different points in time, it would be challenging to detect longitudinal change. Or, during biopsy, the collapsed vein would be more difficult to target with a needle. If instead the contact force were consistently applied, it would be easier to visually compare the images and the vein could be more precisely targeted.

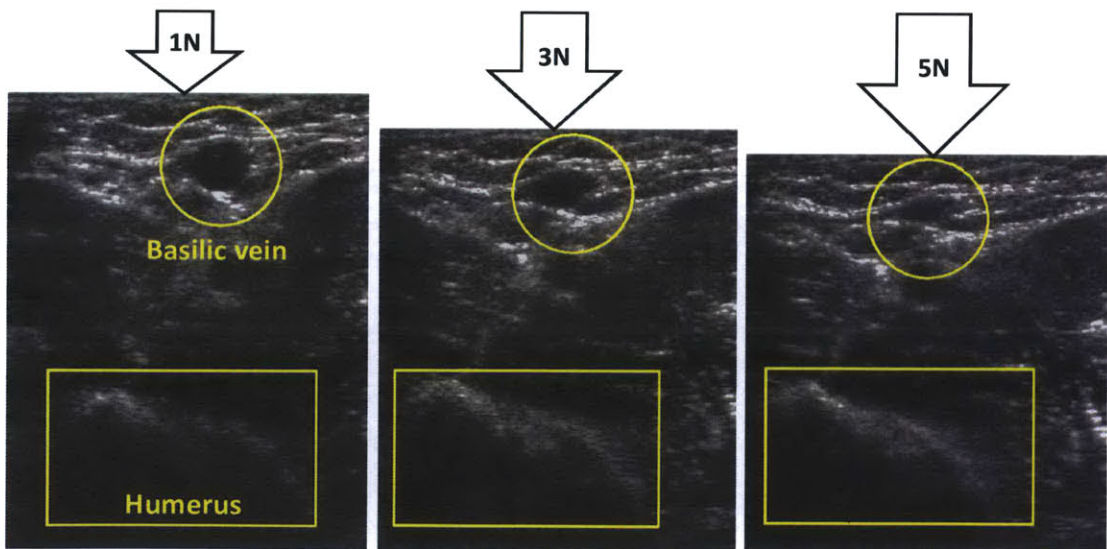


Figure 1-7: The basilic vein imaged at three different contact forces. “N” refers to Newtons of force. The images are difficult to compare due to the different levels of compression.

Image repeatability, and therefore diagnostic quality, could be improved by im-

proving the repeatability of the contact force.

### 1.4.2 Contact Force and Sonographer Fatigue & Injury

As discussed at length in Section 3.2, contact force has been implicated as a major risk factor in fatigue work-related musculoskeletal disease (WRMSD) amongst sonographers. Of the approximately 110,000 sonographers in the United States [2], more than 90% scan in pain [89], and one-in-five will experience a career-ending injury [1]. Little is known about the correlations between contact force and injury, but it is hypothesized that holding the probe in awkward positions at high forces for long periods of time could be an important factor. Given the high prevalence of injury, there is great interest in understanding the causes of WRMSD.

### 1.4.3 Contact Force and Mechanical Properties Estimation

As discussed at length in Chapter 7, the mechanical properties of tissue can be measured by varying the contact force of the probe while recording the force-displacement-image variation. In shear wave imaging, the ultrasound probe is moved with small, sub-millimeter amplitudes at high frequencies, generating shear waves. The shear wave propagation speed, which can be measured with ultrasound, directly correlates to the elastic modulus of the tissue. The elastic modulus, in turn, is related to the health of the tissue; tumors, for example, are stiffer than healthy tissue.

Because tissue exhibits non-linear stress-strain characteristics, the measurement of the elastic modulus is dependent upon the preload force. In current practice, contact force is neither measured nor controlled, leading to limitations on the repeatability of elasticity measurements. By measuring and/or controlling the contact force, the elastic modulus could be more accurately estimated.

Fig. 1-8 highlights the preload dependence of the elastic modulus measurement. In the three images, which are taken at different preload forces from 1N to 18N, the elastic modulus of a particular region of interest (white circle) is presented in white text in units of kPa. The colored region corresponds to elastic modulus; red indicates

stiffer, blue indicates softer. The colormap scale, which is the same for all images, is shown on the bottom right. Here we can see, both qualitatively and quantitatively, that the elastic modulus estimate is strongly dependent upon the preload force. For example, in the 1N image, the elastic modulus of the region of interest is 21.1 kPa (blue), while in the 18N image, the elastic modulus is 64.1 kPa (red) – a factor of three difference.

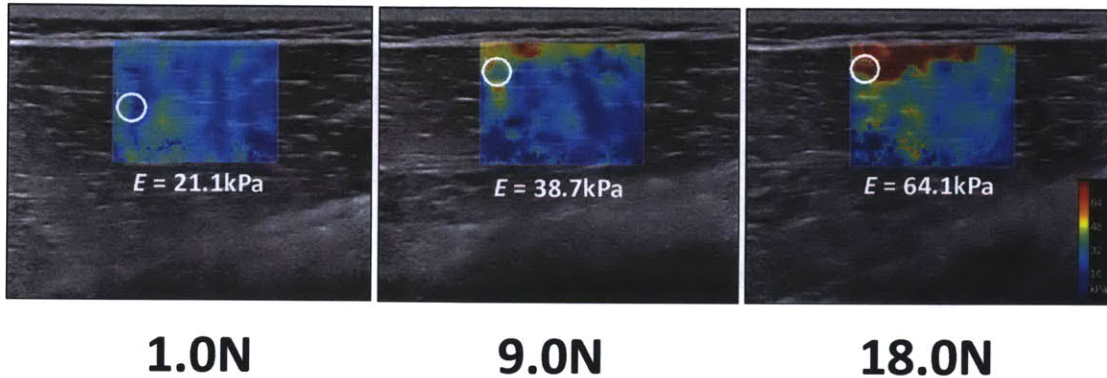


Figure 1-8: Elastograms of the quadriceps at 1N, 9N, and 18N preload forces. The colored region indicates the elastic modulus of the tissue; the colormap scale, which is the same for all three images, is depicted in the lower right of the 18N image. The elastic modulus estimates, expressed in kPa, are calculated for the region of interest highlighted by the white circle. It is evident in these images that variations in preload force result in different estimates of elastic modulus.

Both Figs. 1-7 and 1-8 point to the need for systems which can help the sonographer achieve better control over the contact force in order to obtain more repeatable images and more repeatable estimates of tissue elastic properties.

## 1.5 Thesis Scope

This thesis describes the design and evaluation of three hand-held electromechanical devices that measure and/or control ultrasound probe contact force. The three devices were designed to address each of the three important attributes of contact force from Section 1.4, as listed below:

1. *Tissue deformation:* Force-controlled ultrasound probes 2 & 3.

2. *Sonographer fatigue & injury*: Force-measuring probes: Series 1 & 2.
3. *Measure mechanical properties*: High-speed dynamic imaging probe.

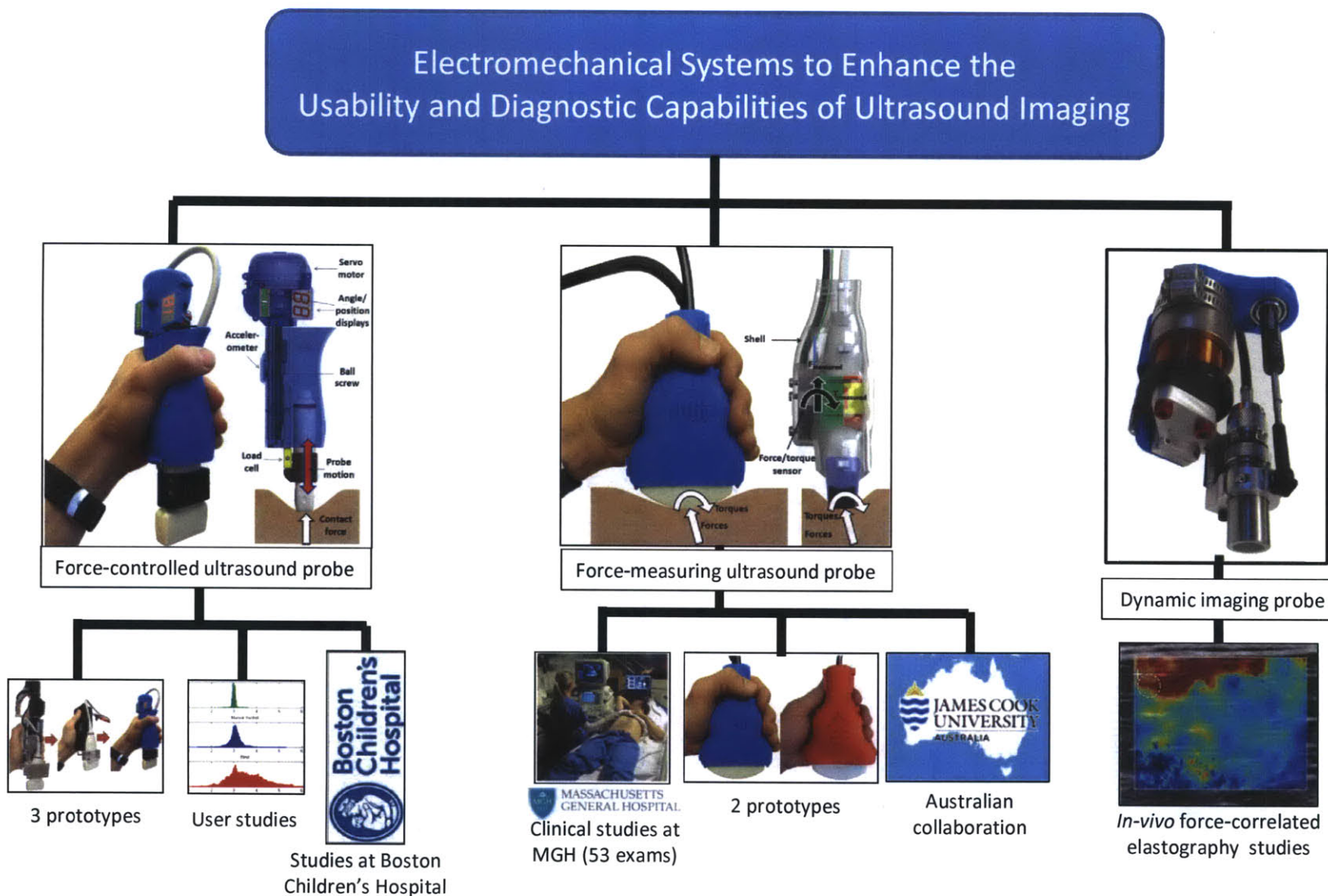
Brief descriptions of the three systems presented in the thesis are as follows:

1. Force-measuring ultrasound probe: A non-actuated device that measures contact forces, torques, and orientation angles of the ultrasound probe. The device, featuring a novel mechanical system that permits rapid probe attachment/detachment, was used in the first rigorous clinical study to measure contact forces and torques. Data are presented and analyzed with respect to patient and sonographer characteristics. An improved prototype was developed for a collaboration with an Australian University.
2. Force-controlled ultrasound probe: A single-DOF ball screw-driven device that controls the relative contact force between the ultrasound probe and patient. By attenuating hand tremors and providing a programmable contact force, the device reduces the necessary level of sonographer skill and improves acquisition state repeatability. Tremor attenuation is quantified through user studies. Early results demonstrating the clinical relevance of force control in the detection of Duchenne Muscular Dystrophy at Boston Children's Hospital are presented.
3. High speed dynamic imaging probe: A single-DOF voice-coil actuated device that enables high-bandwidth constant-force ultrasound scanning, as well as the measurement of tissue elastic properties at programmable preload forces. *In vivo* results are presented and compared with the literature.

A hierarchy of the systems and subsystems presented in the thesis is shown in Fig. 1-9.

The three systems are presented in the order listed above in Chapters 3- 7. Chapter 2 describes the process for the design of a force-controlled ultrasound probe for an arbitrary application, and specifically within the context of abdominal and musculoskeletal imaging. Conclusions and suggested future work are presented in Chapter 9.

Figure 1-9: The hierarchy of the systems and studies presented in this thesis.  
48



# Chapter 2

## “Meta” Design

In this chapter, we present the design process that can be followed to design a force-controlled ultrasound probe for an arbitrary imaging application. First, we present an overview of the design process, and characterize the inputs and the outputs. Next, we present the important functional requirements, and discuss the three most critical functional requirements: the range of motion, the power, and the contact force. Finally, we discuss in detail how the necessary range of motion and power are determined for an arbitrary ultrasound imaging application. Chapter 3 discusses how the necessary contact force is determined. We calculate the necessary values of the critical functional requirements specifically within the context of abdominal and musculoskeletal imaging, for which the force-controlled probe was designed.

We present a deterministic design process modeled after that discussed by Prof. Slocum in FUNdaMENTALS of Design [99]. We follow a coarse-to-fine, qualitative-to-qualitative approach. In this process, we start out with an abstract set of high-level qualitative objectives for the device; i.e., we answer the question: “what does it need to do?” Next, we translate the qualitative objectives into a list of functional requirements (FRs). Based upon investigation of what the device needs to do, we quantify the functional requirements with numbers. Next, design parameters (DPs)—potential mechanisms or solutions that accomplish the functional requirements—are brainstormed and analyzed for the most critical module or subsystem. The risks associated with the design parameters are assessed and countermeasures are devel-

oped. The most promising DP is selected and we proceed with the design of the next-most-critical subsystem. The process is followed until all subsystems have been designed.

An overview of the design process is shown in Fig. 2-1. The objective is to design a device that controls ultrasound probe contact force for a specific type of ultrasound exam. The design process proceeds as follows: given the specific intended use (ultrasound exam type), the typical range of sonographers, and the typical range of patients, specify the functional requirements the device must meet, and suggest which design parameters (e.g., actuator, force sensor, and other components) would best satisfy the functional requirements.

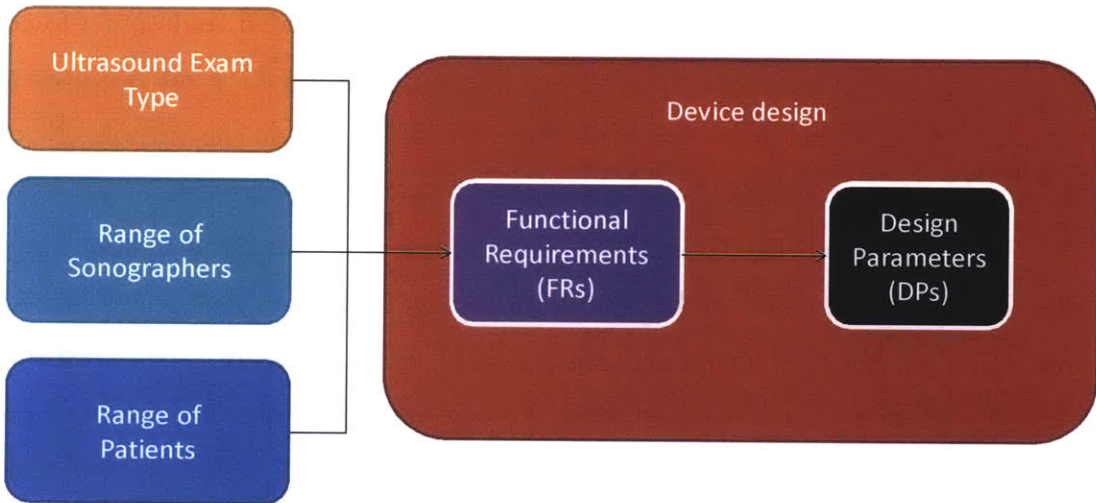


Figure 2-1: Overview of the design process. The input is the intended use, typical range of sonographers and patients, and the outputs are the device functional requirements and suggested design parameters.

Each of the inputs shown on the left side of Fig. 2-1 is characterized by a number of different variables, as shown in the following lists.

### 1. Ultrasound Exam Type

- (a) *Type of exam*: For example, abdominal, vascular, needle guidance, etc.
- (b) *Measure or control force?*: The design can likely be much simpler if force measurement alone is sufficient and no force control is necessary.

- (c) *Exam duration.*
- (d) *Scan characteristic dimensions and area.*
- (e) *Probe inclination angles.* To what angles must the probe rotate?
- (f) *Workspace constraints:* Are there any obstructions associated with the exam that limit the workspace? For example, do the neck or legs interfere with the probe?
- (g) *Contact forces & torques:* What is the range of forces expected to be applied?
- (h) *Ultrasound probe:* What are the dimensions, mass, and shape of the probe?

## 2. Range of Sonographers

- (a) *Movement characteristics:* What are the motion and frequency characteristics due to tremors and other involuntary motion?
- (b) *Arm & hand dynamics:* Stiffness, damping, and mass.
- (c) *Arm range of motion:* How large of a workspace can the arm cover?
- (d) *Fatigue characteristics:* How does the sonographer's hand/arm move when fatigued?
- (e) *Force & position control capabilities:* How accurately can an unassisted sonographer control the probe acquisition state?
- (f) *"Heavy-handedness":* Some sonographers are known to apply consistently higher or lower forces than others.

## 3. Range of Patients

- (a) *Movement Characteristics:* What motion should be expected due to respiration, heartbeat, and other voluntary/involuntary motions?
- (b) *Tissue stiffness:* Potential implications for controller stability.
- (c) *Scan area.*

- (d) *Age & level of cooperation:* Special usability considerations may apply for less cooperative patients.
- (e) *Mobility:* Can the patient move to accommodate the probe? (Typical during abdominal scanning, for example.)

The important functional requirements are articulated in the following list.

**Functional Requirements:**

1. *Range of motion:* The necessary stroke length, in the case of one linear DOF.
2. *Power requirements.*
3. *Force range and resolution.*
4. *Form factor:* grip style; limits on mass, size, and length.
5. *Feedback:* Any need to inform the sonographer of the actuator position or inclination, for example?
6. *Moving mass.*
7. *Control:* Necessary bandwidth, tremor attention characteristics, stability with different environment stiffnesses, ergonomic considerations (such as endpoint avoidance).
8. *Cost.*

Finally, the most critical design parameters are listed, along with examples:

**Design Parameters:**

1. *Actuator:* voice coil, rack and pinion, ball screw.
2. *Linear constraint:* bearing, bushing, or flexure.
3. *Power transmission:* gears, pulleys, lead/ball screws.
4. *Sensors:* load cells with 1-6 axes, pressure sensors.

5. *Component layout*: orientation of actuator, bearings, and transmission.
6. *Control techniques*: endpoint avoidance, soft limits.
7. *User feedback*: LEDs, digital displays, audio cues.

At this point, it is informative to highlight several examples of the interconnections between the input variables, the functional requirements, and the design parameters. Three examples are discussed below.

- *Range of motion*: The necessary range of motion of the device, also referred to as the necessary stroke length, is influenced by: 1) the characteristic scan dimensions, and 2) the motion characteristics of the sonographer’s hand and that of the patient. We show in Section 2.2 that scanning larger areas translates into a longer necessary range of motion. Intuitively, we expect that larger-amplitude hand tremors and patient motion also necessitate longer range of motion. The range of motion functional requirement, in turn, influences the type of actuator that is selected, as well as the way the components are laid out.
- *Power requirements*: The necessary power that the device must supply is governed by: 1) the contact forces, 2) the mass of the ultrasound probe, and 3) the tremor characteristics of the sonographer’s hand. Higher contact forces, heavier probe, and higher-amplitude sonographer hand motion all contribute to higher power requirements. The power requirement guides the selection of the actuator.
- *Contact force range*: The force capabilities of the device are influenced by 1) the forces typically encountered during that particular exam, 2) whether or not the sonographer is “heavy-handed,” and 3) the size of the patient. We show in Section 3.7.1 that heavier patients require more force. The maximum force that the device must be capable of applying influences the selection of the actuator, as well as the components in the power transmission, which must be able to withstand the forces.

### **2.0.1 Range of Ultrasound Exams**

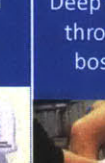
Next, we investigate the first input into the design process, namely the ultrasound exam type. Ten of the most common types of ultrasound exams are listed in Fig. 2-2, along with some of the variables associated with each exam. In Fig. 2-2, we see that exams vary considerably in terms of the size and shape of the probe used, the scan area, as well as the maximum forces applied.

Fig. 2-3 shows the distribution of the five types of ultrasound exams most typically performed on Medicare patients [78]. Data for the general population could not be found. Although this represents data from only a very limited population (i.e., only people  $>65$  years of age), relevant conclusions can still be drawn. The most commonly-performed exam is the cardiovascular exam, constituting more than 50% of all exams. In conventional trans-thoracic cardiovascular ultrasound imaging, the probe is held between the ribs, and images through the rib-to-rib gap. In this scenario, since the ribs support the entire contact force of the probe and, due to their high stiffness, the underlying tissue is not deformed, the use of a force-controlled probe is not necessary. If instead the heart is imaged through the soft tissue below the rib cage, force control would be more relevant. The other 50% of exams are performed on soft tissues, and force control could be used to enable more repeatable imaging in these scenarios.

### **2.0.2 Range of Sonographers**

Next, we investigate the parameters associated with the second variable: the sonographer. The most important variables related to the sonographer are listed in Table. 2.1. The hand tremor frequency and amplitude characteristics were obtained from the Micron microsurgical tool project [62], and the power spectrum versus frequency is reproduced in Fig. 2-4. From the plot, we see that a majority of the tremor amplitude lies below about 10 Hz; for example, the tremor power is ten times higher at 0.1 Hz than at 10 Hz. As discussed in Section 5.6.5, in the literature, tremors at frequencies higher than 10 Hz are frequently neglected.

Figure 2-2: A sampling of ten of the most common types of ultrasound exams, along with the parameters associated with each exam.

Ultrasound Exam Types										
Exam type	Abdominal	Cardiac	Musculo-skeletal	Needle guidance	Vascular		Ophthalmic	Neonatal fontanelle	Transient abdominal	Small structures
										
Purpose/Example	Abnormality detection; fetal; FAST exam	Trans-thoracic echocardiogram	Quadriceps scan	Biopsy; central line placement; regional anesthesia	Atherosclerotic plaque detection	Thrombus detection	Abnormality detection	Infant neurological exam	Liver elasticity measurement	Musculo-skeletal; vascular
Parameter	40 x 40	25 x 25	10 x 15	4 x 4	15 x 40	10 x 15	1 x 1	5 x 5	5 x 5	3 x 3
Scan area (cm x cm)	40 x 40	25 x 25	10 x 15	4 x 4	15 x 40	10 x 15	1 x 1	5 x 5	5 x 5	3 x 3
Tissue stiffness w/probe (N/m)	800 [1]	800 [1] (tissue) >>800 (rib)	~800	800 [1]	800 [1]	~ 800	~800	?	~800	~800
Force: max/continuous [N]	36/8 [3]	< 40/10	< 40/10	< 40/10	< 10/3	< 60/15	< 5/2	< 15/4	< 20/5	< 10/5
Workspace constraints	Table	Table	Appendages; table	Needle; guide	Head, shoulder	Leg, arms; table	Eye socket; nose	Table	Table	Table
Probe contact area (mm x mm) [4]	10x23 – 17x74	19x28	10x23 – 17x74	11x35	10x23 – 18x62	10x23 – 18x62	10x10	17x28	10x10	4x18
Probe mass (g)	 200-400	 20-150	 200-400	 150-250	 20-200	 20-200	 200	 150	 20-50	 20

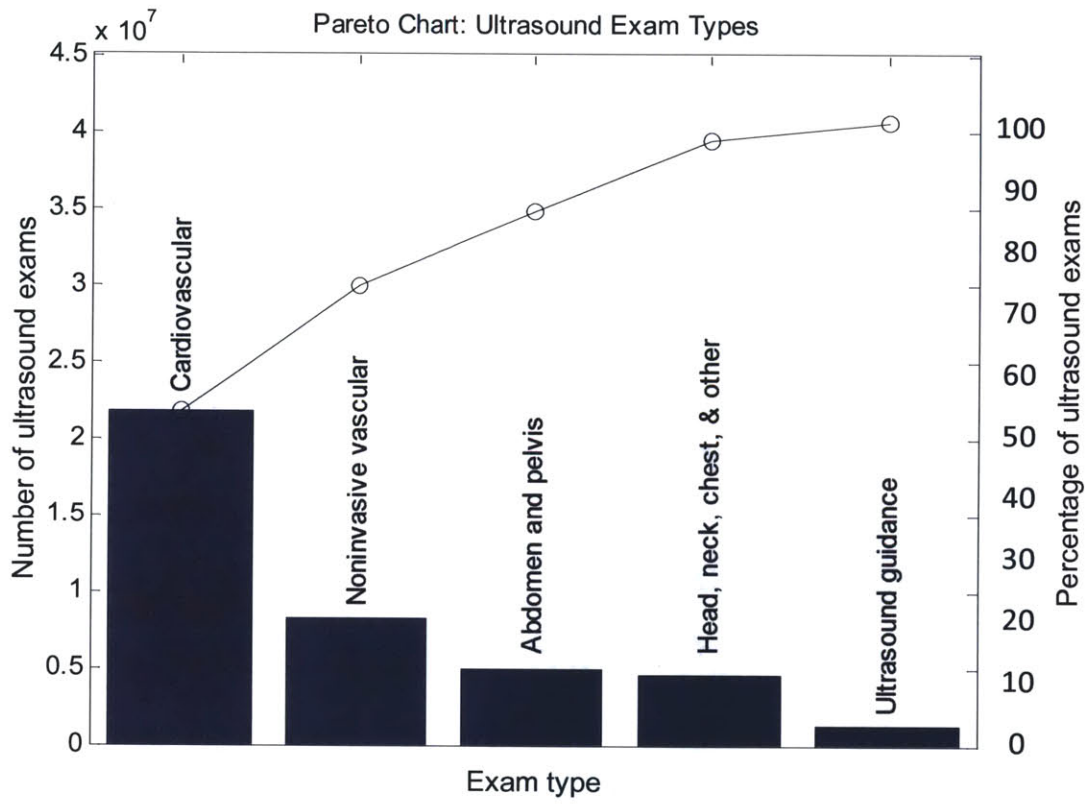


Figure 2-3: A Pareto Chart showing the distribution of five most commonly performed ultrasound exam types. Data are from the GAO Analysis of Medicare Part B claims for 2005, so it therefore represents exams for patients  $>65$  years [78].

Table 2.1: Parameters associated with the sonographer.

Parameter	Value
Hand tremor	Frequency [62] $<10$ Hz
	Amplitude $<10$ mm
Arm/hand characteristics	Stiffness [41] 5500 N/m
	Damping [41] 27 Ns/m
Force	Mass 3 kg
	Workspace 1.5 m x 1.5 m
	Control capabilities [41] $\pm 0.8$ N for 30 s
	Max [35] 36 N
	Guideline [77] "Use minimal transducer pressure"

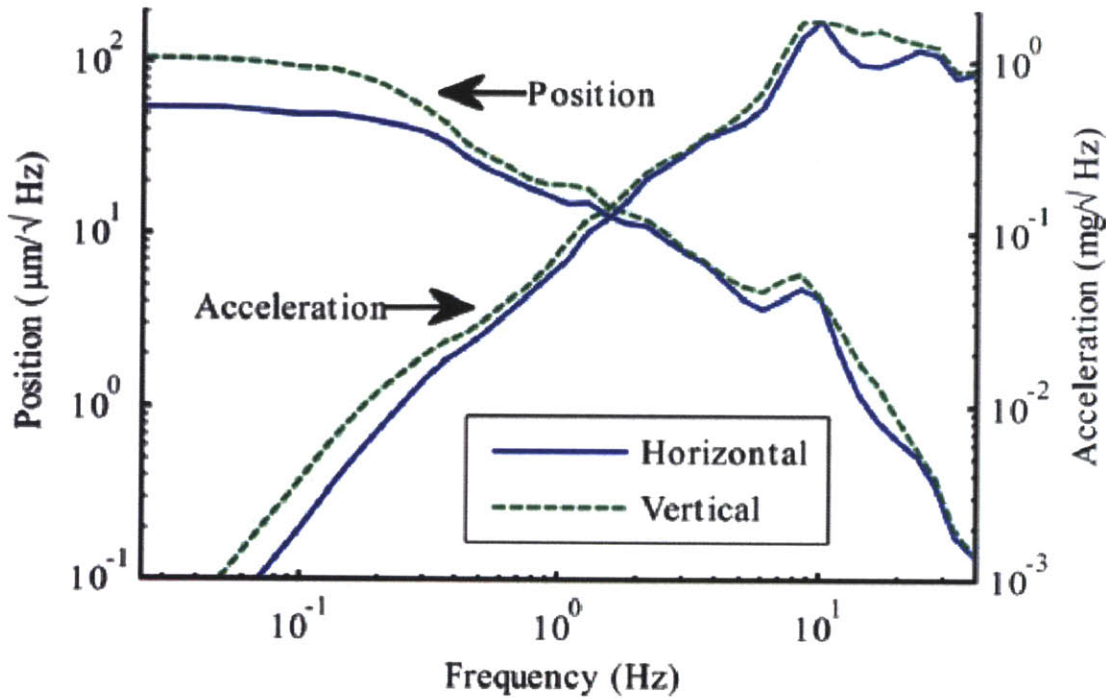


Figure 2-4: Hand tremor power spectrum, from MacLachlan [62]. A majority of the tremor characteristics lie below 10 Hz.

### 2.0.3 Range of Patients

The third category of input variables deals with the parameters associated with the patient. Ideally, the device should be designed for the average patient, which we define as the patient who falls within  $\pm 2\sigma$  (two standard deviations) of the average value of a particular parameter. But, the design must take into consideration the likelihood that the device will be used on some patients who fall outside of the  $\pm 2\sigma$  range. Table 2.2 lists some of the special design considerations that must be taken into account for patients outside  $\pm 2\sigma$  for various parameters.

## 2.1 Most Critical Functional Requirements

Perhaps the most critical first step in the design process is to determine the necessary number of degrees of freedom (DOF) of the device. Because tissue exhibits elastic properties, an increase in strain results in an increase in stress; in other words, indenting tissue with an ultrasound probe causes the contact force to increase. This means

Table 2.2: Special design considerations for patients  $\pm 2\sigma$  from the mean value of the given parameter.

Parameter	(Literature Value), Special Design Consideration(s)		
	$-2\sigma$ patient	Median patient	$+2\sigma$ patient
BMI [11]	(18.5) Less tissue damping, higher stiffness if bony. Smaller scan area	(25.1)	(34) Thicker adipose layers, apply more force. Larger scan area.
Age (years) [5]	(6) Fragile: apply lower forces; smaller transducer; need extra stroke length for uncooperative patients	(37.2)	(68.2) Fragile: apply lower forces
Mobility	Less mobile patients: can't rotate patient into position; device must be less obtrusive to prevent interference		More mobile patients: patient can be moved, enabling more ergonomic probe grip

that in order to control the contact force, it must be possible to move the ultrasound probe respect to the patient's tissue. The simplest motion that could control the contact force is one DOF of linear motion. Therefore, for simplicity, it can almost immediately be determined that the system should have one linear DOF.

With the input variables fully characterized, the next step in the design process is to list the mapping between the input variables and the functional requirements. Table 2.3 lists the input variables that influence the seven most critical functional requirements.

It can be argued that the range of motion, the power, and the contact force are the three most important functional requirements in the design of the system. All three of these affect actuator selection, as well as the design of many of the other system components. Therefore, we explore these functional requirements in more detail. First, we explore the necessary stroke length, followed by the power. In Chapter 3, we discuss contact force.

Table 2.3: Mappings between the input variables and the functional requirements.

Device Functional Requirement	Input(s)	
Range of motion	Scan length; tremor characteristics; patient motion	
Power	Exam type; tremor characteristics; actuator type	
Force	Exam type; patient type	
Form factor	Workspace constraints; sonographer hand size	
Feedback	Range of motion: actual vs. target	
Moving mass	Exam type	
Control	Bandwidth	Tremor characteristics
	Stability	Tissue Stiffness
	Force control tolerance	Exam type; study objective (i.e., force control or force measurement?)

## 2.2 Range of Motion vs. Characteristic Scan Length

In this section, we calculate the first of the three most critical functional requirements, namely the necessary range of motion. We demonstrate that the necessary range of motion of the device is positively correlated to the characteristic scan length. Intuitively, one would expect that the range of motion that the actuator must have should be related to the tremor characteristics of the sonographer's hand. Furthermore, one would also expect that if the sonographer scans a larger area or a longer appendage, his/her hand will involuntarily tremor a greater distance than if he/she held the probe stationary. We tested this hypothesis with an OptiTrack V120:Trio infrared 3D tracking system (Natural Point, Inc.), which consisted of a 3-camera infrared tracker and a marker with four infrared-reflective spheres of known dimensions. A human volunteer (who was not a sonographer) held the marker in his hand above the tracker, as shown in Fig. 2-5. To test the effect of different scan lengths, the volunteer moved his arm back and forth with different scan lengths  $L_{scan}$ , while the tracker recorded the vertical height of the marker,  $Z(t)$ . After each test, the total range of  $Z(t)$  (i.e.,  $Z_{max} - Z_{min}$ ), as well as the standard deviation, were calculated.

The user performed this procedure for three different scenarios that corresponded to different structural loop sizes typically encountered during ultrasound imaging.

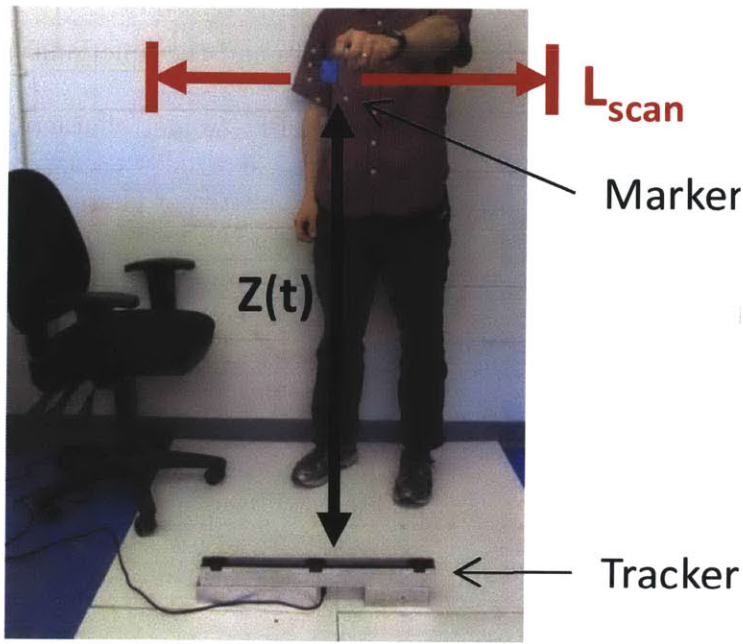


Figure 2-5: To test the effect of scan length upon necessary device range of motion, a human volunteer moved an infrared marker with different scan lengths  $L_{scan}$  above a tracking system, which measured height  $Z(t)$ .

While scanning, sonographers often rest their hand, elbow, or arm upon the patient, and alternate between standing up and sitting down. The three most common configurations are shown<sup>1</sup> in Fig. 2-6. As discussed in Section 1.3.1, smaller structural loops have higher stiffness, and therefore, we expect that smaller structural loops also correspond to less involuntary hand motion during scanning. Hence, we hypothesize that smaller structural loops and shorter scan lengths require lower device range of motion.

To test this hypothesis, the user performed the scans of varying lengths in each of the structural loop configurations in Fig. 2-6. Each scenario was conducted three time to reduce measurement noise. Example  $Z(t)$  versus time plots are shown in Fig. 2-7 for two imaging scenarios.

From Fig. 2-7, at first glance, we see qualitative confirmation that the range of motion in the Z-direction is smaller (and has smaller standard deviation) with

---

<sup>1</sup>Images were borrowed from (L-R): <http://ie.ismycv.com/resources/jobs/health-practitioners/sonographer.aspx>, <http://www.kumc.edu/school-of-health-professions/cardiac-sonography.html>, <https://www.youtube.com/watch?v=YrMsDu2f3U0>. Accessed April 2014.



Figure 2-6: Three most common structural loop configurations encountered during hand-held ultrasound scanning. A: seated, elbow supported. B: seated, elbow not supported. C: standing, elbow not supported.

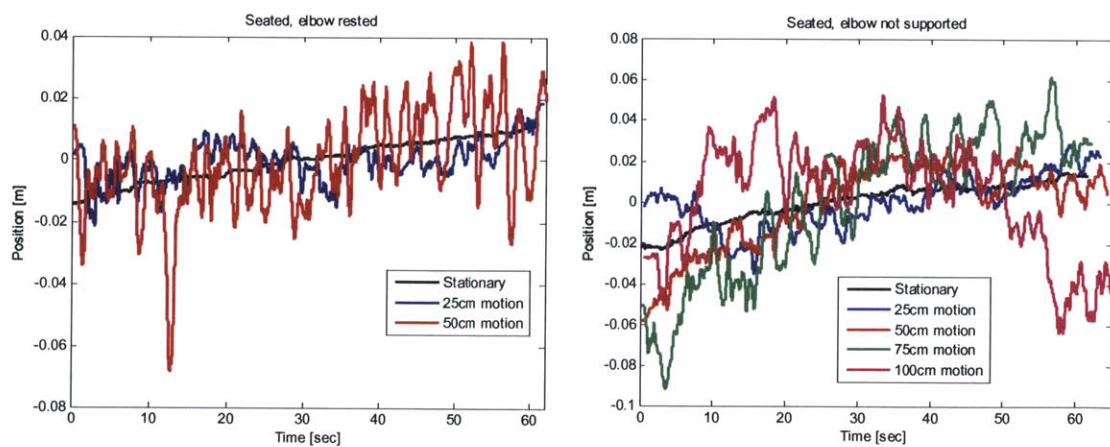


Figure 2-7: Example  $Z(t)$  versus time plots for seated, elbow resting (left) and seated, elbow not supported (right).

stationary imaging (black) than with larger scanning lengths such as 25 cm (blue), 50 cm (red), and 100 cm (pink). A plot of the Z-motion range versus scan length for the three structural loop scenarios is shown in Fig. 2-8, in which each of the three duplicate runs for each scenario have been averaged.

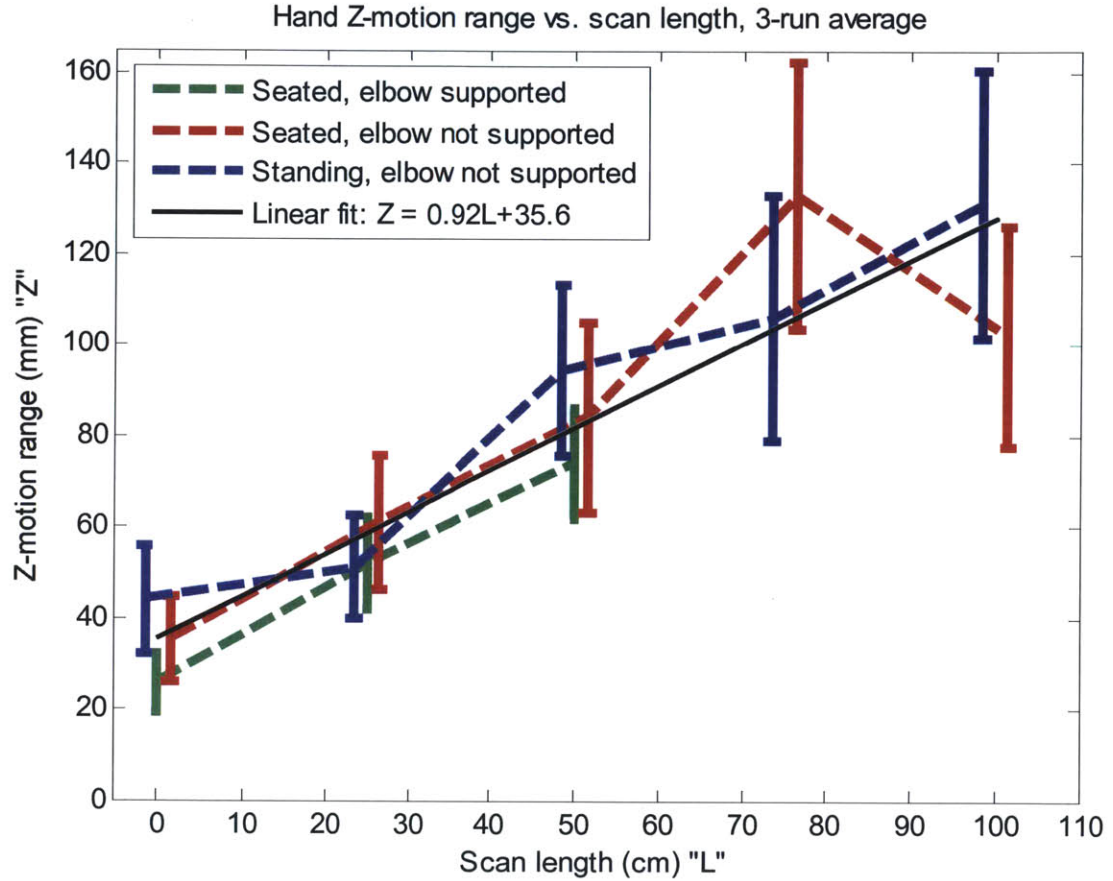


Figure 2-8: Z-motion range versus scan length for the different structural loop scenarios shown in Fig. 2-6. Runs are slightly horizontally offset for clarity. Vertical bars span  $\pm 1\sigma$ , while the middle of the bars is the average. Black line represents linear fit.

In Fig. 2-8, we see that longer scan lengths result in greater Z-motion range, as expected. The standard deviations (height of vertical bars) also increase with longer scan lengths. The smallest structural loop (seated, elbow supported—green trace) shows lower Z-motion range for scan lengths of 0 cm, 25 cm, and 50 cm, as expected (due to the limited range of motion of the elbow and shoulder, it was not possible to scan with  $L_{scan} = 75$  cm and 100 cm when seated with elbow supported). However, the two scenarios in which the elbow was not supported (seated [red], and standing

[blue]), show similar Z-motion ranges for different scan lengths. This suggests that Z-motion range does not depend upon whether the user is seated or standing; it depends most strongly upon scan length and whether or not the elbow is supported.

With regards to device design, the linear fit of  $Z_{range} = 0.92L + 35.6$  (units: L in cm, Z in mm) provides a convenient way of estimating the required range of motion of the device for a given scan length. Let us zoom in on the plot in Fig. 2-8 and focus on the range of characteristic scan lengths from Fig. 2-2, which are all less than about 45 cm. A zoomed-in plot of Fig. 2-8 is presented in Fig. 2-9, with the different ultrasound exam types displayed.

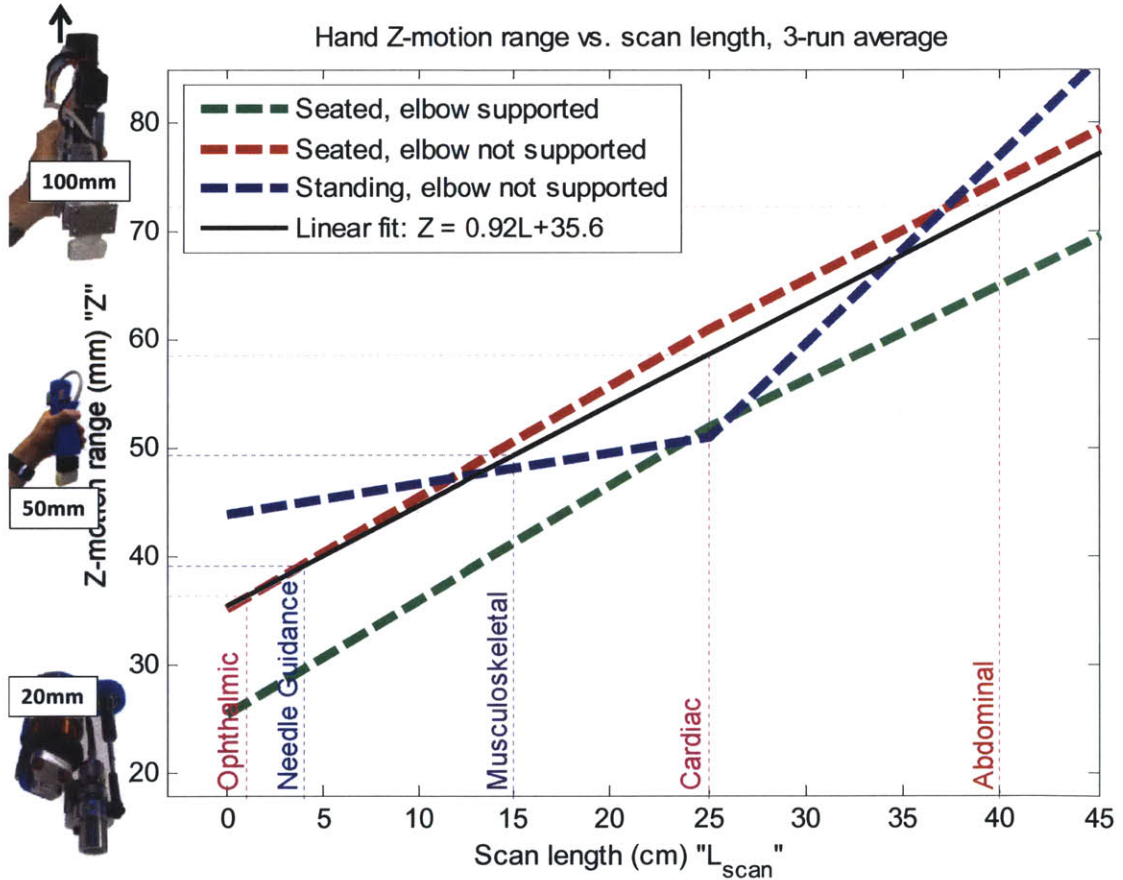


Figure 2-9: Zoomed-in version of Fig. 2-8, with characteristic scan lengths for different types of ultrasound exams displayed. The devices presented in this thesis are shown on the Y-axis; the corresponding stroke lengths are noted.

The exam type with the largest characteristic scan length of 40 cm is abdominal imaging, which suggests, based upon the linear fit, a necessary stroke length of about

70 mm. This is reasonable, because it was found with the first prototype of the force measuring probe (top left of the figure) that a stroke length of 100 mm was more than sufficient when scanning phantoms of similar length [40]. For musculoskeletal imaging, with  $L_{scan} \approx 15\text{cm}$ , corresponding necessary stroke length is 50 mm. This is also reasonable, because the stroke length of the third prototype of the force-controlled probe, shown on the Y-axis, is 50 mm, which was found to be just sufficient for musculoskeletal imaging in the DMD study. For an exam involving nearly stationary imaging, such as ophthalmic, the suggested stroke length is about 35 mm.

Therefore, for abdominal and musculoskeletal imaging, for which the force-controlled probe is designed, we need a range of motion between 50-70 mm. The first of the three most critical functional requirements has now been determined.

### **2.2.1 Influence of Patient Cooperativeness and User Training & Feedback**

Throughout the design of the second and third force-controlled probes, it was found that providing the user with visual feedback (in the form of a linear LED array) to indicate the position of the ball screw carriage, as well as training, helped the user to keep the device within its usable range of motion. It was also found in the DMD study patient motion necessitated greater stroke lengths; uncooperative patients, who might move during the exam, caused the actuator to move with a greater range.

How does this information fit within the context of these studies? The effects of patient motion and sonographer feedback and training are shown in Fig. 2-10. Uncooperative patient motion shifts the necessary stroke length curve up by about 1 cm (shown in gray dotted line), while sonographer training and visual feedback shifts the curve down by about 1 cm (shown in dotted blue-green). Therefore, when designing a device to control contact force, by referring to Fig. 2-10, one can select the necessary stroke length of the device for different ultrasound exam types and different sonographer and patient variables.

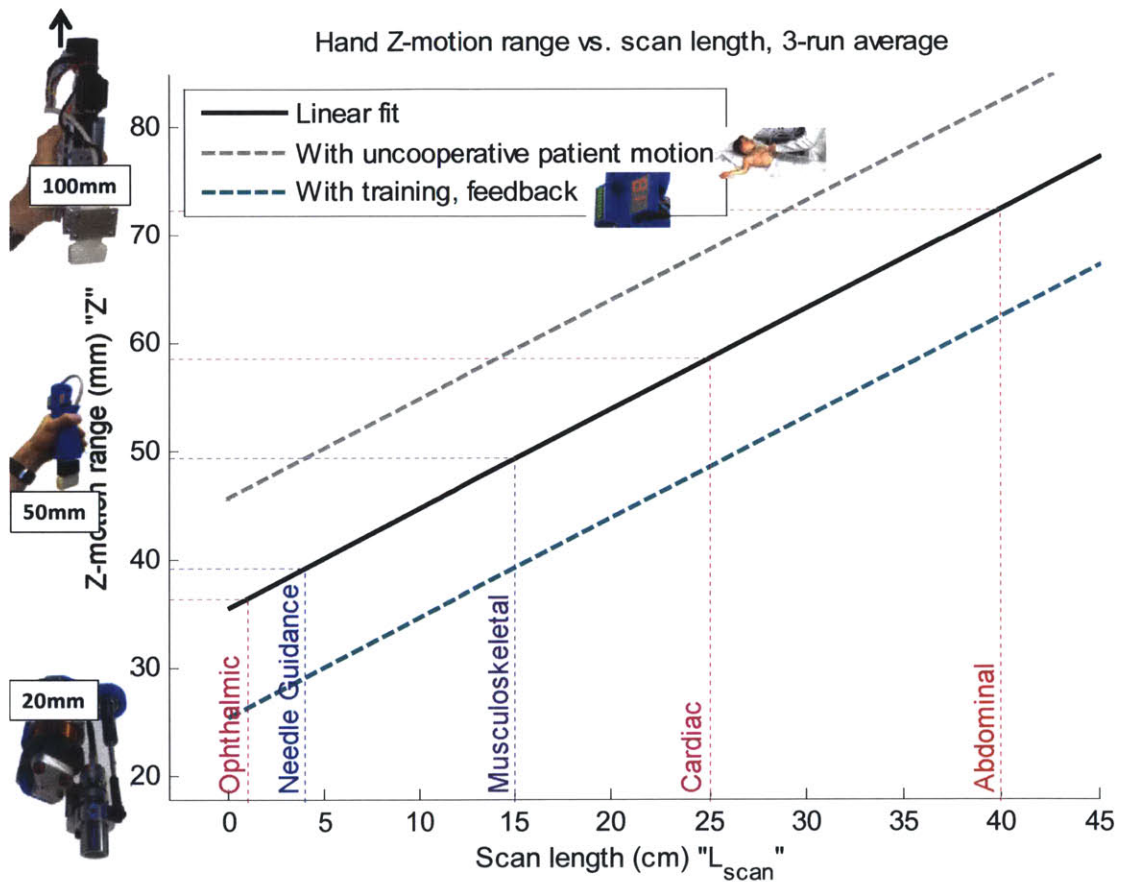


Figure 2-10: Minimum necessary device stroke length versus scan length, with uncooperative patient motion and user training & feedback.

## 2.3 Power requirements

As mentioned, the most critical functional requirements in the design of the device are the necessary stroke length, power, and contact force. In this section, we discuss the power requirements. During ultrasound scanning, we can consider the contact force to consist of a DC bias component along with AC oscillations caused by hand tremors. When using a force-controlled ultrasound probe, the user will still apply the DC bias force, but the device must suppress the tremor-induced AC oscillations to maintain a constant force. We can calculate the necessary device power by calculating the power for both components of the force. *Static power* is consumed to maintain the constant DC bias force while *dynamic power* is used to suppress the oscillating AC component. Next, we discuss the two components in detail.

### Static Power

For many electromagnetic actuators, the actuator force or torque is directly proportional to the applied current,  $I$ . The static power  $P_{static}$  can therefore be calculated from the following simple electrical equation:

$$P_{static} = I^2 R \quad (2.1)$$

Assuming that the constant of proportionality between actuator force  $F$  and current  $I$  is  $K$ , the static power required is then

$$P_{static} = (KF)^2 R \quad (2.2)$$

Thus, the static power can be easily calculated for an arbitrary actuator by knowing the contact force (discussed in Chapter 3), winding resistance  $R$ , and constant of proportionality  $K$ . In Section 5.3.3, we demonstrate that the two actuators that are most appropriate for the range of ultrasound imaging applications are a voice coil actuator (VCA) or a ball screw actuator. We can thus calculate the static power requirement depending upon the actuator type, which is determined by the constant

K:

$$K = \begin{cases} 1/K_a - VCA \\ L/K_t - ballscrew \end{cases} \quad (2.3)$$

Where  $K_t$  is the motor torque constant of the servo (units: Nm/A),  $K_a$  is the force constant of the voice coil (units: N/A), and  $L$  is the ball screw lead in units of length/rotation. For the voice coil in the static case, the force applied to the motor is equal to the force by the ultrasound probe to the patient's tissue.

### Dynamic power

In addition to the static electrical power to hold a constant force, the actuator must also apply mechanical power to move the actuator in order to attenuate hand tremors. Assume that the hand tremors sinusoidally at a frequency  $\omega$  with amplitude  $A$  and position  $x(t)$ , so that

$$x(t) = A\sin(\omega t) \quad (2.4)$$

Therefore, the velocity  $v(t)$  and acceleration  $a(t)$  are given by

$$v(t) = \dot{x}(t) = A\omega \cos(\omega t) \quad (2.5)$$

$$a(t) = \ddot{x}(t) = -A\omega^2 \sin(\omega t) \quad (2.6)$$

If the mass of the probe is  $m_{probe}$ , the force  $F(t)$  required to move the mass is given by

$$F(t) = m_{probe}\ddot{x}(t) = -m_{probe}A\omega^2 \sin(\omega t) \quad (2.7)$$

Since mechanical power  $P(t)$  is given by  $P(t) = F(t)\dot{x}(t)$ , therefore,

$$P(t) = -m_{probe}A^2\omega^3 \cos(\omega t) \sin(\omega t) \quad (2.8)$$

For the purpose of determining the maximum continuous power, the RMS value

of the power is taken. Since the RMS value of the  $\cos(\omega t) \sin(\omega t)$  term is  $1/(2\sqrt{2})$ , the RMS mechanical power  $P_{m,rms}$  applied to the probe is

$$P_{m,rms} = \frac{m_{eff} A^2 \omega^2}{2\sqrt{2}} \quad (2.9)$$

The effective translational inertia  $m_{eff}$  will once again depend upon the type of actuator. Here, we again consider the voice coil and ball screw actuators, which we demonstrate later are most appropriate for the range of ultrasound imaging applications. The effective translational inertia for the two actuator types is thus:

$$m_{eff} = \begin{cases} m_{probe} + J_{rot}/l^2 - ballscrew \\ m_{probe} - VCA \end{cases} \quad (2.10)$$

Where  $J_{rot}$  is the rotational inertia of the ball screw shaft and  $m_{probe}$  is the mass of the ultrasound probe. Once again, we see that the power requirement of the ball screw is related to the square of the lead  $L$ .

Thus, the total power  $P$  required is

$$P = P_{static} + P_{rms} = R(KF)^2 + \frac{m_{eff} A^2 \omega^2}{2\sqrt{2}} \quad (2.11)$$

If we consider a worst-case scenario with tremor frequency of 5 Hz, motion amplitude as high as 10 mm, probe mass of 300 g, and static force of 15 N, the continuous power required by the voice coil is 23 W, while that of the servo + ball screw is only 7 W. It would be prudent to place a suitable safety factor on the power requirement in the case of unexpectedly high forces or tremor amplitudes. In Section 5.3.3, we discuss the selection of the actuator based upon these power requirements.

### 2.3.1 Summary

In this chapter, we presented the process for designing a device to measure and/or control ultrasound probe contact force for an arbitrary imaging application. We characterized the range of possible input variables associated with ultrasound exam type, the sonographer, and the patient. We outlined the most critical functional

requirements for the device (i.e., the range of motion of the device, the power, and the contact force) and identified classes of design parameters, along with some examples, that would fulfil the functional requirements. We mapped the connections between input variables, functional requirements, and design parameters. We investigated the correlations between input variables such as contact forces, ultrasound probe type, hand tremor characteristics, patient motion, and scan length, upon two of the three most critical functional requirements, i.e., the necessary stroke length and power requirement. Experiments were conducted to quantify the relationship between scan length and necessary stroke length.

The range of motion and power were discussed in general and the values for the particular application that we target, namely abdominal and musculoskeletal imaging, we calculated. In the next chapter, we discuss the third critical functional requirement: the contact force.



# Chapter 3

## The Force-Measuring Ultrasound Probe

### 3.1 Summary

This chapter describes the design and experimental evaluation of two ultrasound probes that measure probe contact force. The force-measuring probe has multiple purposes: first, it can be used to determine the third of the three critical functional requirements for the design of the force-controlled ultrasound probe, namely, the contact force. Second, it can be used to help the sonographer to standardize the contact force. Third, it could be used to understand the correlations between contact force and sonographer musculoskeletal injury and fatigue. We discuss its use specifically within the context of abdominal imaging.

In contrast to the force-controlled probe, the force-measuring probes are not actuated, and passively measure contact forces in one or more axes. Two versions of the device, referred to as “Series 1” and “Series 2,” were created, and the design process of each is presented. Series 1 measures contact forces and torques in six axes while Series 2, which is lower cost and more compact, measures force in one axis. Experiments were performed with the Series 1 prototype at Massachusetts General Hospital to quantify contact forces. The results from these experiments are presented in this chapter. Portions of this work have previously been presented in [35],[19],[44].

Table 3.1: References corresponding to the labels in Fig. 3-1.

Label	Reference
(1)	Burcher 2005 [25]
(2)	Salcudean 1999 [91]
(3)	Chadli 2012 [29]

## 3.2 Introduction

As discussed in Section 1.4, one unique and significant aspect of ultrasound imaging is that it requires physical contact with the patient. The contact force, controlled by the human operator, is not repeatable and produces non-repeatable tissue compression, especially near the skin surface, resulting in ultrasound images that are difficult to reproduce at a later date [25]. When designing electromechanical devices to control or improve the repeatability of probe contact force, it is important to understand typical ultrasound contact forces to ensure that the devices are capable of applying the appropriate range of forces with appropriate resolution. A lack of understanding of required force range and mean values could lead to devices that are over- or under-designed, too fragile or too large.

Ultrasound probe contact force is also important because it is a significant risk factor for work-related musculoskeletal disorders (WRMSD) among sonographers [66]. In the USA, some 90% of sonographers currently work in pain [37], and one in five will experience a career-ending injury [1]. Contact force is surmised to play a major role in the development of WRMSD, but, to our knowledge, has never been rigorously quantified for any type of ultrasound exam. A more thorough understanding of probe contact forces could therefore lead to a better understanding of the correlation between force and musculoskeletal injury.

To our knowledge, only three studies have been conducted to measure probe contact forces. The devices used in these literature studies are shown in Fig. 3-1, and the corresponding references are shown in Table 3.1.

Salcudean (label 2) [91] used an instrumented probe to measure the contact forces applied by one sonographer during several (number is unspecified) carotid exams. The device consisted of a 6-axis JR3 force/torque sensor attached to an ultrasound

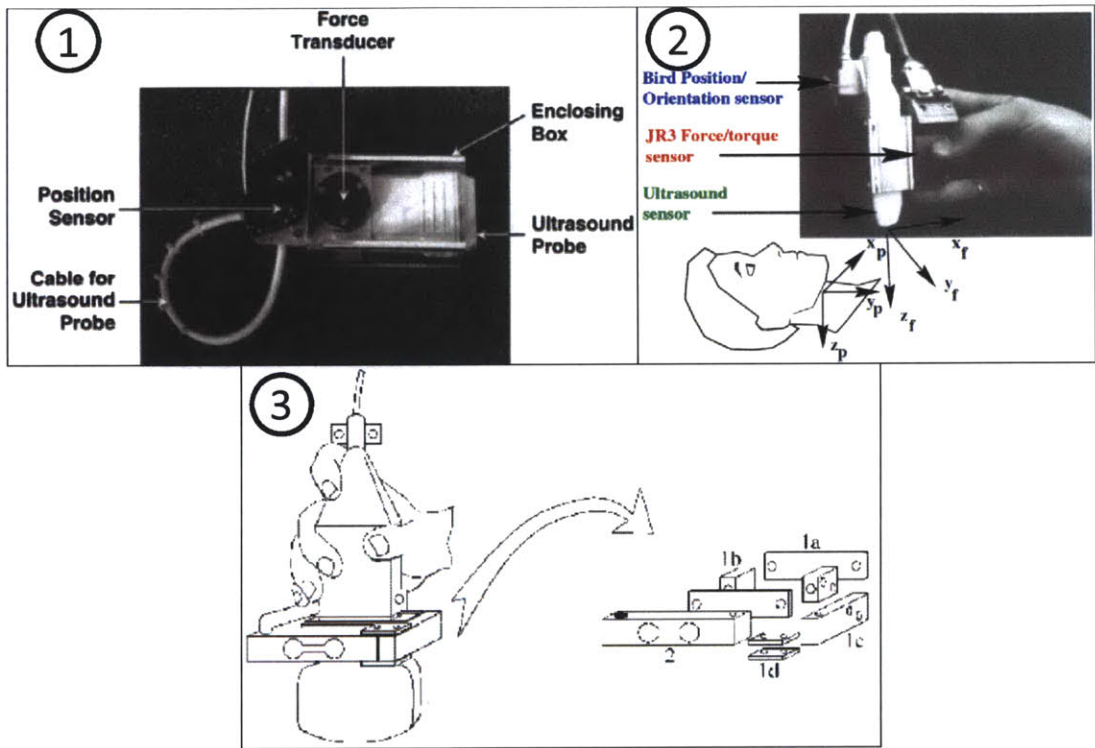


Figure 3-1: Devices from the literature to measure probe contact force. References are listed in Table 3.1.

probe. The measured forces ranges were 3.8 N, 4.2 N, and 6.4 N for the X, Y, and Z axes, respectively (as defined in Fig. 3-1, label (2)), while the corresponding torques were 0.4 Nm, 0.7 Nm, and 0.1 Nm.

Burcher (label 1) [25] presents a similar handheld system that measures probe contact forces and torques in six axes using a Mini 40 load cell (the same one used in the Series-1 force measuring probe). Forces ranged from 0 to 3.5 N during in vivo breast imaging.

Chadli (label 3) [29] presents a system to measure contact forces in one axis. A clamp surrounds the probe and enables it to slide on linear bearings. Four strain gauges enable the contact force to be measured along the axis of the probe. The device can also be used to measure the orientation of the probe. No data are presented from clinical or in vivo use.

Regarding contact force measurement, Guérin [101] specifies a general 5 N-20 N range across cardiac, renal, and abdominal exams. The method used to obtain this measurement is unclear.

From the literature, two conclusions can be drawn 1) there is a lack of—and strong need for—a thorough study of contact forces in ultrasound imaging, and 2) none of three force-measuring probes from the literature is naturally gripped and none permit rapid attachment and detachment of the ultrasound probe from the device (an important requirement that we discuss later).

In this chapter, we present a compact, ergonomic, six-axis force/torque measuring system that attaches to an off-the-shelf ultrasound probe. In the design and clinical evaluation of the device, we choose to target abdominal imaging, one of the most common ultrasound exam types. The device, which is not much larger than the probe itself, is shown in Fig. 3-5, and permits rapid, hand-operated, tool-free attachment and detachment of the ultrasound probe. We describe force data gathered from 53 abdominal ultrasound exams conducted by 13 professional sonographers on 10 healthy volunteers.

### 3.3 Series 1 Force-Measuring Probe: Design Process

In this section, we discuss the mechanical design process of the Series 1 force-measuring ultrasound probe. As discussed previously, the high-level objectives of the study are as follows:

1. Quantity the forces applied during abdominal ultrasound imaging.
2. Help sonographers to apply a repeatable contact force.
3. Examine the correlations between contact force and sonographer injury and fatigue.

The next step in the design process is to transform the qualitative high-level objectives into a set of quantitative functional requirements. The functional requirements are discussed in the following list.

Ergonomic: To accurately measure the forces applied during typical ultrasound imaging, the exam should be kept as typical as possible. From one perspective, the Heisenberg Uncertainty Principle states that it is not possible to measure something without also influencing it in some way. Within the context of this study, we seek to minimally modify the way in which the sonographer conducts the exam by making the ergonomics of the device match the ergonomics of a standard ultrasound probe as closely as possible. This means that the device must be:

1. ***Unobtrusive:*** The probe must fit comfortably in the sonographer's hand, which means it must be as close as possible to the size, shape, and mass of a standard ultrasound probe. The GE C1-5D probe targeted for use with this device has a mass of 200 g, thickness of 2 cm, maximum width of 9 cm, and a total volume of about  $96 \text{ cm}^3$ . For the force-measuring probe, it is believed that a device three times heavier and three times the volume could still be held ergonomically.

2. ***Permit rapid attachment/detachment of the ultrasound probe from the device:*** In hospitals, ultrasound probes are highly utilized pieces of equipment. The device, therefore, must permit quick attachment and removal of the ultrasound probe, without the use of tools, so that the probe can be used for other clinical tasks in the hospital.
3. ***Safe:*** The device must post no risk to the sonographer and patient.
4. ***Portable:*** For ergonomic operation, the system be readily transportable from one location to another, which places limits on the size of the total system. It is desired that the total volume of the packaged system be smaller than a 30 cm cube, a volume of roughly  $30,000 \text{ cm}^3$ .

Measure contact force: This functional requirement is characterized by a number of factors:

1. ***Number of axes of measurement:*** Because we seek to thoroughly quantify the contact state of the probe, we require the system to measure contact force in all three axes and contact torques in all three axes. Of course, we hypothesize that the force along the axis of the probe will be most significant.
2. ***Record rate:*** the device must record contact force at a high enough rate to capture all of the dynamics of interest. Hand tremor frequency characteristics taper off after about 10 Hz, so therefore we require the device to measure faster than 20 Hz.
3. ***Maximum force:*** The device must be able to withstand and measure the maximum forces that will be applied. Data on contact forces were scarce to non-existent prior to this study, but, as discussed in Section 5.3.1, the existing literature suggests approximate maximum forces of 20 N [101].
4. ***Display force:*** In addition to recording the force, the measured force must also be visible to the sonographer through some sort of GUI, display, audio tones, etc., so that he/she can manually control force, if desired. (This is similar to

Table 3.2: Functional requirements for the force-measuring probe, Series 1.

Requirement	Parameter	Value
Ergonomic	Probe mass	<600 g
	Thickness	<6 cm
	Width	<10 cm
	Length	<15 cm
	Probe volume	<300 cm <sup>3</sup>
	Attach time	<30 sec
	Removal time	<30 sec
	Total system mass	<10 kg
	Total system volume	<30k cm <sup>3</sup>
	Number of axes of force/torque	6
Measure force	Force resolution	<0.5 N
	Max force	>20 N
	Record rate	>20 Hz
	Cost	<\$10,000

the “Visual Control” scenario for the force-controlled probe, as discussed in Section 5.7.4.)

5. **Resolution:** Forces are expected to be on the order of 5 N, so we therefore require the force sensor noise level and resolution to permit 0.5 N of force to be measured.

Cost: It is desirable to keep the cost of the system less than that of the ultrasound probe, which ranges in price from US\$5,000-\$10,000.

The functional requirements are quantified in Table 3.2.

### 3.3.1 Design Parameters: Component Selection

The next step in the design process is the selection of the most critical components and design concepts. The single most important component is the force sensor, which transforms the contact force into a voltage which can be sampled with the computer. The other components include the probe clamp and clamshell.

Force sensor: In selecting the force sensor, there are two options: 1) a single, integrated 6-axis force/torque sensor, or 2) multiple <6 axis force sensors. There are a handful vendors of integrated 6-axis load cells (e.g., ATI-IA, AMTI, SRI, and

Bertec), several 3-axis load cell vendors (e.g., Futek, JR3, and ME-Meßsysteme), and many vendors of 1-axis load cells. After browsing the different offerings, the 6-axis Mini40 force/torque sensor from ATI seemed to provide the necessary force capabilities (in terms of the range and resolution in Table 3.2) in the smallest form factor, while still satisfying the cost functional requirement. Therefore, the Mini40 was selected.

After the load cell has been selected, the next step in the process is to design the remainder of the mechanical components. The load cell consists of a (very stiff) stainless steel flexure instrumented with strain gauges. As force is applied, the flexures deflect; the deflection is measured with the strain gauges. This means that, to properly measure force, the device must permit a small amount of relative motion between the ultrasound probe and the sonographer's hand. The remaining components which must be designed can be categorized into those which will attach to the "probe-side" of the load cell and those that will attach to the "hand-side."

Probe clamp: The function of the probe-side components is to attach the ultrasound probe to the device. As discussed in the previous section, it must be possible to rapidly insert and remove the probe, which suggests the need for a quick-release probe clamp. Early versions of the probe clamp were designed based upon the solid model obtained by 3D scanning the GE C1-5D probe, and employed four M2 screws to secure the probe. While this provided a robust solution, it was too cumbersome for clinical use, and a quicker-release mechanism was sought. Inspired by the mechanical latch used to secure the force-controlled probe's electronic enclosure, a probe clamp was designed in SolidWorks and 3D printed from ABS plastic. The clamp is demonstrated in Fig. 3-2.

The clamp consists of three 3D printed parts—the top (red in Fig. 3-4), bottom (green), and a latch (yellow)—as well as a small wire bail and wire hinge. The top pivots about the bottom via the wire hinge and opens wide enough to accommodate the ultrasound probe. To close the latch, the wire bail is slipped over a lip on the bottom piece, the latch is pivoted, and locks in position. A diagram showing the attachment procedure of the probe to the clamp is shown in Fig. 3-2. Attachment is

readily accomplished in less than 5 seconds, with a similar time for detachment.

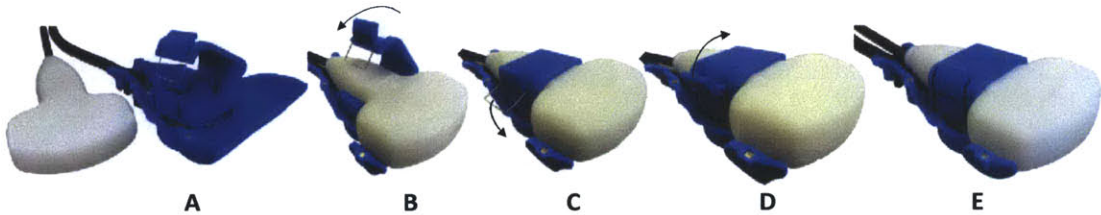


Figure 3-2: Attaching the ultrasound probe to the device with the locking 3D printed clamp.

Clamshell: The function of the hand-side components is to provide a grippable surface for the user while separating his/her hand from the probe-side components (in order to permit relative motion). For this, we envision a plastic “clamshell,” with two halves that go around the probe. The clamshell is subject to the same constraints as the clamp, namely the requirement that it permit rapid attachment and detachment of the ultrasound probe. Early versions of the clamshell were prototyped, and employed a number of M3 screws. As with the clamp, while this solution was robust, it was far too slow. A quicker-release design was required.

The solution that was eventually employed involves the use of magnets to hold the two shells together, and was first proposed by a UROP student named Javier Ramos. Six 1/8” cube magnets are embedded in each side of the clamshell. The magnets hold the two halves together in the Z-direction (as defined in Fig. 3-9), while ridges prevent the two halves from sliding in the X and Y directions.

To attach the shells, the top shell is first brought into proximity with the bottom shell (B). The shells begin to magnetically attract at a distance of about 1 cm (C), and the top shell snaps into place (D). The average top-bottom shell holding force was measured to be 5 N. The process is illustrated in Fig. 3-3.

The probe is removed from the device by following these steps in reverse. The average total insertion and removal times (including fastening and unfastening the clamp) were measured to be 13 sec and 16 sec, respectively.

With the design parameters for the three major subsystems chosen, the next step was to layout the components in a way that meets the rest of the functional

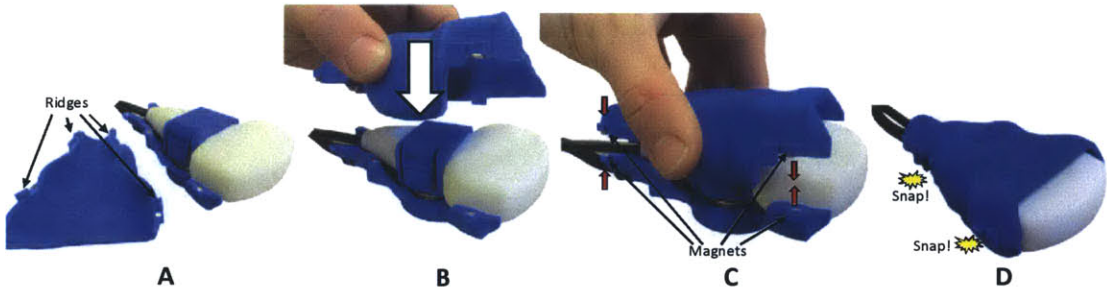


Figure 3-3: Mating the top shell with the bottom shell. The shells are held together by magnets.

requirements. The device was designed in SolidWorks and a rendering of the solid model is shown in Fig. 3-4. Photographs of the device from various angles are shown in Fig. 3-5.

### 3.3.2 3D Laser Scanning the Ultrasound Probes

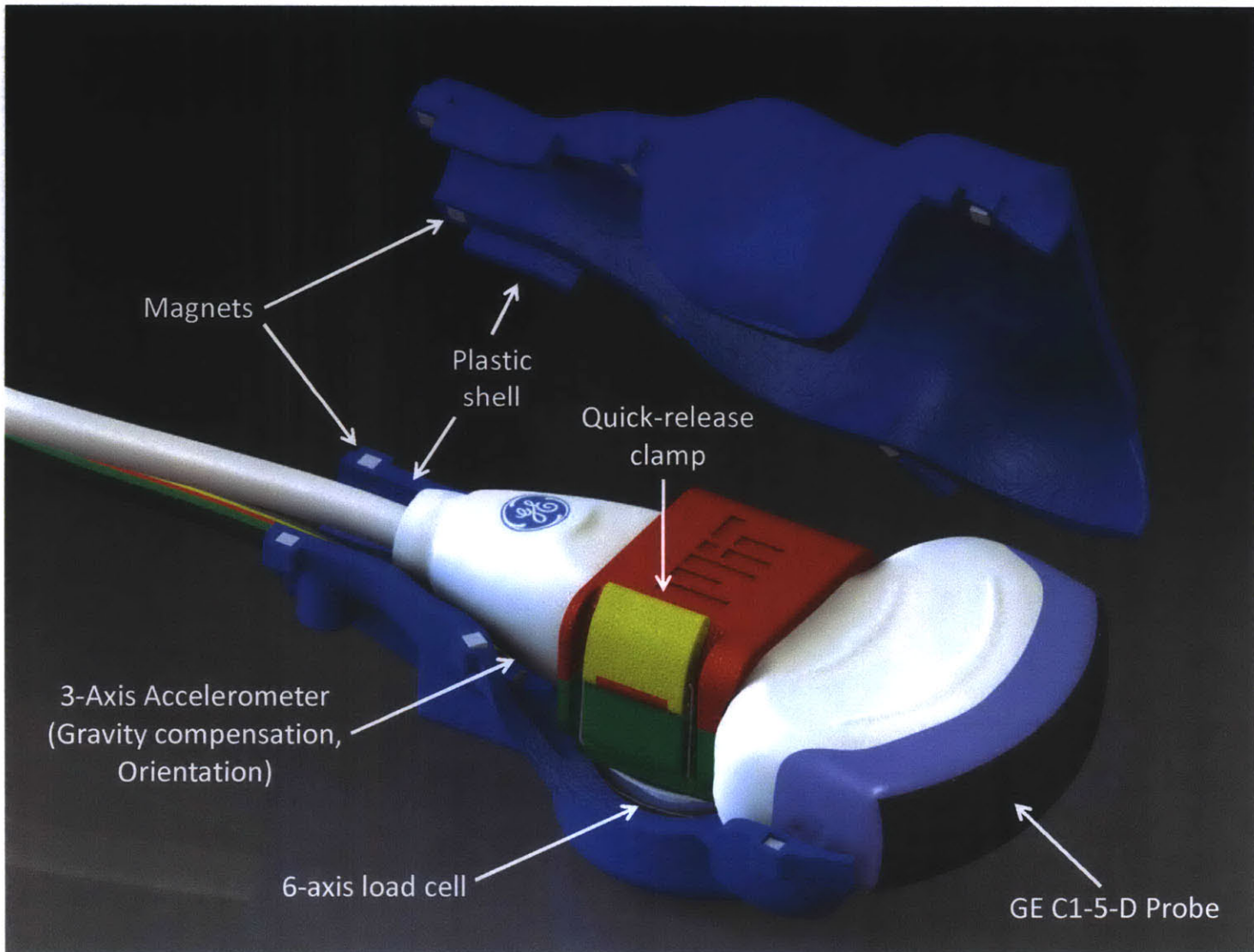
To aid in the design process, the GE C1-5D transducer (used for the force-measuring probe), as well as the six other probes involved in this thesis, were 3D laser scanned with a portable NextEngine scanner. As ultrasound probes are highly-utilized pieces of equipment, it was not feasible to bring the probes to the scanner; the scanner had to be brought to the hospital to scan the probes. A photograph of the scanning process, as well as images of the seven probe solid models, are shown in Figs. 3-6 and 3-7, respectively.

## 3.4 System Description

The device is shown in Fig. 3-5. The sonographer grasps the blue portion of the device and places the ultrasound probe (white) in contact with the patient. The load cell measures the 6-DOF relative forces and torques applied between the sonographer's hand and the ultrasound probe. In Section 3.6.1, we show that the probe is moved quasi-statically during ultrasound exams. Therefore, the relative contact forces and torques between the ultrasound probe and the patient can be calculated.

Fig. 3-8 shows an exploded view of the assembly. The device contains six total

Figure 3-4: SolidWorks rendering of the force-measuring probe, Series 1.



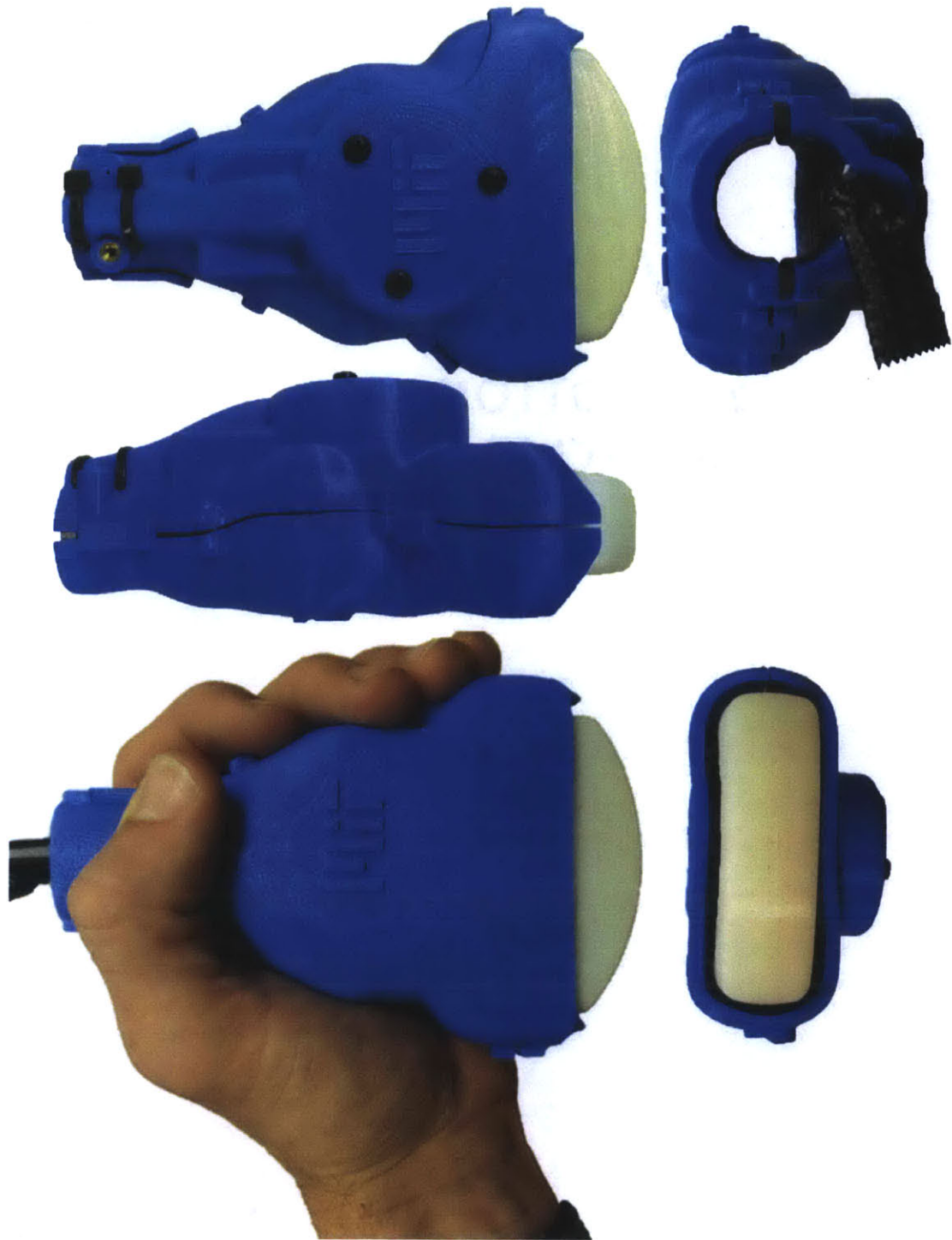


Figure 3-5: Front, side, and back views of the six-axis force/torque-measuring ultrasound probe. Depicted with a 3D-printed ultrasound probe mock-up.

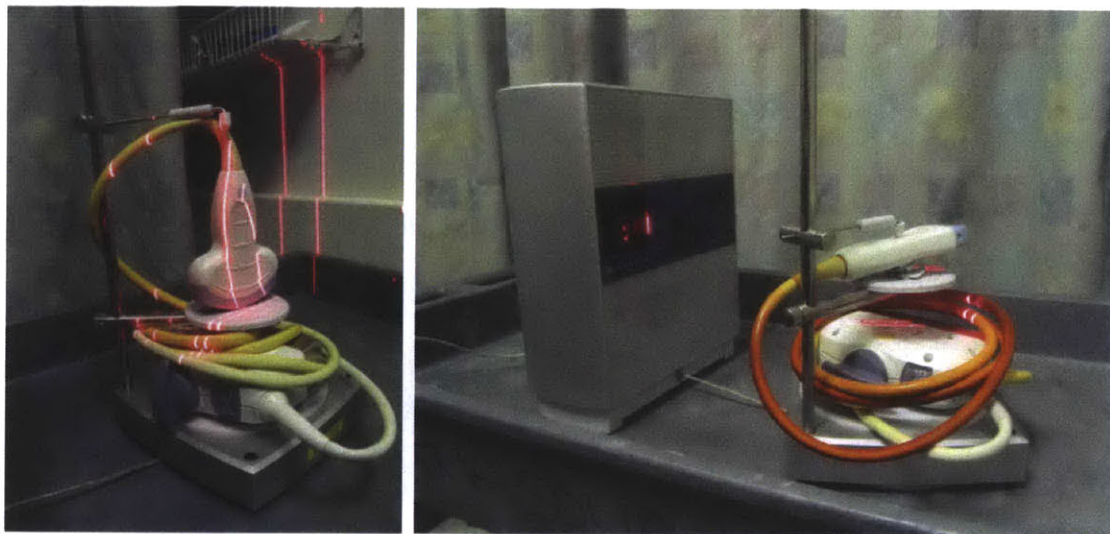


Figure 3-6: 3D laser scanning the GE C1-5D transducer with the NextEngine scanner.



Figure 3-7: Solid models of the seven ultrasound probes associated with this thesis research, obtained by 3D laser scanning the ultrasound probes.

fasteners, which secure the hinged, locking probe clamp (**5** and **3**) and the bottom shell **7** to the six-axis Mini40 load cell **6** (ATI Industrial Automation). Twelve high-strength neodymium magnets **2** embedded in the top **1** and bottom **7** shells hold the two shells together with 5 N of force. Ridges present on the top shell prevent shell-to-shell movement in the Y and X directions (refer to Fig. 3-9, left), while the magnets prevent motion in the Z direction.

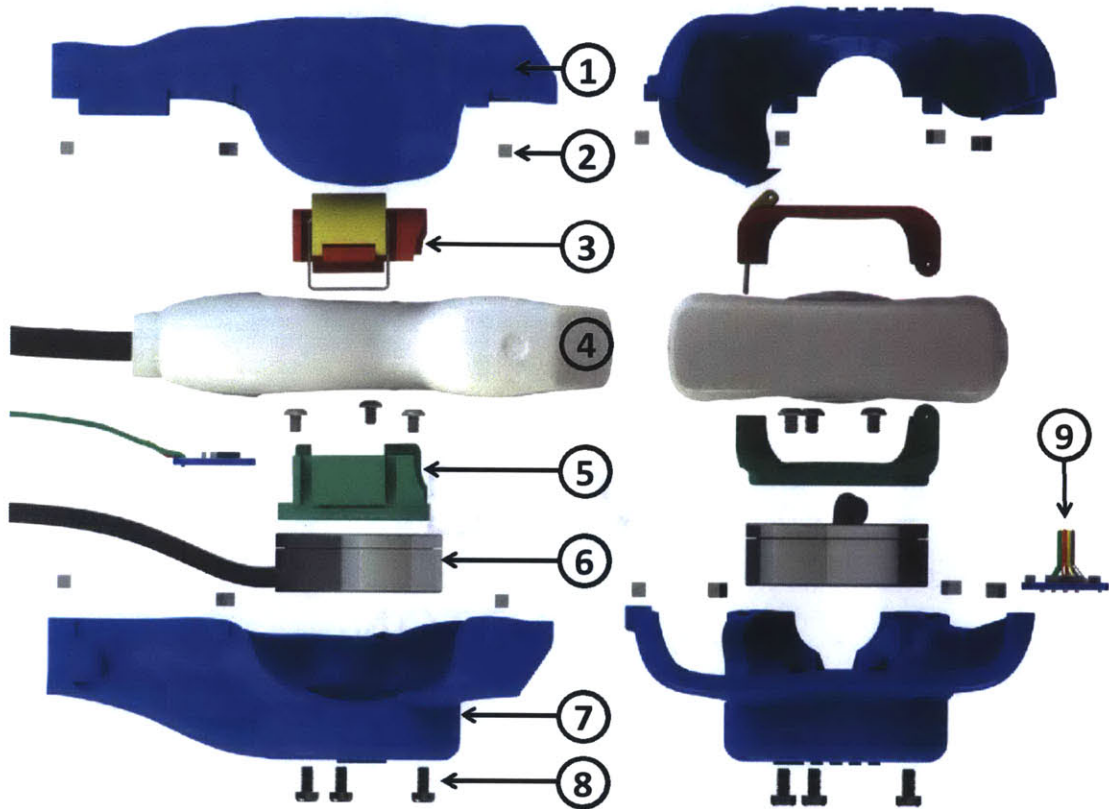


Figure 3-8: Exploded view of the device.

A three-axis analog-output accelerometer **9** (Analog Devices ADXL 335, mounted to an Adafruit PCB) is mounted to a recessed shelf within the bottom shell. Plastic cable ties secure the load cell and accelerometer cables to the bottom shell, providing strain relief. The accelerometer is used to measure the orientation of the device with respect to gravity, as discussed in Section 3.5.

This device is custom-designed to fit the GE C1-5-D ultrasound probe **4**, commonly used for abdominal exams. As discussed in Section 3.3.2, the probe was 3D-scanned

with a NextEngine Desktop 3D scanner at Massachusetts General Hospital (MGH) in Boston, MA. SolidWorks was used to design the clamps and shells (average thickness 2.5 mm), ensuring a shell-probe air gap of no less than 3.6 mm. The five parts were 3D-printed from ABS plastic with a Stratasys Dimension Elite 3D printer.

Two National Instruments USB-6009 DAQ boards, housed in a shielded electronics enclosure (4 in Fig. 3-12), read the load cell and accelerometer voltages. A LabVIEW virtual instrument running on a laptop records data at a rate of 60Hz.

The goal of this study is to measure the forces  $F_x$ ,  $F_y$ , and  $F_z$  and torques  $\tau_x$ ,  $\tau_y$  and  $\tau_z$  that the ultrasound probe applies to the patient's body, based on the coordinate system defined in Fig. 3-9.

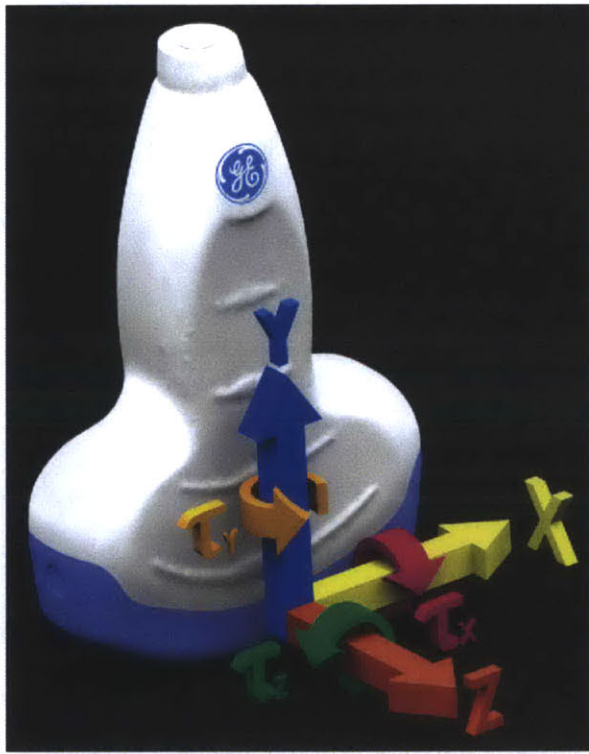


Figure 3-9: Left: probe-tip coordinate system. It is hypothesized that  $F_y$  is greatest during scanning.

### 3.5 Gravity Compensation

The tri-axial analog accelerometer is used to measure the orientation of the device with respect to gravity in order to perform gravity compensation. As the sonographer rotates the device through different angles with respect to gravity, the weight of the ultrasound probe will appear in the measured forces and torques. We compensate for the effect of gravity by subtracting off the weight of the ultrasound probe based on the angle of orientation in order to improve the accuracy of the system.

The three accelerometer output voltages,  $g_x$ ,  $g_y$ , and  $g_z$ , are the projections of the gravitational acceleration vector  $\vec{G}$  onto accelerometer X, Y, & Z axes, as depicted in Fig. 3-10.

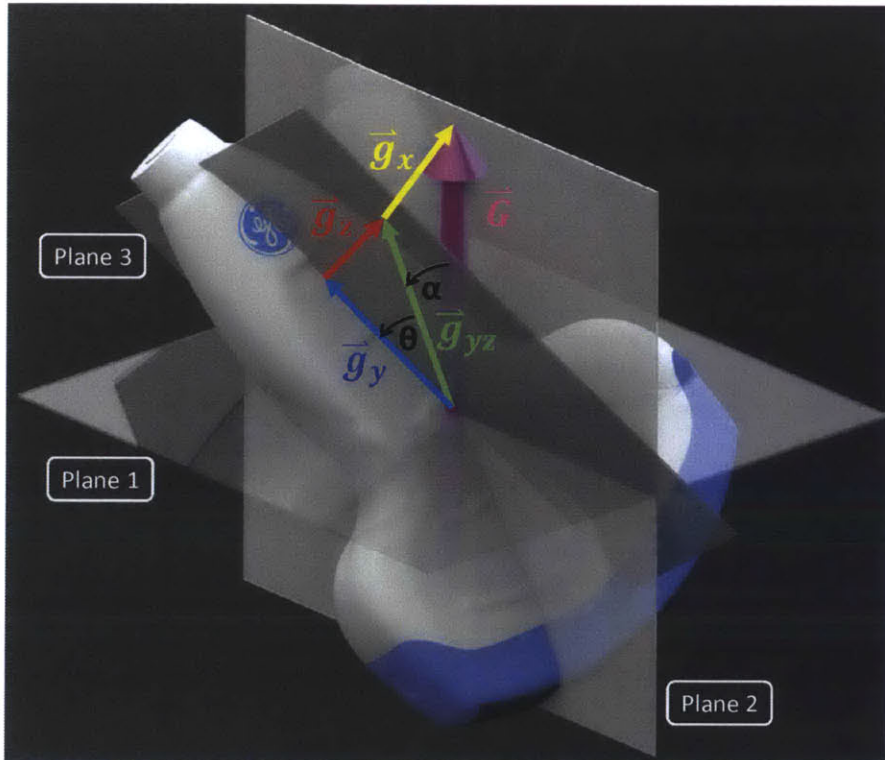


Figure 3-10: Projections of the gravitational acceleration vector onto the X, Y, and Z planes. Pitch angle  $\theta$  is the angle between vertical and the Z-plane; roll angle  $\alpha$  is the angle between vertical and the X-plane. Yaw angle cannot be accurately measured with an accelerometer alone.

Assuming negligible inertial effects due to hand tremors (Section 3.6.1), the equation relating the probe-tip forces and torques  $\mathbf{F}_P$  to the load cell readings  $\mathbf{F}_{LC}$  and

accelerometer readings  $\mathbf{A}$  is thus:

$$\mathbf{F}_P = \mathbf{F}_{LC} + \frac{m_2}{S} \mathbf{A} + \mathbf{N}_T \quad (3.1)$$

where sensitivity  $S = 300mV/(9.8m/s^2)$ ,  $m_2 = 146g$ , and

$$\mathbf{F}_P = \begin{pmatrix} F_x^p \\ F_y^p \\ F_z^p \\ \tau_x^p \\ \tau_y^p \\ \tau_z^p \end{pmatrix}, \mathbf{F}_{LC} = \begin{pmatrix} F_x^m \\ F_y^m \\ F_z^m \\ \tau_x^m \\ \tau_y^m \\ \tau_z^m \end{pmatrix} + \begin{pmatrix} 0 \\ 0 \\ 0 \\ r_y F_z^m - r_z F_y^m \\ r_z F_x^m \\ r_y F_x^m \end{pmatrix}$$

$$\mathbf{A} = [g_x, g_y, g_z, -g_y r_z + g_z r_y, g_x r_z, g_x r_y]^T$$

$$+ [0, 0, 0, -g_y c_z + g_z c_y, g_x c_z, g_x c_y]^T$$

where  $\mathbf{N}_T$  represents the contributions from the noise sources, as discussed in Section 3.6. Quantities with superscript  $p$  are probe-tip forces and torques; superscript  $m$  denotes measured forces and torques.  $c_y$  and  $r_y$  are the Y-distances from the load cell origin to the center of mass and probe tip, respectively; similarly,  $c_z$  and  $r_z$  are the Z-distances. Trigonometry is used to calculate the probe roll and pitch angles from the accelerometer voltages.

## 3.6 Measurement Accuracy and Precision

In the system, there exist numerous sources of noise which degrade the accuracy and precision of the force, torque, and angle measurements. These noise sources include involuntary hand tremors, cable tug induced by the ultrasound probe cable, and sensor noise. In this section, we discuss the different sources of noise and evaluate their magnitudes.

### 3.6.1 Inertial Forces Induced by Involuntary Hand Tremors

Here we demonstrate that involuntary sonographer hand tremors contribute negligibly to the measured contact forces and accelerations. As the sonographer grasps the probe, his or her hand will tremor sinusoidally in the X, Y, and Z directions with frequencies  $\omega = 5 - 9\text{Hz}$  [103] and amplitude  $A$ , inducing forces on the ultrasound probe through the load cell and accelerations in the accelerometer. For the moment, consider tremors in the Z-direction only, with the patient as reference ground position. The relative position between the hand-side of the load cell and the patient,  $z_1(t)$ , is thus  $z_1(t) = A \sin(\omega t)$ . Compliance  $k$  and damping  $b$  within the load cell and mounting clamp cause the ultrasound probe to move quasi-independently, with trajectory  $z_2(t)$  relative to the patient. A diagram of the system model is shown in Fig. 3-11.

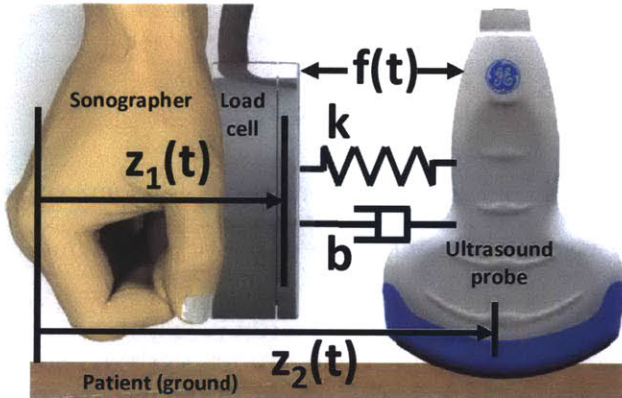


Figure 3-11: System model. Stiffness  $k$  and damping  $b$  are present in the load cell-to-probe connection.

The force  $f(t)$  measured by the load cell is

$$f(t) = k(z_1(t) - z_2(t)) + b(z_1(t) - z_2(t)) \quad (3.2)$$

And the probe equation of motion is  $m_2 \ddot{z}_2(t) = f(t)$ . Converting to the frequency domain via the Laplace Transform, (3.2) becomes

$$F(s) = \frac{m_2 s^2 (k + bs)}{m_2 s^2 + bs + k} Z_1(s) = C(s) Z_1(s)$$

For a given frequency  $s = \omega$ , the maximum value of the measured force is thus  $f_{max}(\omega) = c(\omega)A$ . Using the results from [103], the worst-case tremor-induced forces occur for  $\omega = 8.0\text{Hz}$ , with amplitude  $A = 75\mu\text{m}$ , giving the result  $f(8.0\text{Hz}) \approx 0.03\text{N}$ . This is insignificant compared to the measured forces in Table 3.3, and can therefore be ignored.

### 3.6.2 Accelerations Induced by Involuntary Hand Tremors

As the hand tremors, the accelerometer, which ideally measures only the orientation of the device with respect to gravity, also measures tremor-induced accelerations. To evaluate the magnitude of these accelerations, we take the second derivative of the hand position to obtain  $\ddot{z}_1(t) = -A\omega^2 \cos(\omega t)$ . The maximum acceleration is  $\ddot{z}_{1,max} = A\omega^2$ . Based on the worst-case values of  $\omega$  and  $A$  from [103],  $\ddot{z}_{1,max} \approx 0.20\text{m/s}^2$ , which is less than 5% of the gravity-induced accelerations (up to  $9.8\text{m/s}^2$ ) and can therefore be ignored. Thus, the probe can be assumed to move quasi-statically (relative to the applied forces) during ultrasound exams.

### 3.6.3 Noise From Cable Pull Force

Another source of signal noise is produced by the ultrasound probe cable. Although the ultrasound cable is strain-relieved by Velcro-strapping it to the device cable as shown in Fig. 3-12, as the probe is moved and rotated through different orientations the cable flexes slightly, resulting in small, non-repeatable forces and torques applied to load cell.

### 3.6.4 Noise Sources

The 6x1 vector of the signal noise,  $\mathbf{N}_T$ , from (3.1) is comprised of the noise from the load cell, accelerometer, hand tremors, and the ultrasound cable, by

$$N_T = N_{l.c.}^{sensor} + N_{l.c.}^{tremor} + N_{accel}^{sensor} + N_{accel}^{tremor} + N_{cable} \quad (3.3)$$

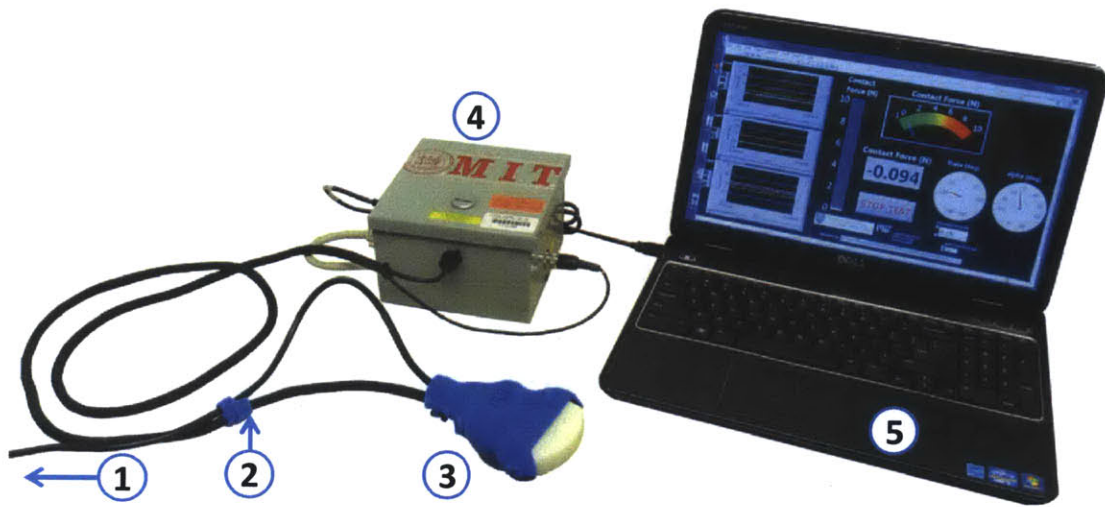


Figure 3-12: Photograph of the complete system. The ultrasound probe cable **1** is Velcro-strapped **2** to the device cable to provide strain relief. A steel enclosure **4** houses the electronic components while the laptop **5** displays and records the probe contact state.

The quantity  $N_{l.c.}^{sensor}$ , for example, represents the contribution of the load cell ('l.c.') sensor noise to the total noise. The relative contributions from each of the five noise sources were measured and are shown in Fig. 3-13 for  $F_y$  and  $\tau_x$ .

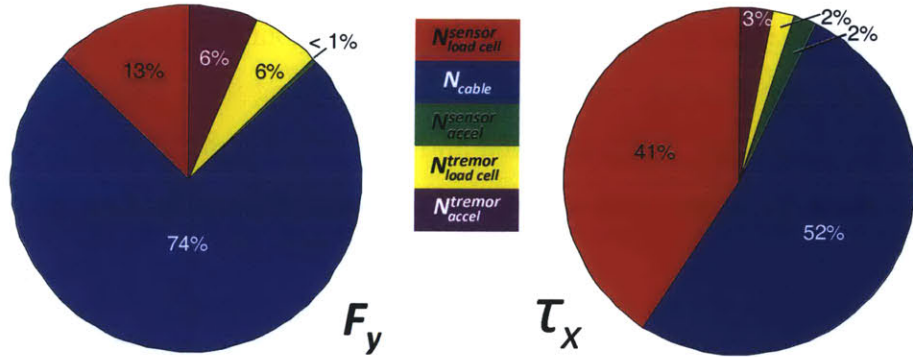


Figure 3-13: Contributions from each noise source to noise in  $F_y$  and  $\tau_x$ .  $F_x$  and  $F_z$  (not shown) are similar to  $F_y$ ;  $\tau_y$  and  $\tau_z$  are similar to  $\tau_x$ . The non-repeatable tug of the cable comprises the majority of total signal noise, followed by the load cell sensor noise.

## 3.7 Sonographer Studies

To evaluate the performance of the device and to collect early use data, 13 professional sonographers used the device to conduct 53 total abdominal ultrasound exams on 10 patients at MGH. Forces, torques, and accelerometer readings were recorded. A plastic bag was placed over the device to ensure sterility (Fig. 3-15). Mean exam duration was 419 sec. During each run, videos were recorded and sonographers were instructed to speak aloud the organ/region being scanned.

Fig. 3-14 shows an example force versus time plot for the axial forces ( $F_y$ ) applied during a sample run. Text at the top of the plot indicates the organ being imaged. While this represents data from only one exam, there are a number interesting observations to point out. The greatest force was applied to the left kidney and spleen, peaking at about 18 N. In some of the organs, for example, the left kidney, spleen, and distal aorta, force starts out low and is increased towards the end. In other organs, for instance, the main portal vein, sagittal IVC, and right kidney, the force stays relatively constant. Some organs, such as the spleen, gallbladder, and aorta take less time to image than others like the common bile duct and left kidney. Correlations between contact force, exam duration, and organ across different exams have not yet been rigorously investigated. We suggest this as a potential topic for future work.

In the following analyses, we investigate the average force applied throughout the entire duration of the exam. Example force/torque data from the first nine runs are presented in Fig. 3-16, and data from all 53 runs are shown in Fig. 3-17.

Table 3.3 summarizes the force/torque data for all 53 runs.  $\bar{\sigma}$  is the mean standard deviation of the 53 runs.  $\sigma_{noise}$  is the standard deviation of the noise. Forces are expressed in N and torques in mNm. The data demonstrate that the mean force along the axis of the probe (Y-axis) is much greater than the forces in the X and Z directions.  $F_z$ ,  $\tau_y$ , and  $\tau_z$  are so small that they lie within the measurement noise.  $F_x$ ,  $F_y$ , and  $\tau_x$  lie outside of the measurement noise.

Because, as expected, the axial forces ( $F_y$ ) have a much greater magnitude than the other forces, we investigate  $F_y$  in more detail. A histogram of  $F_y$  from all exams

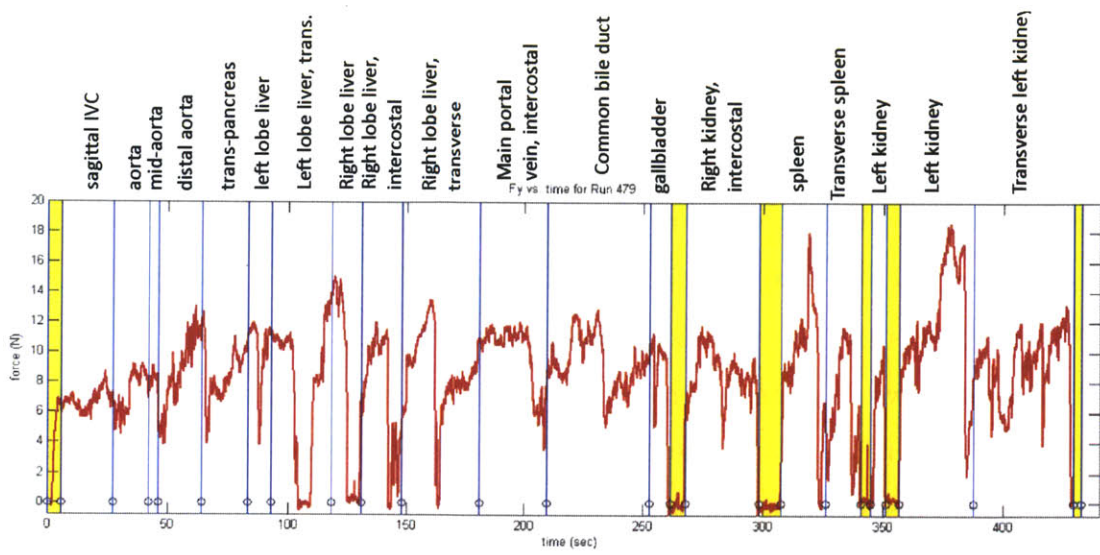


Figure 3-14: An example plot of axial force,  $F_y$ , versus time for Run 479. Yellow regions indicate time during which the probe was not in contact. Text annotations at the top denote the organ or tissue that was investigated, while vertical blue lines demarcate different organs.



Figure 3-15: One of the 53 ultrasound exams conducted at MGH - Boston. The device was approved for use by the MGH Internal Review Board.

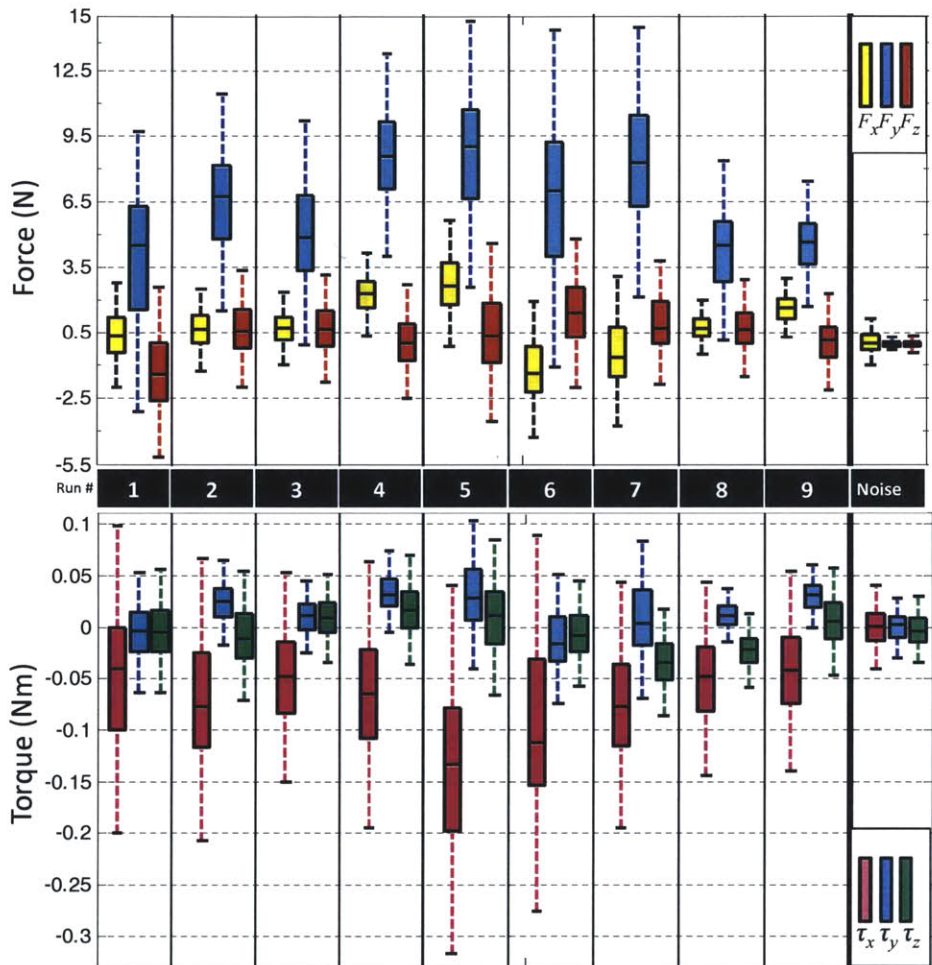


Figure 3-16: Box and whisker plot of the forces (top) and torques (bottom) for Runs 1 - 9. Solid horizontal black line within each box indicates median value; boxes enclose 50% of the data. Whiskers extend  $\pm 2.7\sigma$  from the median value; assuming a normal distribution, 99.3% of the data fall within the whisker bounds. A noise-measurement run is shown on the right.

Figure 3-17: Forces and torques from all 53 runs.

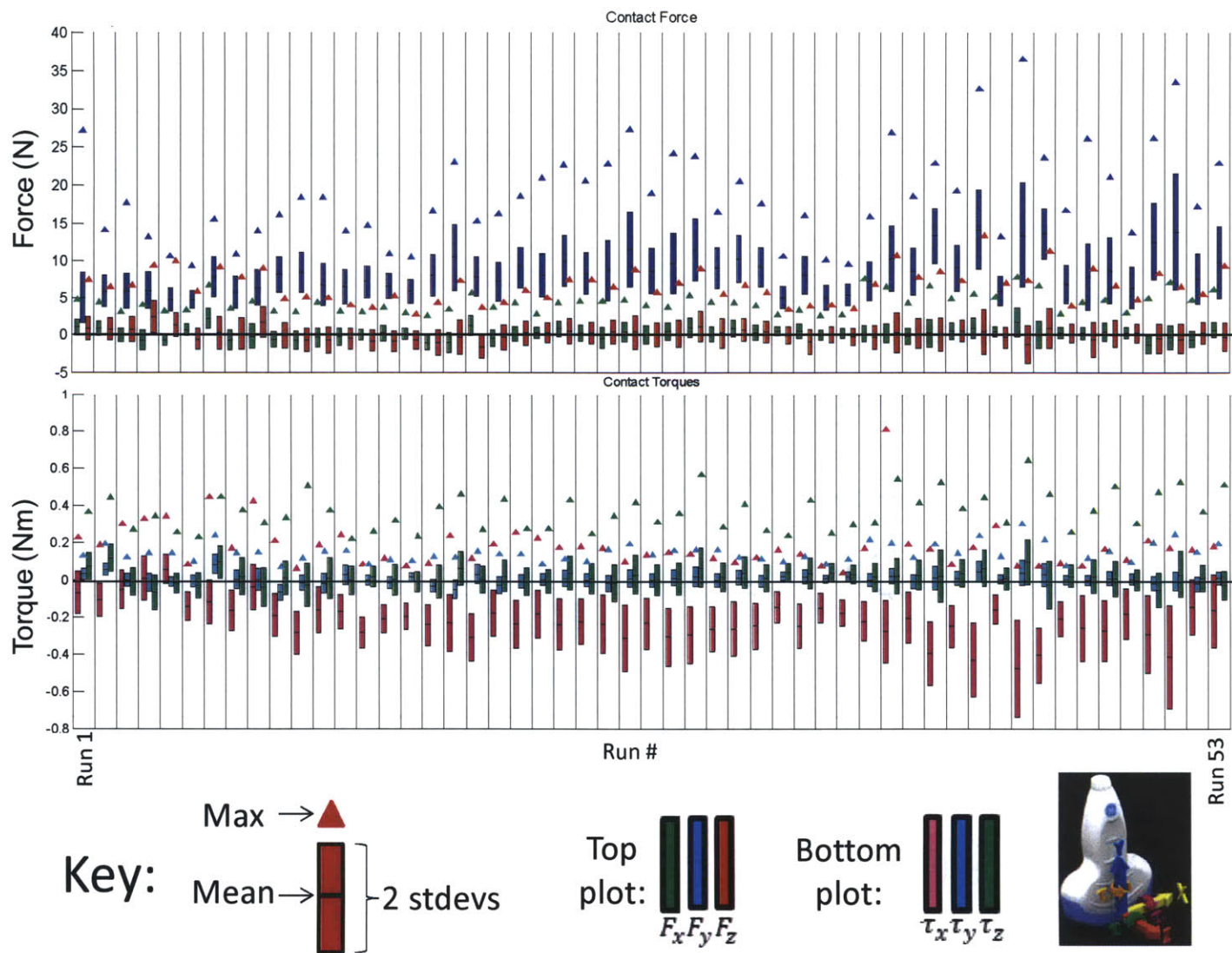


Table 3.3: Summary of force [N] and torque [mNm] data for the 53 runs.

	$F_x$	$F_y$	$F_z$	$\tau_x$	$\tau_y$	$\tau_z$
Mean	0.3	8.3	-0.01	-190	1	11
Max	5.7	36.5	10.4	460	190	570
$\bar{\sigma}$	1.6	4.2	1.6	110	37	68
$\sigma_{noise}$	0.25	0.35	0.45	32	20	20

is plotted in Fig. 3-18.

In the force histogram, we see two prominent peaks: one around the median force of 5.8 N, and one around 0 N. The peak at 0 N indicates times during which the probe was not in contact. There are a small number of measurements below 0 N due to a combination of signal noise and possible pushing of the ultrasound probe cable during scanning. In the subsequent analysis presented, the force is thresholded at 1.2 N in order to eliminate data from the times at which the probe was not in contact.

### 3.7.1 Correlations with BMI and Sonographer Experience

#### BMI Correlation

In this section, we investigate the correlations between sonographer level of experience, patient BMI, and axial force. In conversations with sonographers, they qualitatively report applying more force to image heavier patients, for some of the reasons listed in Section 1.4. We therefore expect that higher forces are applied to patients with higher Body Mass Indices (BMI). BMI is calculated as the ratio of a person's mass (in kg) to the square of the person's height (in m) and can be coarsely categorized into the following ranges: <18.5 (underweight), 18.5-25 (healthy weight), 25-30 (overweight) , >30 (obese) [80]. A scatter plot of the mean axial force (for each of the 53 exams) versus volunteer BMI is shown in Fig. 3-19.

While most sonographers apply quite different forces for different patients, it is interesting to note that some sonographers apply consistently higher force (e.g., pink triangle and blue star) or consistently lower forces (pink star). In this plot, we see somewhat of a trend towards higher forces with higher-BMI volunteers, but the sparsity of the data points limits the strength of the conclusions that can be drawn. When

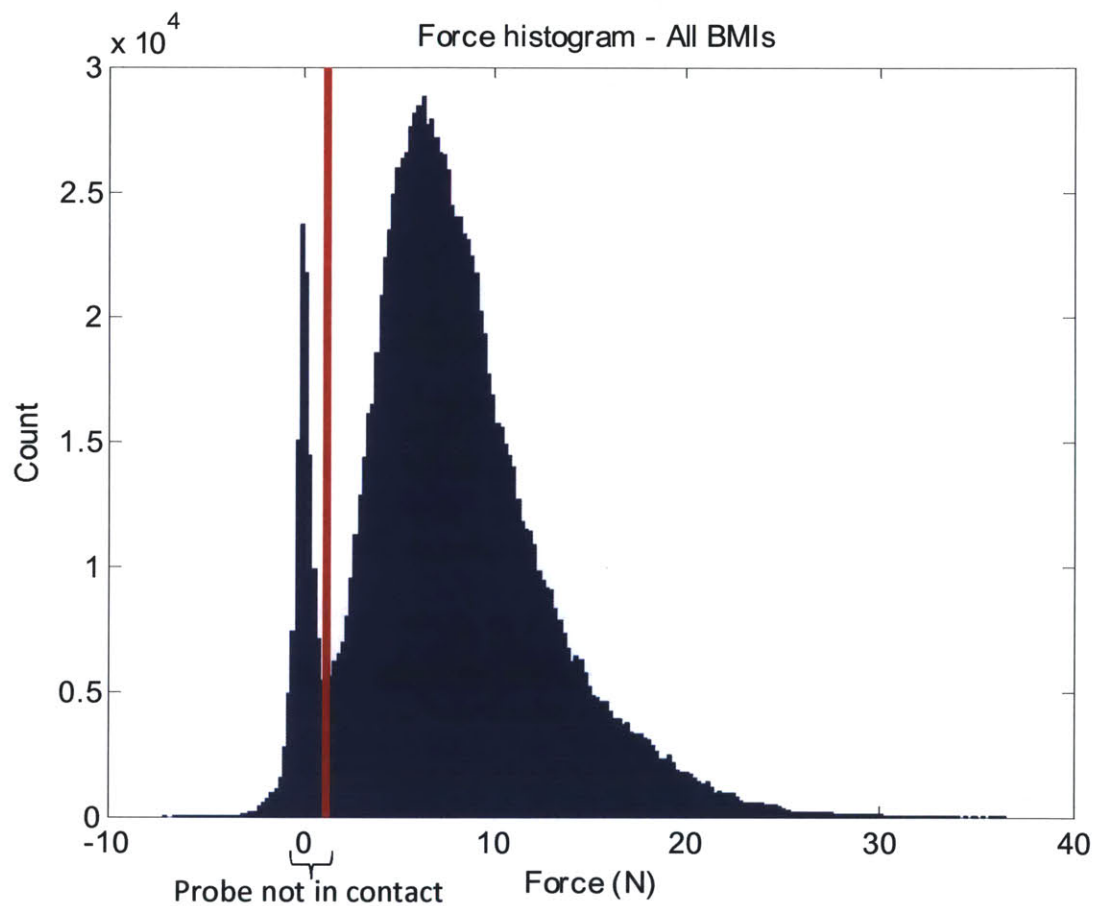


Figure 3-18: Histogram of the axial force  $F_y$  for all of the 53 exams. X-axis indicates force range; Y-axis is the number of times that force range was recorded.

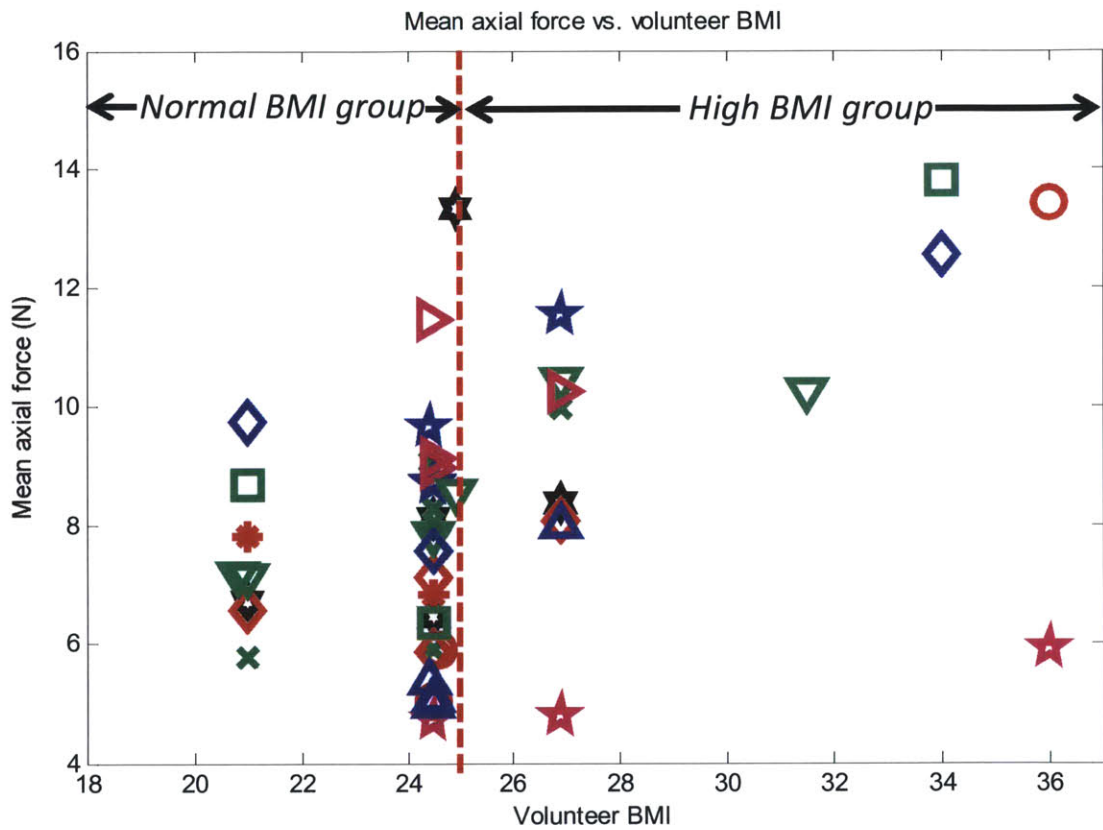


Figure 3-19: Mean axial force versus volunteer BMI. Each unique icon represents a unique sonographer. In the plot, we observe a wide spread in contact forces from 5 N to 14 N. Certain sonographers (e.g., pink star) apply consistently lower force, while other sonographers (e.g., blue star and pink triangle) apply consistently higher forces. The data were split into two groups with a BMI = 25 cutoff, and it was found that a statistically significantly higher maximum force was applied to higher BMI subjects.

the contact forces are averaged for each volunteer, the force versus BMI characteristics are shown in Fig. 3-20.

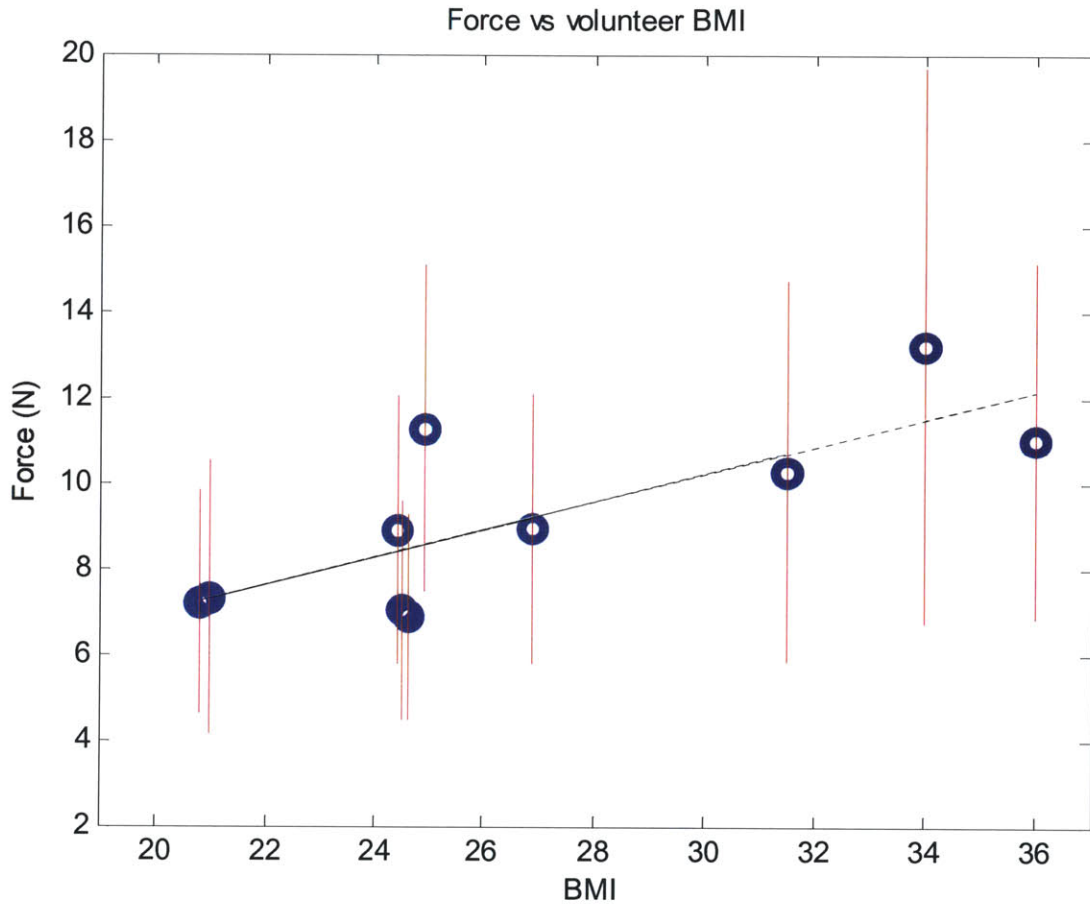


Figure 3-20: Mean axial force versus volunteer BMI, averaged for each volunteer. Blue circles indicate average force, red line spans  $\pm 1\sigma$ .

In this plot, higher forces show some correlation with higher BMI, as evidenced by the trendline. The equation for the trendline is  $y = 0.32x + 0.5$ , with an  $R^2=0.61$ , indicating a relatively weak correlation.

To rigorously evaluate any correlations between sonographer contact force and patient BMI, the patient population was split into two groups: a “high BMI” group ( $>25$ ,  $n = 4$ ) and a “normal BMI” group ( $\leq 25$ ,  $n = 6$ ). The mean force and mean maximum force were calculated for each of the two groups, and are presented in Table 3.4.

Mean contact force was 9.8 N (22.4 N max) for subjects in the high BMI group

Table 3.4: Statistical correlations between contact force and subject BMI.

Group	Mean force		Mean max. force	
	Value	p-value	Value	p-value
Normal BMI (18.5-25, n=6)	7.9 N	0.056	17.4 N	0.019
High BMI (>25, n=4)	10.5 N		23.7 N	

and 7.5 N (17.3 N max) for subjects in the normal BMI group, but the difference was not statistically significant ( $p = 0.056$ , which is greater than the  $p = 0.05$  threshold commonly used in medical literature). However, the average maximum force in the normal BMI group was 23.7 N, which is statistically significantly higher than that of the normal BMI group (17.4 N), with a p-value of 0.019.

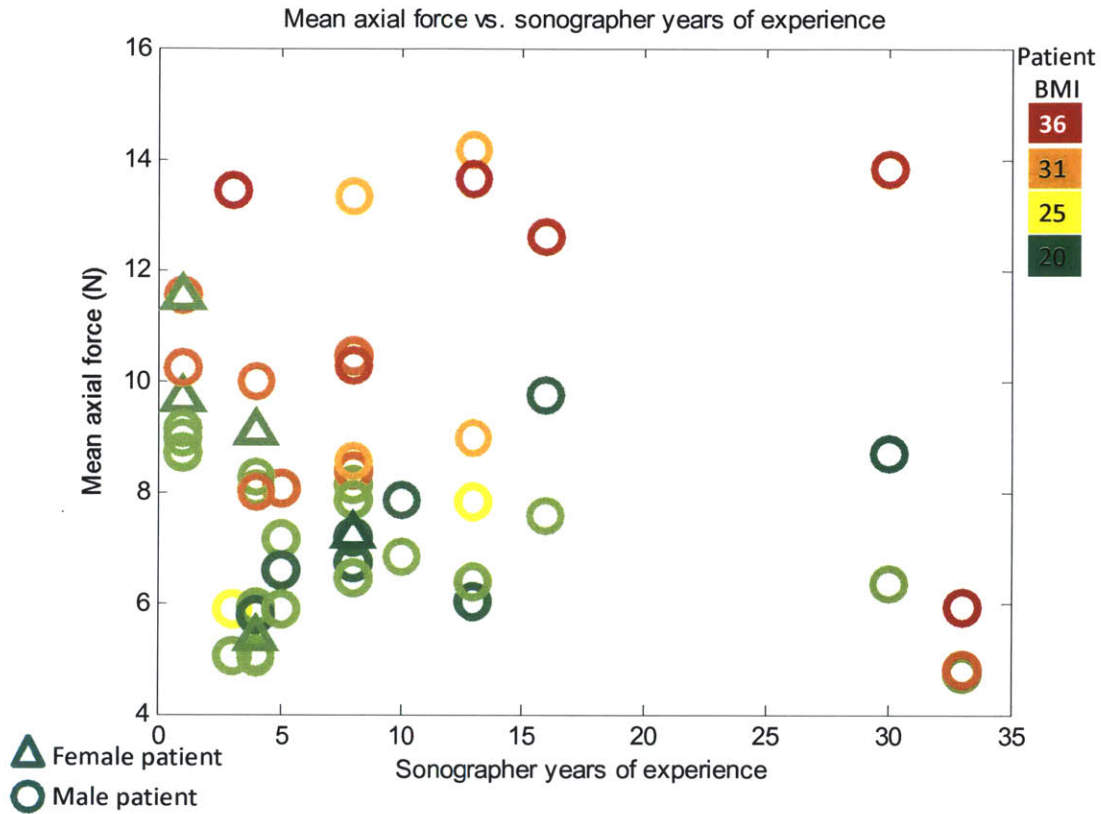
### Sonographer Level of Experience Correlation

In this sub-section, we investigate the presence of any correlations between sonographer years of experience and contact force. Intuitively, we expect that sonographers who have been scanning for longer have learned to apply less force to obtain diagnostic quality images, in order to reduce the likelihood of fatigue of WRMSD. To test this hypothesis, the sonographers were split into two groups: “more experienced” ( $\geq 5$  years, n=6) and “less experienced” ( $< 5$  years, n=6).

Force applied by experienced sonographers averaged 8.3N (18.4N max); the less experienced sonographers averaged 8.0N (19N max). The difference between the two groups was not statistically significant ( $p>0.05$ ). A scatter plot of sonographer years of experience versus mean contact force is shown in Fig. 3-21. In this plot, we see no clear correlation between years of sonographer experience and applied force.

## 3.8 Force-Measuring Probe - Series 1: Conclusions

In this chapter, we presented a device that measures ultrasound probe contact force, torques, and orientation angles during abdominal ultrasound scanning. The device, which is mechanically-robust and consists of five 3D printed plastic parts (all of which are easily injection-moldable), along with several fasteners, permits rapid attachment



and removal of the ultrasound probe. This chapter discussed the design process of the device, from the formation of functional requirements, to the selection of components.

In 53 full-length abdominal scans, involving 13 professional sonographers and 10 healthy volunteers, totalling 7.5 hours of total exam time, contact forces, torques, and angles were quantified. It was found that forces applied along the axis of the probe, which we refer to as the “axial forces” were an order of magnitude greater than the forces applied along the other two axes. The axial forces were further analyzed to investigate any correlations between force and sonographer years of experience as well as patient BMI.

It was found that grand mean axial force across all exams was 8.3 N, with a standard deviation of 4.2 N. The average forces applied to the high BMI patients were higher than the forces applied to the low-BMI patients, and the correlation was shown to be statistically significant. No statistically significant correlation was found between contact force and sonographer years of experience.



# **Chapter 4**

## **Force-Measuring Probe: Series 2**

### **4.1 Introduction**

In this chapter, the design of a second force-measuring ultrasound probe is discussed. The purpose of the second version was to reduce the cost of the first system while improving portability and ergonomics.

### **4.2 Objectives**

The data collected with the Series-1 force-measuring probe represent the first thorough study on ultrasound probe contact forces. While these data are a promising start, there are compelling reasons to collect more data:

1. To understand contact forces in other types of exams (in addition to abdominal)
2. To perform a prospective study on the ability of the device to influence sonographer behavior. Specifically, one important objective is to use the probe to reduce the incidence of sonographer fatigue and injury.
3. Use the device to standardize forces in other clinical applications. Shortly after the MGH data were collected with the 6-axis probe, we were contacted by a researcher from an Australian university who is interested in investigating long-term changes to deep abdominal muscles in patients with long-term lower back

pain, before and after a clinical intervention. Her goal is to standardize the amount of pressure applied by the probe to enhance image repeatability.

A combination of these three factors motivated the collection of more data. To enable expanded data collection, it was necessary to improve upon the Series-1 design in a number of key areas, and to produce an improved “Series 2” probe. The high-level objectives for the design of the Series-2 force measuring probe are:

1. *Reduce cost*: The first force-measuring probe employed a six-axis force-torque sensor, which cost about \$6,000 and constituted a large portion of the cost of the system. It is desired to reduce the cost of the system to enable the device to be produced in larger quantities which could be deployed in larger-scale clinical studies. Lower cost would increase the feasibility of fabricating more prototypes.
2. *Improve portability*: It would be desirable to reduce the total device mass from 5 kg and the volume from 25,000  $cm^3$  so that the device could be more easily transported. Improved portability could make sonographers more likely to use the device.
3. *Improve ergonomics*: The Series 1 transducer triples the volume of the probe, potentially altering the way in which sonographers grasp the probe, which could lead to skewed results. Ideally, the probe should alter the grip style and exam as minimally as possible, and not produce any additional discomfort due to a painful grip. The most significant factor in the size and shape of the probe is the six-axis load cell. It is desired to change the shape the probe so that it is more smoothly contoured and therefore more comfortably gripped.

These three qualitative functional requirements, which are defined relative to the Series 1 probe, can be quantified using the same reasoning as in Section 3.3, and are presented in Table 4.1. The probe also inherits the additional functional requirements in (previous) Table 3.2, for example the need to record contact force.

Table 4.1: Functional requirements of the force-measuring probe: Series 2.

<b>Meta Objective</b>	<b>Functional Requirement</b>
1) Reduce parts cost of probe	Cost <\$6000
2) Improve Portability	Total system mass <5 kg Total system volume <25,000 $cm^3$
3) Improve ergonomics	Probe volume <250 $cm^3$ Thickness <53 mm

## 4.3 Mechanical Design

Referring back to the list of design parameters for the Series 1 probe (Section 3.3.1), it appears that replacing the six-axis load cell with a single-axis load cell could enable the device to satisfy nearly all of the new functional requirements. But the use of the single-axis load cell is not without trade-offs; the most significant disadvantage is that it can only measure force in one direction, and cannot measure torques. This reduces the information that can be measured in the ultrasound exam. In the next paragraph, we describe why the use of the single-axis load cell is acceptable.

As discussed in Section 3.7, the experiments performed with the six-axis force-measuring ultrasound probe demonstrated that, as expected, the forces applied along the axis of the probe, denoted  $F_y$  and labeled “Y-axis” in Fig. 4-1, were more than an order of magnitude greater than the forces applied in the X and Z directions. Furthermore, for the particular sensor used in these studies (the ATI Mini40), the mean X forces were on the same order as the sensor noise (about 0.25 N), while the mean Z forces were within the noise threshold. The torques showed similar characteristics;  $\tau_y$  and  $\tau_z$  were within the noise thresholds (about 20 mNm), while  $\tau_x$  had greatest absolute value, averaging -190 mNm. Because  $F_x$ ,  $F_z$ ,  $\tau_y$ , and  $\tau_z$  are so small, it is likely that they contribute negligibly to sonographer fatigue or injury and likely have minimal effect on image quality. Therefore, for future studies measuring probe contact forces, is likely acceptable to neglect these forces and torques. Thus, the use of the single axis load cell fulfills the functional requirements.

With the single-axis load cell selected, it is possible to proceed with the design of the device. The single-axis load cell presents a design challenge, because its shape

is quite different from that of the six-axis load cell; it is designed to be used in Instron-type systems, in which the load cell axis of compression lies along the line of force application, and total axial length has no stringent constraints. In ultrasound imaging, as discussed in the previous paragraph, most of the force is applied along the axis of the probe, labeled “Y-axis” in Fig. 4-1. However, connected to the ultrasound probe through the probe axis is typically a thick cable, with minimum bend radius no less than 2 cm. Thus, it is not possible to mount the load cell through the axis of force application and closer to the face of the probe than about 15 cm, which would give a total system length of more than 17 cm, and violates the max length functional requirement. Therefore, it is not possible to mount the load cell along the axis of force application without making the system too long, and therefore requires the load cell to be mounted off the Y-axis.

Mounting the load cell off axis poses a design challenge, because the application of a force  $F$  at a distance  $R$  between the Y-axis and the origin of the load cell induces a bending moment  $M = FR$  about the origin of the load cell, as shown in Fig. 4-1.

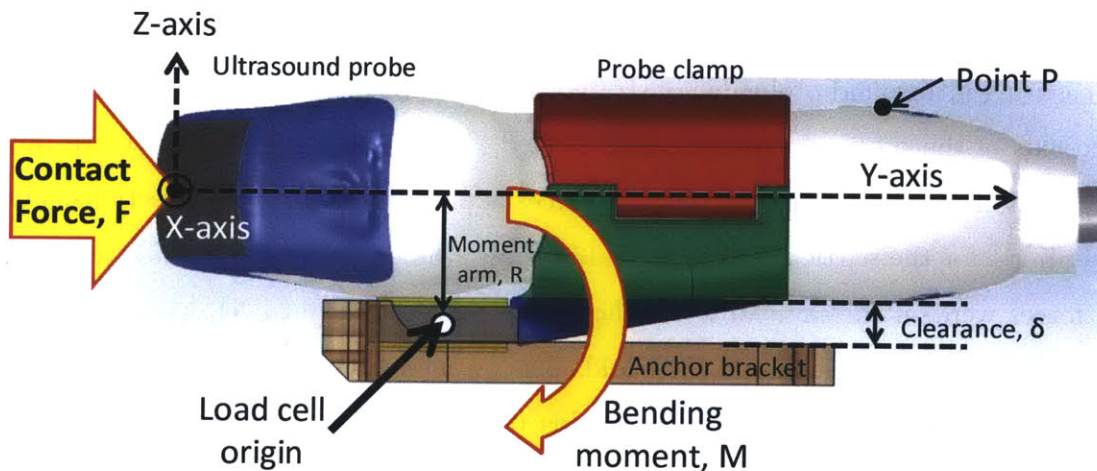


Figure 4-1: Side view of the ultrasound probe showing the application of force  $F$  along the Y axis, which induces a bending moment  $M$  about the load cell. Note: the X-axis is out of the page.

Because the single-axis load cell is less stiff than the six-axis load cell in torsional bending, one concern is that the bending moment  $M$  will cause the probe to bend about the X-axis (out of the page). This could reduce the clearance  $\delta$  between the

probe and the anchor bracket (which, in the case of the Series 1 probe, is the bottom plastic shell) and cause interference. If the two surfaces touched, extension of the load cell along the Y axis would be impaired due to friction, causing the force to be measured with less accuracy. Another concern is that the bending moment could exceed the load cell torsional deflection ratings (which are not specified by the manufacturer). Therefore, in proceeding with the incorporation of the single-axis load cell into the design, special considerations must be taken.

To determine whether the worst-case bending moment (induced by a contact force of approximately 45 N) would damage the load cell, a finite element analysis was conducted. A solid model of the load cell was created by tracing a 2D drawing of the load cell provided by the manufacturer (Futek). A moment arm with length  $R$  was attached to the load cell and a force  $F$  of 45 N was applied. The stress was calculated using SolidWorks' FEA tool, and a screenshot is shown in Fig. 4-2.

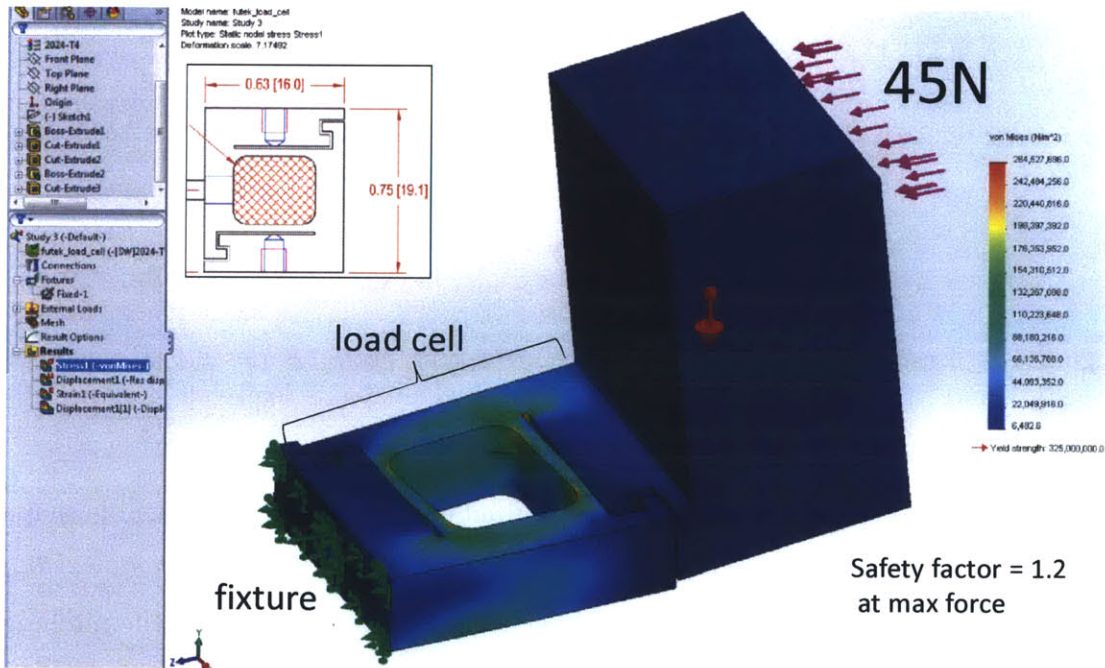


Figure 4-2: Image of the finite element analysis for the load cell with a worst case bending moment applied. Deformation is exaggerated by a factor of 7.2. The stress in load cell, which is indicated by the colormap, is highest in the regions with highest radius of curvature. The maximum stress of 264 GPa is less than the 325 GPa yield stress of the 2024 aluminum. This suggests that, even at the highest forces, the load cell is not expected to be damaged.

Fig. 4-2 displays, in color, the stress in the load cell, which is highest in the inner regions with high radius of curvature. The maximum expected stress is about 17% less than the yield stress of the 2024 aluminum, which suggests that, even at the worst-case force, the load cell will not be damaged. Thus, from a stress point of view, this design is feasible.

To evaluate the feasibility of the design from a kinematic point of view, the first iteration of Series 2 was 3D printed from ABS plastic and is depicted in Fig. 4-3, ②. The load cell (labeled “LC”) was connected to the plastic bottom shell on one side and the plastic probe clamp on the (labeled “P” for “plastic”).

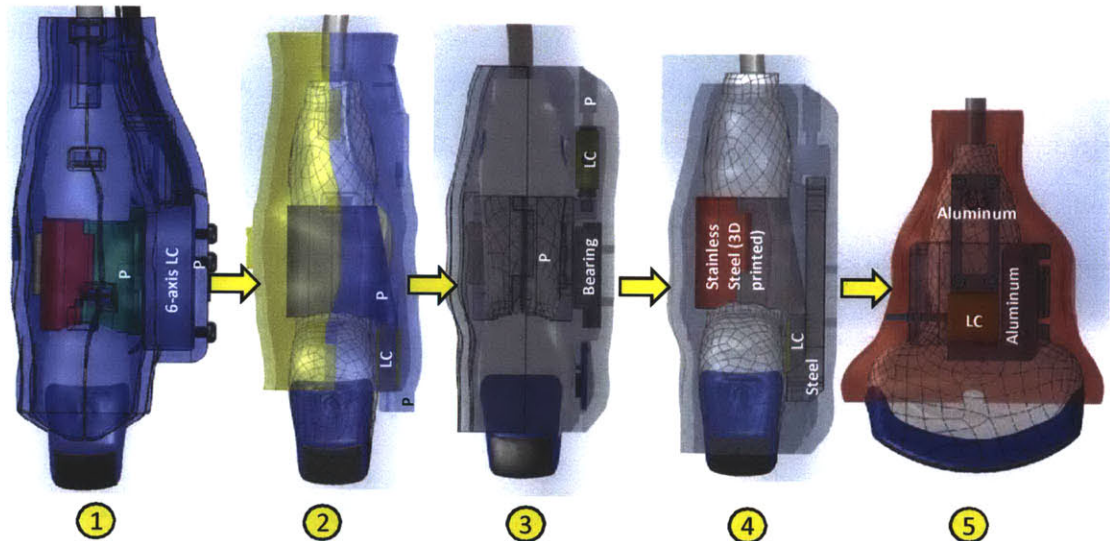


Figure 4-3: Design iterations for the force-measuring probe, Series 2. “P” denotes “plastic” and “LC” denotes “load cell.” The original 6-axis load cell design ① is shown on the left, final design ⑤ is shown on the right.

While this design (②) was simple and resulted in a thinner, more grippable shape than the original six-axis design (① in Fig. 4-3), it was found that the design was too compliant, and force along the Y-axis caused the probe to deflect about the pitching direction, causing the probe to touch the bottom shell. It was surmised that the torsional compliance was due to the compliance of both the load cell and the plastic clamps.

To eliminate the transmission of a bending moment through the load cell, a new version was conceived, in which the probe is mounted to a small linear bearing and

pushes against the load cell. The concept is shown in Fig. 4-4. With this design, the bending moment, as well as the Z and X contact forces, are supported entirely by the linear bearing. As the contact force  $F_y$  varies, the probe clamp causes the load cell to deflect; deflection is converted into an analog voltage. The linear bearing permits the sub-millimeter deflection of the load cell. To prevent kinematic overconstraint, the probe clamp is attracted to the load cell via a small magnet.

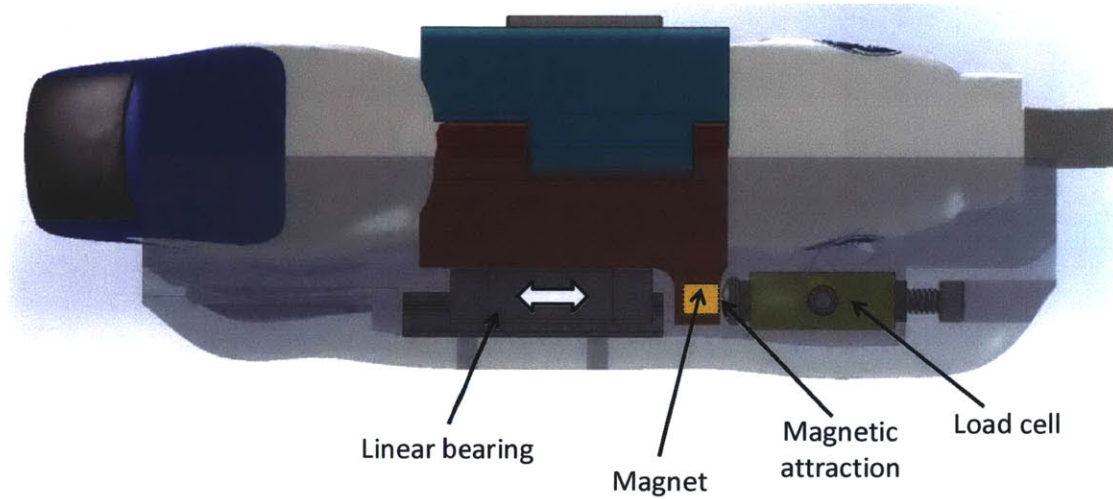


Figure 4-4: Linear bearing concept for Series 2 of the force-measuring probe. The linear bearing resists all bending moments and forces except for the contact force along the Y-axis, which is transmitted directly to the load cell.

This design was fabricated and evaluated. While the device operated as expected, there were a number of concerns. First, the addition of a moving part (the linear bearing and carriage) introduces one more failure mode for the system, a failure mode that is not present with design ②. Second, the linear bearing is not frictionless, and therefore the measurement accuracy is limited to the friction force of the bearing. Over time, the bearing lubrication might decrease, and therefore the force would be read less accurately. Third, the magnetic attraction between the probe clamp and the load cell meant that the two parts were not rigidly connected; sufficiently high force could cause the two to detach. The use of a flexure instead was considered, but the design was ruled out due to the other concerns mentioned. Due to its simplicity, it was desired to stiffen the design of concept ②.

As discussed, the torsional compliance of concept ② could be due to a combination of the compliance of the load cell and the compliance of the 3D printed plastic components. To stiffen the parts to which the load cell is mounted, a new design was conceived, ④, which consisted of a steel probe clamp and steel anchor bracket. The probe clamp was 3D printed from stainless steel by Shapeways, Inc.<sup>1</sup>, while the anchor bracket was waterjetted and machined from steel. A photograph of the design, concept # ④ is shown in Fig. 4-5.

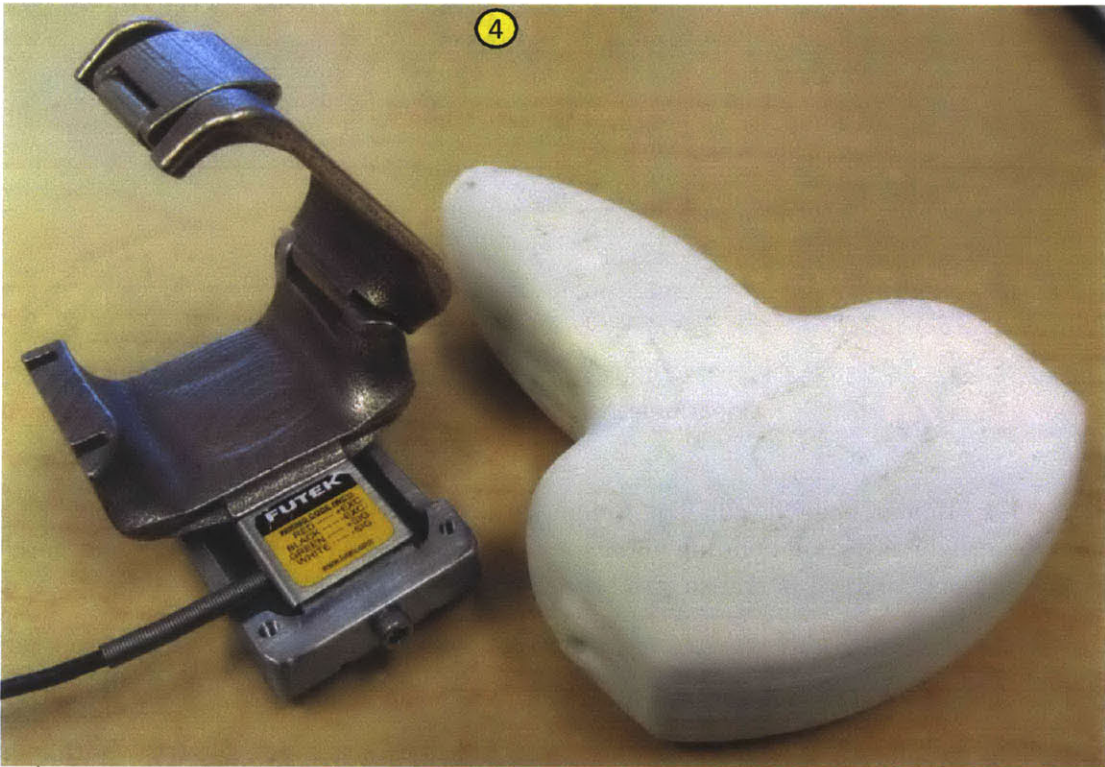


Figure 4-5: Force-measuring probe concept ④, consisting of a 3D printed stainless steel probe clamp and a waterjetted/machined anchor bracket.

While ④ was considerably stiffer than ②, it too suffered from a number of drawbacks. First, the total mass of the components was nearly 200 g, similar to the weight of the probe itself, which was near the limit total mass of the functional requirement in Table 3.2. Second, ultrasound probe did not fit as well within the probe clamp. The original probe clamp accommodated the probe due to the principle of elastic av-

<sup>1</sup>The resulting composition is actually 70% stainless steel and 30% bronze.

eraging [99]: the plastic probe clamp was compliant, and bent around the ultrasound probe. The stainless steel probe clamp is rigid, and therefore the probe itself needed to bend in order to fit within the clamp. This is undesirable, because it increases the likelihood of the probe being marred and scratched. Due to these concerns, design ④ was ruled out.

Although ④ was ruled out due to its weight and tendency to damage the ultrasound probe, it did have sufficient torsional stiffness. This demonstrated that the concept of mounting the load cell via steel (instead of plastic) connections on each side stiffened the system. To reduce the mass of the device while maintaining stiffness, design ⑤ was conceived. The load cell would be attached to on each side by an aluminum bracket. The aluminum brackets would attach to 3D printed plastic parts. The role of the aluminum was to provide high stiffness at the high-stress load cell contact interfaces, then distribute the stress over a larger surface area to the plastic components. A transparent view of the concept is shown in Fig. 4-6.

Concept ⑤ was fabricated via plastic 3D printing, machining and waterjetting.

The most critical questions to answer were: 1) what is the maximum torsional stiffness that can be achieved using the single-axis load cell?, and 2) is that maximum stiffness high enough to prevent interference? To address the first question, a number of experiments were conducted with designs ② - ⑤ as well as slight variations. In each of these experiments, the effective torsional stiffness about the load cell was measured through a force-displacement test. The various designs were rigidly fixed beneath a miniature Instron-type machine (discussed in [42]). The indentor was placed in contact with the end of the ultrasound probe, at the point P shown in Fig. 4-1, force was applied in the Z direction, and the force-displacement characteristics were measured. The linear stiffness was mapped back to an effective torsional stiffness at the load cell based upon the length of the lever arm (the distance along the Y-axis from P to the load cell origin).

A bottom view of the various configurations tested is shown in Fig. 4-7. Several configurations (#4, 5, and 7) used a mock-up load cell, a solid aluminum block with the same dimensions as the actual load cell, in order to measure the stiffness of the

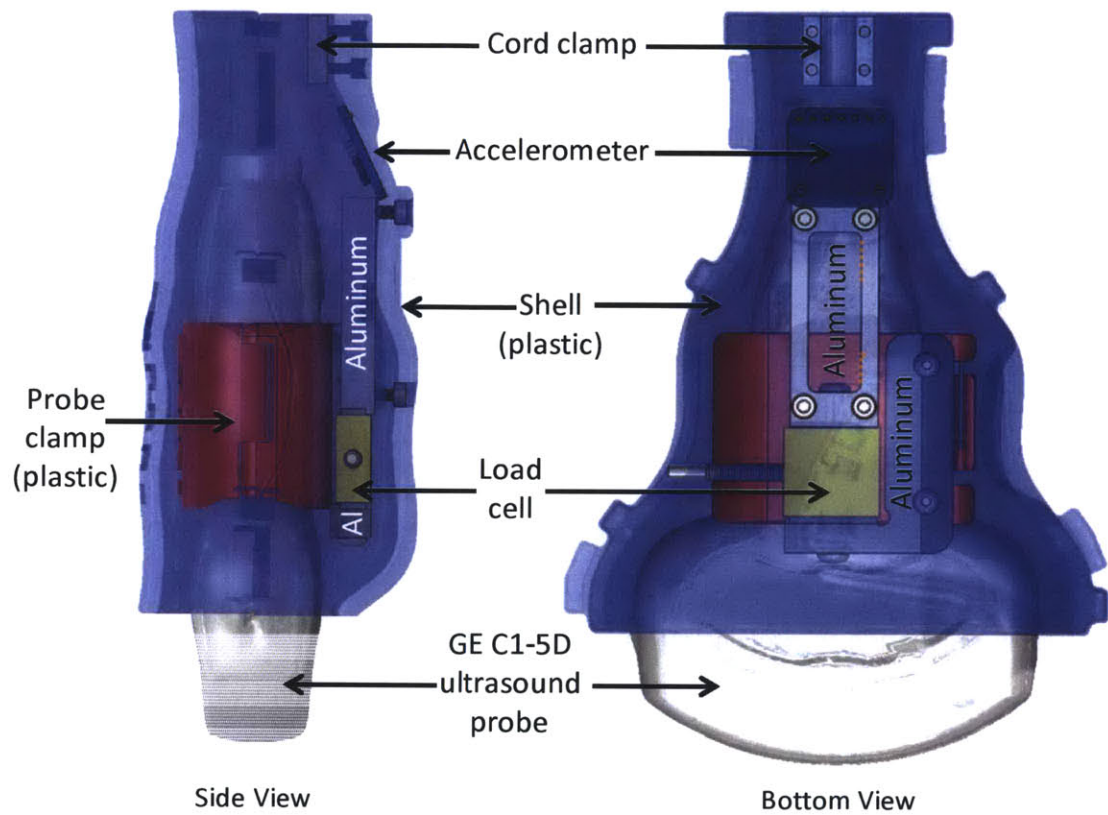


Figure 4-6: Force-measuring probe, Series 2, concept ⑤, in which the load is sandwiched between aluminum mounting brackets, which are secured to the 3D printed plastic probe clamp and bottom shell.

Table 4.2: descriptions of each of the configurations, along with the measured torsional stiffness of each.

Run #	Anchor bracket material	Real load cell?	Probe clamp mounting material	Torsional stiffness (Nm/rad)
4	Aluminum	Mockup	Aluminum	35.8
5	Aluminum	Mockup	Aluminum	48.5
7	ABS Plastic	Mockup	ABS Plastic	10.7
9	Linear bearing	Load cell	Linear bearing	46.6
10	Aluminum	Load cell	Aluminum	23.2
11	ABS Plastic	Load cell	ABS Plastic	11.5
12	Steel	Load cell	ABS Plastic	13.1
14	Steel	Load cell	Stainless steel	23.4

other components.

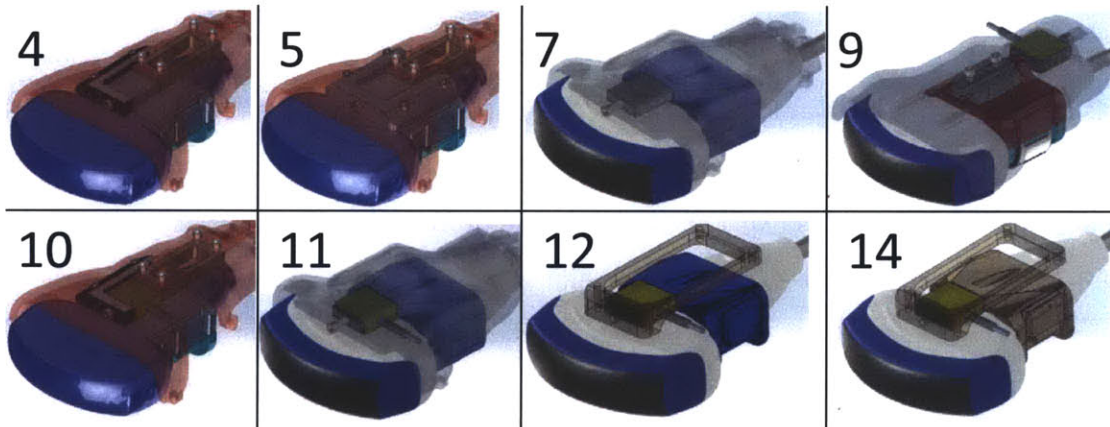


Figure 4-7: Bottom views of the configurations tested. The configurations varied in terms of the material of the part mounted to each side of the load cell (3D printed plastic, aluminum, or steel) and whether the real load cell or mock-up load cell was used. Black arrows indicate chronological direction of development.

The measured torsional stiffness of each of the various configurations tested is shown in Table 4.2.

From Table 4.2, the torsional stiffness of Run 14, with load cell mounted between the steel probe clamp and steel anchor bracket, was approximately 23.4 Nm/rad. Since the steel probe clamp and anchor are considerably stiffer than the load cell, this stiffness measurement represents the torsional stiffness of the load cell itself. Therefore, this is the maximum stiffness we expect to see in any of the runs. Run 10

shows similar stiffness to Run 14, which therefore indicates that the stiffness in these designs is limited by the compliance of the load cell. Thus, these designs are all as stiff as possible given the Futek LSB200 load cell.

Thus, both of the questions posed above have been answered: 1) maximum possible stiffness given the single axis load cell was found to be about 23.4 Nm/rad, and 2) it was found in design #14 that it is stiff enough. The next step in the design process is to select from the maximum-stiffness designs the design that best fulfills the functional requirements, specifically the mass constraint.

Design 10 has maximum stiffness and also employs lighter-weight aluminum components. It therefore fulfills the functional requirements better than design 14 and is consequently selected as the most appropriate design for the single-axis force-measuring probe.

In proceeding with the mechanical design, the next important consideration is ensuring that the shape of the device is ergonomic. This means minimizing the size of the device and making sure there are no sharp edges. Using the 3D scanned solid model for the probe, various designs were prototyped. Various part thicknesses and clearances were tested to find a design with sufficient stiffness with no areas of interference. Different strategies for strain-relieving the cable were also prototyped, including plastic zip ties, hot glue, and a machined aluminum clamp. The aluminum clamp was used in the final design. Images of the various 3D printed prototypes are shown in Fig. 4-8.

The final design is shown on the bottom right of Fig. 4-8. Three prototypes of the system were fabricated, two of which were brought over to MGH for validation. During two full-length abdominal scans with a real sonographer and the real GE C1-5D probe on a healthy volunteer, the device performed as expected, and the design was finalized.

## 4.4 System components: Series 2

A photograph of the complete system is shown in Fig. 4-9.

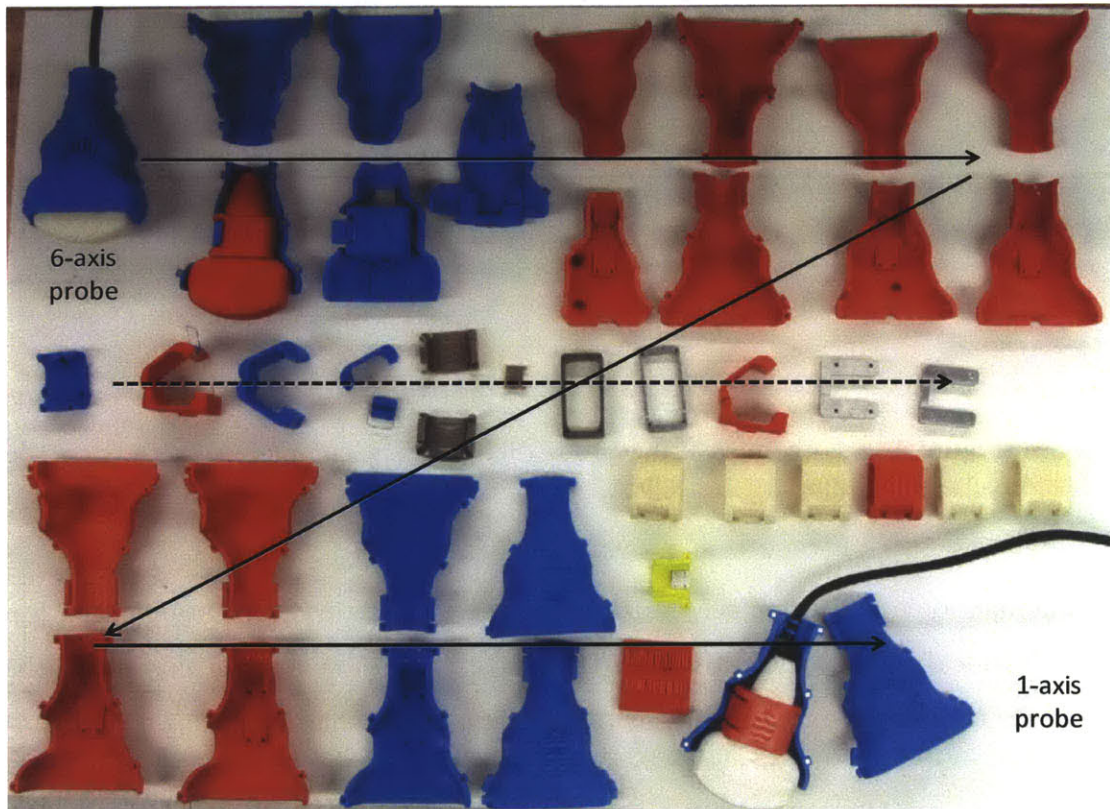


Figure 4-8: Prototypes of the Series 2 force-measuring probe. The prototypes differ in terms of part thickness, clearances, and cord grip. A major factor that necessitated a number of additional iterations was due to the kinematics of how the probe clamp fit around the probe. Black lines indicate the chronological progression of the various design iterations.

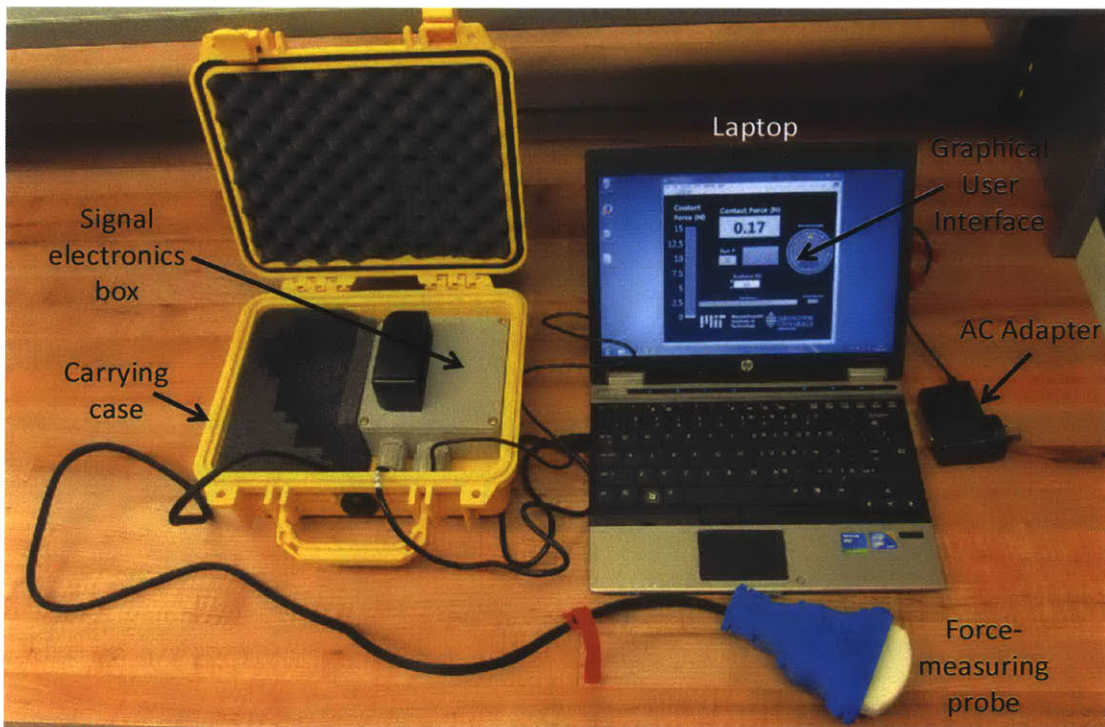


Figure 4-9: Force-measuring probe, Series 2: the complete system.

The one force and three accelerometer voltages (X, Y, &Z) are sampled with a single National Instruments USB-6009 DAQ board, which is housed, along with the Futek CSG110 signal amplifier, in the plastic signal electronics box, shown in Fig. 4-10.

Signals from the DAQ board are passed to a laptop, and read with an executable file written in LabVIEW. Force and device angles are displayed on a graphical user interface (GUI), a screenshot of which is shown in Fig. 4-11.

The program records forces and angles at a rate of about 40 Hz; the GUI displays the force with a vertical bar, and the angles in form of an aviation-style display. To restrain the components during transport, the AC adapter magnetically attaches to a black 3D printed plastic holder, as shown in Fig. 4-12.

A photograph of the system prepared for clinical use is shown in Fig. 4-13.

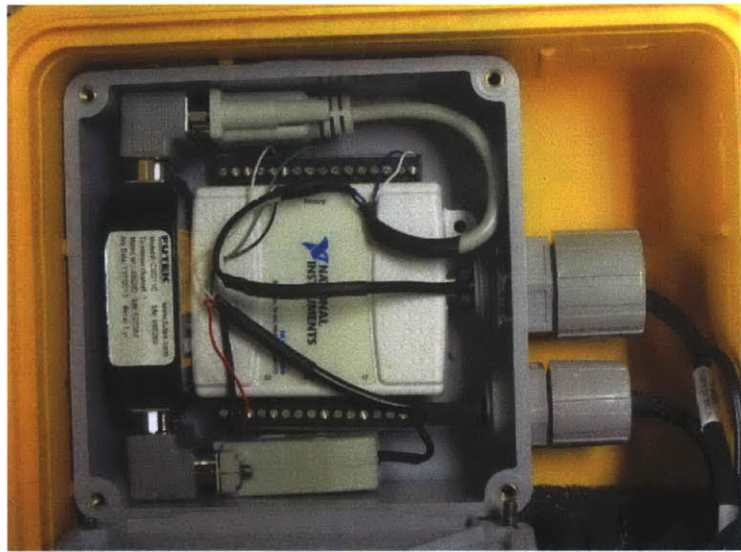


Figure 4-10: Photograph of the signal electronics box, which contains the Futek CSG110 signal amplifier and NI USB-6009 DAQ board. Wires are all strain-relieved with cord clamps. Components were laid out to minimize overall volume to maximize portability.

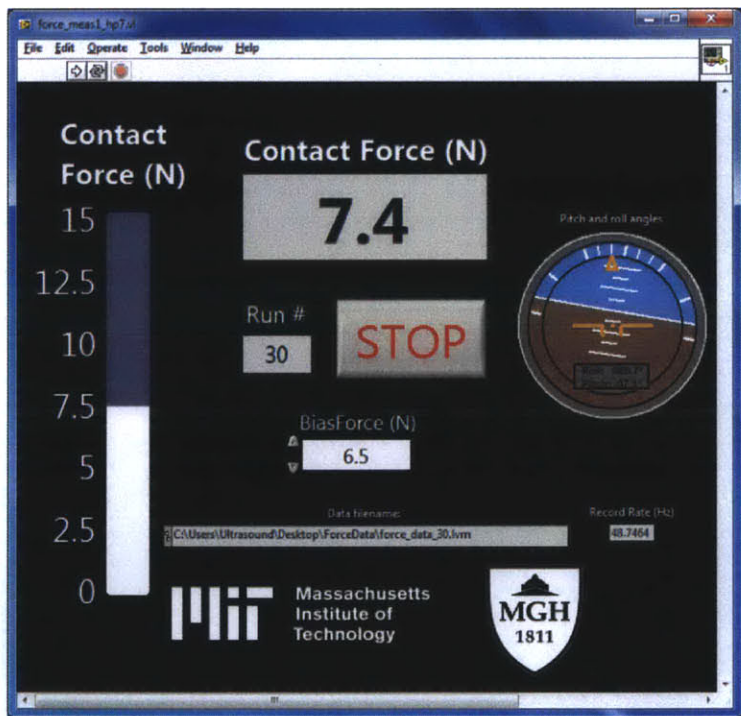


Figure 4-11: Screenshot of the graphical user interface (GUI) for the Series 2 force-measuring probe. The GUI displays the contact force as well as the pitch and roll angles of inclination of the probe.



Figure 4-12: Magnetically attaching the AC adapter to the black plastic holder.

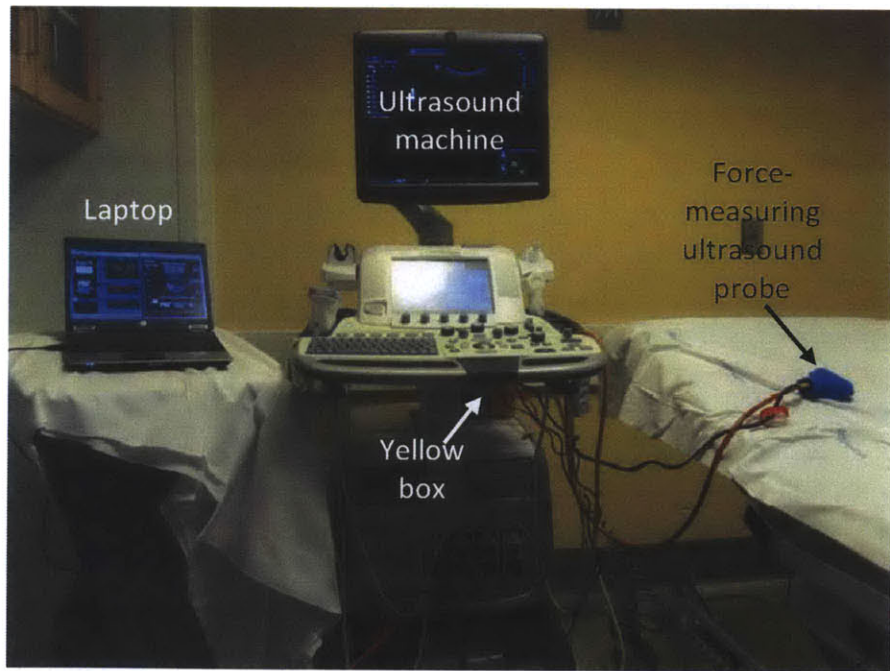


Figure 4-13: The force-measuring ultrasound probe, Series 2, after clinical use at MGH.

Table 4.3: Comparison between the Series 1 and Series 2 force-measuring probes.

Series	Measures	Mass	Volume	Parts cost	Custom parts	# built
1	6-axis force/ torque	5 kg	25k $cm^3$	\$7k	5 plastic	1
2	1-axis force	1.8 kg	7.5k $cm^3$	\$1.5k	5 plastic, 2 Al	3

## 4.5 Comparison: Series 1 vs. Series 2

The Series 2 probe achieves the cost and system mass functional requirements better than the Series 1 probe. Specifically, the total system has about one-third the weight, one third the volume, and one-fifth the parts cost as compared to the Series 1 design, while satisfying all of the other functional requirements from Table 4.1. The important differences between Series 1 and Series 2 are shown in Table 4.3.

A photograph showing both systems is shown in Fig. 4-14.



Figure 4-14: Size comparison of the Series 1 and Series 2 force-measuring probes.

The performance and capabilities of each of the prototypes are compared with

Table 4.4: Comparison between functional requirements ( $FR_p$ ) and measured capabilities ( $D_p$ ) of the force-measuring probe, Series 1 and 2.

Parameter	$FR_p$	$D_p$		N	Safety Factor	
		Series 1	Series 2		Series 1	Series 2
System Mass (kg)	10	5	1.8	-1	2	5.6
Attach + remove time (s)	60	30	30	-1	2	2
Cost (\$)	10k	7k	1.5k	-1	1.4	6.7
$F_{max}$ (N)	20	80	45	+1	4	2.3
Thickness (mm)	60	51	53	-1	1.2	1.1
Probe mass (g)	600	168	180	-1	3.6	3.3

the original functional requirements in Table 4.4. As discussed in Section 6.2 and Equation 6.1, the parameter  $N$  is +1 for functional requirements with favorable high values (e.g., maximum measurable force), and  $N$  is -1 for functional requirements with favorable low values (e.g., system mass).

A graphical comparison of the original functional requirements with the actual design specs for the Series-1 and Series-2 force-measuring probes is shown in Fig. 4-15. In this spider plot, for type  $N = -1$  functional requirements, the reciprocal of the functional requirement is taken so that favorable values are farther outward on the “spider web.”

## 4.6 Conclusions

This chapter presented two ergonomic, instrumented ultrasound probes that measure ultrasound probe acquisition state. The first device measures contact forces and torques in six axes, along with pitch and roll angles of orientation. The second device measures contact force in one axis, and is considerably lower-cost.

The devices both consist of robust designs with 5 or fewer 3D printed plastic parts, all of which could be injection molded. Both devices employ quick-release probe clamps and magnetic shell-to-shell attachment, which permits rapid attachment and removal of the ultrasound probe from the device.

The first device was used to measure contact forces and torques during 53 abdom-

### Functional Requirements vs. Device Specs - Force-Measuring Probe

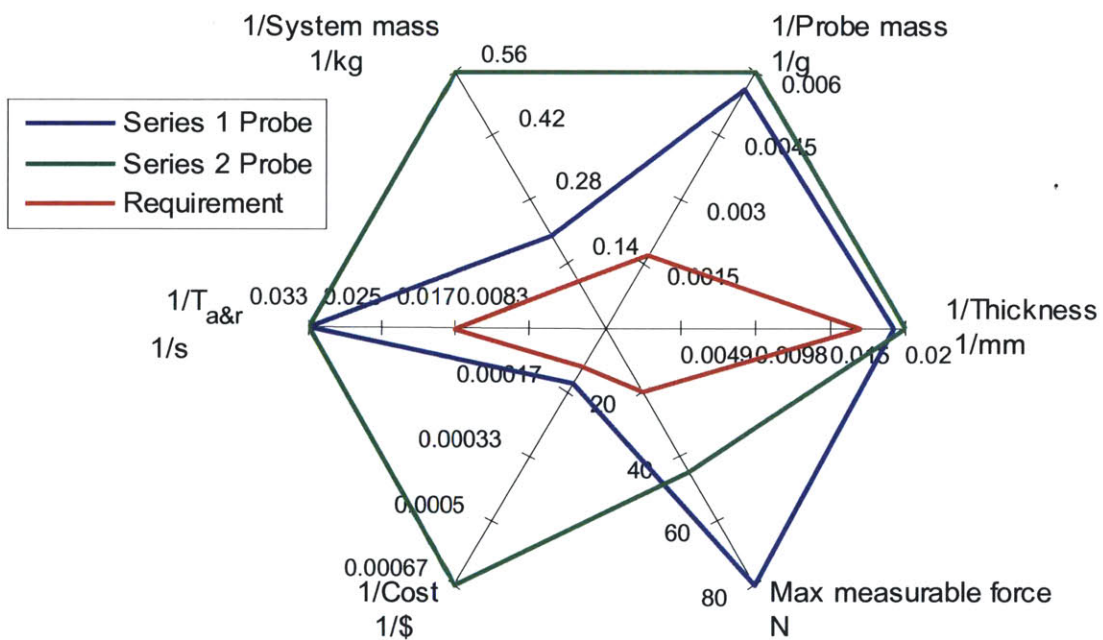


Figure 4-15: Spider plot comparing the original functional requirements with the actual values for the force-measuring probes. ' $T_{a\&r}$ ' refers to the total time to attach and remove the probe.

inal ultrasound exams conducted by 13 professional sonographers on 10 patients at Massachusetts General Hospital. The mean axial force (8.3 N) was found to be in close agreement with that measured by Salcudean [91] in carotid exams (6.4 N), and within the 5 N-20 N range specified by Guérin [101] in abdominal, cardiac, and renal exams. Contact force was found to be higher for high-BMI patients than for low-BMI patients. No statistically-significant correlation was found between sonographer level of experience and contact force.

This work represents the first rigorous study of ultrasound probe contact forces. Future work includes using the device in a much greater number of exams of different types with more sonographers in order to develop a more comprehensive understanding of the forces applied during ultrasound imaging. These data could be used to better-understand the correlations between sonographer contact force and the risk of fatigue and musculoskeletal injury.

Finally, we can now specify the third of the three critical functional requirements in the design of the force-controlled ultrasound probe, namely the contact force. The maximum force that the force-controlled probe will need to be able to apply is the maximum force recorded by the force-measuring probe, i.e., 36.5 N. Of course, it would be prudent to place an appropriate safety factor upon the functional requirement.

# Chapter 5

## The Force-Controlled Ultrasound Probe

### 5.1 Summary

In this chapter, we present two hand-held devices that apply a programmable contact force between the ultrasound probe and the patient. The purpose of these devices is to control one of the acquisition state variables of the ultrasound probe, namely the contact force, in order to improve the repeatability of ultrasound imaging and reduce the level of operator skill necessary to obtain diagnostic-quality images. The mechanical portion of the device consists of a ball screw linear actuator driven by a servo motor, along with a load cell, accelerometer, and limit switches. The performance of the second prototype was assessed in terms of the frequency response to simulated sonographer hand motion and in hand-held image feature tracking during simulated patient motion. The system was found to attenuate contact force variation by 97% at 0.1 Hz, 83% at 1 Hz, and 33% 10 Hz, a range which spans the typical human hand tremor frequency spectrum. In studies with fifteen human operators, the device applied the target contact force with ten times less variation than in conventional ultrasound imaging. An ergonomic, human-in-the-loop, imaging-workflow enhancing control scheme, which combines both force- and position-control, permits smooth making and breaking of probe-patient contact, and helps the operator keep

the probe centered within its range of motion. By controlling ultrasound probe contact force and consequently the amount of tissue deformation, the system enhances the repeatability, usability, and diagnostic capabilities of ultrasound imaging.

In this chapter, we discuss a system—a handheld, electro-mechanically actuated, programmable-force ultrasound probe—and control techniques to provide a known contact force and reduce image and imaging-workflow variations. The three force-controlled ultrasound probe prototypes developed as part of this research are shown in Fig. 5-1.

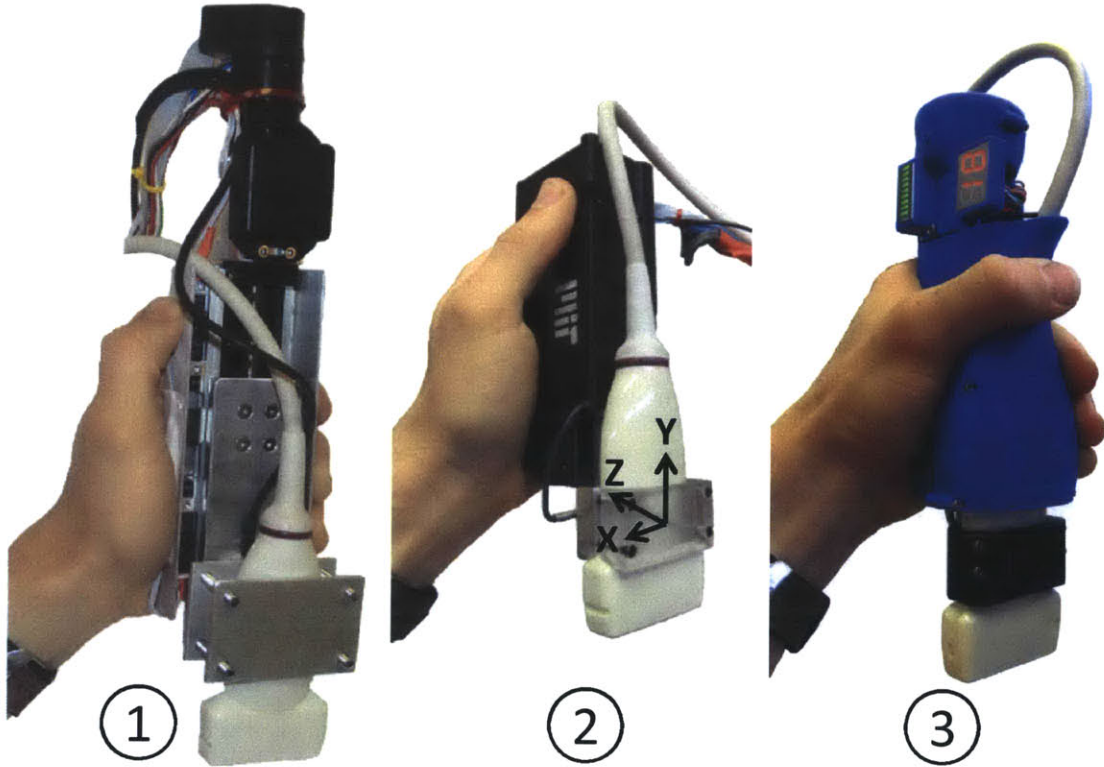


Figure 5-1: The three force-controlled ultrasound probes that have been developed. Prototype 1 was the subject of the author's masters research [40]; Prototypes 2 and 3([15],[16],[17],[18],[41],[43]), which are discussed in this thesis, were developed during the author's PhD research.

Table 5.1: References corresponding to the prior art shown in Fig. 5-2.

Label	Name/Affiliation; Reference
(1)	CMU Micron; MacLachlan [62]
(2)	JHU Steady Hand; Mitchell [67]
(3)	Harvard; Yuen [117]
(4)	Da Vinci; Broeders [24]
(5)	Tokyo; Ueta [109]

## 5.2 Related Work: Hand Tremor Suppression Systems

The relevant literature for this work is any medical device that attenuates hand tremor. A sampling of five relevant hand tremor-suppressing devices from the literature is shown in Fig. 5-2.

As discussed by MacLachlan, et al, in the Micron project [62], most manipulation aids developed for medical applications can be classified into one of two categories: *cooperative control* or *master/slave control*. In cooperative control, both the operator and robot arm hold the tool. The robot arm, which is very stiff and not easily backdriveable, filters out the operator's hand tremors due to its high stiffness. A force sensor positioned between operator's hand and the tool measures the applied force, and the actuator moves in response to the applied force in an effort to reduce it to zero. The JHU Steady-Hand Robot (label 2) represents the cooperative control technique, in which the surgeon and robot share control of the tool, which is mounted to the 5-DOF robot via a force sensor. The tool is moved by leadscrew-driven and planetary gear-driven stages. Admittance control is used to move the stages with velocities proportional to the applied forces, and tremor compensation is achieved due to the stiffness of the system. The system, which is designed for retinal microsurgery, is fixed to the table and has an XYZ range of motion of  $\pm 50$  mm, which makes the device less suitable for large-area ultrasound imaging, such as the abdomen, in which scanning dimensions are on the order of 300 mm.

A number of devices fall into the latter category of master/slave control, in which the user manipulates a master controller, the positions of which are measured and

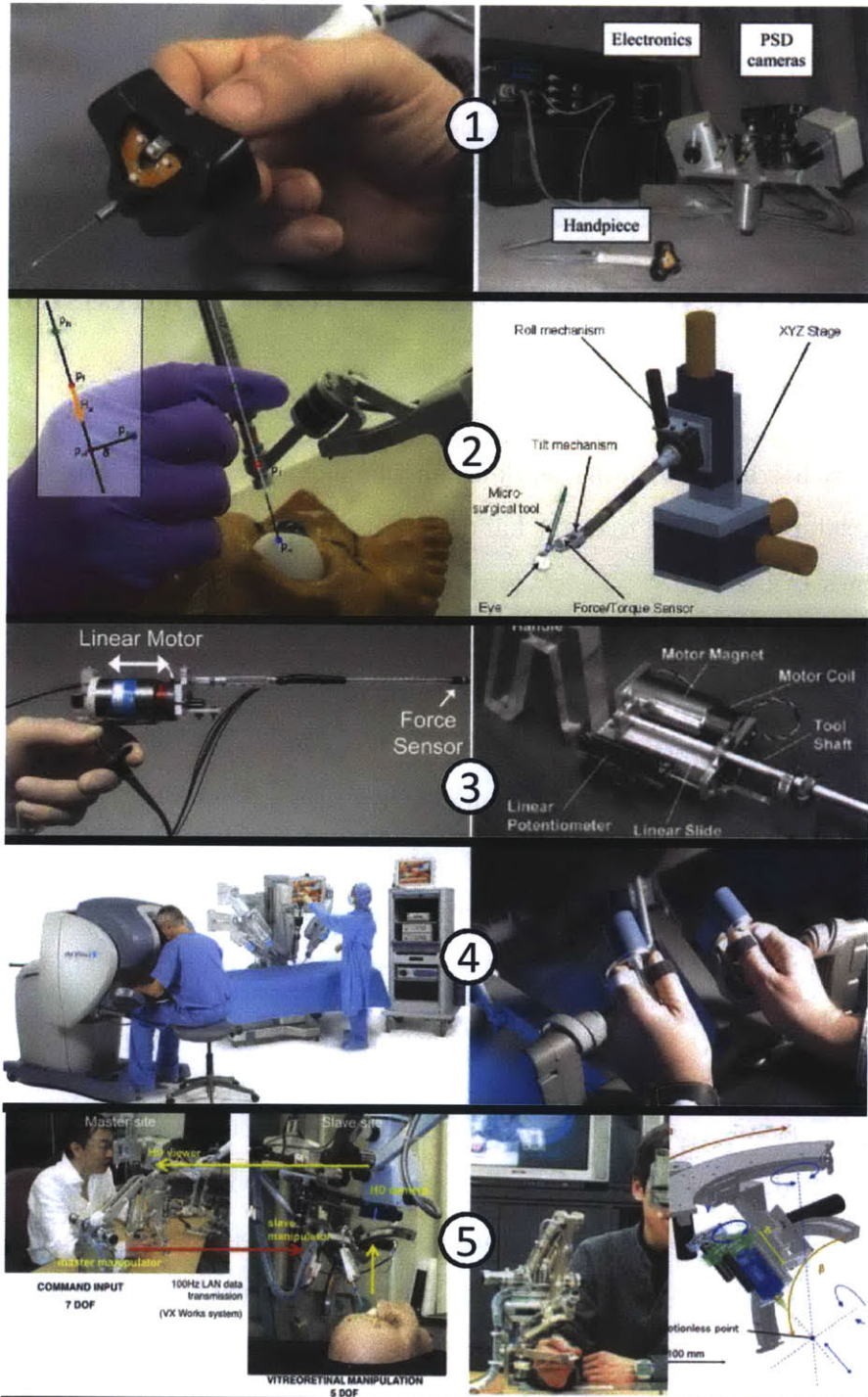


Figure 5-2: Five hand tremor suppression devices from the literature. Labels are identified in Table 5.1. Note: the photos in a given row are for a particular device.

digitized, then transmitted electronically to an actuated slave manipulator, which is commanded to move according to the master’s motions. As discussed in Section 1.3.2, a number of ultrasound-scanning robots are designed for tele-echography, which is a form of master/slave control. The master/slave technique has the advantage of enabling digital or electronic filtering of hand position, in addition to scaling, in order to suppress tremor. The Tokyo 5-DOF vitreoretinal surgical system (label 5) [109] and the Intuitive Surgical da Vinci Robot (label 4) [24] are both examples of master/slave control.

A third actuation technique which shares some aspects of both master/slave control and cooperative control is exemplified by the CMU Micron system (label 1), developed for microsurgical applications, as well as the Harvard beating heart surgical tool (label 3), in addition to the force-controlled ultrasound probes presented in this thesis. With this third actuation technique, which we shall refer to as “macro/micro” control, the operator essentially provides coarse control of the tool, while the actuator provides fine control and suppresses hand tremors. An actuator separates the user’s hand from direct contact with the tool.

The CMU Micron system [62] consists of a handheld microsurgical tool which is gripped by the user and placed in contact with the patient. In between the user’s hand and the tool endpoint is a 3-DOF piezoelectrically-actuated stage with  $400\mu m$  range of motion. Mounted to both the hand-side and tool-side of the stage is a series of infrared LEDs, whose position is tracked by an earth-grounded camera system. A control system actively stabilizes the tool endpoint with respect to the camera ground, enabling high-bandwidth ( $> 100$  Hz) hand tremor suppression and higher-precision tool manipulation.

Micron, which is designed for microsurgery, would be less suited for force-controlled ultrasound imaging. While Micron’s  $400\mu m$  range of motion (in 3 DOFs) is adequate for microsurgery, it would not be sufficient for large-area ultrasound scanning. In [43], we found that a range of motion of approximately 4-5 cm was necessary to accommodate undesired hand motion in abdominal imaging. In addition, because Micron’s two position-detecting cameras are fixed to the ground, rather than the patient, the

system is sensitive to patient motion. In ultrasound imaging, the patient is typically not immobilized, and limbs can move during respiration or under an applied force. As discussed in [105], systems that are patient-referenced, rather than earth-referenced, can achieve higher positional accuracy in ultrasound imaging. For these two reasons, Micron's architecture would be less suitable for force-controlled ultrasound imaging.

Yuen and colleagues [117],[118] have developed a handheld voice coil-actuated 1-DOF surgical tool that enables a surgeon to operate on a beating heart. A fixed 3D-ultrasound probe placed a distance away from the tool monitors the position of the heart's mitral valve while a predictive filter, along with a feed-forward controller, deliver a control signal to the voice coil. The device reduces variations in contact force by up to 75%, as compared with unassisted freehand operation. The device could potentially be adapted to enable high-bandwidth constant-force ultrasound imaging.

Both Micron, the Harvard beating heart tool, and the force-controlled ultrasound probe described in this paper share the common aspect of a hand-held device in which user's hand is separated from the tool by an actuator, which is used to reduce undesired hand motions and stabilize the tool's position. The force-controlled ultrasound probe differs from these systems in terms of its range of motion and its ability to translate the moving mass of an ultrasound probe.

In terms of control, the voice coil-actuated tool by Yuen [117],[118] employs an extended Kalman filter and PID controller to actuate the voice coil. The 6-DOF ultrasound robot by Zhu [119] uses a shared control strategy to simultaneously control the probe velocity, position, and force. The TER robot by Vilchis [111] uses open-loop position control. None of these control strategies alone can ensure endpoint avoidance (i.e., staying away from the range of motion limits) and the ability to make and break probe contact, two important attributes of our system that we discuss in more detail in Sections 5.9 & 5.10.

This and the following chapter describe the design, use, and analysis of an ergonomic, handheld, force-controlled ultrasound probe suitable for large-area scanning. The device controls one of the probe's translational DOFs, while measuring two of the probe's angles of orientation. A combined force/position control system permits

ergonomic use of the device.

### 5.3 Force-controlled probe: design process

As mentioned, three prototypes of the force-controlled ultrasound probe have been developed (shown in Fig. 5-1). The three devices differ in terms of range of motion and ergonomics, but all were designed for general abdominal and musculoskeletal imaging. Prototype 1 was developed in the author's masters research, and the design process is described in [40]. Prototypes 2 and 3 were a component of the author's PhD research, and are discussed in detail in this thesis.

In this section, we present the process followed in the design of the second prototype, a photograph of which is shown in Fig. 5-3, along with a solid model rendering.

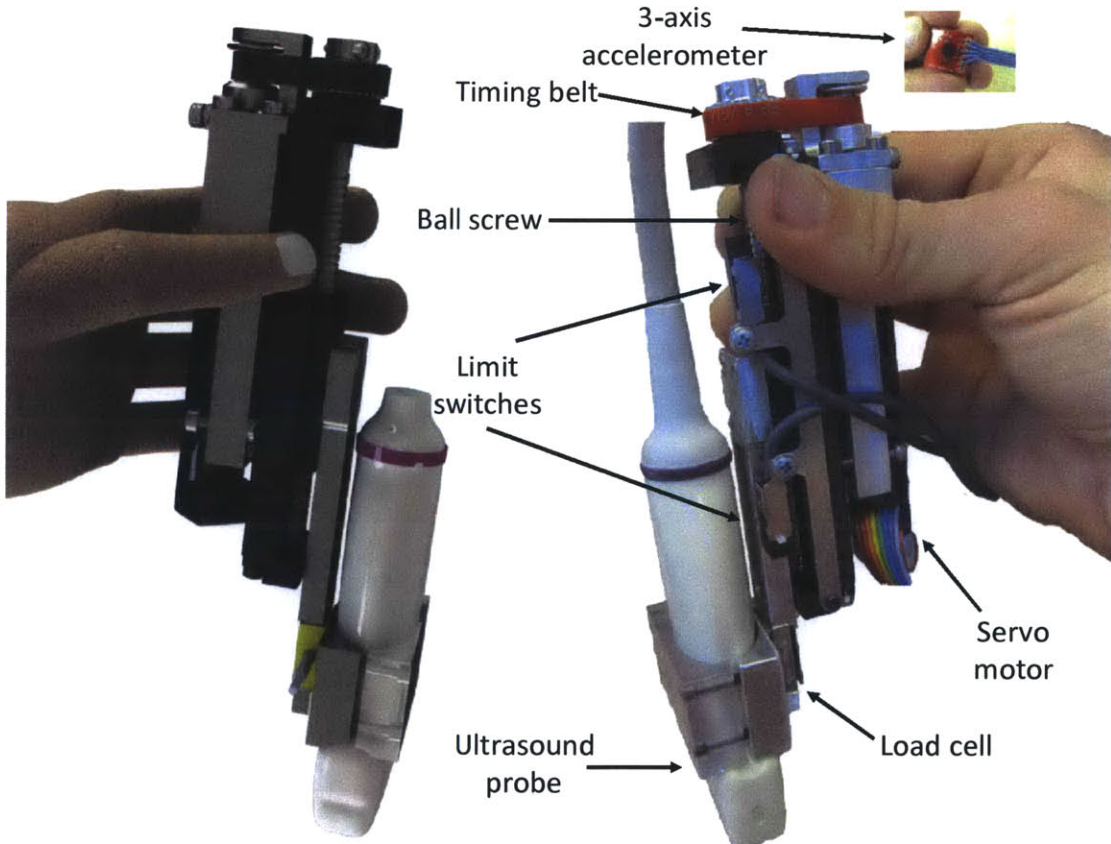


Figure 5-3: Solid model (L) & photo (R) of the force-controlled ultrasound probe, Prototype #2. The device is depicted without the protective plastic cover.

### 5.3.1 Functional Requirements

Thus far in this thesis, we have determined the three most critical functional requirements for the force-controlled probe, namely the necessary range of motion, power, and contact force. Next, we discuss the evaluation of the other important functional requirements.

The primary objective of the force-controlled ultrasound probe is to help the sonographer control one of the acquisition state variables of the ultrasound probe, namely the contact force, as discussed in Section 1.4. This implies a number of attributes that the device must possess:

1. Handheld. The device must fit comfortably in the sonographer's hand and must be able to be used for approximately 10 minutes at a time, the typical ultrasound exam duration [44]. This places requirements upon the mass and dimensions of the probe itself:
  - (a) *Mass*: The device must have sufficiently low mass that it can be held in an intermittently outstretched arm for up to ten minutes without causing the sonographer's muscles to fatigue. During use, the probe will be in contact with the patient for a large portion of the time; during this time, the patient will support the programmed contact force of the probe while the sonographer will support the weight of the device minus the contact force. When the probe is moved from one scan area to another, or the desired contact force is reduced, the device's mass will need to be supported entirely by the sonographer's hand. Examples of objects that are used in a similar intermittently outstretched/supported manner are cordless drills, cordless vacuum cleaners, and hand tools such as hammers and wrenches. The mass of these items ranges from approximately 0.5 to 5 kg. We desire for the force-controlled probe to be on the lighter-weight end of this spectrum, therefore, we require a probe mass of less than 2 kg.
  - (b) *Length*: Ultrasound probes are used to scan all areas of the body, and occasionally need to fit in tight areas due to patient geometry (e.g., behind

the leg, under the chin, etc.). Thus, the device must be short enough to fit in these areas. Lengths less than 20 cm will suffice.

- (c) *Girth/diameter*: The most ergonomic grip in ultrasound imaging is the “power grip,” in which the thumb and fingers grasp completely around an object; the fingers are tucked under the thumb. To reduce the risk of injury and fatigue, sonographers are advised to use the power grip when possible and avoid the “pinch grip,” in which the fingers and thumb barely meet [70]. To maximize the amount of time sonographers can spend in pinch grip, we require a diameter of less than 8 cm.
2. Portable. It must be possible to move the device occasionally from one ultrasound exam room to another, which places requirements upon the mass and volume. We require a mass of less than 20 kg and volume less than a 0.4 m cube.
  3. Intuitive and easy to use. In order for the device to be ergonomic, both the sonographer and patient must be able to interact with the device naturally and intuitively. This places requirements upon:
    - (a) *Tremor attenuation*: As the sonographer scans, his/her hand inevitably tremors involuntarily. Hand tremor frequencies are typically below about 10 Hz [62],[36], which means the device must be able to produce measurable motion at 10 Hz in order to attenuate the tremors and maintain a constant force.
    - (b) *Maximum force*: The device must be able to apply at least the maximum force it is expected to encounter; from [44], the maximum force is approximately 20 N.
    - (c) *Control system*: The control system must be able to accommodate both sonographer and patient motion. Special considerations that the controller must be able to handle include: probe collisions with hard objects, such as bone; initiating and breaking probe/patient contact (force goes to zero);

and times when the actuator reaches a travel limit.

- (d) *Range of motion:* Due to the involuntary hand motion mentioned above, the sonographer cannot keep his/her hand in a fixed position. Since, as discussed below, compressing tissue results in a change in contact force, the device must have a certain range of motion in order to prevent sonographer hand motion from changing the contact force. We hypothesize that for larger scan lengths, the sonographer's hand will tremor more, resulting in the need for greater range of motion. It is theorized that a range of motion of 5 cm will be sufficient for this application. (The correlation between scan length and necessary range of motion is discussed at length in Section 2.2.)

4. Safe. Above all, the device must power no risk to the sonographer or the patient.

This suggests that special considerations must be taken into account for:

- (a) *Pinch protection:* Because the device contains moving parts, the user and the patient must be protected from the risk of being pinched.
- (b) *Maximum force:* The contact force must be monitored to ensure that the device never applies too much force to the patient.
- (c) *Maximum continuous power:* The total electrical power that the device can provide should be limited to reduce the severity of any electrical shocks. An upper limit of 100 W is chosen. At the same time, the device must also be able to supply a certain minimum amount of mechanical and electrical power to ensure tremor attenuation and constant force application. As discussed in Section 2.3, both hand tremors and the application of static force contribute to the power requirements; the power requirement actually depends upon the type of actuator chosen. For the sake of continuity, we present the power requirements for two types of actuators (voice coil and ball screw) in Table 5.2, and discuss the origin of these numbers in Section 2.3.

5. Easy to sterilize. As with any medical device, the system must also be easily

Table 5.2: Summary of the quantitative functional requirements for the force-controlled ultrasound probe, Prototype 2.

<b>Functional Requirement</b>	<b>Parameter</b>	<b>Value</b>
Handheld	Probe mass	<5 kg
	Probe length	<20 cm
	Probe girth/diameter	<8 cm
Portable	Total system mass	<20 kg
	Total system volume	<0.06 m <sup>3</sup>
Permits natural interaction	Bandwidth	>10 Hz
	Maximum force	>20 N
	Range of motion	>5 cm
Power	Max continuous power	
	0.3 W <P <100 W (screw/servo)	
		40 W <P <100 W (voice coil)

sterilizable. Potential methods of achieving sterility include covering the device with a plastic bag or putting in an autoclave after each use.

The functional requirements for the force-controlled ultrasound probe are summarized in Table 5.2.

### 5.3.2 Design Parameters

This section discusses the selection of the system components (also known as the design parameters) based upon the functional requirements. Considering the need to provide one DOF of linear motion, as discussed in Section 2.1, the most critical components of the system are listed below:

1. Actuator
2. Power transmission
3. Linear motion constraint
4. Force sensor
5. Component layout

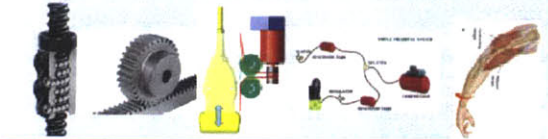
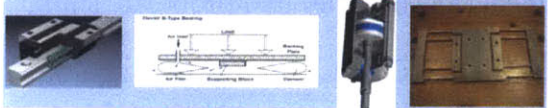
Design parameter	Examples
<b>Actuator</b> 	Servo motor, voice coil, linear motor, pneumatic, piezo, constant force spring, <i>sonographer's arm</i>
<b>Power transmission</b> 	Ball screw, rack and pinion, cable drive, compressed air, <i>muscle</i>
<b>Linear motion constraint</b> 	Ball bearing, air bearing, bushing, <i>flexure, none</i>
<b>Force sensor</b> 	1 or 6-axis load cell, pressure sensor: single or array, <i>sonographer's proprioception</i>
<b>Component layout</b> 	Motor orientation; mass distribution; shape

Figure 5-4: The five most critical components in the system, along with examples of each.

These five critical components, along with examples of each, are shown in Fig. 5-4.

The two most important components in the system are the actuator and the power transmission. The actuator converts electrical power to mechanical power, while the transmission converts the actuator's mechanical force or torque into linear motion of the ultrasound probe. Therefore, in the design process, it is sensible to select the actuator and power transmission first. A Pugh chart was constructed to evaluate the various actuation options across a range of attributes, and is shown in Fig. 5-5.

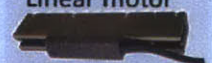
Attribute	High band-width	Simplicity	Stroke/size ratio	Programmability	Force/power ratio	Force control accuracy	Power/weight ratio	Sum
Actuation method								
Ball screw + servo 	0	0	0	0	0	0	0	0
Voice coil motor 	+	+	+	0	---	0	-	-1
Linear motor 	+	+	+	0	---	0	--	-2
Pneumatic 	--	-	+	0	0	--	++	-2
Constant force spring 	+	+	+	--	+	--	++	0
Piezo actuator 	++	+	---	0	0	0	--	-2

Figure 5-5: Pugh chart comparing the various linear actuation options to the baseline rotary motor + transmission option.

1. Actuator: Each of the actuation options is discussed below.

(a) *Rotary motor + transmission*: By itself, a rotary motor (i.e., servo or stepper) provides only rotational motion, which must be converted into linear motion through a transmission. Options for transmission include ball screw, rack and pinion, belt drive, and cable drive, and are illustrated in Fig. 5-6.

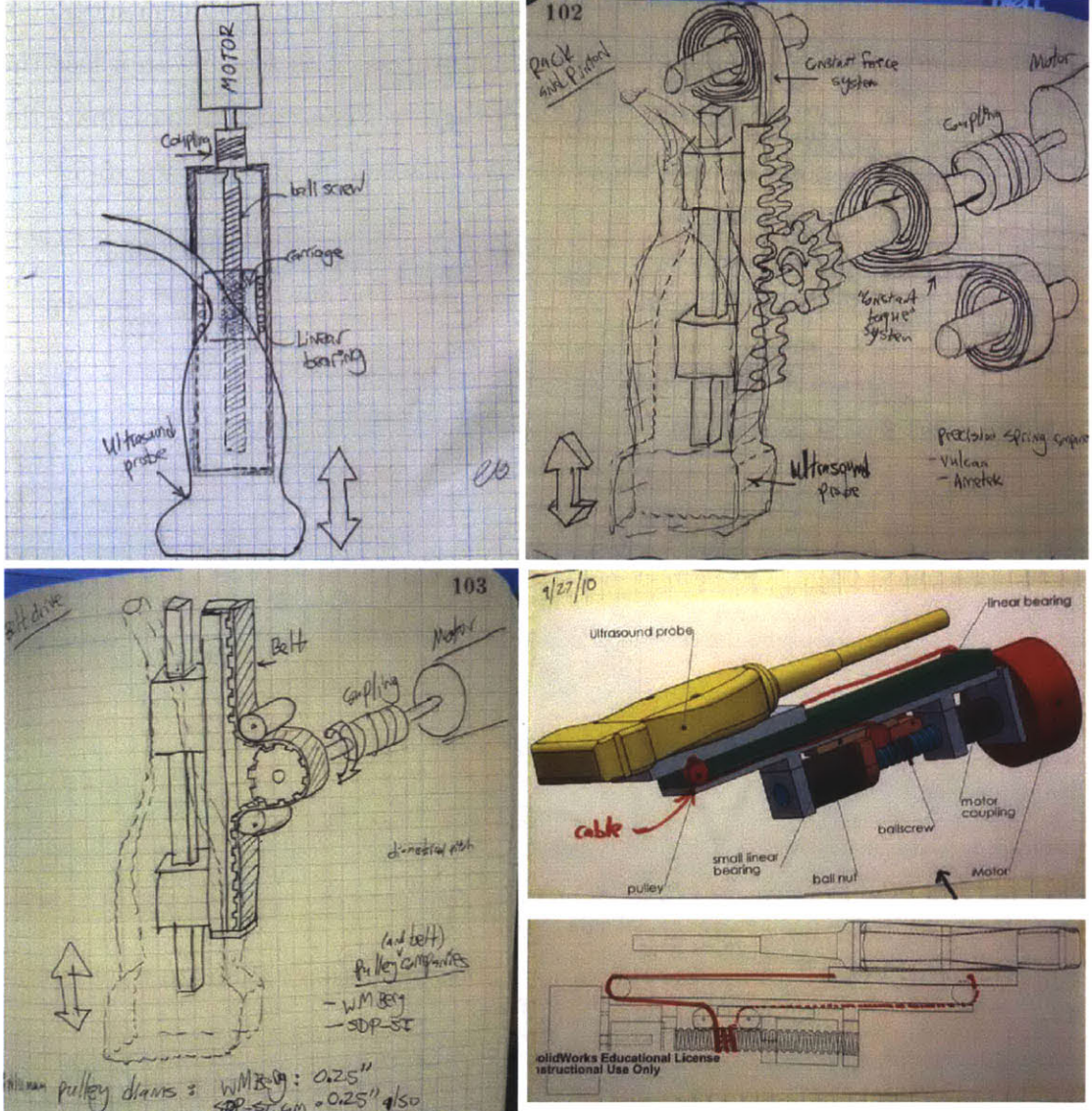


Figure 5-6: Candidate mechanisms for converting rotational motion into linear motion: ball screw, rack and pinion, belt drive, and cable drive. Clockwise, from top-left: ball screw, preloaded rack and pinion, cable drive, and belt drive.

The primary concern associated with converting rotational motion into linear motion is backlash. Because this device must compensate for tremors of up to 10 Hz, the motor will be moving back and forth rapidly; backlash must be reduced to ensure continuous probe position information and reduce mechanical wear. In the case of the rack and pinion, the pinion gear must be preloaded through some sort of rotational spring; for the belt drive or the cable drive, the belt/cable must be appropriately tensioned. As long as it is preloaded, the ball screw requires no additional measures to eliminate backlash. Due to its simplicity, the ball screw was chosen as the most appropriate choice for the rotary motor, and is therefore included in Fig. 5-5.

- (b) *Voice coil motor*: Compared to the ball screw + servo, the voice coil motor requires more power to hold a constant force, but has the advantage of being direct-drive, enabling it to move faster and achieve higher bandwidths.
- (c) *Linear motor*: the linear motor is similar to the voice coil, although the linear motors investigated as potential candidates for this application used heavy magnets which were near the limit of the mass functional requirement.
- (d) *Pneumatic actuator*: A potentially more appropriate choice than the high transmission-ratio ball screw due to its backdriveability, the main drawback of the pneumatic actuator is the limited bandwidth of the compressed air system.
- (e) *Constant force spring*: The use of a passive, purely-mechanical force-controlling device (such as a constant force spring attached to a low friction stage) instead of an electronically-controlled system is appealing due to its simplicity. It could apply a constant force without requiring any power whatsoever. However, there are a number of major limitations associated with such a design. First, the contact force is determined by the spring stiffness and cannot be easily adjusted; *a priori*, the appropriate contact

force is not known and therefore it seems appropriate for the device to be able to apply a range of contact forces, not simply one set force. While it is possible to design a mechanism to adjust the spring stiffness on the fly, such a system would introduce a considerable amount of complexity. An electromechanical system provides the flexibility to easily change the contact force for different areas of the body, or for conducting a sweep through a range of different forces. Second, unlike an electromechanical system, such a passive device cannot achieve gravity compensation. If the ultrasound probe (mass 120 g) were rotated from vertical to upside-down, for instance, a passive mechanical system would read an artificial 2.4 N change in contact force (twice the probe's weight), therefore limiting the accuracy to  $\pm 1.2$  N. An electromechanical system can attain the required 0.1 N force accuracy by actively compensating for the weight of the probe by measuring the angle of orientation of the device.

- (f) *Piezo actuator:* There are various piezo actuators on the market today (Physik Instrumente and Dynamic Structures, for example) that amplify tiny amounts of strain in each individual piezo element via a mechanical flexure. Although these devices provide the appeal of an ultra-high bandwidth system with integrated linear motion constraint, the main drawback is that their stroke length is extremely limited. No piezo actuators on the market today provide the necessary range of motion in the required form factor.
- (g) *Simple mass (not shown):* Another potential option with similar simplicity to the constant force spring is simply a mass with a weight that is equivalent to the desired force. For example, if the desired force is 8 N, then one could simply attach enough mass to the ultrasound probe so that its total mass was about 800 g. As long as the probe is vertical, the contact force would simply the mass of the probe, provided that the user was not supporting much of the weight with his/her hand. An added benefit besides simplicity is the fact that the mass of the device would result in some low-

pass filtering of hand tremors, thereby smoothing the fluctuation in the contact force<sup>1</sup>. The main drawback with this extremely simple concept is that it would require that the probe be held vertical. As soon as the probe deviates from vertical, the contact force would no longer be constant. This is imposes a severe constraint, because verticality is not often maintained during ultrasound scanning, particularly for the abdominal exams that were observed during the studies with the force-measuring probe. Future work could include identifying those exams in which the probe is typically held vertical, but for now, we choose to rule out the simple mass option because the verticality constraint significantly limits applicability.

Based upon the Pugh chart analysis, the voice coil and ball screw were identified as the most appropriate actuation concepts, and were selected for further analysis with respect to the functional requirements.

### 5.3.3 Voice coil vs. Ball screw + servo motor: Power requirements

Previously, in Section 2.3, we demonstrated that the required power, which depends upon the actuator type, consists of both static and dynamic components, and is reproduced below:

$$P = P_{static} + P_{rms} = R(KF)^2 + \frac{m_{eff} A^2 \omega^2}{2\sqrt{2}} \quad (5.1)$$

where

$$m_{eff} = \begin{cases} m_{probe} + J_{rot}/l^2 - ballscrew \\ m_{probe} - VCA \end{cases} \quad (5.2)$$

$$K = \begin{cases} 1/K_a - VCA \\ L/K_t - ballscrew \end{cases} \quad (5.3)$$

---

<sup>1</sup>Of course, such low-pass filtering would be accomplished by any device with sufficiently high mass.

For abdominal and musculoskeletal imaging, we saw in Section 2.3 that the voice coil would require nearly 23 W of continuous power while ball screw would require less than 7 W. Of course, we would want to place appropriate safety factors on each of these requirements. While voice coils capable of continuously sustaining 23 W exist, there are none that can also fulfil both the stroke and size/mass functional requirements. The ball screw power of 7 W can be easily supplied by nearly any servo motor.

Therefore, in the case of the force-controlled probe, the ball screw + servo motor is selected as the best actuator/transmission combination. (It is shown in Chapter 7 that a voice coil actuator is the appropriate choice for the dynamic imaging probe due to the relaxed stroke length requirement and higher bandwidth requirement.)

### **5.3.4 Component Selection & Layout**

#### **Ball screw & servo motor**

Next, the particular servo motor and ball screw must be selected. Various options were considered and evaluated with respect to the functional requirements. A Maxon EC-16 232241 (16 mm diameter) brushless servo motor is chosen, along with an NSK Monocarrier MCM2002P02K integrated ball screw/linear ball guide. Three of the five most important design parameters have now been selected: the 1) actuator, 2) power transmission, and 3) linear motion constraint. The last step is to select the force sensor and layout the system components.

#### **Force sensor**

As shown in Fig. 5-4, numerous force sensor options are available, from 1-axis to 6-axis load cells to pressure sensors. Pressure sensors would need to be situated directly in between the ultrasound probe and patient in order to properly measure contact force. While these sensors would give an accurate estimate of the force, they would block transmission of the ultrasound pulses and could therefore not be used. With respect to number of axes of measurement of the load cell, since the device only

needs to control force in one direction, it only needs to measure force in one direction. Therefore, a single-axis load cell is chosen. The particular load cell that best fulfils the functional requirements is the Futek LSB200, with  $\pm 45$  N force-measuring capability.

### **Component layout**

Finally, the last step is to lay out the important system components (servo motor, ball screw linear actuator, load cell, and ultrasound probe) and design the parts to attach the components to each other.

It was found that the most hand-ergonomic configuration was to mount the servo motor behind the ball screw actuator, and to connect the two via a small toothed timing belt and pulleys. Since the timing belt must be tensioned to eliminate backlash, hardware must allow the entire motor assembly to be moved relative to the ball screw.

## **5.4 Force-controlled probe prototype 2: Mechanical components**

Images of Prototype 2 (shown without its protective plastic cover) are shown in Fig. 5-7.

The device consists of an NSK Monocarrier MCM02002P02K ball screw linear actuator driven via a 2:1 reduction timing belt by a Maxon EC-16 232241 brushless servo motor. Probe position is measured by the motor's 2000 count/rotation rotary encoder. A custom 3D-machined aluminum and polycarbonate mount clamps around the ultrasound probe, and a  $\pm 45$  N Futek LSB200 load cell measures the applied force. A protective 3D-printed ABS case protects the user's hand from the moving parts (Fig. 5-1). Within the ABS case, an Analog Devices ADXL335 3-axis accelerometer is mounted and is used to measure the orientation of the device with respect to gravity, discussed in Section 5.4.1. Omron E2S proximity sensors are triggered when the carriage nears either travel limit. The outside dimensions of the protective case measure 5.5 cm x 14 cm x 4 cm, and the total mass of the device is 750 g. An exploded

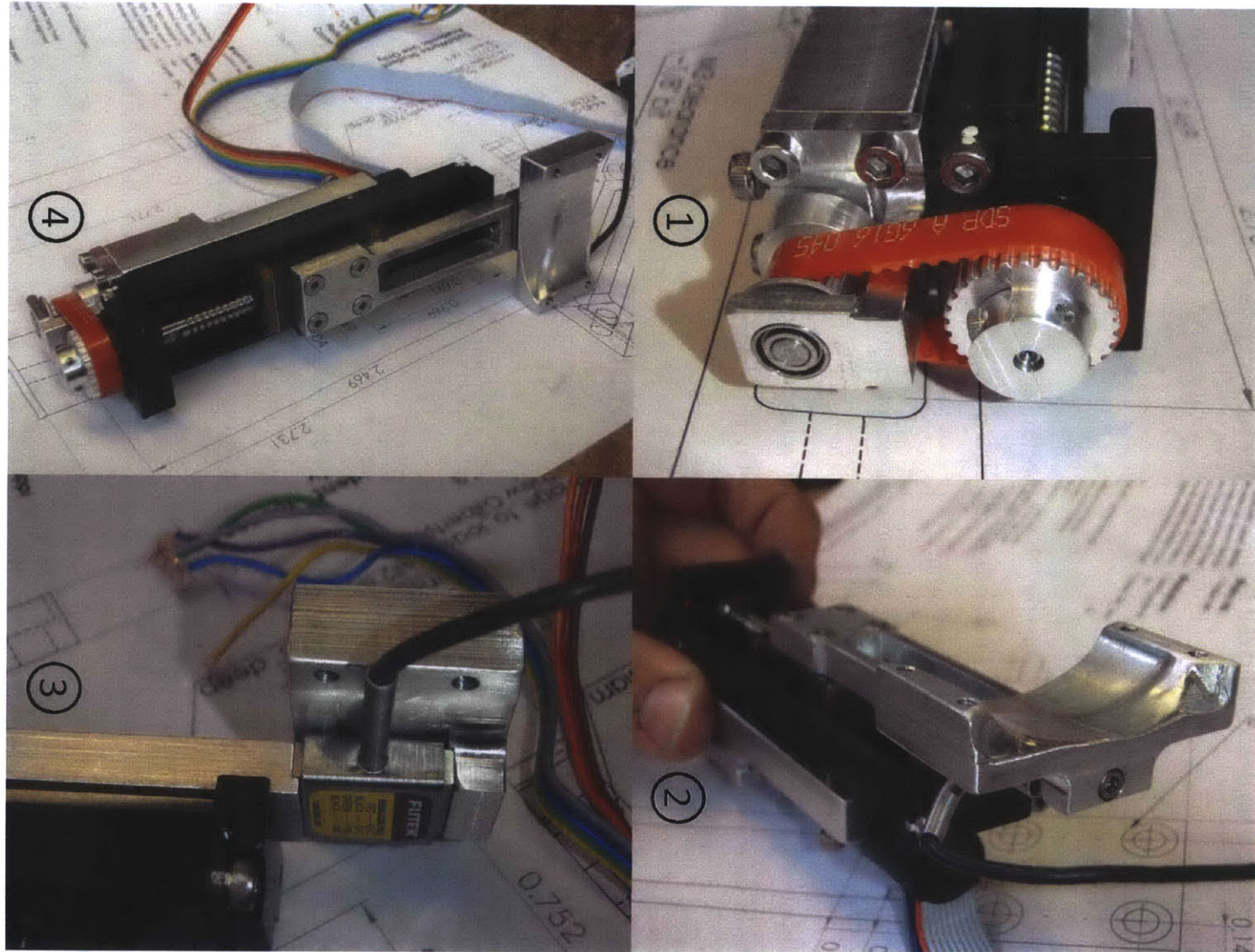


Figure 5-7: Images of the force-controlled probe, Prototype 2.

view of the device is shown in Fig. 5-8, and the components are listed in Table 5.3.

The device maintains a user-defined contact force throughout its range of motion of 5.0 cm, as shown in Fig. 5-9. Due to the low-backlash drivetrain, which consists of the ball screw (linear backlash:  $<20\mu m$ ), timing belt/pulley (rotational backlash:  $0.15^\circ$ , which translates into  $0.8\mu m$  linear backlash), and backlash-free helical beam coupling, the motor's 2000-count rotary encoder provides an accurate, repeatable measure of the linear position of the carriage to within  $\pm <11\mu m$ .

#### **5.4.1 Angle Measurement and Gravity Compensation with the Accelerometer**

The tri-axial analog accelerometer is used to measure the orientation of the device with respect to gravity. Because the ultrasound probe (mass 86 g) is mounted between the load cell and the point of patient contact, the load cell reading will consist of a combination of the weight of the ultrasound probe and the contact force. The load cell measures the contact force along the Y-axis only, as defined in Fig. 5-1. As the orientation of the device is varied, the magnitude of the projection of the gravity vector onto the Y-axis will also vary, which will result in a varying ultrasound probe weight. To isolate the contact force measurement, the weight of the ultrasound probe must be subtracted.

The accelerometer outputs three analog voltages, which correspond to the acceleration in the X, Y, and Z axes. Accelerations are produced by both gravity and hand motion (including hand tremors), the latter of which we seek to reject. From the analysis in [44], hand-induced accelerations are small compared to gravity and result in negligible inertial forces induced upon the ultrasound probe. Therefore, the accelerometer can be used to estimate and compensate for the weight of the ultrasound probe, and the contact force can be accurately calculated.

Figure 5-8: Exploded view of the force-controlled ultrasound probe, Prototype 2. Labels are discussed in Table 5.3.

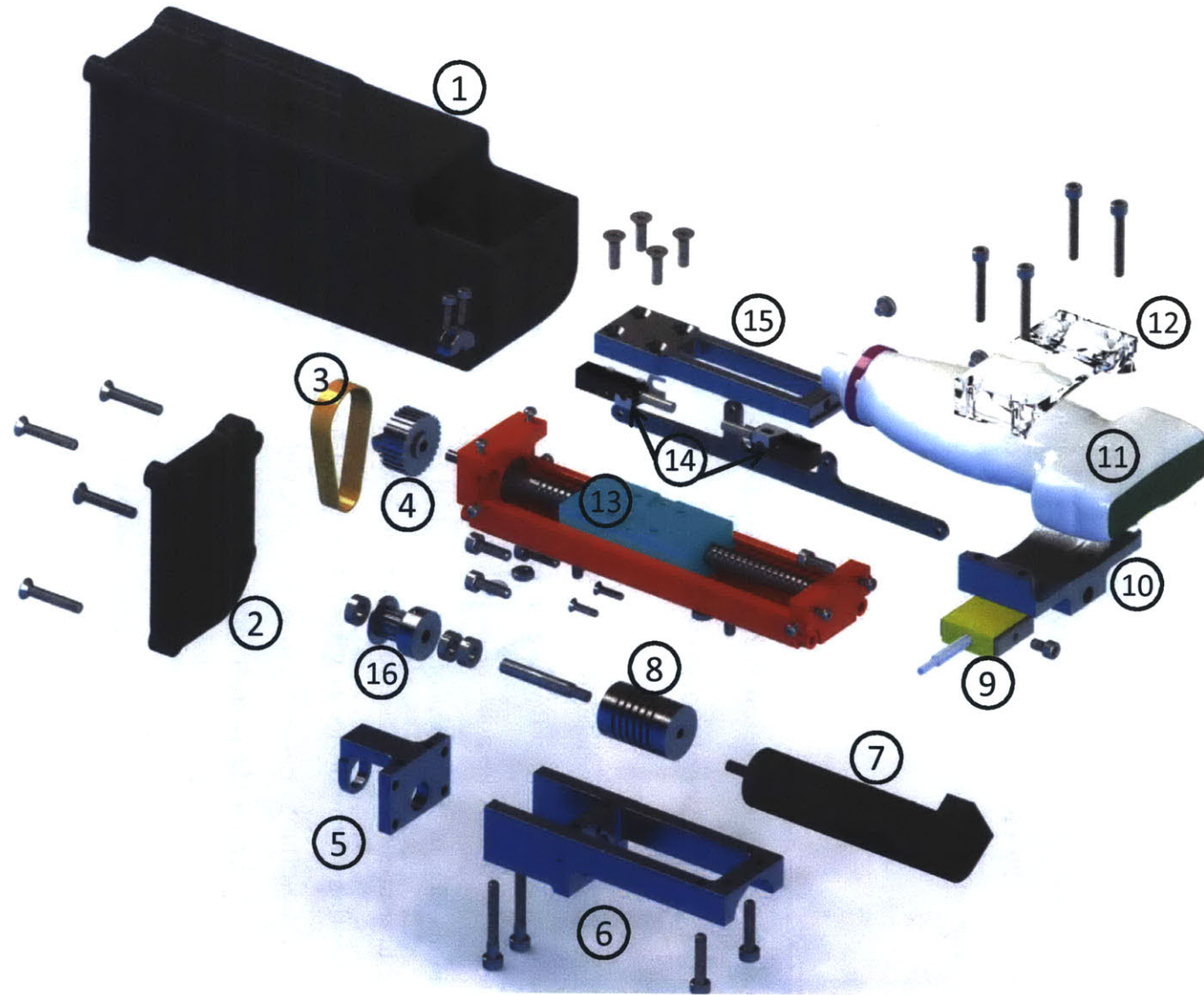


Table 5.3: Descriptions of the components of Prototype 2

Component number	Description	Purpose	Part number
1 & 2	Protective cover and back	Grasped by sonographer; protects hand from moving parts. Mounts accelerometer (not shown)	3D printed
3	Toothed timing belt	Transmits torque from motor shaft pulley (16) to ball screw pulley (4)	SDP-SI 6B16-045025
4	Ball screw pulley	Provide torque to ball screw	SDP-SI/ machined
5	Outrigger bearing	Holds motor shaft pulley; permits easy removal of timing belt	Machined from aluminum
6	Motor support	Holds motor and shaft; screws adjust pulley/pulley distance, belt tension	Machined from aluminum
7	Brushless servo motor	Provides torque; diameter: 16 mm	Maxon EC-16 232241
8	Coupling	Transmits torque; permits axial misalignment of motor and shaft	McMaster 2463K1
9	Load cell	Converts contact force to an analog voltage; mounts probe	Futek LSB200
10 & 12	Probe clamp	Clamps around probe, attaches to load cell	3D machined polycarbonate (12) and aluminum (10)
11	Ultrasound probe	Images the tissue of interest	Terason 7L3V
13	Ball screw linear actuator	Converts rotational to translational motion; constrains to 1 DOF	NSK Mono-carrier MCM02002P02K
14	Proximity (limit) switches	Triggered when carriage approaches endpoint	Omron E2S
15	Mounting bar	Mounts probe clamp to ball screw carriage	Machined from aluminum
16	Motor shaft pulley	Transmits motor torque to timing belt tension	SDP-SI 6A15-028MXL05

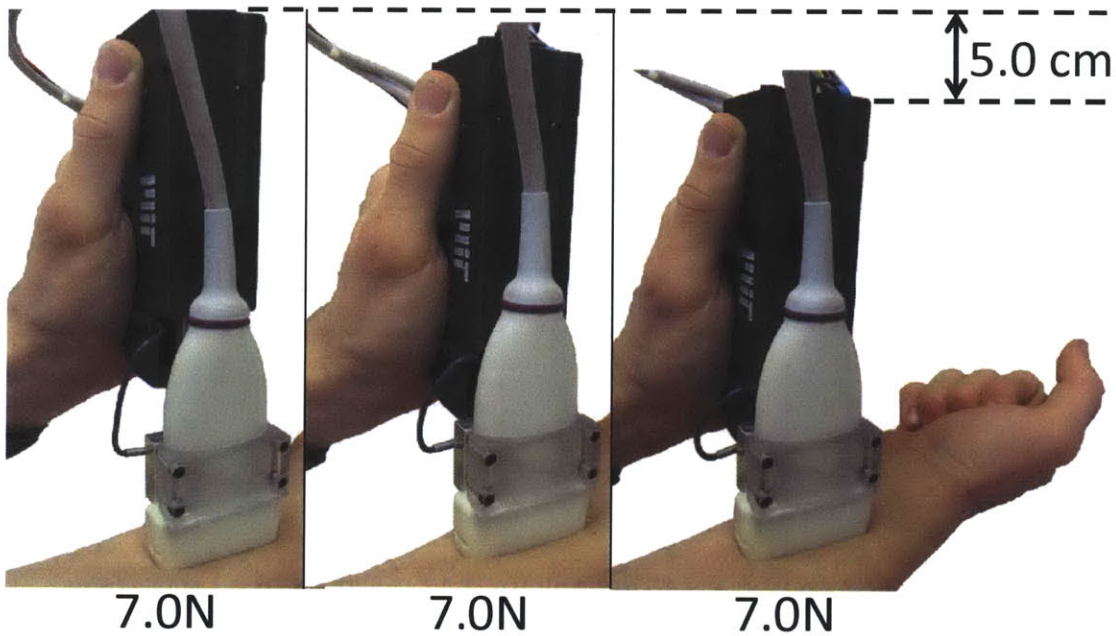


Figure 5-9: The device compensates for up to 5.0 cm of relative motion between the sonographer and patient.

#### 5.4.2 Electronics and Software

A custom, 3-layer, surface-mount PCB handles signal routing and gravity compensation, and is shown in Fig. 5-10. The analog accelerometer delivers a voltage proportional to the magnitude of the gravity vector projected onto the axis of the load cell.

An op-amp circuit on the PCB amplifies the signal, which corresponds to the weight of the ultrasound probe, and subtracts it from the force feedback from the Futek load cell. The resulting signal, which represents the actual contact force, is fed back to the motion card. The amplifier, PCB, and power supplies are housed in an insulated electrical enclosure, shown in Fig. 5-11. The complete system, shown in Fig. 5-12, is portable for clinical use.

Control software is written in LabVIEW. When operating in force-control mode, the target force is input to a PD (Proportional-Derivative) controller running on an NI PCI-7538 motion card. The controller compares the target force to the feedback force and generates a command signal. When operating under combined position

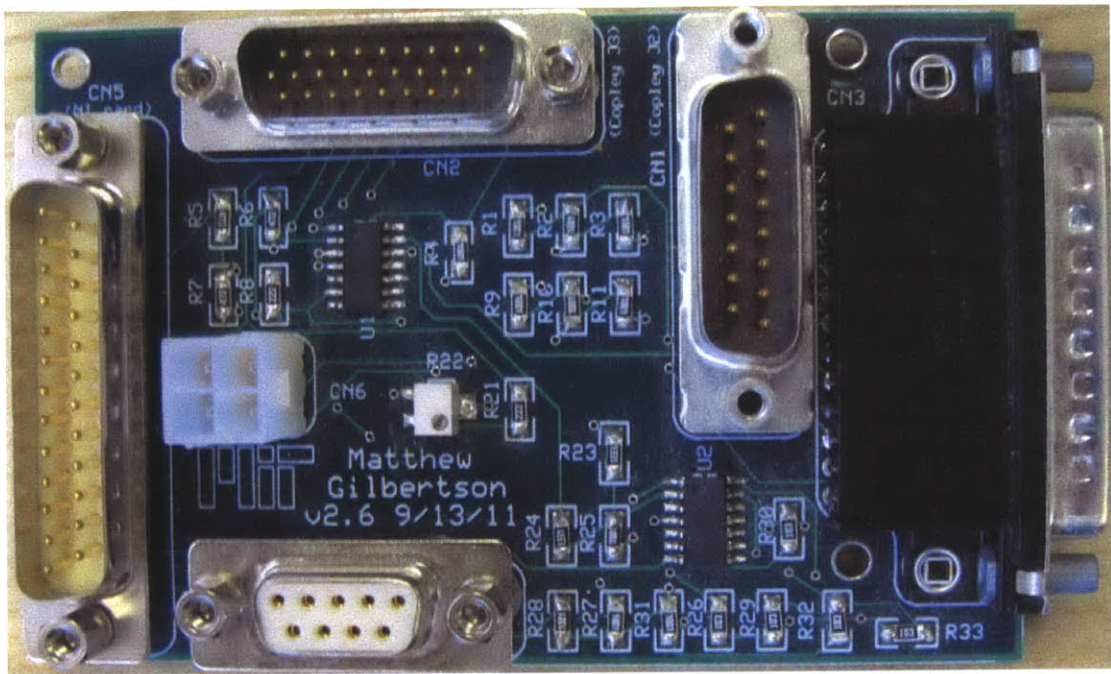


Figure 5-10: The 3-layer, surface-mount PCB for Prototype 2. Routes signals between device, amplifier, DAQ board, and power supplies. Op amp performs gravity compensation with accelerometer and load cell voltages.

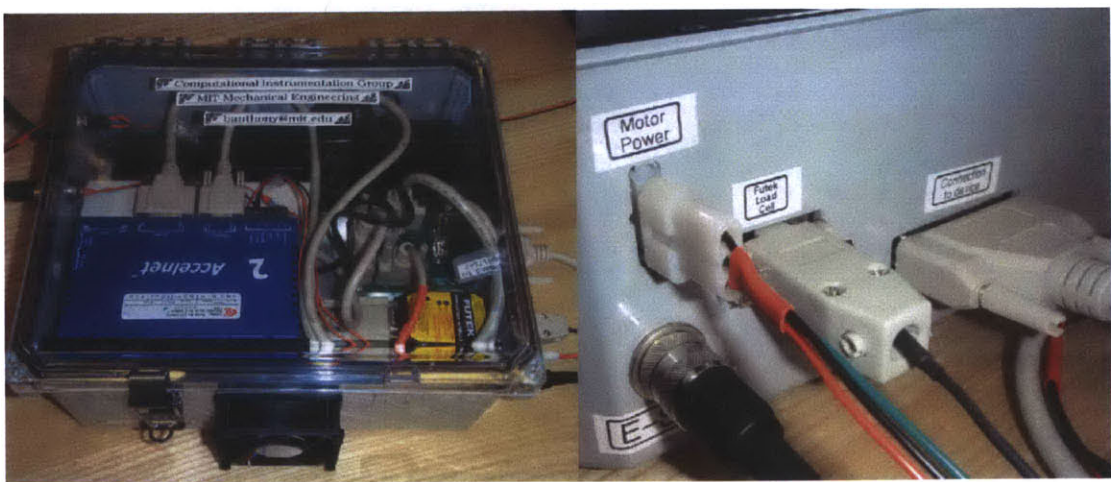


Figure 5-11: The electrical enclosure for prototype 2 (left), which contains the PCB (Fig. 5-10), amplifier, AC adapters, UMI-7744 screw terminal board, and Futek CSG110 signal amplifier.

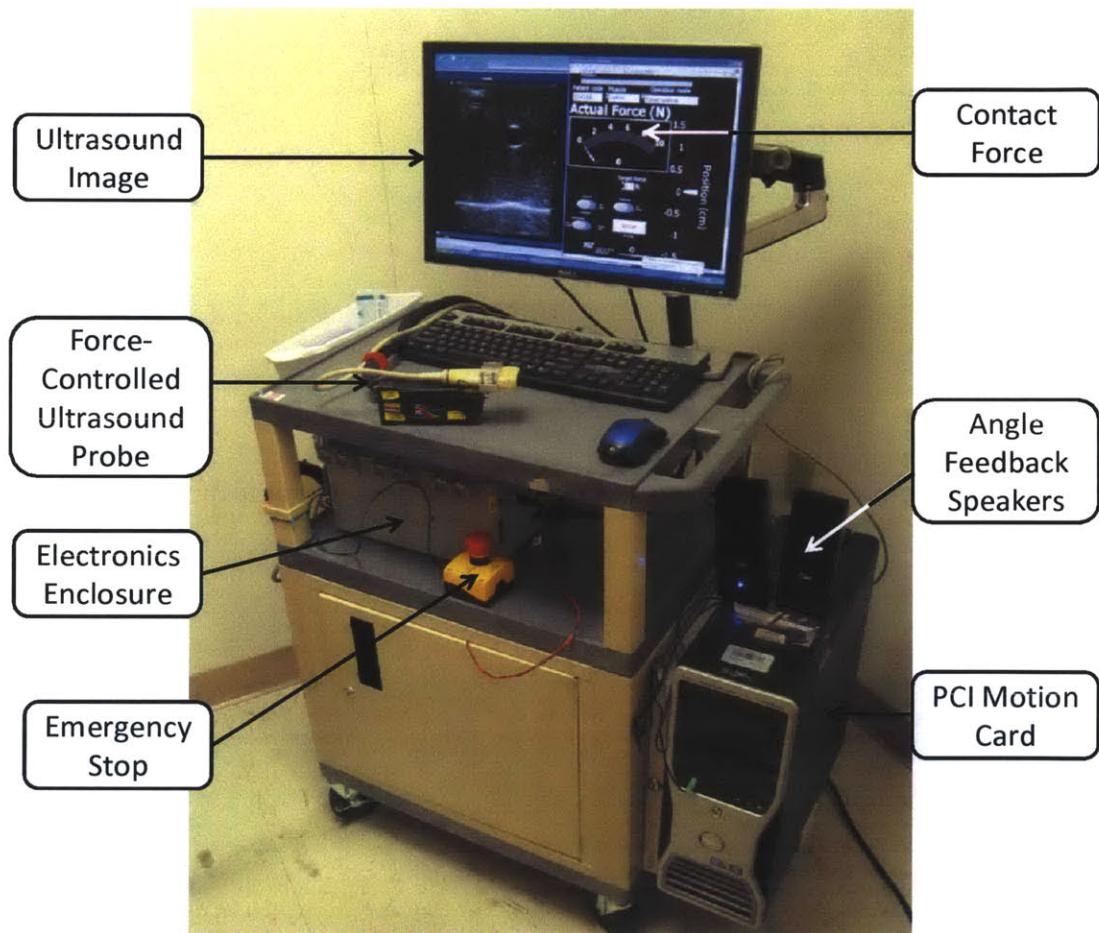


Figure 5-12: The system, equipped for clinical use.

and force control (discussed in Section 5.9) the force command signal is summed with the command signal from a position control loop, and the resulting signal is sent to a Copley Controls ADP-090-09 amplifier. The Copley amplifier acts as a voltage-controlled current source, delivering a current to the motor in proportion to the command voltage.

During operation, the LabVIEW control program monitors the position, velocity, current, force, and limit switches and disables the amplifier output if any limits exceed safe parameters. A GUI (graphical user interface), visible in Fig. 5-12, allows the user to change the target force and monitor the actuator position, contact force, and angular orientation.

### 5.4.3 Selecting the Appropriate Contact Force

Typical and appropriate probe contact forces are expected to be different for different ultrasound exam types; for example, it is expected (although not yet quantified) that near-surface imaging of delicate structures, such as the carotid artery, require less contact force than does imaging of deep abdominal tissues. To ensure diagnostically-acceptable image quality, sonographers qualitatively report applying more force when imaging through thick layers of fat or in the presence of gas, as discussed previously in Section 1.4. Within a specific exam type, contact forces have been found to exhibit significant variation across sonographers. In [44], we found that forces applied by 10 professional sonographers during 36 abdominal exams averaged 7.0 N, with a standard deviation of 3.0 N, and ranged from 0 N to 27.3 N.

How then does the sonographer select the appropriate contact force setpoint to use for the force-controlled probe? One strategy would be to scan at the literature value of the average force for the particular exam type (7.0 N for abdominal imaging, for example). More studies are needed to quantify contact force in different types of exams. Another strategy would be to turn off the actuator and passively measure the contact force while capturing an image, then use that measured force as the force setpoint for subsequent scanning. For this purpose (and for the user studies described in Section 5.7.4), the force-controlled probe includes a force-measuring mode, in which

the sonographer can turn off the actuator and still measure the applied force. The system is capable of measuring and controlling contact force up to 45 N.

For longitudinal imaging, in which a specific region of interest is scanned over time to investigate change, in each exam, the contact force setpoint could be set to the value from the previous exam. In elastography imaging, which involves capturing images at a range of forces, the force controlled probe could be set to sweep through the range of appropriate contact forces while synchronously recording force and ultrasound images.

## 5.5 Control System Overview

Next, we present a brief overview of the control strategies employed in the device. In this system, we utilize a combination of force control and position control; the force controller allows the actuator to apply a constant force throughout 80% of its range of motion, while the position controller prevents the actuator from reaching its travel limits. We discuss the role of the position control system in more depth in Section 5.9. The two control loops are selectively enabled or disabled in software depending upon the position of the actuator within its range of motion. A diagram of the combined force and position control loops is shown in Fig. 5-13.

In this figure, the primary input to the system is the target force  $F_{target}$ , which can be modified by the user. The patient position  $X_P$  and sonographer hand position  $X_S$  (Fig. 5-15, discussed in Section 5.6.1) are modeled as disturbance inputs. This control strategy is similar to a switched strategy of Impedance Control [50], in which a combination of force and position are simultaneously controlled.

During the experiments discussed in Section 5.7, the position control loop was disabled, and the device operated under pure force control only. Fig. 5-14 shows a block diagram of the force control loop. The purpose of the force control system is to provide a constant contact force in spite of disturbances caused by 1) sonographer motion, and 2) patient motion. The controller  $G(s)$  compares the target force with the measured contact force and delivers a voltage command to the amplifier, which converts the voltage to a current via the gain  $K_A$ . The current, which is supplied

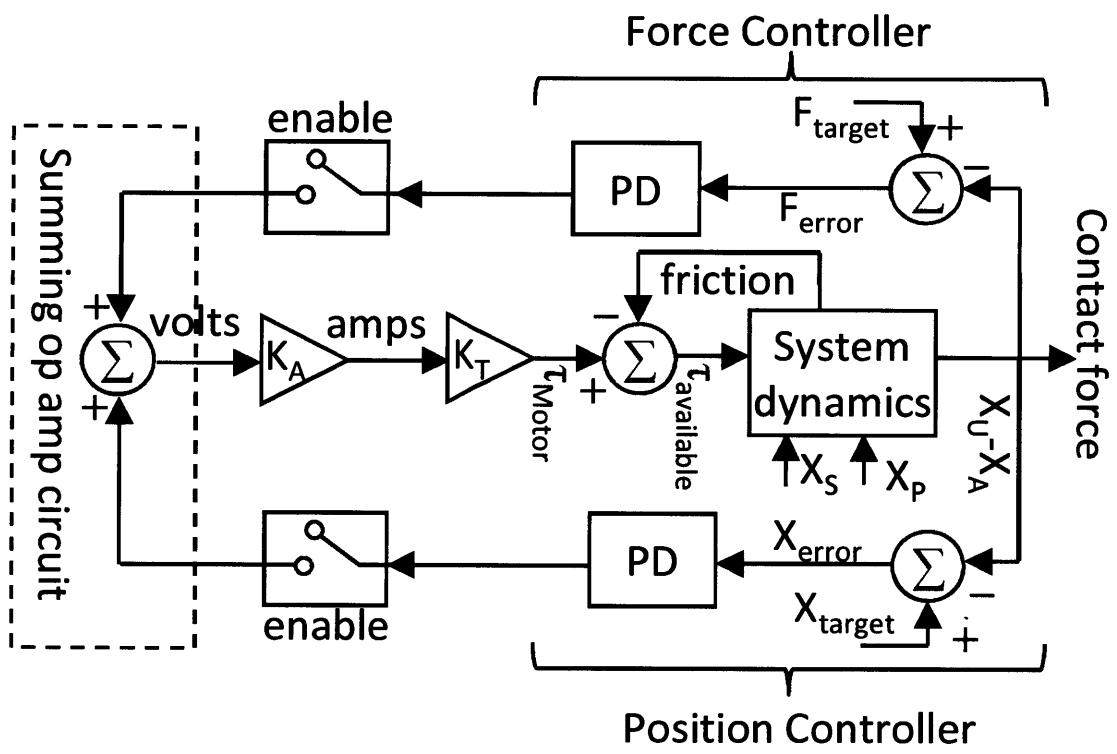


Figure 5-13: A block diagram of the control system, which consists of both a closed loop force controller and closed loop position controller. The signals are summed together via an analog operational amplifier circuit. Both loops can be independently enabled or disabled.

to the motor, produced a torque  $\tau_{motor}$  upon the windings based upon the motor torque constant  $K_T$ , which results in rotation of the ball screw to position  $\theta(t)$ . The disturbance inputs resulting from sonographer hand motion,  $X_s(s)$ , and patient motion,  $X_p(s)$ , are injected into the system via transfer functions  $A(s)$  and  $B(s)$ , respectively. The resulting motion of the ultrasound probe is translated to the contact force via the patient contact dynamics  $C(s)$ .

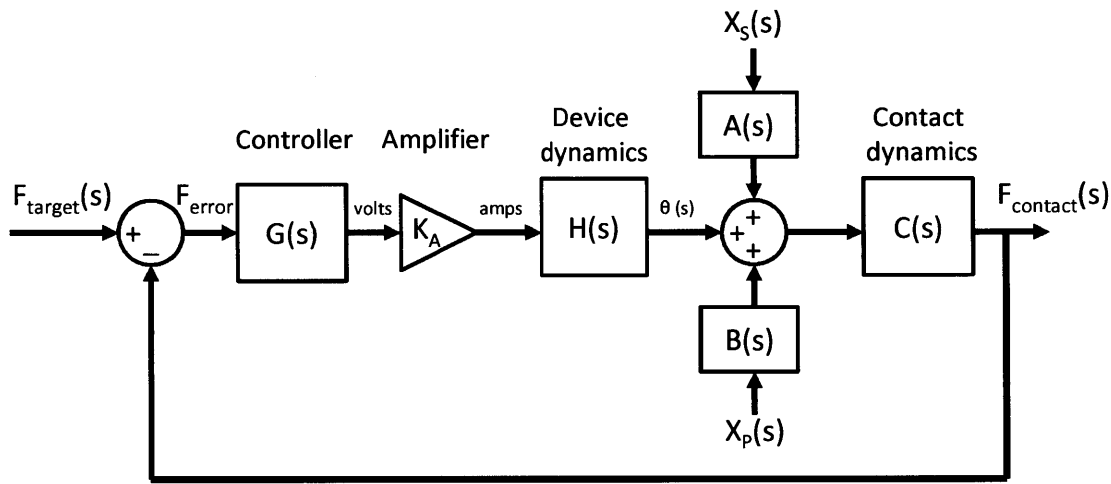


Figure 5-14: A block diagram showing the force controller only, which was used in the experiments in Section 5.7.

## 5.6 System Modeling and Experimental Testing

In the following sections, we first present a model of the system, followed by experiments to evaluate its performance. In Section 5.7.1, we describe experiments to evaluate the frequency response of the system across a range of sonographer hand tremor frequencies. In Section 5.7.3, we discuss the ability of the system to stabilize ultrasound images during patient motion. Finally, in Section 5.7.4, we present the results of user studies which compare the ability of the system to maintain a constant contact force with that of fifteen human operators.

### 5.6.1 System Model

A diagram of the system model is shown in Fig. 5-15. The device is gripped by the sonographer and placed in contact with the patient. The two human-device interfaces are denoted as Interface A, at which the sonographer grips the handle of the actuator, and Interface B, at which the ultrasound probe makes contact with the patient. Interfaces A and B, described in detail in Sections 5.6.2 and 5.6.3, are both modeled as viscoelastic [53].

The device itself consists of three independent moving masses: 1) the ultrasound probe and carriage, of combined mass  $M_U$  and position  $X_u(t)$  (all positions are relative to the fixed reference position at the bottom); 2) the ball screw, motor rotor, and transmission, of total rotational inertia  $J$  and rotational position  $\theta(t)$ ; and the actuator itself, which consists of the motor stator, linear bearing, and protective shell, of combined mass  $M_A$  and position  $X_A(t)$ .  $X_A(t)$ ,  $X_u(t)$ , and  $\theta(t)$  are coupled by Equation 5.4, where  $l = 2\text{mm}/\text{rotation}$  is the ball screw lead:

$$\theta = \frac{(X_A - X_U)}{l} \quad (5.4)$$

The motor is modeled as a torque source, converting current to torque  $\tau_M$  by the torque constant  $K_T$ . The ball screw transmits to the carriage axial and radial forces  $f_1$  and  $f_2$ , respectively, which are related by the screw thread angle  $\alpha$ . The carriage and ball screw experience internal frictional force and torque, respectively, described in Subsection 5.6.4. The ultrasound probe of mass  $M_U$  exerts a force  $F_{contact}$  on the patient's tissue of mass  $M_T$ . The contact force is sensed by the load cell and is fed back to the control system.

Model parameters were determined through a combination of experiments and a literature review. Next, we describe modeling of both human-device interactions, followed by a discussion of device friction characteristics.

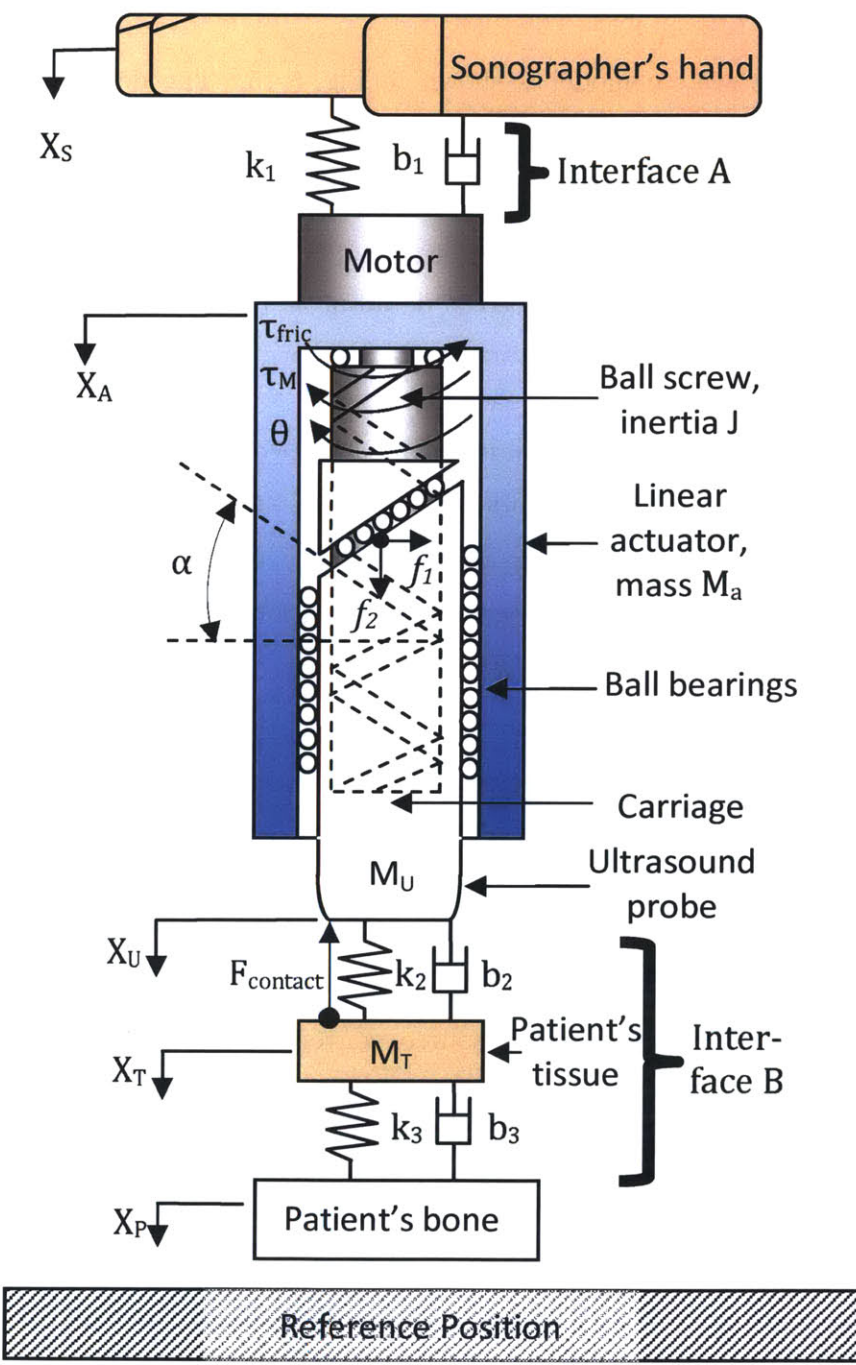


Figure 5-15: A model of the system while the device is grasped by the sonographer and placed in contact with the patient.

### 5.6.2 Model Parameters - Interface A

The purpose of the force-controlled ultrasound probe is to maintain a constant contact force between the ultrasound probe and the patient in spite of disturbances. The disturbance inputs to the system consist of patient motion and sonographer motion. In this section, we discuss the effects of sonographer hand motion and its impact upon the performance of our system .

While the sonographer grips an object, his or her hand moves due to a combination of tremors and involuntary motion, as discussed in Section 5.6.5. The dynamics of the arm-hand system are known to present significant modeling difficulties, and have been extensively studied in the literature [61],[102],[103],[36],[114],[57],[86]. Rakheja [86] presents a thorough comparison of many of the arm/hand models developed in the literature within the context of the injury risks associated with mechanical vibrations. Speich [102] compares four arm/hand models from the literature developed for tele-manipulation applications.

All models treat the human-machine interface as viscoelastic, and differ in terms of the number of masses, springs, and dampers. The models show orders-of-magnitude variation in parameter values such as the stiffness and damping coefficients, making it challenging to determine which values to assume for this particular mechanical system. As described in Section 5.6.5, hand tremor has been studied extensively in the literature and is well-characterized in terms of frequency content and tremor amplitude. In modeling our system, we therefore choose to treat Interface A as consisting of the hand grip only. We treat the skeleton of the sonographer's hand as a position source coupled to the actuator through one spring and one damper. Because the sonographer's hand is treated as a position source, it is not necessary to model the moving mass of the hand.

Literature values of hand stiffness range from  $k = 44,000N/m$  (effective) [114] to  $k = 40N/m$  [102] – more than three orders of magnitude. Damping values lie within two orders of magnitude, from  $b = 3.6Ns/m$  [102] to  $b = 175Ns/m$  [57]. The most similar study to ours is that of Wood [114], in which the forearm is modeled as two

flexural beams representing the radius and ulna, and the hand as two mass-spring damper pairs. Because bone stiffness is much higher than that of the hand, the hand model can be simplified to one lumped mass-spring-damper with effective damping  $b = 27Ns/m$ .

Given the wide range of literature values for hand grip stiffness, we conducted several experiments of our own to determine the hand grip stiffness value within the context of our system. In the experiments, a human subject gripped an object of similar mass to the force-controlled ultrasound probe and rested his wrist upon a rigid support. As the subject held the mass, a linear actuator and load cell were placed in contact with the hand-held object and the force-displacement characteristics were quantified. The experimental setup utilized the load frame hardware shown in page 796816-7 of [42]. The average stiffness over ten runs was found to be  $k = 5500N/m$ .

With a stiffness of  $k = 5500N/m$  and damping coefficient  $b = 27Ns/m$ , the sonographer's hand grip of the device (Interface A) is fully characterized.

### 5.6.3 Model Parameters - Interface B

Next, we discuss and model the interface between the ultrasound probe and the patient. Regardless of whether the patient is stationary or moving, it is necessary to model the probe/patient interface in order to accurately model the behavior of the contact force as the ultrasound probe moves. As the probe moves in contact with the patient, a non-negligible volume of the patient's tissue moves as well, and this is modeled as a five-element system consisting of mass  $M_T$ , which is positioned between the ultrasound probe and the patient's skeleton, and connected by two springs,  $k_2$  and  $k_3$ , and two dampers  $b_2$  and  $b_3$ , as discussed in Speich [102]. We model the stiffness and damping as being equally distributed between the springs and dampers, i.e.,  $k_2 = k_3$  and  $b_2 = b_3$ .

For the frequency-sweep experiments described in Section 5.7.1, we placed the device in contact with a 500 g tissue-mimicking phantom. The phantom was constructed from mineral oil and styrene-ethylene/butylene-styrene copolymer [82], which is known to exhibit similar mechanical properties to human tissue. Experiments were per-

formed to evaluate the stiffness of the phantom utilizing the force/displacement hardware in [42]. Contact force was measured as the actuator extended 1 cm. A line was fit to the force-displacement data, and the slope was found to be 345 N/m, similar to the mechanical properties of the human heart [118]. Because this stiffness is equally distributed between the two springs, each spring has half the stiffness; i.e.,  $k_2 = k_3 = 173\text{N}/\text{m}$ . The damping coefficient, which is more challenging to measure directly, was calculated based upon the phantom dimensions and the literature values of the mineral oil-type phantom damping characteristics [82] to be  $b_2 = b_3 = 1.0\text{Ns}/\text{m}$ . With  $M_T$ ,  $k_2$ ,  $k_3$ ,  $b_2$ , and  $b_3$  quantified, Interface B is fully characterized.

#### 5.6.4 Model Parameters - Friction

Previously, we demonstrated that the internal frictional forces and torques within the ball screw actuator are non-negligible, consisting of both dynamic and static components [43]. Sources of friction include ball bearing viscosity and bearing wiper friction. Both the linearly translating carriage as well as the rotating ball screw experience friction; since the two are coupled, we lump all friction into the rotational domain. We modeled friction as having two discrete regimes: 1) ball screw is rotating, and friction torque is constant; and 2) ball screw is stationary, and friction torque matches applied torque, saturating at a critical value. The switching between these two discrete regimes based upon velocity was found to introduce modeling difficulties. To simplify the model, we seek to model friction as a continuous function.

During actual use, the ball screw is stationary for a very small fraction of the time that it is moving. We therefore approximate friction as having one regime, in which friction torque  $\tau_{fric}(t)$  depends solely upon the direction of the rotational velocity,  $\omega(t)$ , i.e.,  $\tau_{fric}(t) = \tau_{crit} \cdot sign(\omega(t))$ , where  $\tau_{crit}$  is the critical friction torque. Experiments were performed to evaluate the friction torque characteristics of the ball screw. The motor was commanded to rotate the screw at constant velocities from 500 - 2500 RPM (typical rotational velocities during device operation), while motor current and rotational speed were simultaneously measured. Friction torque was estimated via the motor torque constant  $K_t = 5.5\text{ mNm/A}$ . Over four runs, friction

torque was found to average 14 mNm. Therefore, in this friction model,  $\tau_{crit} = 14$  mNm.

Modeling the friction characteristics of the ball screw have proven quite challenging for a number of reasons. First, the linear translation of the carriage is coupled to the rotation of the screw, so it is not possible to independently measure the friction characteristics of the linear ball bearing and the rotating ball screw; the two friction characteristics are therefore lumped together. Second, friction has low repeatability and high variation between experiments. In some experiments, it was found that the friction forces varied by 50%, even though all other variables in the experiments were held constant. Therefore, the friction characteristics used in these models represent the averages from multiple runs.

### 5.6.5 Hand Tremors

In this section, we discuss the frequency and amplitude characteristics of hand motion, represented as  $X_s(s)$  in the model. Involuntary hand motion has been studied extensively in the literature. In the Micron project [62], the tip position of a 40 g hand-held tool was recorded during a hold-still task at a rate of 200 Hz for a total of 27 minutes. The spectrum of tool-tip motion was found to have the highest amplitude at DC (low frequencies), and decreased by approximately a factor of ten per decade of frequency beyond 0.3 Hz. The amplitude of vertical motion at 0.1 Hz, for example, was found to be about 30 times greater than that at 10 Hz. Stiles [103] and Elble [36] present similar findings, in which nearly all of the power in the hand tremor spectra lies below 10 Hz when subjects held masses of approximately 500 g (similar to the mass of the force-controlled ultrasound probe). The control system of the force-controlled ultrasound probe must therefore be effective in stabilizing the device for hand motion frequencies up to 10 Hz.

### 5.6.6 Simplified Model

In modeling this system, we could choose to model the variation of contact force with sonographer hand motion and/or patient motion. In [43], we demonstrated agreement between simulation and experimental data for the reduced model in which the actuator was fastened to a fixed location  $X_A$  relative to the reference position, while the position  $X_P$  of the patient's bone is free to move. This would simulate the effect of an infinitely stiff grip holding the actuator at a fixed position (rigid Interface A) with the ultrasound probe in contact with a moving patient.

In a clinical setting, it is likely that patient motion will introduce less disturbance than the motion of the sonographer's hand. Therefore, in this paper, we investigate the effect of sonographer hand motion upon contact force, assuming the patient's bone position  $X_P$  is fixed. For the purposes of investigating the relation between the disturbance input  $X_s$  and the contact force  $F_{contact}$ , we assume that the target contact force,  $F_{target}$ , is fixed.

### 5.6.7 Experimental Evaluation: Frequency Response

Experiments were performed to evaluate the ability of the device to maintain a constant contact force across a range of sonographer hand motion frequencies. To replicate the sonographer's hand, a mechanical hand phantom stage was constructed which, as discussed in Section 5.6.9, consisted of a ball screw-driven linear stage along with a spring and a dashpot which mimicked the stiffness and damping of the hand grip. The force-controlled ultrasound probe was mounted to the hand phantom stage, affixed to the spring and dashpot, and placed in contact with the mineral oil/copolymer phantom. The controller was programmed to maintain 3.0 N of contact force between the ultrasound probe and the phantom. To simulate sonographer hand motion, the hand phantom stage was moved sinusoidally at amplitudes ranging from 0.1 mm to 10 mm across frequencies of 0.1 Hz to 30 Hz, a typical range of hand tremor frequencies studied in the literature [62]. As the hand phantom stage oscillated, contact force and stage position were recorded with a digital oscilloscope

and later analyzed with Matlab.

The ultimate goal of this system is to help the sonographer to achieve a more stable contact force than is possible in conventional (unassisted) ultrasound imaging. To evaluate the performance of the system with respect to this criterion, it is necessary to compare the force fluctuation of the force-controlled ultrasound probe with that of a standard, conventional ultrasound probe. In conventional ultrasound imaging, the sonographer grasps the probe and places it in direct contact with the patient. Tremors and involuntary hand motion move the probe and, due to the dynamics of the patient's tissue, the contact force fluctuates. Therefore, the most appropriate analogue for conventional ultrasound imaging, within the context of this experiment, would be to mount an ultrasound probe to the same hand phantom stage and perform the same frequency sweep as with the force-controlled ultrasound probe, while measuring the contact force and stage position.

To that end, we also performed the 0.1 Hz to 30 Hz frequency sweeps with a force-measuring ultrasound probe *proxy* mounted to the hand phantom stage. The proxy probe consisted of an object of mass 108 g (similar to the 86 g mass of the Terason 7L3V probe for which the force-controlled probe is designed) instrumented with a Futek  $\pm 45$  N LSB200 load cell. The proxy probe was mounted to the hand phantom stage via the same springs and dashpot used for the force-controlled probe. The proxy probe, with a contact area of  $4.5\text{cm}^2$  (also the same as the Terason 7L3V probe), was placed in contact with the same phantom, which was moved to such a position that the DC bias force was also 3.0 N. The hand phantom stage was then swept through the range of frequencies while the contact force and stage position were recorded.

### 5.6.8 Equations of motion

In this simplified model, in which the position of the patient's bone  $X_P$  is fixed, the parameter of interest is the contact force and the input is the motion of the sonographer's hand. We proceed to derive the transfer function between  $X_s$  and  $F_{contact}$ , and begin with the frequency-domain equations of motion for the actuator,

ultrasound probe, ball screw, and patient's tissue, respectively:

$$(b_1s + k_1)(X_s(s) - X_a(s)) - f_2(s) = M_a s^2 X_a(s) \quad (5.5)$$

$$f_2(s) - F_{contact}(s) = M_u s^2 X_u(s) \quad (5.6)$$

$$\tau_m(s) - \tau_{fric}(s) + f_2(s)l = \frac{J s^2}{l} (X_a(s) - X_u(s)) \quad (5.7)$$

$$F_{contact}(s) - (b_3s + k_3)X_T(s) = M_T s^2 X_T(s) \quad (5.8)$$

where

$$F_{contact}(s) = (b_2s + k_2)(X_U(s) - X_T(s)), \quad (5.9)$$

$$\tau_{fric}(t) = \tau_{crit} \cdot sign(\omega(t)) \quad (5.10)$$

By combining Equations 5.4- 5.10 and solving for  $F_{contact}$ ,

$$F_{contact}(s) = Y(s)X_s(s) + Z(s)sign(\theta(s)) \quad (5.11)$$

Due to the nonlinear nature of the friction torque, it is not possible to eliminate  $\theta(s)$ .

The dynamic model for the ultrasound probe by itself when it is gripped by the sonographer and placed in contact with the patient is a simplified version of Fig. 5-15, and is shown in Fig. 5-16.

For this experiment, in which the position of the patient's bone  $X_P$  is fixed and the sonographer hand position  $X_S$  is treated as a position source, the model consists of two moving masses: the ultrasound probe and the moving mass of the patient's tissue. The transfer function between the contact force and sonographer hand position can be derived by combining Equation 5.11 with the Equation 5.12 below

$$(X_s(s) - X_u(s))(b_1s + k_1) - F_{contact}(s) = M_u s^2 X_u(s) \quad (5.12)$$

to obtain the expression

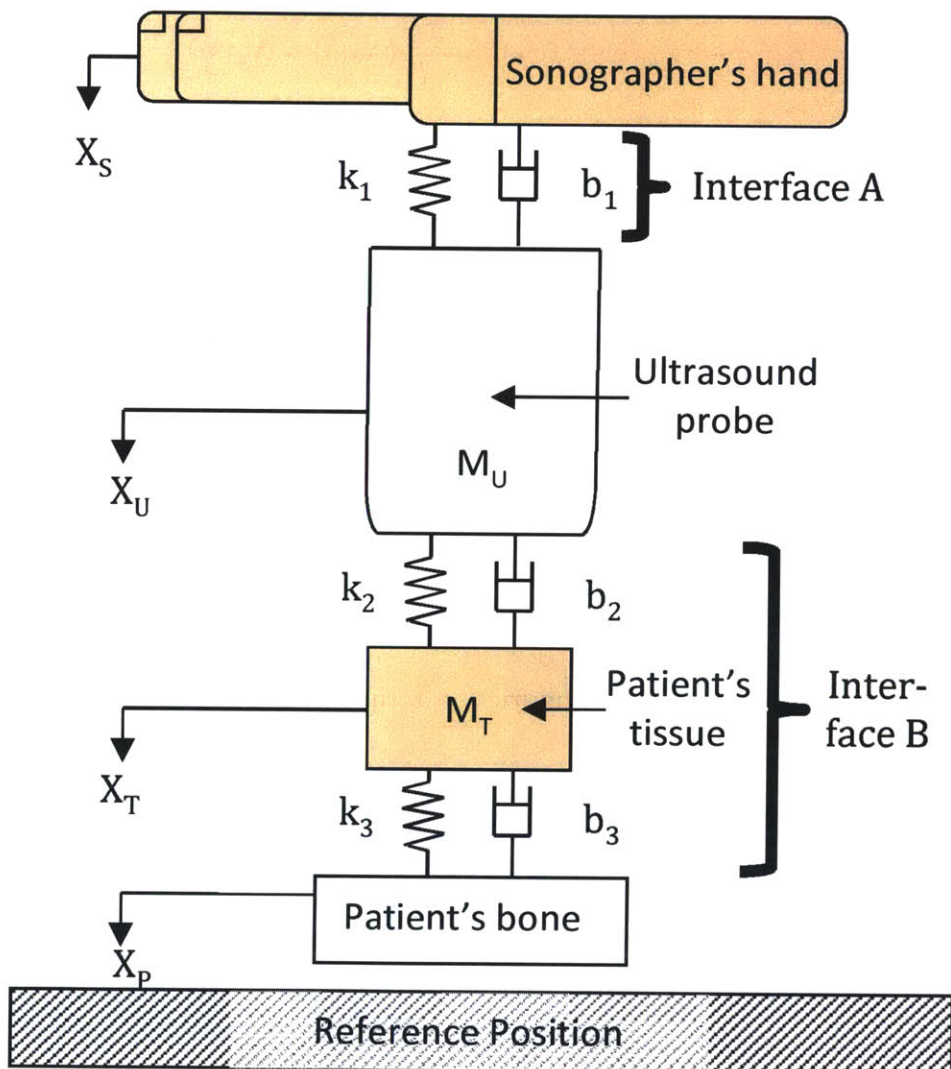


Figure 5-16: Model of the ultrasound probe gripped by the sonographer.

$$F_{contact}(s) = L(s)X_s(s) \quad (5.13)$$

where  $L(s)$  is a transfer function of fourth order in the numerator and denominator.

### 5.6.9 Hand Phantom Stage

The purpose of the hand phantom stage was to mimic both the grip dynamics and tremor frequency/amplitude characteristics of the sonographer's hand. Diagrams of the two hand phantom stage experimental setups are shown in Fig. 5-17. Experiments were performed first with the force-controlled ultrasound probe, followed by the force-measuring proxy probe. A ball screw linear stage driven by a Maxon EC-Max 30 272768 brushless servo motor provided linear motion. The force-controlled ultrasound probe was mounted to the carriage of the hand phantom stage via a small linear bearing (labelled "Linear Bearing 2" in Fig. 5-17) and was connected to rest of the stage via a spring. To provide damping, an adjustable Airpot Precision Dashpot 2KS95 was connected between the ball screw carriage and the force-controlled ultrasound probe. The axes of motion for the dashpot and spring were parallel to the motion of Linear Bearing 2. Experiments were conducted with the system oriented in the horizontal plane to eliminate the effects of gravity.

In Fig. 5-17 (A) and (B), parts that share the same colors move together, with the exception of the spring and damper, which are colored in yellow for emphasis. The parts colored red are affixed to a rigid table; the parts in blue translate linearly as the ball screw rotates; the force-controlled ultrasound probe and proxy probe are shown in black, while the actuated components of the force-controlled probe, including the load cell and ultrasound probe, are colored green.

The values of the spring stiffness and dashpot damping were chosen to match the parameter values discussed in Section 5.6.2. A candidate spring was selected, and the force-displacement measuring machine from [42] was used to measure the stiffness of the spring, which was found to be 5400 N/m, close enough to the target

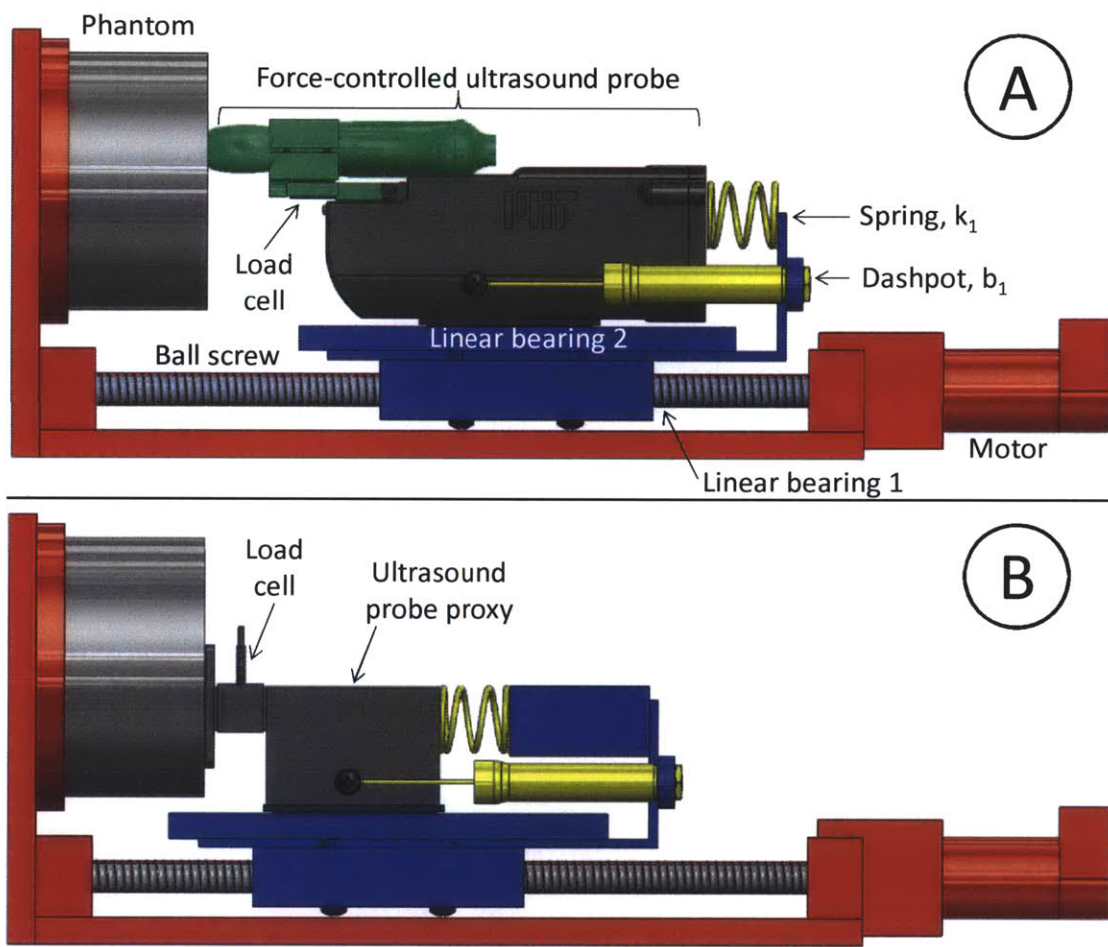


Figure 5-17: Diagrams of the hand phantom stage evaluating the frequency response of (A) the force-controlled ultrasound probe, and (B) the force-measuring ultrasound probe proxy

value of 5500 N/m; this corresponds to the spring stiffness  $k_1$  in Figs. 5-16 and 5-15. By rotating a small screw, the dashpot was tuned to achieve similar damping to the target value of  $27Ns/m$ . To evaluate the damping coefficient of the dashpot, the force-displacement measuring machine was moved at constant speeds while the change in force was recorded. A line was fit to the force-velocity data. Over ten runs, the damping coefficient of the dashpot was found to average  $24.8Ns/m$ , which corresponds to the damping coefficient  $b_1$  in Figs. 5-16 and 5-15.

## 5.7 Experimental Data

### 5.7.1 Frequency Response: Model vs. Data

A total of nine frequency sweeps were performed with the force-controlled ultrasound probe mounted to the hand phantom stage, while two sweeps were performed with the force-measuring proxy probe. Sinusoids were fit to both the contact force vs. time and the hand phantom stage position vs. time traces. At each frequency, the force amplitude/position amplitude gain (measured in N/mm) and relative phase (degrees) were calculated. The data from the various runs were averaged at each frequency. The system dynamics from Equations 5.11 and 5.13 were modeled in Simulink with input  $X_s(t)$  and output  $F_{contact}(t)$ . The frequency responses for the model and actual system are compared in Fig. 5-18.

### 5.7.2 Frequency Response: Discussion

We first discuss the data for the force-controlled ultrasound probe, shown in blue in Fig. 5-18. In terms of magnitude, both the model and experimental data exhibit close agreement below 15 Hz. If the force-controlled probe attenuated sonographer hand motion perfectly at all frequencies, the contact force would not fluctuate and the gain would be zero across all frequencies. But, due to the system dynamics and the presence of actuator friction, the gain is non-zero, and the magnitude response exhibits a roughly constant slope of slightly less than 1 decade/decade below 6 Hz.

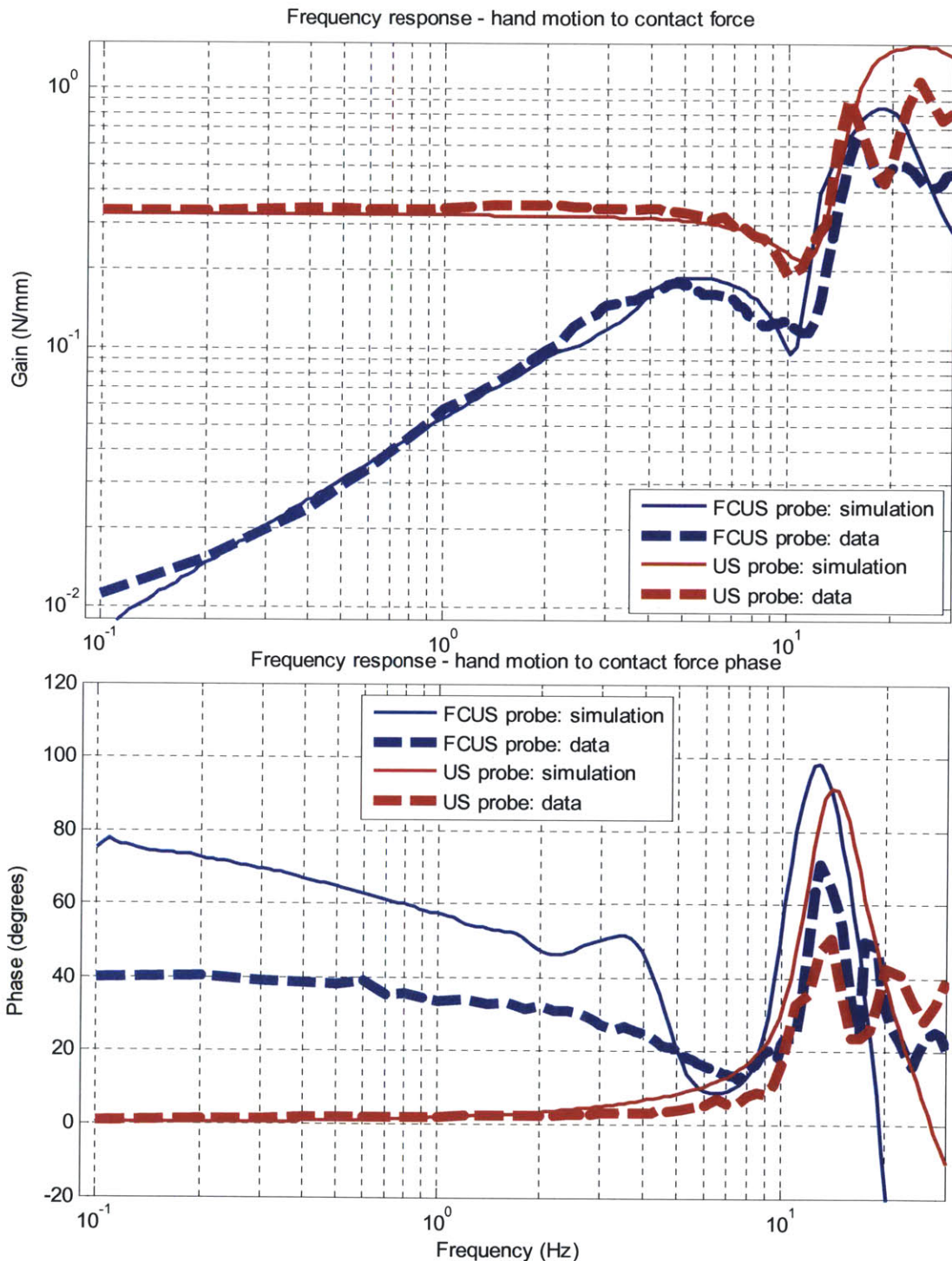


Figure 5-18: Magnitude (top) and phase (bottom) response with moving hand phantom stage. Averaged experimental data are shown as dotted lines; simulated response is solid. Magnitude is expressed in N/mm as the relative amplitude between contact force and input motion. Data for the force-controlled ultrasound (FCUS) probe are shown in blue; data for the force-measuring proxy probe are red.

This indicates that the attenuation of sonographer hand motion degrades as hand motion frequency increases. At around 6 Hz, the gain is 2 N/mm, indicating that if the sonographer's hand moved sinusoidally with amplitude 1 mm and frequency 6 Hz, the force would oscillate sinusoidally with amplitude 2 N. The dynamics of the phantom begin to come into effect beyond 6 Hz; given the stiffness and mass of the phantom, the estimated natural frequency of the phantom (based upon  $\omega_n = \sqrt{k/m}$  [75]) is approximately 8.3 Hz. At higher frequencies, the dynamics of the hand phantom stage become significant; the estimated natural frequency of the spring/force-controlled probe system (using the same equation) is 16.1 Hz.

In terms of phase, the model and data exhibit roughly the same shape; contact force leads the sonographer hand motion across all frequencies, with a peak in phase around 13 Hz, between the natural frequencies of the patient phantom and the hand phantom systems. The experimental data indicate lower relative phase than the model below 4 Hz, which suggests that the friction approximation described by Equation 5.10 is not fully descriptive of the system at lower frequencies, in which friction forces dominate inertial forces.

Next, we discuss the data for the force-measuring ultrasound proxy probe, depicted in red. As the ultrasound probe moves in contact with the phantom, the contact force fluctuates due to the phantom stiffness. We expect that at low frequencies, in which inertial effects are negligible, that the ultrasound probe-phantom system acts as a simple spring of stiffness  $k_2 + k_3$ , which is the equivalent stiffness of the phantom, and was found in Section 5.6.3 to be 345 N/m. This reasoning would therefore predict a constant gain of 345 N/m and relative phase of 0° at low frequencies, which is indeed confirmed by both data and simulation. At frequencies above 10 Hz, the magnitude and phase both increase, as predicted by the model; above 15 Hz, both exhibit unmodeled dynamics.

### **Comparison: Force-controlled imaging vs. conventional imaging**

In the magnitude plot, the gap between the red and blue experimental data represents the performance enhancement of the force controlled probe over a conventional ultra-

sound probe. Low gain in the plot indicates less contact force variation for a given hand motion amplitude. The force-controlled probe exhibits 97% less force fluctuation than the ultrasound probe at 0.1 Hz, 83% less at 1 Hz, and 33% less at 10 Hz. The gain of the force-controlled probe is less than that of the ultrasound probe itself at all frequencies studied. The force-controlled probe shows higher relative phase than the ultrasound probe, but in terms of contact force stabilization, phase has less relevance than gain.

As discussed in Section 5.6.5, the hand tremor frequency spectrum has highest power at low frequencies; the frequency content is 30 times higher at 0.1 Hz than at 10 Hz. Therefore, within the range of expected hand tremor frequencies, the force-controlled probe exhibits significant attenuation in contact force fluctuation as compared to a conventional ultrasound probe.

### 5.7.3 Experimental Evaluation: Image Stabilization

We also tested the ability of the system to obtain stable ultrasound images while the tissue of interest is in motion. Such motion could be induced by movement of the sonographer’s hand, motion of the patient’s body, or both, and would be expected during an ultrasound exam. In a real exam, the patient could move in all six degrees of freedom; for simplicity, in these experiments we investigate the effect of motion in one direction only.

In these experiments, an ultrasound phantom was vertically translated on a linear stage, as in the experiments in [43]. A human operator held the force-controlled ultrasound probe in contact with the moving phantom and attempted to maintain a constant probe/phantom contact force for two cases: 1) automatic force control off and 2) automatic force control on.

Initially, the phantom was translated sinusoidally, but we found that users quickly learned to compensate for the sinusoidal motion due to its predictability. Therefore, we extracted patient motion data from an on-going clinical trial in which the device is used to track muscle changes in patients with Duchenne Muscular Dystrophy [13]. (The study was approved by an institutional review board.) A 10.1-second motion

trajectory from a representative patient was extracted and applied to the phantom stage, with a range of 2.6 cm. Thus, the phantom was moved in a biologically-mimicking manner. The exams were performed one hour apart to mitigate the effects of user training through repetition.

The cross-section of the mineral oil/copolymer phantom measured 8 cm x 5 cm, and contained a 1 cm-diameter cylindrical ‘blood vessel’ inclusion. During imaging, B-mode sonograms were recorded at 10 frames/second. The probe was oriented so that it captured cross-sectional images of the cylindrical inclusion; in each image, the inclusion appeared roughly elliptical, with major and minor axes that varied in length with probe compressive force.

The device’s six degrees of freedom were constrained only by the user’s hand, introducing the possibility that tilting or movement of the ultrasound probe could cause perspective distortion in the images. To assess this potential source of variability, videos of the exams were recorded and analyzed to evaluate motion in the unconstrained DOFs. It was found that the probe face maintained no-slip contact during the exams (which ensured constraint on the translational DOFs), while the pitch, yaw, and roll DOFs exhibited less than  $\pm 5^\circ$  of movement which, within the context of these results, is sufficiently small to assume that the probe imaged in a fixed plane throughout the experiments.

A Matlab script was written to automatically segment the vessels and fit an ellipse to the vessel boundary in each frame. The script utilizes a typical template-matching approach, in which a filter is first constructed with a dark elliptical region representing the vessel, surrounded by a bright region. The filter is moved around the ultrasound image, and the best-fit centroid location is found. Then, the ellipse major and minor axes are adjusted to determine the dimensions of the best-fit ellipse. Fig. 5-19 depicts an illustration of the best-fit ellipses from each of the frames (overlaid upon the first frame) for force control off and force control on.

In Fig. 5-19, the ellipses exhibit greater spread when the force control was turned off, indicating that the vessel experienced more movement. This suggests that force control enhances image stability. Fig. 5-20 shows the vertical position (depth) of the

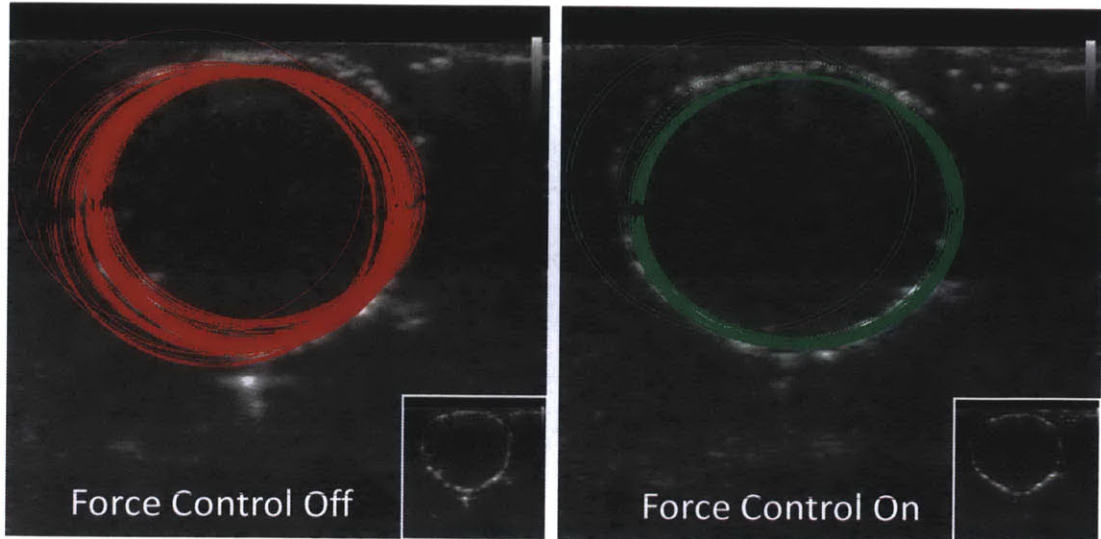


Figure 5-19: Illustration of vessel segmentation with Matlab for one run (run 3) with force control off (left) and force control on (right) for all frames. Best fit ellipses from each of the 193 frames are overlaid upon the first ultrasound image, which is also shown in the bottom right corner.

Table 5.4: Mean value of the standard deviations  $\bar{\sigma}$  in centroid and height for the three runs.

Force control scenario	Standard Deviation (mm)	
	$\bar{\sigma}_{\text{centroid}}$	$\bar{\sigma}_{\text{height}}$
Force Control off	0.30	0.42
<b>Force Control on</b>	0.19	0.11

ellipse centroids versus time for six runs: three runs with control off (dashed line) and three runs with control on (solid line). The runs are offset from each other along the Y-axis for clarity. Table 5.4 shows the mean standard deviation in centroid position and inclusion height over six tests.

Qualitatively, the centroid position traces in Fig. 5-20 are smoother with force control enabled, suggesting that force control stabilizes the inclusion position better than an unassisted human operator. This is quantitatively supported by the lower standard deviations on centroid position (0.19 mm vs. 0.30 mm) and vessel height (0.11 mm vs. 0.42 mm) for force control on, as shown in Table 5.4. In Table 5.4, ‘height’ refers to the width of the vessel in the vertical direction, which was the ellipse minor axis. The force-controlled ultrasound probe can therefore be used to stabilize

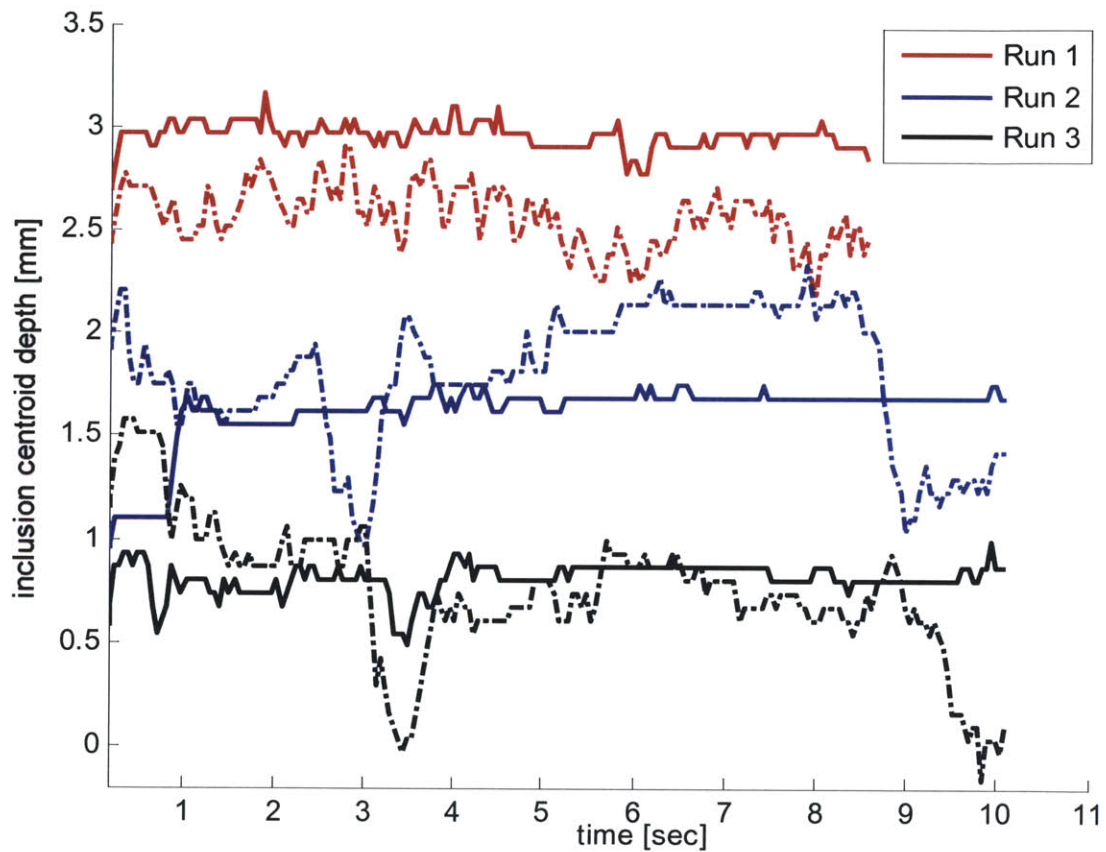


Figure 5-20: Inclusion centroid depth vs time for moving phantom. Centroid depth refers to the depth of the best-fit ellipse centroid for the vessel wall. Dashed line denotes force-control (FC) off; solid line denotes force-control on. The traces are vertically offset from each other for visual clarity; the mean value for all three traces was approximately 1.6 mm.

the acquired ultrasound images, in spite of patient motion.

#### 5.7.4 User Studies to Evaluate Force Control

User studies were performed to evaluate the performance of the system in a realistic scanning scenario. Similar studies were previously performed and reported with Prototype 1 [42], and here we repeat the studies with Prototype 2. In these experiments, the ability of the system to apply a stable force was compared to that of 15 untrained human operators. Each of the fifteen operators held the system in his/her hand and placed the probe in contact with a 18 cm x 13 cm x 5 cm Blue Phantom (Blue Phantom, Inc., Sarasota, FL). To mimic the motions of an actual ultrasound exam, the operators first held the probe stationary for ten seconds, and then conducted a slow, linear sweeping motion across the phantom for twenty seconds, for a total of thirty seconds. The phantom was lubricated with ultrasound gel. The goal was to maintain a constant vertical contact force of 3.0 N while not looking at the probe. The device itself weighed 6.0 N, so in order to apply 3.0 N, the operators needed to pull upward with 3.0 N of force. Each operator performed this procedure in each of the following four scenarios (performed in the order listed):

1. *“Blind”*: With the actuator off and with no force gauge visible (except at the very beginning of test), the operator tried to maintain 3 N from his/her muscle memory. The operator was instructed to look at the ultrasound image on the computer screen and not the device.
2. *“Automatic Control”*: The controller was turned on and the operator held the system in his/her hand. The operator looked at the ultrasound image on the computer screen while the actuator translated to maintain 3 N of contact force.
3. *“Visual Control”*: The controller was turned off and the actuator locked in position. The operator held the system in his/her hand and attempted to maintain 3 N of contact force by focusing on a force gauge displayed on the computer screen.

4. Blind scenario from 1) was repeated for comparison purposes.

The time history of force was recorded over the entire thirty seconds for each of the 15 operators in each of the four scenarios. A typical example of one such force vs. time plot is shown for Subject 6 in Fig. 5-21.

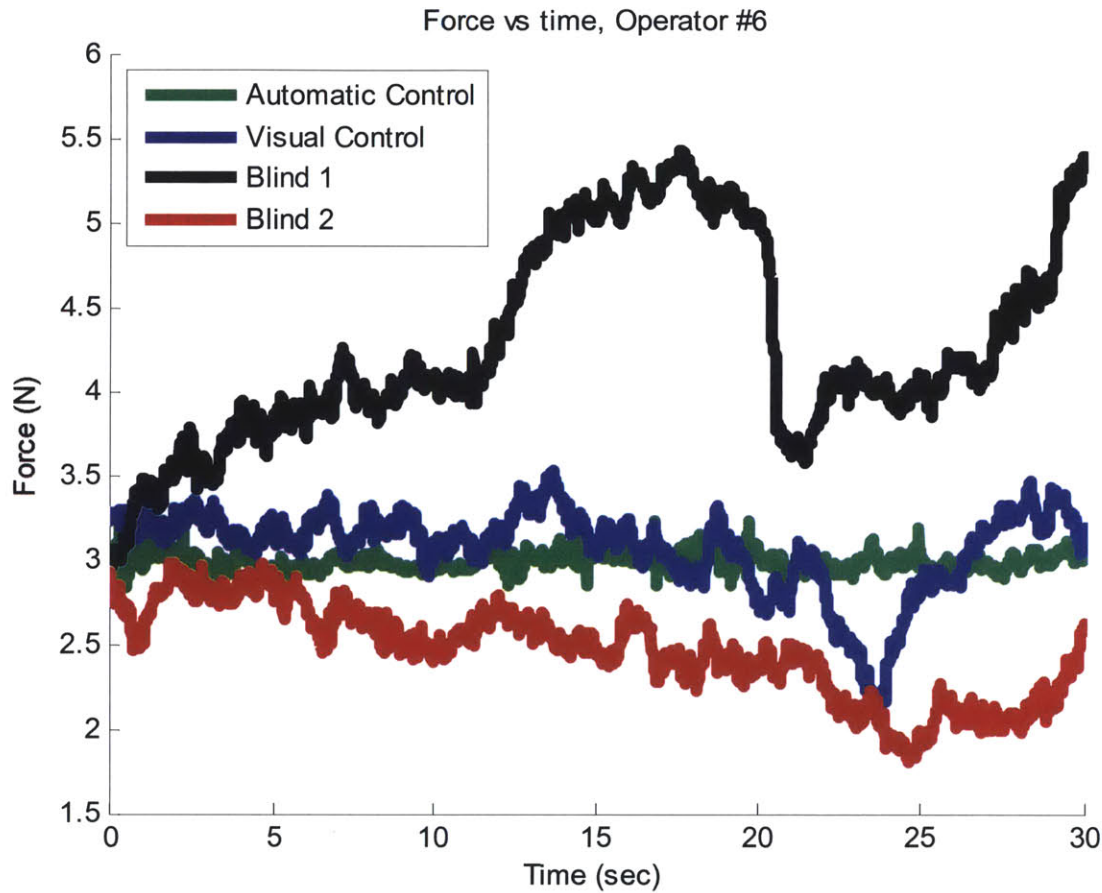


Figure 5-21: Contact force versus time for Subject 6 in each of the four scenarios. The operator held the probe stationary during the first ten seconds and conducted a sweeping motion for the subsequent twenty seconds.

The two “blind” traces in Fig. 5-21 demonstrate that over time, the user’s perception of applied force degrades, and the contact force tends to drift. While performing the moving scan between 10 - 30 seconds, the subject’s applied force showed more fluctuation than in the stationary-scanning period. Both the visual and two blind traces exhibit low-frequency drift (“wander”) and shorter-duration “jerks,” similar to studies performed with the hand-held Micron microsurgical tool in [62]. The visual

and blind cases exhibited more variation than the case with automatic force control enabled. Fig. 5-22 depicts the average forces and standard deviations for each of the 15 subjects in each of the three distinct scenarios.

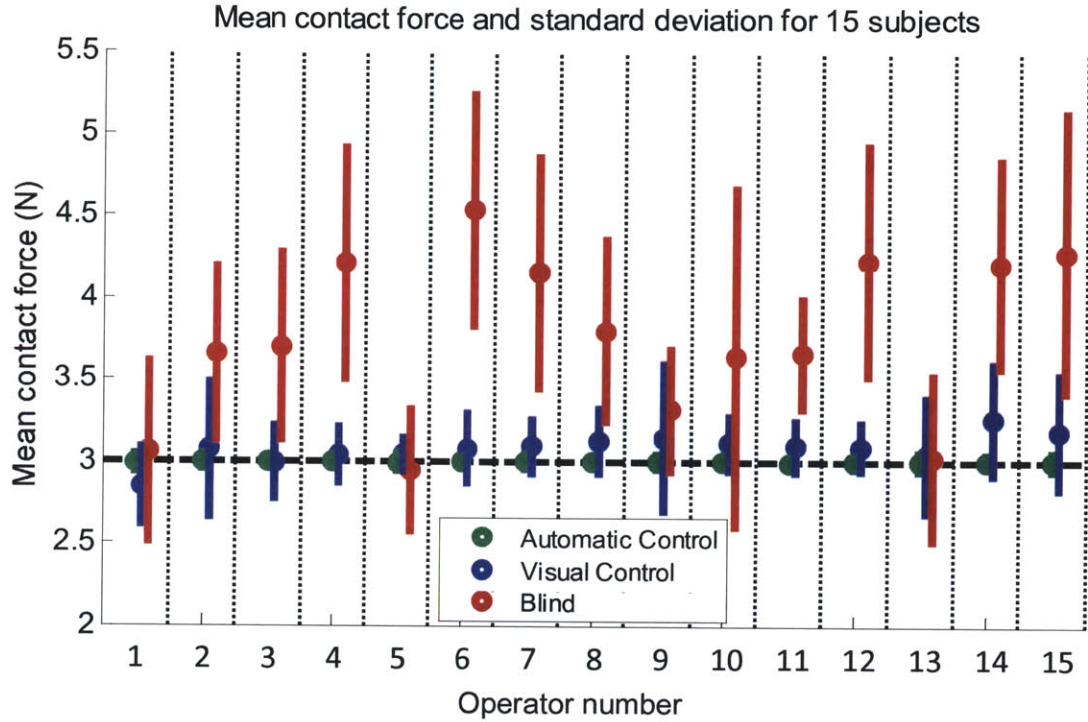


Figure 5-22: Mean contact forces and standard deviations for all fifteen operators in the three scanning scenarios, with 3.0 N target force. Dots represent mean forces while the vertical bars extend  $\pm$  one standard deviation from the mean.

These same experiments were performed previously with Prototype 1 in 2011 [42], and are reproduced in Fig. 5-23. From Figs. 5-22 and 5-23, we observe less variation (smaller standard deviation) with automatic control than with visual control or blind control. In addition, in both cases, the average forces are also closer to the target forces with automatic control than with visual or blind control.

Histograms of the forces applied by all operators in the three scenarios (for Prototype 2) are shown in Fig. 5-24. For clarity, results are plotted from only the second blind trace.

Figs. 5-22 and 5-24 demonstrate greater fluctuation in force for the visual and blind data than with force control enabled, with the greatest spread in forces occurring in

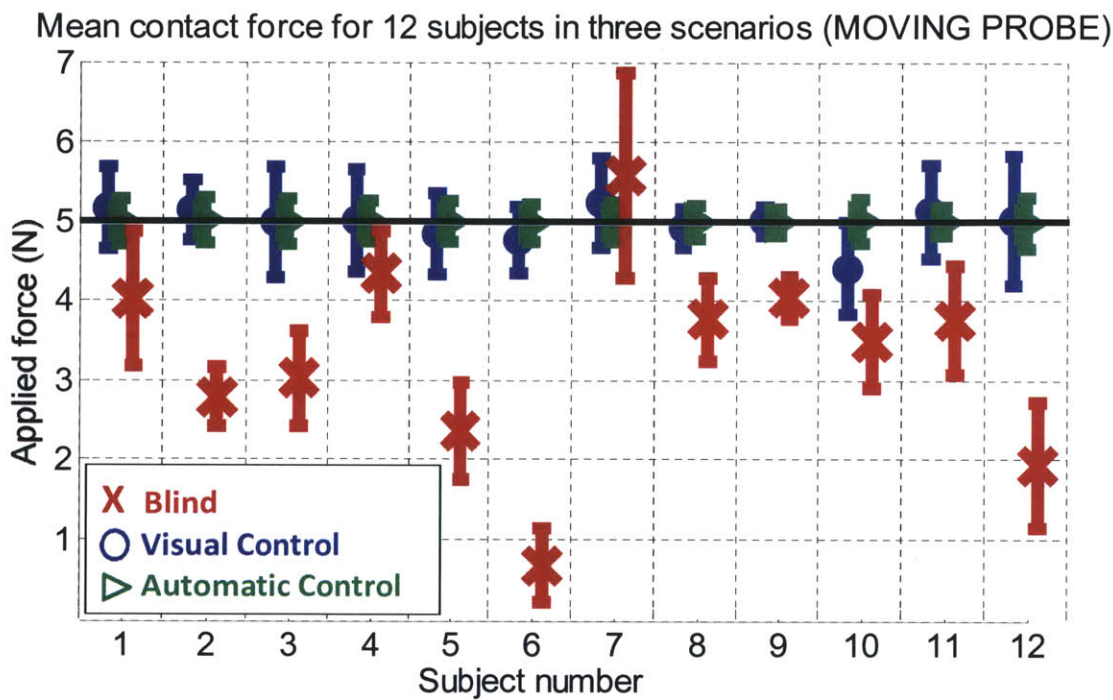


Figure 5-23: Mean contact forces and standard deviations for all fifteen operators in the three scanning scenarios for Prototype 1, with 5.0 N target force, reproduced from [42]. Icons represent mean forces while the vertical bars extend  $\pm$ one standard deviation from the mean.

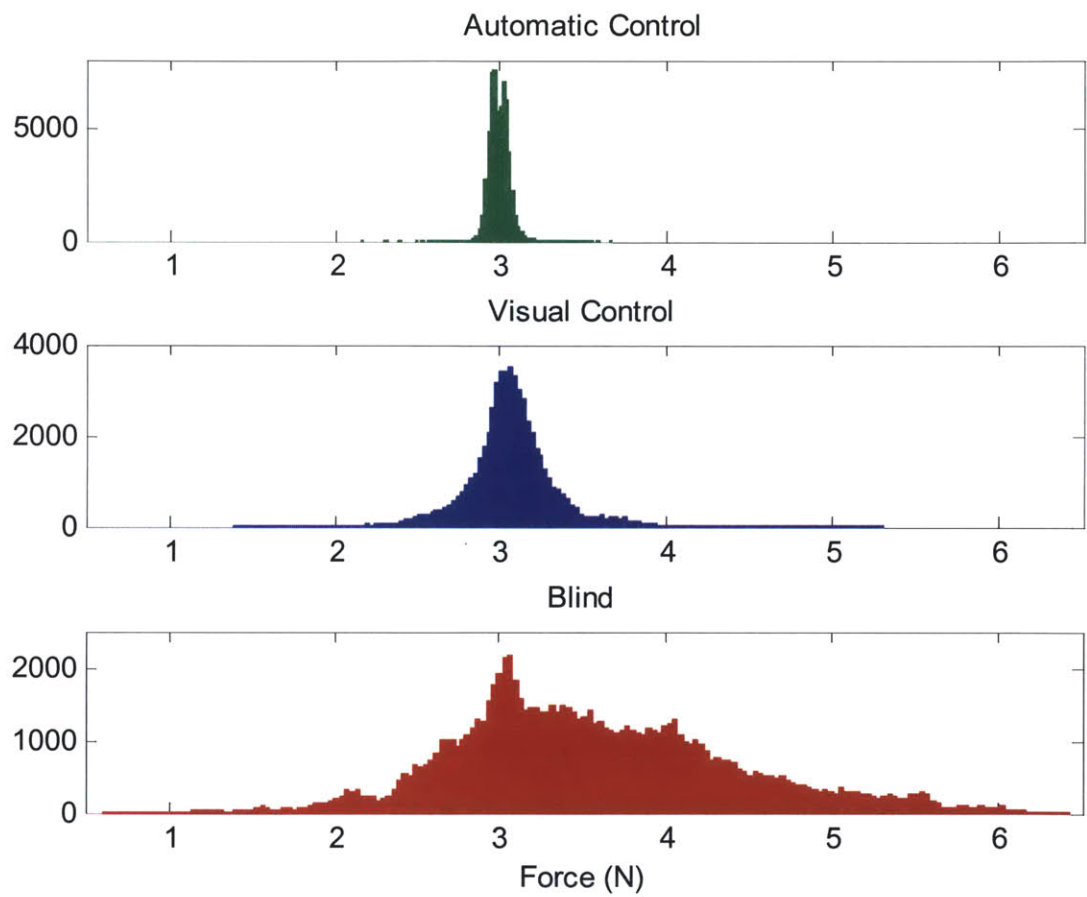


Figure 5-24: Histograms of the forces applied by all fifteen operators in the three scenarios, with 3.0 N target force.

Table 5.5: Measures of the mean contact force for all exams. “P1” denotes Prototype 1, while “P2” denotes Prototype 2. P1 data are reproduced from [42].

Parameter	Automatic Control		Visual Control		Blind	
	P1	P2	P1	P2	P1	P2
$ D_{mean} $	0.01 N	0.005 N	0.15 N	0.098 N	1.78 N	0.762 N
$\sigma_{mean}$	0.25 N	0.063 N	0.51 N	0.267 N	0.63 N	0.631 N

the blind scenario. The blind data also show a bias towards higher forces, which means that, due to the 6.0 N weight of the probe and 3.0 N target force, operators generally supported less of the probe’s weight than in the visual and automatic control scenarios. The means and standard deviations across all exams are quantified for both Prototypes 1 (“P1”) and 2 (“P2”) in Table 5.5.

In Table 5.5,  $|D_{mean}|$  refers to the mean absolute value of the difference between the operator’s average force and the target force (5.0 N for Prototype 1 and 3.0 N for Prototype 2), while  $\sigma_{mean}$  represents the mean standard deviation in contact force. For Prototype 2, the forces applied in the automatic control case average 0.005 N from the 3.0 N target; the visual control data show an order of magnitude greater departure from 3.0 N, and the blind data show another order of magnitude greater departure from the target force. In terms of variation, the standard deviation in contact force with force control on is 0.063 N, which is an order of magnitude less variation than in the blind-control scenario.

The values of  $|D_{mean}|$  and  $\sigma_{mean}$  for Prototype 1 follow the same trends as Prototype 2, and are 1-4 times higher for Prototype 1. This suggests that Prototype 2 provides even greater force stability than Prototype 1, which was about 50% heavier than Prototype 2.

The results demonstrate that even if the operator focuses all of his/her attention on manually maintaining the contact force at the target value (“Visual” case), the actuated and controlled device is still better able to maintain the target force, and enables the operator to focus his/her full attention on the ultrasound image rather than the force gauge, which would be critical during a real ultrasound exam.

## 5.8 Tissue Dynamic Viscosity Measurements

The mechanical response of soft tissue to dynamic excitation can be described by a variety of viscoelastic models, including the Kelvin-Voigt, Maxwell, and Zener models [53]. Pathologies such as malignant lesions exhibit different viscoelastic properties than healthy tissue, and palpation has long been used to detect the presence of pathologies [98]. Next, we demonstrate the use of the force-controlled ultrasound probe to measure the viscoelastic properties of the forearm.

The force-controlled ultrasound probe was fixed rigidly to a frame and a healthy human subject placed his brachioradialis muscle in contact with the ultrasound probe. The probe was commanded to move sinusoidally with amplitude 1 mm, at frequencies from 1-15 Hz. The contact force, which was not controlled and varied from approximately 1 N - 5 N, was recorded, along with the probe position.

The tissue was modeled as a Kelvin-Voigt system [53], consisting of a spring in parallel with a damper. Considering the system model from Fig. 5-15, with  $X_T$  fixed, and solving for the damping coefficient  $b_2$  (which could vary with frequency),

$$b_2(s) = \frac{1}{s} \left( \frac{F_c(s)}{X_U(s)} - k_2 \right) \quad (5.14)$$

Thus, the damping coefficient can be estimated at every frequency. Converting the damping coefficient  $b_2$  to dynamic viscosity  $\mu$  enables comparison with tissue properties from other areas of the body. To calculate  $\mu$ , we normalize by the characteristic length scale  $l$  of the tissue under compression, i.e.,  $\mu = b_2/l$ . The subject's brachioradialis diameter, from skin to ulna, was measured with ultrasound and found to be  $l = 3.5\text{cm}$ . Tissue stiffness  $k_2$  was determined by quasi-statically compressing the patient's tissue, and found to be 600 N/m.

Fig. 5-25 shows the measured dynamic viscosity of the subject's tissue versus frequency for three experimental runs. The four dashed lines show experimental data from other studies on different types of tissue: human vocal fold tissue [30], porcine kidney [73], bovine orbital connective tissue [116], and canine liver [52]. In the case of [116] and [52], viscoelastic parameters were given in terms of the loss modulus  $G''$ ,

which was converted to dynamic viscosity  $\mu$  by  $\mu(\omega) = G''/\omega$  [38].

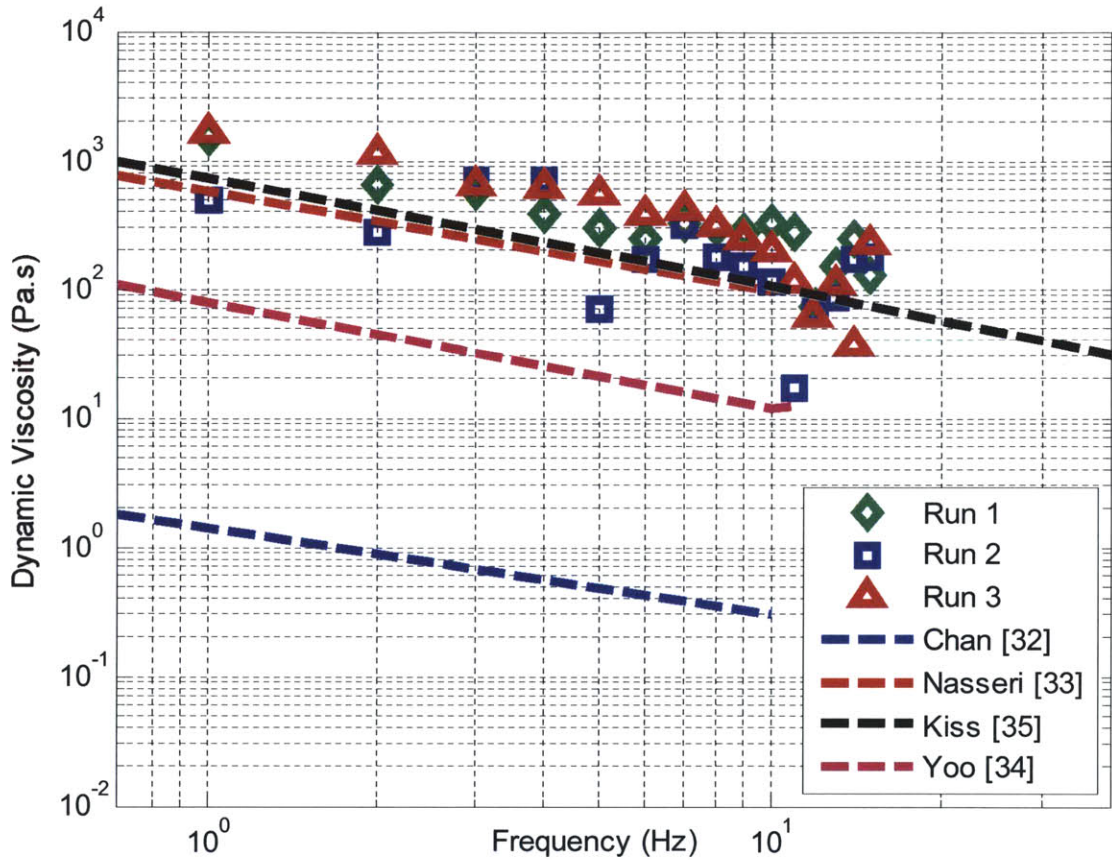


Figure 5-25: Tissue dynamic viscosity  $\mu$  versus frequency: data with the force-controlled ultrasound probe compared with other studies.

The dynamic viscosity, as measured with the force-controlled ultrasound probe, decreased with frequency, consistent with the other four studies. This effect, called *shear thinning*, is often observed in soft biological tissues [30]. The viscosity characteristics of the subject's brachioradialis muscle showed close agreement with [52] and [73], and differed by several orders of magnitude from those of [116] and [30].

## 5.9 Workflow Enhancements: Endpoint Avoidance and Contact State Change

The experiments performed in the preceding sections were obtained while the device operated under pure force control only, as shown in the Fig. 5-14 block diagram. In the following sections, we discuss the usability improvements of selectively employing closed-loop control on contact force and actuator position (Fig. 5-13).

In early tests, when operators were first given the force-controlled ultrasound probe, some had difficulty recognizing when the linear actuator had reached an endpoint. To prevent the actuator from reaching the endpoints and to improve the imaging-workflow performance of the system, we developed a strategy called “Endpoint Avoidance,” which is achieved through software and hardware.

### 5.9.1 “Soft” Limits

The *endpoint-avoidance* scheme sums the outputs from the position controller and a force controller to create two “soft” limits to prevent the actuator from reaching one of the “hard” limits such as a limit switch or an end of travel. The physical configuration of the limits is shown in Fig. 5-26.

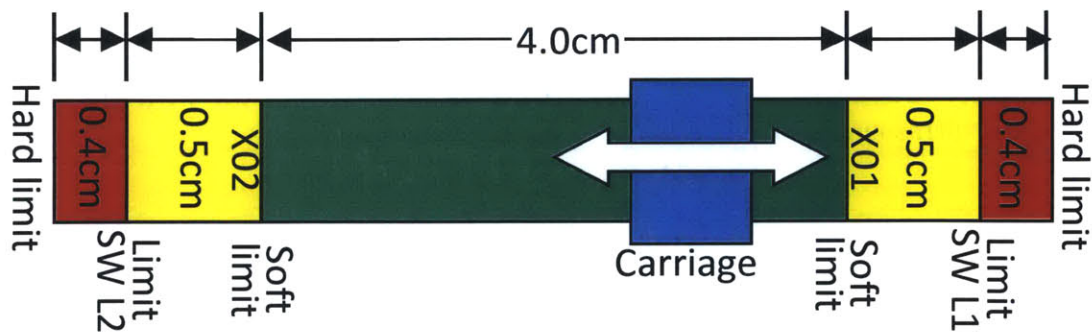


Figure 5-26: The device’s usable range of motion is 5.0 cm. ‘SW’ = ‘switch.’

Avoiding the travel limits while maintaining a constant force suggests the need for both a position controller and a force controller. However, because this device has only one DOF and the actuator position is coupled to the contact force due to the

patient's tissue, only one state variable (either force or position) can be independently controlled at a time.

If a pure force controller is used, a problem arises when the actuator reaches one of the physical limits and needs to be moved back into the permissible range of motion. At that limit, the actuator must be disabled to prevent further motion, but cannot be moved back to the center of motion with a force controller alone. Therefore, a position controller is needed. The challenge lies in switching between the two control loops.

One potential alternative would be to employ Impedance Control [50], in which a combination of force and position are simultaneously controlled. However, in the current experimental setup, we use a motion control card which is capable of PID control only, limiting the ability to implement more sophisticated control strategies, and necessitate the analog circuitry-based solution. Future work includes switching to more customizable control hardware, such as an FPGA-based system that could perform Impedance Control.

The system presented in this paper achieves "soft" limits by using an analog op-amp circuit to sum the outputs from the position and force control loops. The position control loop is enabled only near the limits. In the  $\pm 2.0$  cm region from the center of travel, the force controller is active while the position controller is disabled. At the limits of this region, X01 and X02, the position control loop is enabled with a target position of X01 or X02, as appropriate. If the user continues to press with a high force, the actuator continues backing up until the output from the position control loop balances the output from the force control loop and the control signal sum from the op amp circuit becomes zero. At this point, the actuator stops moving. We refer to this point as a "soft" limit. Once the user's contact force finally decreases, the actuator begins to move again and is driven away from the soft limit. A similar behavior occurs at the forward soft limit when the user's applied force is less than the target force. The exact location of the soft limits will depend upon the target force.

Fig. 5-27 shows the position control loop signal versus carriage position for three different possible operation modes. In operation Mode 1, which is implemented in

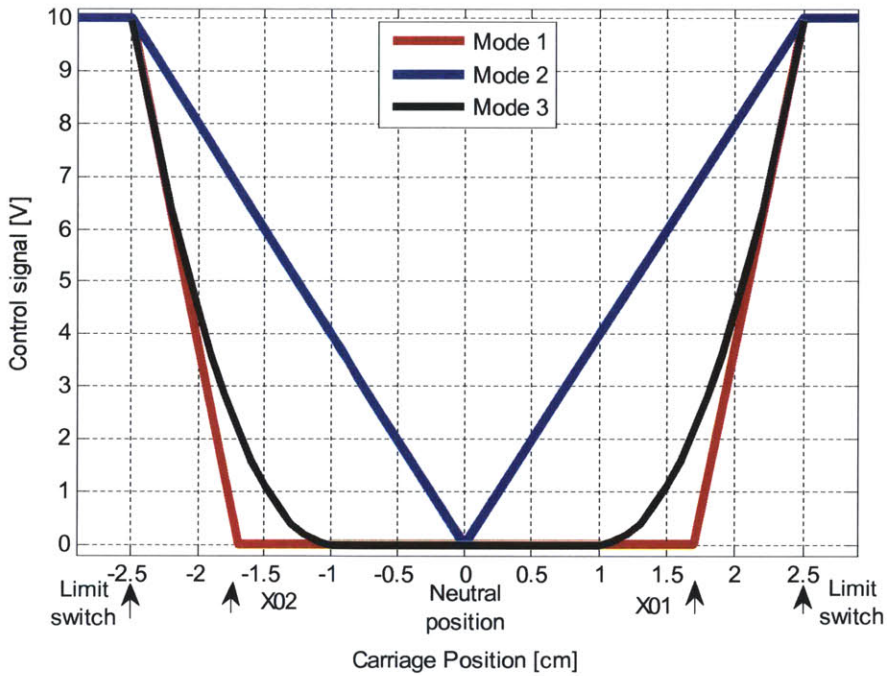


Figure 5-27: Absolute value of the position controller output signal versus position for three possible modes of operation. Due to the fixed PID-based controller, Mode 1 was exclusively implemented in the system.

this device, the position PD controller output signal is linearly proportional to the carriage position outside of positions X02 and X01, when the position controller is enabled. This simulates the effect of a virtual compression spring which engages near each travel limit. Another option would be to employ Mode 2, in which the position controller is always active and generates a control signal that tries to push the user back to the center. This would simulate the effect of a virtual spring that is always in contact with the carriage, the neutral position of which is the center of travel. However, this would not provide constant contact force, and is therefore not used in our system.

A sharp transition occurs when the position controller enables at X02 and X01, and this is perceivable by the user. One strategy to smooth the transition would be to use a PD controller with non-linear gains as shown in Mode 3. This would simulate a virtual non-linear spring that engaged only near the limits and stiffened dramatically when compressed. Due to its smoothness, Mode 3 would be preferred over Mode 1,

however, as mentioned previously, because our control hardware is limited to PID-based control only, we employ Mode 1 with the device.

### 5.9.2 Varying the target force

In this section, we discuss techniques called “Endpoint Avoidance” that help to prevent the user from reaching the soft limits. The purpose of this section is to evaluate the performance of the different techniques for potential implementation in a future version of the force-controlled ultrasound probe; none of the Endpoint Avoidance techniques was employed in the experiments in Section 5.7.

When the device is pushed to one of the soft limits, the target contact force is no longer maintained. Instead, the controller maintains a combination of position and force. In previous user tests [42], we found that occasionally users would reach a soft limit without realizing it. The rear soft limit was most frequently reached, indicating that the users had applied too much force. As a result, the contact force would deviate from the target force and ultrasound image consistency would be degraded. In order to maintain the target force, we have developed two software strategies to prevent the users from dwelling at the soft limits: Endpoint Avoidance 1 and 2.

For Endpoint Avoidance 1 (EA1), while the user dwells at a soft limit, the target force slowly increases, pushing the user away from the limit. As the user departs the soft limit, the new target force is locked in. This way, the user can change the target force intuitively, without needing to press any buttons.

Endpoint Avoidance 2 (EA2) is similar to EA1 except that once the user departs from the soft limit, the target force slowly decreases back to the initial value. As discussed in [43], these strategies also enable the user to break ultrasound probe-patient contact without the turning off the controller.

To demonstrate the endpoint avoidance strategies, the device was placed in contact with a long phantom and was scanned horizontally back and forth over the surface for 35 seconds in five separate tests. In four of the five tests, the controller was set to maintain a target force of 4.0 N. The force and position were recorded, and the results are shown in Fig. 5-28.

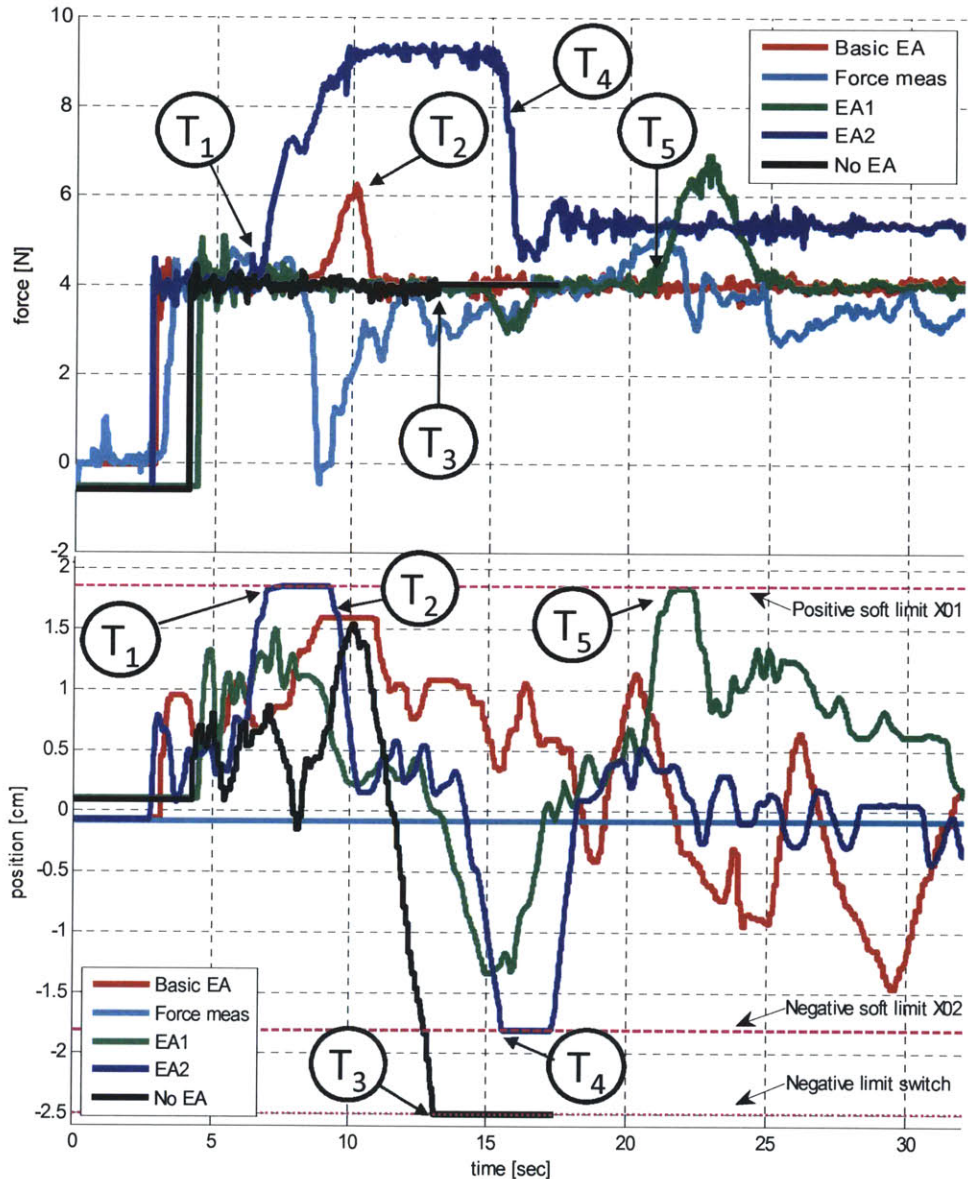


Figure 5-28: Force versus time (top) and ultrasound probe position versus time (bottom) during a phantom scan for five endpoint avoidance strategies. “EA” refers to “Endpoint Avoidance”.

The plots demonstrate that the three endpoint avoidance strategies (red, green, blue) push the user back towards the center of travel and help maintain constant force. With no endpoint avoidance (**black** trace), the user reached a physical travel limit at  $T_3$  and the actuator was automatically turned off to avoid damage. The **cyan** trace demonstrates how the contact force varied during the exam with the controller turned off, in the passive “Force Measurement” mode.

*Basic Endpoint Avoidance (red):* This operation mode consists of force control with the addition of the front and rear soft limits. Target force remains constant. While operating under this mode in Fig. 5-28, at around  $T_2$  the user reached the soft limit X01 and the force momentarily increased before the user’s force backed off.

*EA1 (green):* The EA1 trace demonstrates the implementation in which the force setpoint increases at the soft limit in an attempt to push the user back toward the center of motion. To illustrate this, at  $T_5$ , the user reached the X01 soft limit and the contact force momentarily increased from 4 N to 7 N, pushing the user back towards the center. As the user approached the center, the force setpoint decreased back to the original 4.0 N.

*EA2 (blue):* shows the other endpoint avoidance strategy in which the force setpoint changes and “locks in” at the soft limits. At  $T_1$ , the user reached soft limit X01 and the force setpoint began to slowly increase. Once the setpoint reached 9.2 N, the user was pushed back towards the center. The user continued scanning at 9.2 N until reaching the forward soft limit X02 at  $T_4$  at which time the force setpoint slowly decreased to 5.2 N, at which time the user began to pull back on the probe.

With these three Endpoint Avoidance strategies, sonographers never reach a hard limit, which means that they never need to reset the device. However, while Endpoint Avoidance keeps the actuator within the safe operating region between the limit switches L1-L2 (Fig. 5-26), it is still possible for the user to apply a contact force that is different from the force set-point if operated in the regions X01-L1 or X02-L2. In exams in which constant force is required, we rely on the user to keep the carriage in the constant force region X01-X02.

## 5.10 Changes in Contact State: Making and Breaking Contact

For fully ergonomic operation, the control system must permit the sonographer to make and break contact with the patient, because sonographers frequently move the probe from one body location to another during exams. In this section, we discuss a control technique for smoothly transitioning between constant-force contact and no contact.

### 5.10.1 Making contact

Let us first consider the simplest control scenario, in which the device operates under pure force control, with no provisions for making and breaking probe/patient contact. If, initially, the actuator was not in contact with the tissue (e.g., hanging from the ultrasound cart), the moment the sonographer pressed “Run,” the actuator would advance rapidly to the forward travel limit, seeking the target contact force. Similar behavior would occur when the sonographer removed the device from the patient. Either scenario could result in mechanical damage when the actuator reached a hard limit.

One possible solution could be to require that the sonographer hold the device in contact when pressing the “Run” or “Stop” buttons. This solution, however, is not ergonomic, requiring coordination by two hands at once. Another possible solution would be to place a foot pedal within easy reach or a small button on the ultrasound probe itself, which the user presses when he/she changes the contact state of the probe. While these methods would provide a robust means of transitioning between contact and no contact, they would rely on the user to consciously remember to trigger the buttons. To reduce the burden on the sonographer, we seek an solution that can be operated more naturally.

To avoid the problems associated with making and breaking contact, the force-controlled ultrasound probe selectively enables/disables force control based upon the

contact state. When the user presses “Run,” the control software waits until the target force is met before enabling the controller. Thus, the user can start with the device initially not in contact, then pick up the device when he/she is ready to place it in contact with the patient. Once the target contact force is reached, the actuator begins moving.

### **5.10.2 Breaking Contact**

When the sonographer pulls the device away from the patient, or “breaks” contact, the actuator quickly reaches the forward soft limit and dwells there until it is placed in contact once again. A flowchart of the complete control strategy, which combines both endpoint avoidance and the ability to make and break contact, is shown in Fig. 5-29.

### **5.10.3 Contact with hard surfaces**

In addition to the ability to smoothly initiate and break contact between the probe and patient, the device must also be able to handle changes in the stiffness of the environment. In most ultrasound imaging applications, the probe is placed in contact with soft tissue (e.g. abdominal, musculoskeletal, and vascular imaging). For these soft structures, it is hypothesized that a relatively low bandwidth of 10 Hz is sufficient to maintain constant force. Occasionally, however, the probe might occasionally make contact with a stiffer structure such as a bone (e.g., rib contact in cardiac imaging and contact with the radius or ulna in forearm imaging). For hard structures such as these, a displacement of the probe results in a much greater increase in contact force, and therefore a higher system bandwidth is necessary to react to the rapid change in contact force.

In experiments, we observed that when the probe was placed in contact with a bony, stiff structure, the probe would tend to vibrate and chatter, suggesting instability in the control system. Stability was restored when the probe was placed back in contact with soft tissue. During use, we therefore instruct the user to move the probe

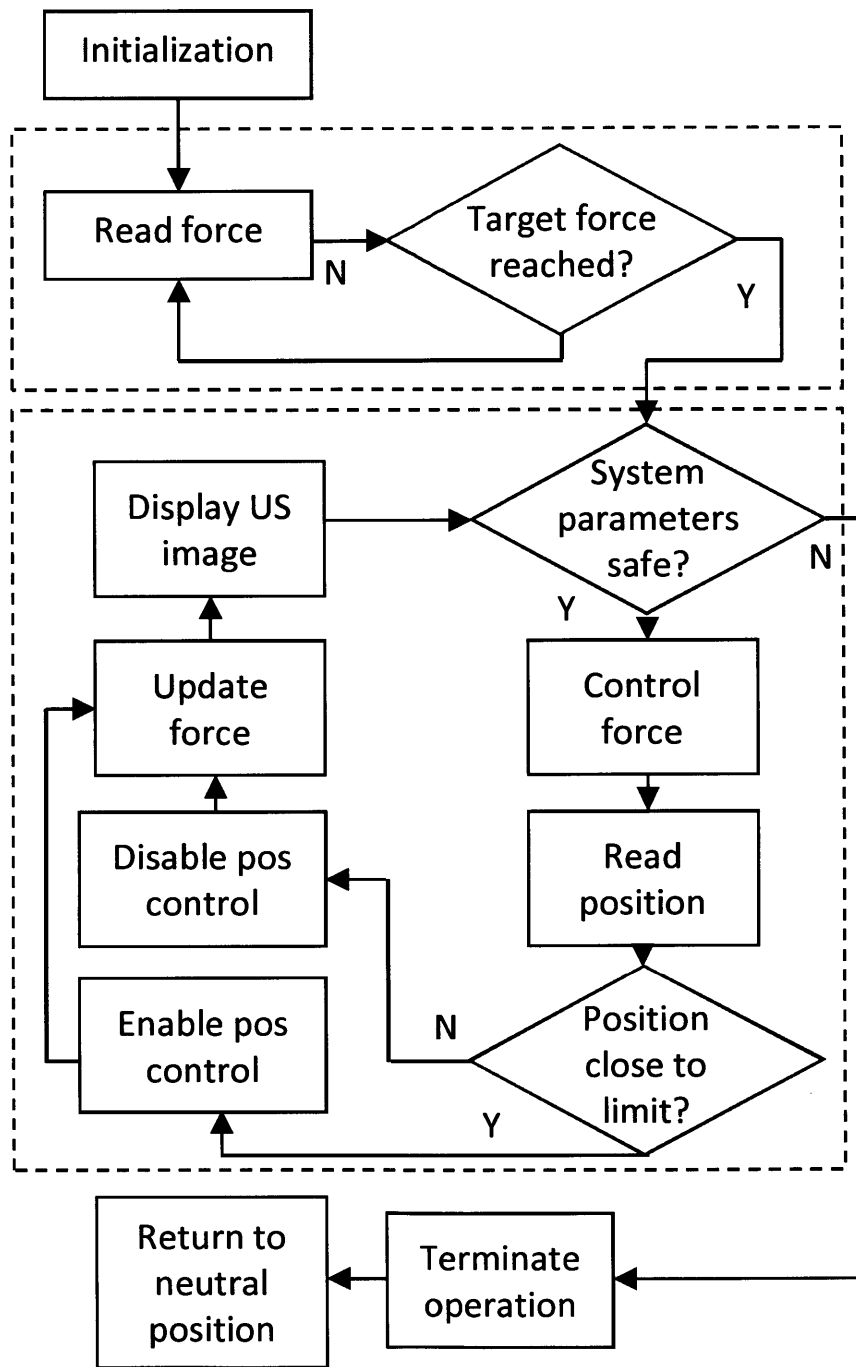


Figure 5-29: A flow chart of the complete control system, which includes endpoint avoidance and the ability to make and break probe/patient contact.

to softer tissue if the probe begins to chatter. While this does limit the usability of the system, the device can still be used for most ultrasound applications. If, for a particular application, contact with the bone were necessary, a higher-bandwidth actuator such as a voice coil could be appropriate (described in more detail in Chapter 7.)

## 5.11 Summary

This chapter described the design process and experimental evaluation of the force-controlled ultrasound probe, Prototype 2. The device, which was developed for general abdominal and musculoskeletal imaging, consists of a ball screw actuator driven via a timing belt by a small 16 mm-diameter servo motor. The frequency response of the system was evaluated across the range of typical human hand tremor frequencies. It was found that the device attenuates hand tremors by 97% at 0.1 Hz, and 33% less at 10 Hz. Below 10 Hz, the model showed good agreement with the experimental data. In fifteen studies with human users, it was found that the device reduces contact force variation by a factor of ten.

Control strategies that permit ergonomic interaction between the user, patient, and device were presented. One aspect of the system consists of combined force and position control loops. During normal operation, only the force controller is active, which ensures that the actuator applies a constant force. When the user causes the actuator to near a travel limit (by applying too little or too much force), the position controlled is enabled. The control signals from the force and position controller are summed, and balance at a certain point called the “soft limit.” The presence of the front and rear soft limits prevents the user from pushing the actuator to a travel limit.

In addition to soft limits, another control strategy called “Endpoint Avoidance” was implemented and evaluated. By varying the target force, the Endpoint Avoidance techniques drive the user back to the center of the range of motion of the device, to reduce the time that the user dwells at the soft limits. Three different Endpoint Avoidance techniques were evaluated. A combination of the soft limits, soft start, and Endpoint Avoidance techniques significantly increase the ergonomics of the de-

vice/human interactions.

# **Chapter 6**

## **Ergonomics Considerations - Enabling Clinical Studies and Use**

This chapter describes the design, fabrication, and evaluation of the third prototype, which includes a number of ergonomic improvements over Prototype 2, and is shown in Fig. 6-4.

### **6.1 Duchenne Muscular Dystrophy Study**

The primary goal with Prototype 3 was to design a force-controlled ultrasound probe for use in a clinical study involving children with Duchenne Muscular Dystrophy (DMD) at Boston Children's Hospital [13],[54],[55]. One of the goals of the study is to determine whether ultrasound can be used to evaluate the degree of muscle dystrophy as the disease progresses over the course of two years.

DMD is a genetically-inherited condition that leads to loss of muscle strength over time, eventually leading to death. Occurring only in males, the disease is present in 1 out of 3,600 male infants [6], making it one of the most common and severe neuromuscular disorders of childhood [54],[55]. Symptoms of DMD appear before age 6, and are characterized by: fatigue, muscle weakness, learning difficulties, and progressive difficulty with motor skills, including walking, climbing stairs, and getting up from a lying position. The ability to walk is commonly lost by age 12, and

breathing difficulties and heart disease develop by age 20. Life expectancy is about 25 years of age.

Steroids and other drugs have been used to slow the loss of muscle function, but no cure currently exists for DMD. The search for an effective treatment for DMD is the subject of active research. To evaluate the effectiveness of different treatments upon muscle health, functional measures are typically performed. For example, the 6-minute walk test (6MWT) is used to measure the distance that a patient can quickly walk over the course of 6 minutes [96]. Although easy to perform, this technique has limitations; it can only be used on ambulatory patients, and it is subject to a considerable amount of noise due to subjective nature of the request upon the patient: “walk as far as you can in 6 minutes.” Variations in patient cooperativeness, mood, and level of motivation, could confound the measurement. Therefore, more quantitative measures of muscle function are sought in order to stage disease progression.

Ultrasound presents a possible method for non-invasively evaluating muscle health in DMD patients. As DMD progresses, muscle is replaced by adipose and connective tissues, making the tissue more ultrasound-echogenic (brighter ultrasound image) and more homogeneous. Images from healthy and DMD patients are shown in Fig. 6-1, in an image borrowed from one of our publications [54] related to this study.

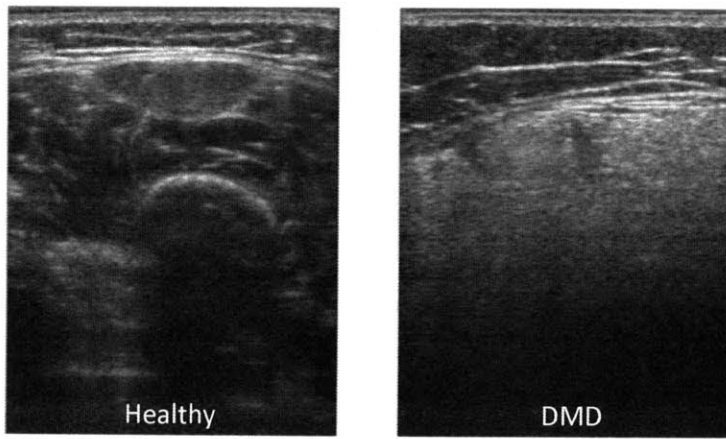


Figure 6-1: Ultrasound images of the quadriceps in a healthy patient (left) and in a patient with DMD (right). Image reproduced from Koppaka, et al [54].

Tissue elasticity could also provide insights into muscle health. As discussed at

length in Section 7.3, a technique referred to as elastography can be used to quantitatively estimate tissue elastic modulus based upon the ultrasound image and the level of force applied. It has been shown that there is a strong correlation between elastic modulus and tissue health. Thus, it is reasonable to assume that the degree of muscular function could be evaluated by acquiring ultrasound images at known forces.

### 6.1.1 Third prototype: objectives

The potential benefits of force-correlated ultrasound imaging in the study of DMD therefore motivates the use of a force-controlled ultrasound probe. It was decided to embark upon the design of a third prototype that would be custom-designed for the DMD study, and would improve upon the design of the second prototype by considering its limitations and shortcomings.

The functional requirements for the third prototype are as follows:

1. Perform force-controlled ultrasound musculoskeletal imaging in DMD patients.
  - (a) *Force sweep*. With this device, the goal is to acquire images as a function of force. This requires the inclusion of additional functionality that changes the target force throughout the range of interest in order to perform a force sweep. In early experiments, the maximum force that could be comfortably applied to young patients was 10 N. The minimum stable force for the actuator was 1 N. Therefore, the device must be able to perform a force sweep between 1 N and 10 N.
  - (b) *Angle sweep*. Muscle exhibits anisotropic mechanical properties; it is stiffer in some directions than others. When imaged at various angles, muscle also exhibits anisotropy to ultrasound, with a change in sound speed depending upon fiber orientation [69]. Based upon our own observations, differences in the angle of orientation of the ultrasound probe with respect to the muscle fibers result in ultrasound images of different brightness. When the probe is placed normal to the skin surface above the quadriceps, for

example, ultrasound images appear brighter than if the probe is tilted at an oblique angle. It is hypothesized that the image brightness vs. probe angle characteristics will differ in healthy and DMD patients, and may help to evaluate disease severity in the latter. Therefore, we require that the device measure orientation angle, and provide feedback to the user when the angles are outside of  $\pm 20^\circ$  from vertical.

2. Improve bandwidth and ergonomics with respect to the second prototype.
  - (a) *Range of motion*: In studies with the second prototype, it was found that even with the Endpoint Avoidance techniques discussed in Section 5.9, users would still occasionally push the actuator to a travel limit without realizing it, which would cause the contact force to deviate from the nominally constant value. With training, users would reach the limits less frequently. To reduce the level of skill necessary to operate the device, as well as the frequency with which the actuator is pushed to the travel limit, it is necessary to provide the user with better feedback of the actuator position.
  - (b) *Hand grip*: The second prototype is gripped with a “pinch grip,” which is known to be less ergonomic than the “power grip” [12]. For the third prototype, we seek a design that permits the user to grasp around the device, rather than behind the ultrasound probe.
  - (c) *Bandwidth*: As discussed in Section 5.9, the second prototype can attenuate tremors up to about 10 Hz. It is desired to improve the bandwidth of the device to 15 Hz so that can produce more stable contact force.

### 6.1.2 Third Prototype: Design Parameters

The main additional functional requirements imposed upon the design of Prototype 3 are primarily: 1) improve feedback to user, and 2) improve bandwidth.

## Improved User Feedback

Linear LED array: A number of options were brainstormed to inform the user of the position of the actuator, including audio feedback, graphical display on the computer screen, and LEDs on the device. LEDs were considered the most promising option, because they would provide the least obtrusive feedback (audible tones might be an annoyance) and would not require the user to focus on the computer screen.

To prototype this option, a 10-LED array was affixed to Prototype 2, as shown in Fig. 6-2. The LEDs, which were controlled by the LabVIEW program, were set up to encode the position of the actuator relative to its usable range of motion. Nine of the ten LEDs are always illuminated; a single darkened LED indicates carriage position. The top LED corresponds to carriage position X02 (Fig. 5-26) and the bottom LED corresponds to X01. Therefore, the range of LEDs maps into the constant force region X01-X02. During an exam, the user monitors the LED bar graph and moves his/her hand to ensure that the top and bottom LEDs are always illuminated, in order to keep the actuator within the constant-force region of operation.

Digital angle display: It was decided that a small digital display would provide the best method to inform the user of the orientation of the probe with respect to gravity. A two-digit, 7-segment LED array was mounted to Prototype 2 and set up to display the angle in degrees, as measured by the accelerometer. An additional green LED illuminates for negative angles. The setup is shown in Fig. 6-3.

## Improved Bandwidth

It was hypothesized that direct-drive transmission could provide higher bandwidth. Prototype 2 employs a small timing belt to transfer torque from the motor axis shaft to the ball screw shaft via a 2:1 reduction. This enables the motor to be mounted behind the ball screw actuator without increasing the overall length of the system. However, this prevents it from being grippable by a “power grip,” one of the functional requirements for the new prototype. Mounting the motor along the ball screw axis instead would make the girth of the device smaller, and potentially enable

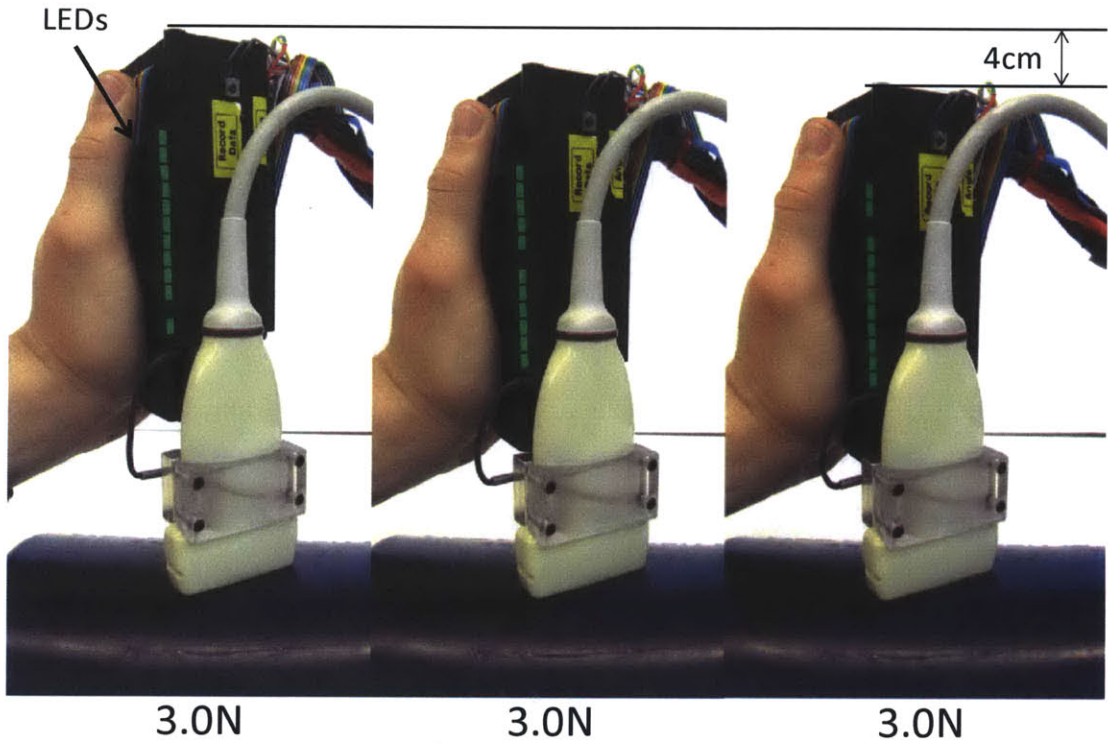


Figure 6-2: Prototype 2 instrumented with the LED array, which displays the position of the actuator.

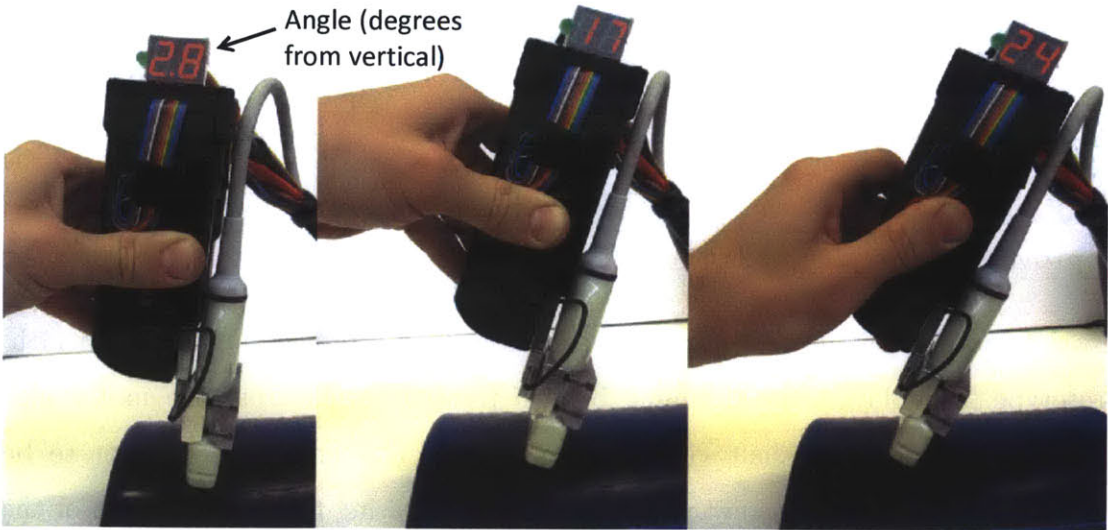


Figure 6-3: The digital display indicates the angle of inclination of the device from vertical. A green LED illuminates when the angle is negative.

a power grip, but the present motor would make the system prohibitively long. It was therefore decided to use a shorter-length, larger diameter motor that could keep both the diameter and length of the device small. A Maxon EC 45 Flat brushless servo motor (part #200142) was selected for this purpose.

## **Additional Components**

Because the new functional requirements of improved user feedback and increased bandwidth are satisfied by the LED array/digital display and new motor, respectively, the remainder of the components were similar to those used in Prototype 2. Due to availability restrictions from NSK, The NSK Monocarrier was replaced by the comparable Kuroda SE1502A-100W-A0NN-NN ball screw actuator, an ADXL 335 triple-axis accelerometer on an +5V Adafruit board was used, along with the same Futek LSB 200  $\pm 45$  N load cell, and a Maxon HEDL-5540 A11 2000 count/turn encoder. Additional components were machined from aluminum and 3D printed with ABS plastic. Magnets were embedded into the top and bottom shells so that the probe can be easily removed (discussed within the context of the Force Measuring Probe in Section 3.3.1). A photograph and solid model of Prototype 3 are shown in Fig. 6-4. An exploded view of the device is shown in Fig. 6-5, and the components are described in Table 6.1.

### **6.1.3 Design Considerations: Motor Wire Strain Relief**

One of the special considerations associated with the use of the new large-diameter motor is due to the fragility of the motor wire, which is an 8-conductor flat flexible wire. In early tests, it was discovered that the wire is incredibly fragile; any bending or creasing of the wire would cause it to fatigue, creating an open circuit. Images of the wire in the first design iteration, in which the wire was subject to active bending, are shown in Fig. 6-6.

To eliminate bending of the motor wire, the layout of the components was modified so that the motor wire attached to an internal connector (part #10 in Fig. 6-5).

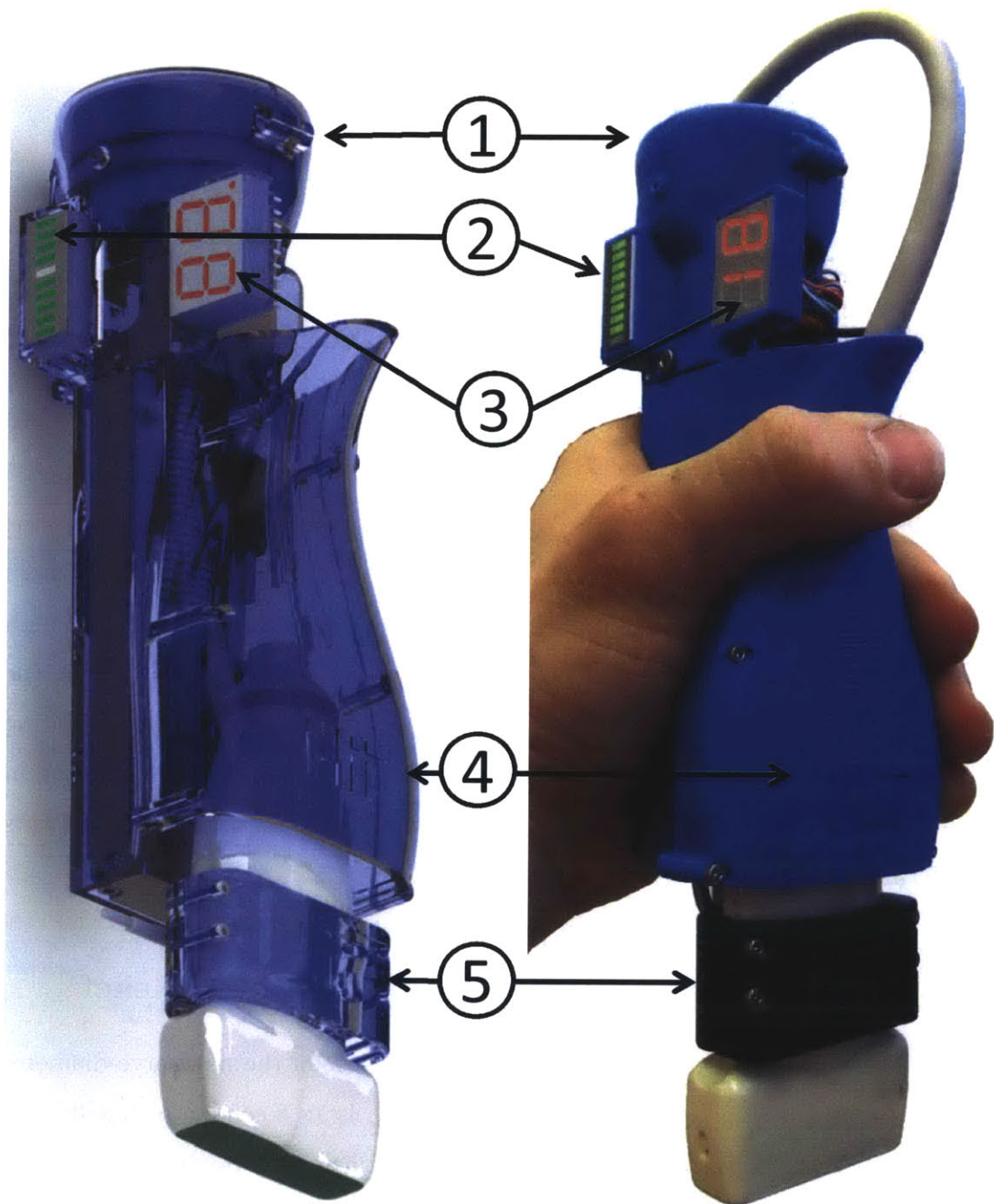


Figure 6-4: Prototype #3. Labels: 1) servo motor, 2) LED bar graph actuator position indicator, 3) two-digit angle display, 4) ergonomic 3D-printed shell, and 5) 3D-printed probe clamp.

Figure 6-5: Exploded view of Prototype 3. Components are described in Table 6.1.

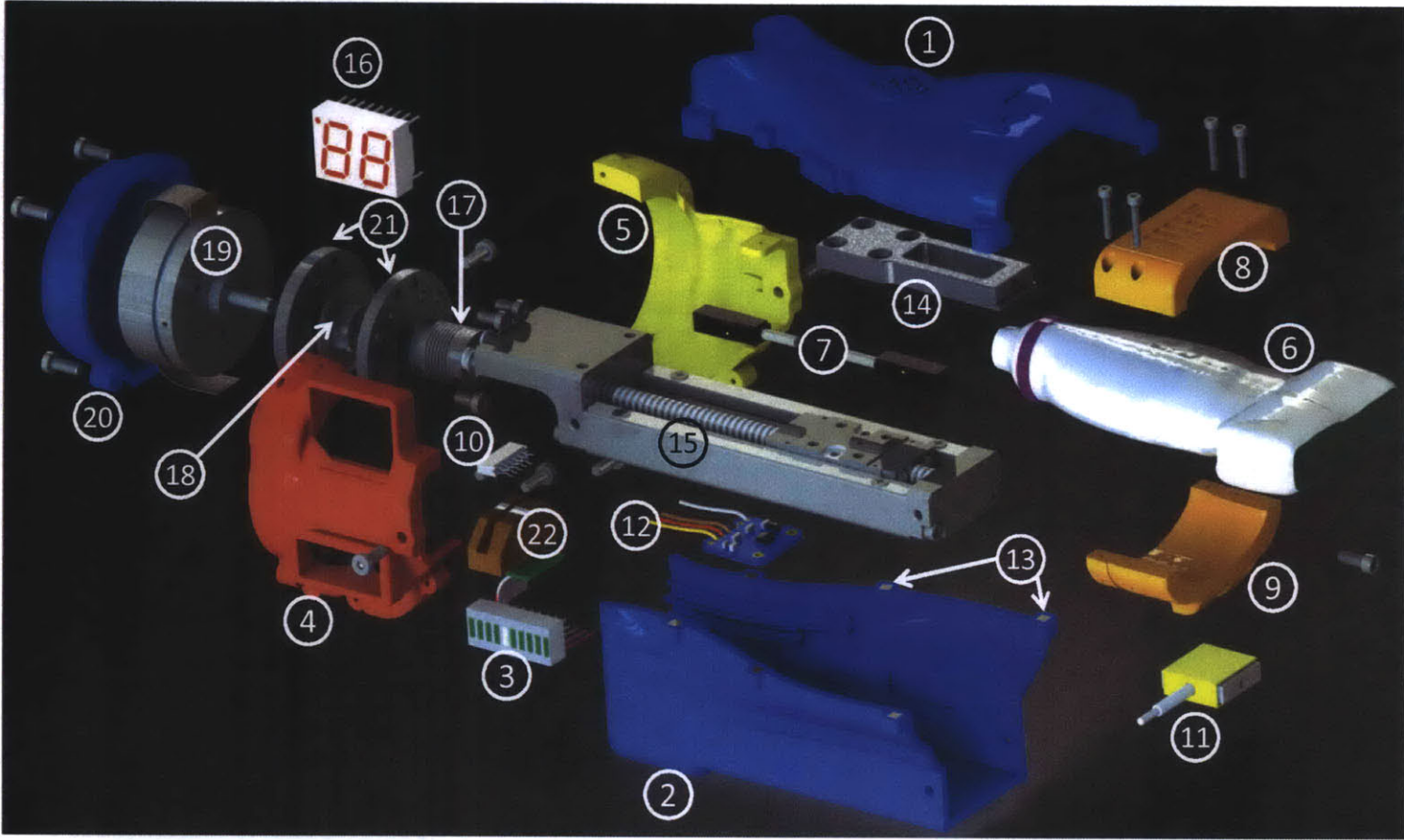


Table 6.1: Description of the components of Prototype 3 shown in Fig. 6-5.

Component number	Description	Purpose	Part number
1 & 2	Protective cover top and bottom	Grasped by sonographer; protects hand from moving parts. Mounts accelerometer (12)	3D printed
3	LED bar graph display	Indicates position of actuator	Digikey 516-1241-5-ND
4, 5, & 20	Motor cover left, right, and back (20) pieces	Protects motor, provides strain relief	3D printed from ABS
6	Ultrasound probe	Images the tissue of interest	Terason 7L3V
7	Proximity (limit) switches	Triggered when carriage approaches endpoint	Omron E2S
8 & 9	Probe clamp	Clamps around probe, attaches to load cell	3D printed from ABS
10	Motor wire internal connection	Strain relieves fragile motor wire	Digikey WM5321-ND
11	Load cell	Converts contact force to an analog voltage; mounts probe	Futek LSB200
12	3-axis accelerometer	Converts XYZ accelerations into analog voltages	Adafruit 163 / ADXL335
13	Magnets	Attaches top and bottom shells, permits rapid assembly/disassembly	McMaster 5848K41
14	Mounting bar	Mounts probe clamp to ball screw carriage	Machined from aluminum
15	Ball screw linear actuator	Converts rotational to translational motion; constrains to 1 DOF	Kuroda SE1502A-100W-A0NN-NN & post-machining
16	2-digit angle display	Displays angle in degrees	Digikey 516-1207-5-ND
17	Shaft coupling	Transmits torque; permits axial misalignment of motor and shaft	McMaster 2463K1
18 & 22	Encoder code wheel (18) and read head (22)	Encodes shaft angle to 0.18°	Maxon HEDL-5540 A11 & post-machining
19	Servo motor	Converts current to torque	Maxon EC45 flat #200142 & post-machining
21	Motor mounting flanges	Mounts motor, shields encoder	Machined from aluminum

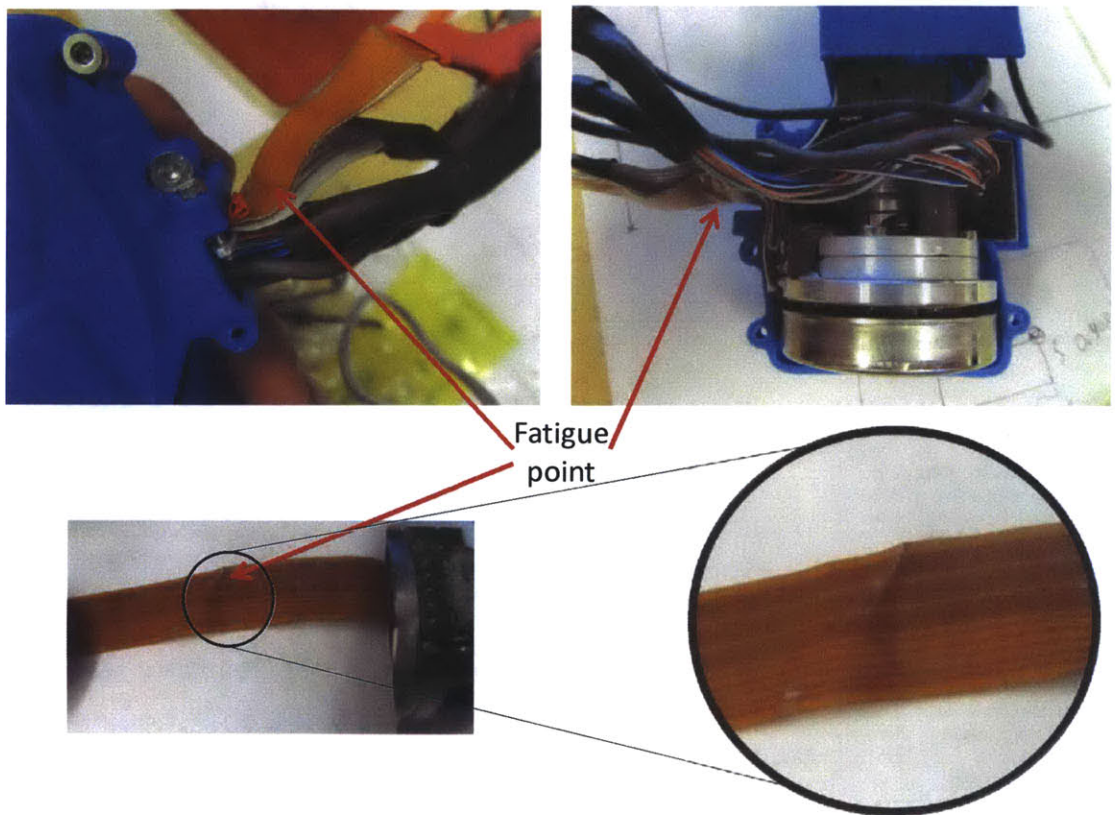


Figure 6-6: In the first design iteration of the motor shell, the motor wire lead was subject to repeated bending and unbending during operation, eventually leading to fatigue and loss of electrical continuity.

The three-piece breakaway motor cover was designed to simplify assembly of the components, and is shown in Fig. 6-7.

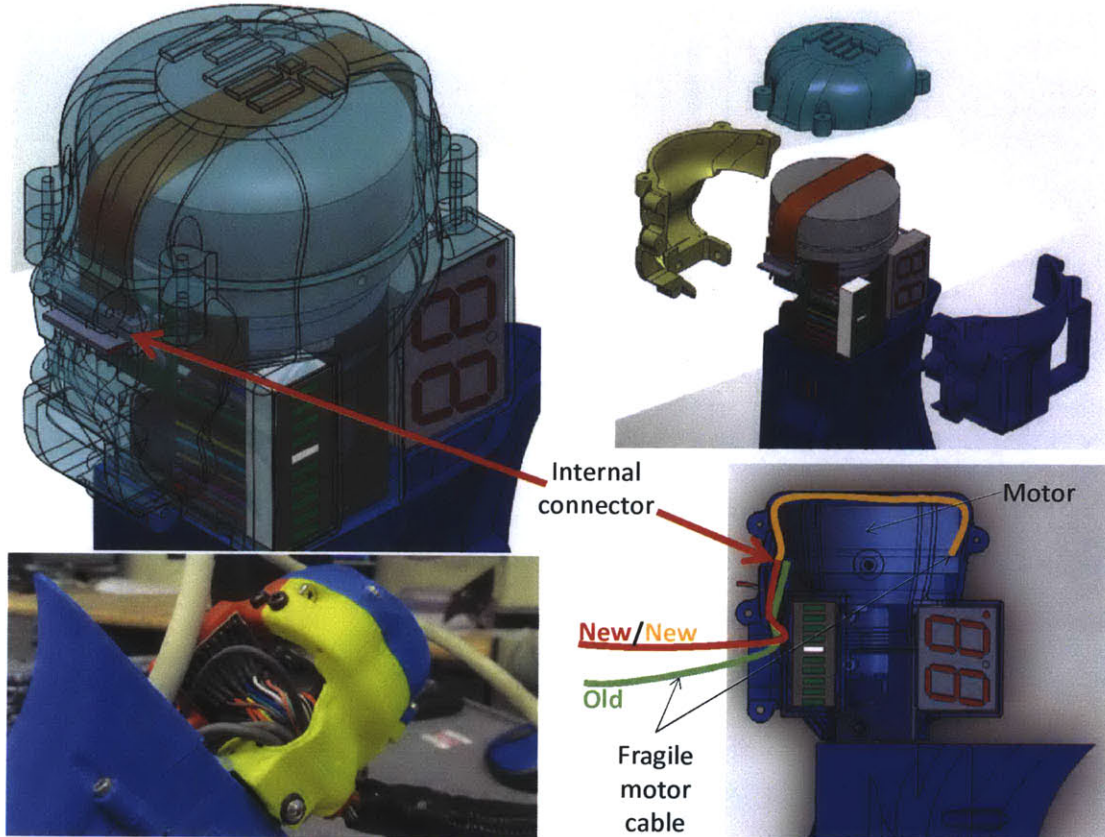


Figure 6-7: Redesigned 3-piece breakaway motor cover, which eliminates strain on the motor cable.

## 6.2 Three Prototypes: Comparison

All three devices employ a ball screw linear actuator, driven by a compact servo motor. The prototypes differ terms of in range of motion and ergonomics. Prototypes #2 and #3 are smaller and more naturally-grasped than #1. Table 6.2 compares the three prototypes with respect to the functional requirements for Prototype 2, from Section 5.3.1. Although Prototypes 1 and 3 were not designed with the same functional requirements as Prototype 2, we still include them the table for comparison purposes.

Table 6.2: Comparison between functional requirements of Prototype 2 ( $FR_P$ ) and measured capabilities ( $D_P$ ) of the three force-controlled probes, Prototypes 1-3. Although Prototype 1 was not designed with the same functional requirements as Prototypes 2 and 3, we include it in this table for comparison purposes.

Parameter	$FR_p$	$D_p$			N	Safety Factor		
		#1	#2	#3		#1	#2	#3
Usable stroke (cm)	>5	10	5	5	+1	2	1	1
Probe mass (g)	<2,000	1,100	750	850	-1	1.8	2.6	2.4
Bandwidth (Hz)	>10	2	10	6	+1	0.2	1	0.6
$F_{max}$ (N)	>20	80	45	45	+1	4	2.3	2.3
Diameter (cm)	<8	7.5	6	5.4	-1	1.1	1.3	1.5
Length (cm)	<20	28	15.8	18.5	-1	0.7	1.3	1.1

In Table 6.2, the last three columns depict the safety factor  $F_p$  for each of the parameters  $p$  which for each of the three prototypes. The safety factor is defined by:

$$F_p = \left( \frac{D_p}{FR_p} \right)^N, N = \pm 1 \quad (6.1)$$

Where  $F_p$  is the safety factor for a parameter  $p$ ,  $FR_p$  is the functional requirement for that parameter,  $D_p$  is the actual measured value of the device (or device capability), and  $N$  corresponds to whether high values or low values of  $p$  are favorable. If high values of  $p$  are favorable (e.g., high stroke is favorable), then  $N = +1$ . If low values of  $p$  are favorable (e.g., low mass is favorable), then  $N = -1$ . Using this definition allows us to easily compare safety factors, and means that safety factors greater than 1 are preferred because they imply that the device performs better than required.

The comparison from Table 6.2 is presented graphically, in the form of a spider plot, in Fig. 6-8. Presenting the comparison in the form of a spider plot allows us to intuitively compare the various prototypes. In the spider plot, parameters for which  $N = -1$  (such as stroke length or mass) are plotted as reciprocals, so that values toward the outside of the “spider web” are favorable.

Hence, parameters for which the device trace lies outside of the red functional requirement trace represent a safety factor greater than one. Conversely, parameters for which the device trace lies inside the red functional trace indicate a safety factor

### Functional Requirements vs. Device Specs - Force-Controlled Probes

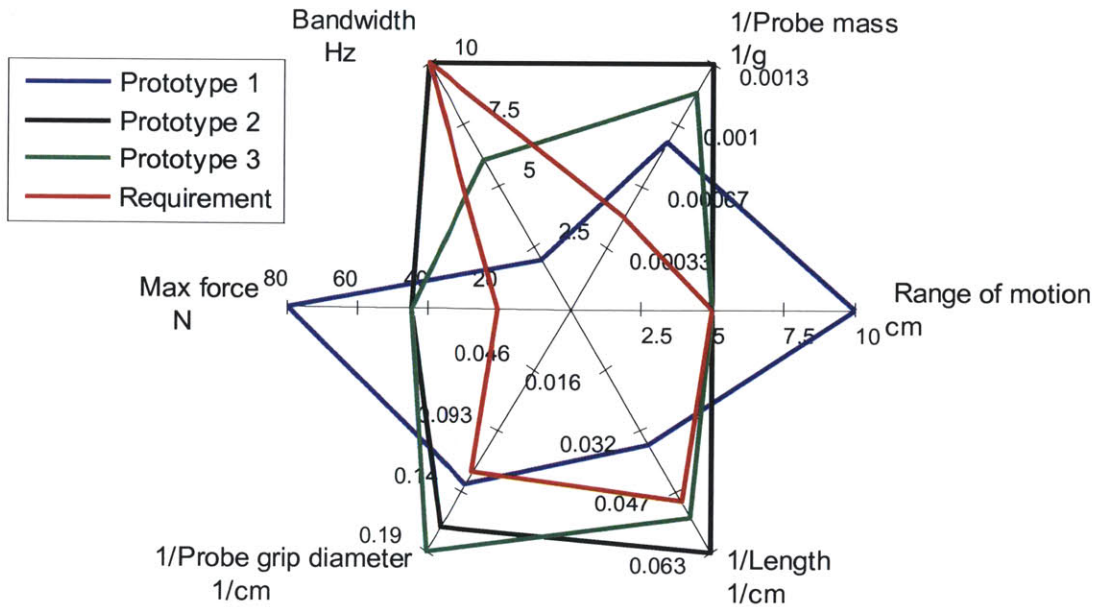


Figure 6-8: Spider plot comparing the functional requirements of Prototype 2 with the actual capabilities of each of the three prototypes.

of  $<1$ , an indication that the capability of the device did not fulfil the functional requirement.

In the plot, we see that the second prototype (black trace) fulfils all of the functional requirements, because the black trace lies outside of the red trace. Prototype 1 (blue trace) would not be suitable for the applications targeted with Prototype 2, because the length is too long. The high rotational inertia due to the large motor diameter of Prototype 3 (green trace) results in a lower bandwidth than that of Prototype 2.

## 6.3 Results

### 6.3.1 DMD Study: Early Results

In each of the DMD exams, images are acquired as a function of angle and contact force, in what are referred to as “angle sweeps” and “force sweeps,” respectively.

Angle sweeps and force sweeps are performed on six different muscle groups for each volunteer (healthy controls and DMD patients): quadriceps, biceps, deltoid, forearm flexor, tibialis anterior, and medial gastrocnemius. As discussed above, the long-term goal is to automatically evaluate disease severity in DMD patients. The short-term goal of the first phase of the study is to evaluate the ability to automatically classify subjects as healthy or DMD based upon the ultrasound images and the corresponding angles and forces.

Sisir Koppaka, a member of our group, demonstrated that, using a combination of image processing and force-correlated images (i.e., images that were acquired at known forces), high classification accuracy can be attained. The procedure, described in detail in [54],[55], is summarized here. In this procedure, 19 images are extracted from the 1 N to 10 N force sweep at specified forces, as illustrated in Fig. 6-9. Then, each of the 19 images undergoes an image processing procedure, which enhances the DMD-specific features, and consists of a box filter of different sizes, then pixel-wise standard deviation image, followed by the calculation of the average grayscale level for each image, as illustrated in Fig. 6-10. The output is thus a numerical array of mean grayscale level versus contact force. Next, a clustering algorithm is applied to classify the set of images as those from a control or a DMD patient.

Fig. 6-11 plots the classification accuracy for each of the muscle groups for different classification procedures. Accuracy is measured in terms of the Adjusted Rand Index [87], in which 0 corresponds to 50% classification accuracy (equivalent to flipping a coin), while 1 corresponds to 100% classification accuracy. The muscle abbreviations on the X-axis (Q, B, DEL, F, TA, & MG) correspond to the quadriceps, biceps, deltoid, forearm flexor, tibialis anterior, and medial gastrocnemius, respectively. Q1 & Q3 and B1 & B3 were repeat measurements acquired by the same sonographer; B1 and B2 were acquired by different sonographers. The various traces correspond to different classification procedures, and are described below:

- Independent EFB-Mode: Image processing applied; no knowledge of force
- Independent B-Mode: No image processing; no knowledge of force

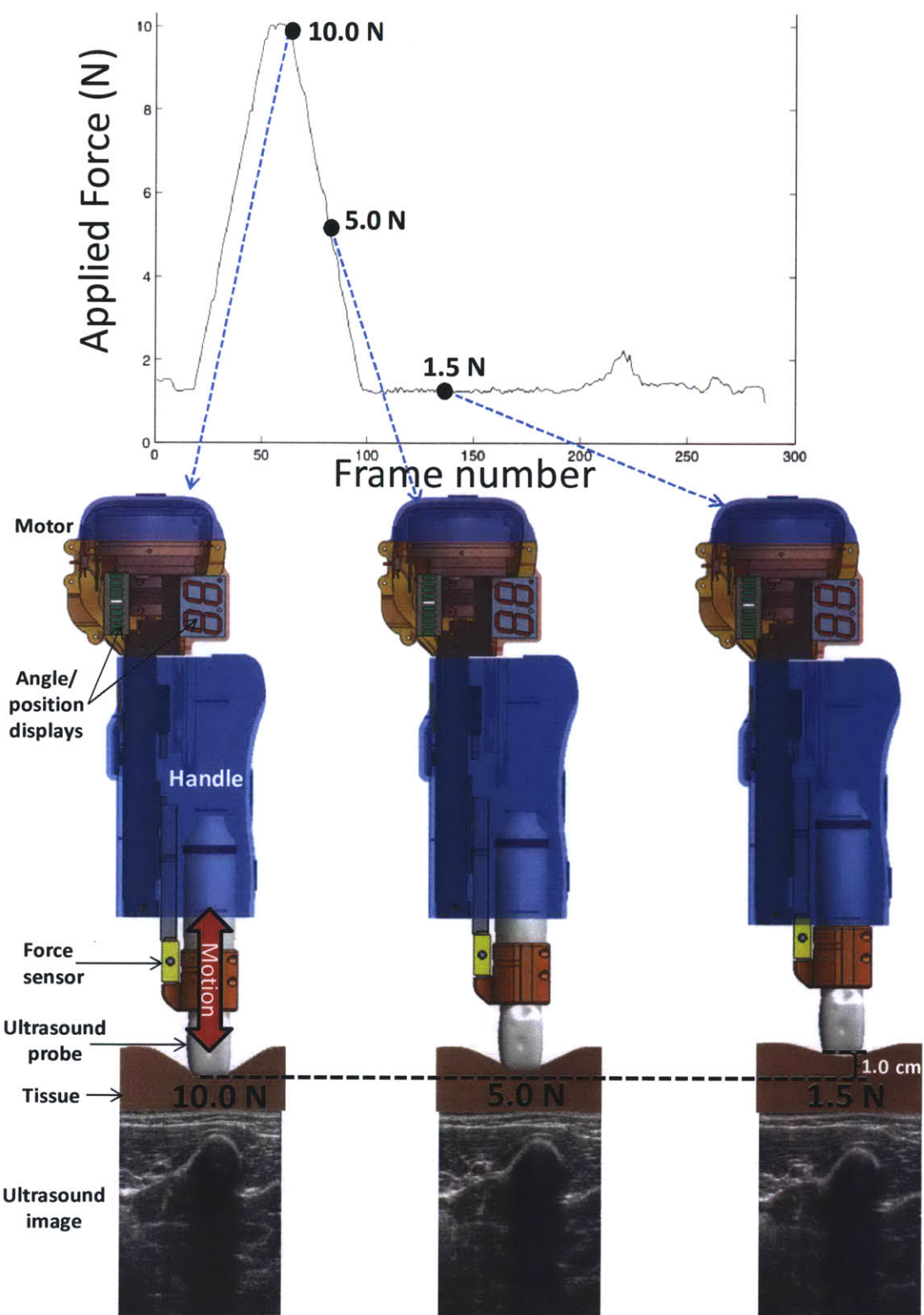
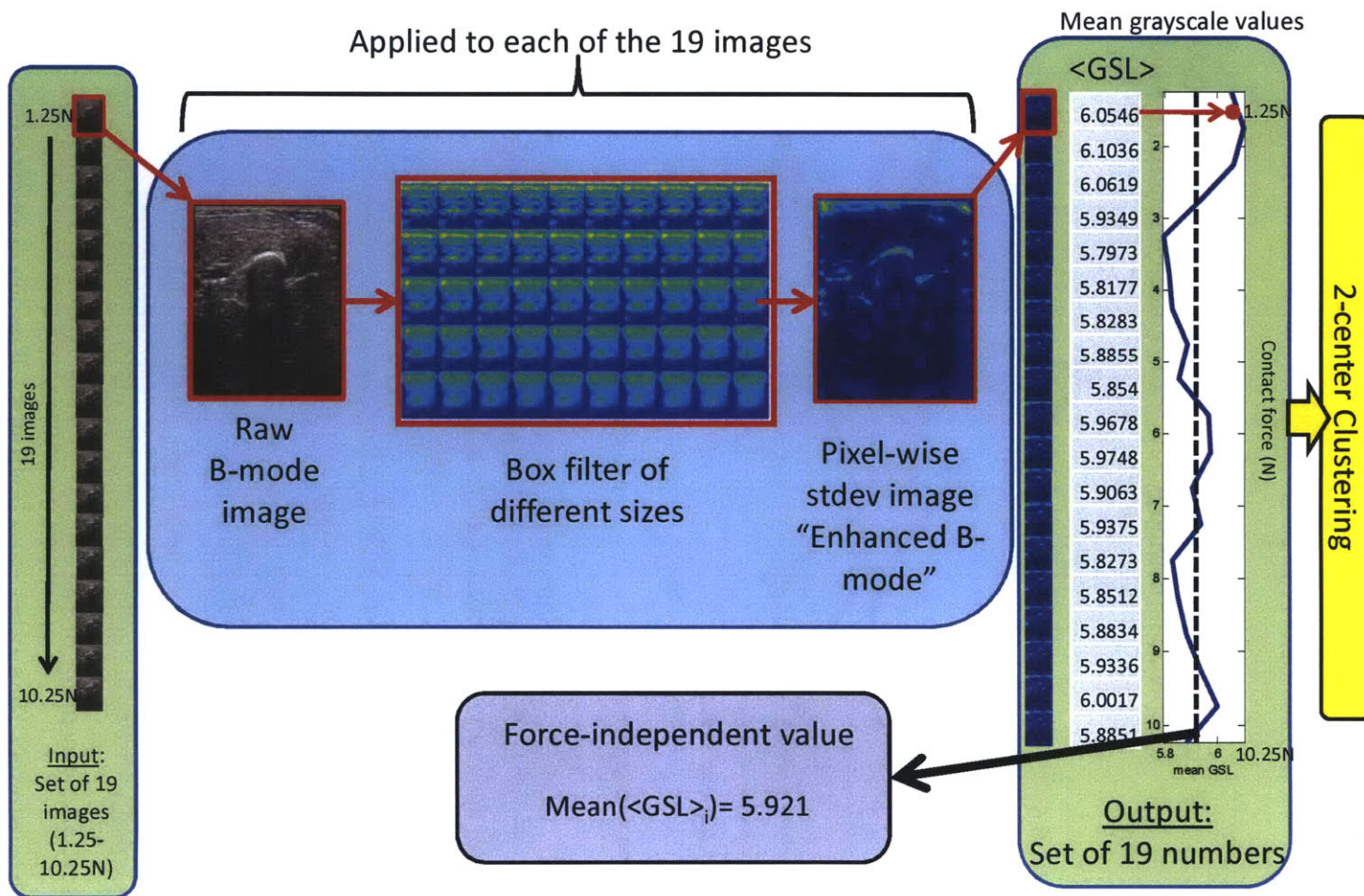


Figure 6-9: Illustration of the extraction of a series of ultrasound images at specified forces from the force sweep.

Figure 6-10: Illustration of the image processing steps applied to the images, described in [54] and [55]. The input is a sequence of 19 images taken at known forces; output is a binary decision: DMD or healthy.



- Force-correlated EFB-Mode: Image processing applied; forces are known
- Force-correlated B-Mode: No image processing; forces are known

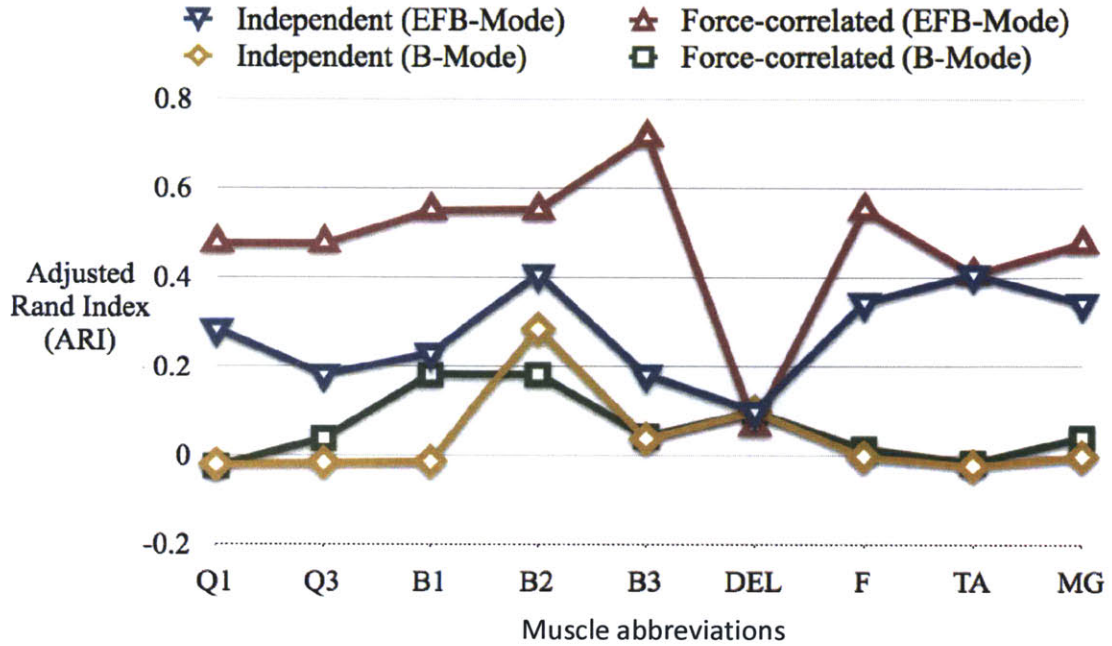


Figure 6-11: Classification accuracy for each of the muscle groups. Accuracy is measured in terms of the Adjusted Rand Index [87], in which higher values indicate higher classification accuracy. Plot borrowed from Koppaka et al [54].

In Fig. 6-11, we observe that classification accuracy is a function of the particular muscle group and classification procedure employed. In general, no image processing and no knowledge of contact force (yellow trace) gives lowest classification accuracy. Performing image enhancement (blue) improves classification, and adding knowledge of contact force to image enhancement (red) results in highest classification accuracy. DMD is equally distinguishable in nearly all muscle groups in force-correlated EFB mode, with the exception of the deltoid. One hypothesis is that DMD affects the deltoid less severely than other muscle groups. It is also evident that quadriceps-based classification is more repeatable than the deltoid, because Q1 & Q3 show less variation than B1 & B3.

These early data demonstrate that knowledge of contact force, combined with

image enhancement, can lead to improved accuracy in the automatic classification of DMD vs healthy patients.

## 6.4 User Feedback: Prototype 3

In this section, we present feedback and comments from users of Prototype 3, which could be incorporated in the design of a future prototype. As of May 22, 2014, Prototype 3 of the force-controlled has been in use for almost two years at Boston Children’s Hospital. During that time, more than 190 ultrasound exams have been performed (9 muscle-runs per exam) on 40 patients aged 2 to 15 years (22 DMD patients, 18 controls), by 10 researchers, with more than 32 hours of total device run time. Throughout the study, the users have provided feedback about the usability of the device. Whenever possible, we have worked to address their comments through modifications to the device, but some of the more significant modifications would require a redesign of the device. Below, we list some of the most critical feedback we that we have received about the system; this feedback could be incorporated in the design of the next prototype.

1. “The device is great because I don’t need to worry about the contact force, it applies the right force for me.”
2. The audible beep that the system provides at the end of the force sweep is very helpful, as is the beep whenever the orientation angle is <20 degrees or >20 degrees from vertical.
3. Users generally do not refer to the angle display or position display on the device because it is not always visible. To keep it within the range of motion, they instead focus on keeping the probe clamp at an approximately constant location with respect to the probe shell housing.
4. The cable protrudes too much and gets in the way when imaging workspace-constrained muscles like the biceps, especially on small subjects.

5. The probe is quite large when imaging small muscles on small kids, especially the biceps. Sometimes the probe face does not make complete contact with the tissue.
6. Occasionally, the probe vibrates. This seems to happen when contact is made with a bone.
7. Users quite frequently push the actuator to one of the travel limits. The device automatically resets, which can be frustrating.
8. It would be desirable if the system were more portable. The hospital is space-constrained and it is difficult to find a location that can store the entire cart (Fig. 5-12).

*Synthesis of user feedback:* Patient visits are often chaotic. Some patients, especially younger ones, tend to be less cooperative, and move around considerably during the entire one-hour visit. During each visit, a number of other studies are conducted, including electrical impedance myography [90]. By the time that studies are performed with the force-controlled probe during the last 5-8 minutes of each visit, there is often significant time pressure to finish the exam, in addition to an often reduced level of patient cooperativeness. Thus, the faster and more easily that the exam can be conducted, the better.

During each visit, one researcher typically operates the computer, while a second researcher operates the device and keeps the subject under control. For certain hand grips and in certain orientations of the probe, is it actually not possible to see the LED bar graph that indicates probe position or the 7-segment angle display. To compensate for this, users have discovered that it is easier to monitor the position of the actuator by observing the position of the probe clamp (labeled 8 and 9 in Fig. 6-5) with respect to the top and bottom protective shells (labeled 1 and 2 in Fig. 6-5).

The fact that the travel limits are often reached suggests that the “Soft Limits” strategy is not working as intended. In a qualitative comparison between Prototypes 2 and 3, it did indeed seem that it is easier to reach a travel limit with Prototype 3,

even though the same circuitry, controller, and gains are used for both prototypes. The likely cause for this is the fact that the motor employed in Prototype 3 has a significantly higher rotational inertia ( $50 \text{ gcm}^2$ ) than that of Prototype 2 ( $1 \text{ gcm}^2$ ). This means that, if the carriage is moving at a certain speed, it takes considerably more braking power to stop Prototype 3's motor than Prototype 2's motor, and could explain why Prototype 3 often exceeds the allowable constant-force range of travel. While the low-profile, high-diameter motor was chosen to make Prototype 3 smaller than Prototype 2 (by eliminating the pulley and reducing the motor length), the unexpected result is that it takes more power to accelerate and decelerate, and results in both a lower bandwidth and a greater tendency to exceed the travel limits.

Suggestions for the next prototype:

1. Use a motor with lower rotational inertia to enable faster system response, higher bandwidth, and reduced likelihood of reaching the travel limits.
2. Reposition the LED angle and position displays so that they are visible in any orientation of the device
3. Provide better strain relief of the motor cable, or use a motor with a more robust cable, as discussed in Section 6.1.3.
4. Use a smaller-diameter or more flexible cable, or change the cable exit point so that the cable does not interfere when imaging workspace-constrained areas.
5. Improve the robustness of the Soft Limits by better-tuning the position controller.

## 6.5 Conclusions

We have developed three compact, hand-held, actuated ultrasound probes that are capable of applying a programmable probe-patient contact force. This and the previous chapter presented data from studies conducted with Prototypes #2 and #3.

Experiments were performed with Prototype #2 to evaluate the impact of sonographer hand tremors upon the ability of the device to maintain a constant contact force. The force-controlled ultrasound probe was mounted to a “hand phantom” stage, which gripped the device with biologically-accurate stiffness and damping characteristics. The hand phantom was oscillated at frequencies ranging from 0.1 Hz to 30 Hz (frequency range of human hand tremor) while the force-controlled probe was placed in contact with a realistic tissue phantom and set to apply a constant force. Compared with a conventional ultrasound probe (not force-controlled), the force controlled probe attenuated hand tremor 33 times better at 0.1 Hz and 6 times better at 1 Hz. Because the human hand tremor frequency spectrum exhibits more than an order of magnitude greater motion amplitude at 0.1 Hz than at 10 Hz [62], the system is expected to provide sufficiently stable contact force to enable constant force in most clinical applications. The dynamic model, which included static friction in the case of the force-controlled probe, demonstrated close agreement with the magnitude data for frequencies below 16 Hz, the resonance frequency of the hand-probe system.

Tests were conducted to evaluate the effect of force control upon image stability. While imaging a tissue phantom that was moved in a biologically accurate manner, force control maintained the position of the top of a phantom inclusion with 75% less variation than with force control turned off. Fifteen user studies were performed to compare the ability of the system to maintain constant force with that of human operators. When force control was enabled, the contact force showed an average variation of 0.06 N; variation was four times higher with visual-based control and ten times higher with blind control.

The control scheme is designed to be intuitive to control and easy to use. By merging the control signals from both a position controller and force controller through a strategy called Endpoint Avoidance, the control system keeps the user centered within the device’s range of motion and handles making and breaking contact.

By controlling the probe contact force and thus the level of tissue deformation, the device is able to improve the repeatability of ultrasound imaging, leading to images that are easier to reproduce and compare. Because ultrasound is extensively used

to image soft tissues, improvements such as these to the usability and diagnostic capabilities of ultrasound imaging could lead to significant improvements in medical care.

## 6.6 Suggested Future Work

Suggested future work includes customizing the device for different ultrasound imaging applications. This device was designed to accommodate a general-purpose linear array probe and apply forces typical for abdominal and musculoskeletal imaging. We hypothesize that for other ultrasound imaging scenarios in which a smaller scan area, smaller probe, and lower force are required (carotid imaging, for example), direct-drive actuators such as voice coil actuators could be more appropriate, and would lead to a system with higher bandwidth that could enable determination of the mechanical properties of tissue. Force-controlled probe Prototype #3 is now being used in clinical research, and is being further developed.

Another potential extension of this work is to move to an image-based control scheme. In the current system, actuator position and contact force are controlled with the ultimate goal of providing a stable view of the tissue of interest at a measured, repeatable contact force. A different—and potentially more clinically valuable—strategy would be to perform closed-loop control around an image-based parameter, such as the diameter of an artery or centroid of an organ, as in Fig. 5-19. The organ centroid position, for example, could be calculated in real time from the ultrasound image, and a control system could actuate the ultrasound probe so as to keep the centroid position at a target value. This would ensure that the tissue of interest is imaged at the same amount of deformation, and could provide greater repeatability for longitudinal imaging. As this is outside the scope of the current research, we leave it for possible future work.

Finally, mechanical modifications could be made to the prototype, as discussed in Section 6.4, to improve the performance and ergonomics. Such modifications include the use of a motor with lower rotational inertia, a repositioning of the LED

feedback for improved visibility, as well as superior motor wire strain relief and cable management.

# Chapter 7

## The High-Speed Dynamic Imaging Probe

### 7.1 Summary

This section describes the mechanical design of and experiments conducted with a voice coil-actuated force-controlled ultrasound probe. Due to the direct-drive nature of the device, it is capable of translating the ultrasound probe with higher linear speed and higher bandwidth than the ball screw-driven force-controlled probe presented in Chapters 5 and 6. The device was used to measure the elastic properties of *in vivo* tissue via shear wave elastography. Results from these experiments, as well as the frequency response of the system, are presented and compared with the system model as well as the literature.

### 7.2 Introduction

It is well-accepted that there is a strong correlation between tissue elastic properties and tissue health [92]. Breast tumors are stiffer than surrounding tissue [92]. In hepatitis C, as the liver progresses through different stages of fibrosis, it stiffens; in stage F4 of the disease, the liver is 5 times stiffer than in stage F1 (20 kPa vs 4 kPa) [26]. Thyroid nodules, which can often be malignant, are stiffer than surrounding

tissue [85]. The underlying biological cause of tissue stiffening with pathology is still an active area of research, but it is hypothesized that the regulation and cross-linking of collagen within the extracellular matrix is a key factor [60].

Manual palpation has been used since ancient Egyptian times (first reported in 2100 B.C [39]) to qualitatively assess tissue stiffness. However, the value of manual palpation is limited due to its inability to investigate deep tissues and its qualitative nature.

It is possible to quantitatively measure the force-displacement characteristics of tissue via indentation test, similar to the Instron system. Equations exist to estimate the elastic modulus based upon the indentor shape and force/displacement characteristics [113]. When such techniques are adapted to measure the elastic modulus of *in vivo* tissue, it is desirable to keep the procedure as minimally-invasive as possible, which therefore constrains the test to the surface of tissue. However, since measurements are only taken at the skin surface, these techniques can only give estimates of the bulk properties of tissue. For the purpose of clinical diagnosis, it is more helpful to know the elasticity throughout the tissue.

A technique called ultrasound elastography, discussed in Section 7.3, was introduced by Ophir et al in 1991 [79], and can be used to measure the elasticity of tissue using ultrasound. The major benefit of this technique is that it can be used to non-invasively measure the elasticity throughout the continuum of tissue. More recently, commercial systems have been developed to perform elastography, and now all five major ultrasound vendors (GE, Philips, Siemens, Toshiba, Supersonic Imagine) have some type of elastography functionality.

However, the commercial elastography systems suffer from a number of drawbacks, including:

1. Low repeatability due to non-repeatable contact pressure and tissue non-linearity.
2. Low intra-platform repeatability due to differences in the elastography implementation across commercial systems.
3. Cautious, slow acceptance due to the relative newness of these techniques in

clinical practice.

Combined, these three drawbacks lead to reduced trust of the elasticity measurements. Even if ultrasound-based elastography systems assess questionable tissue as benign, clinicians frequently choose to perform a biopsy of the tissue to be on the safe side. Biopsy involves inserting a needle into the tissue of interest and removing sample cells, which are assessed for malignancy by a pathologist. However, biopsy, which can be painful and costly for the patient, is not without risk of complications, such as hemorrhaging and pneumothorax [83].

Given the significant diagnostic potential of elastography, improvements to the accuracy of elastography measurements could result in significant improvements in the quality of medical diagnoses. In the 2014 American Institute of Ultrasound in Medicine (AIUM) Convention, the lack of repeatability due to non-repeatable contact force (listed drawback #1 above) was discussed as a significant obstacle in the elastography technique. We believe that the force-controlled ultrasound probe could be used to overcome this obstacle.

The following sections begin with a description of the non-linear stress-strain characteristics of tissue and describe the implications of these nonlinearities upon elasticity estimates. Next, elastography techniques are discussed in more detail, followed by a description of the design of a high-bandwidth voice-coil driven force-controlled ultrasound probe which can be used to perform both constant force imaging and shear-wave elastography.

### 7.2.1 Tissue non-linearity

Many engineering materials exhibit linear stress-strain characteristics. A doubling of the strain, for instance, results in a doubling of the stress. However, for many biological tissues, such as ligaments and tendons, the stress-strain characteristics are nonlinear [56], as shown in Fig. 7-1. One hypothesis to explain the non-linearity is outlined by Kwan et al [56]: at low strains, collagen fibrils are undulated, and increasing stress causes the fibrils to straighten; once all of the fibrils are straightened,

the tissue stiffens dramatically.

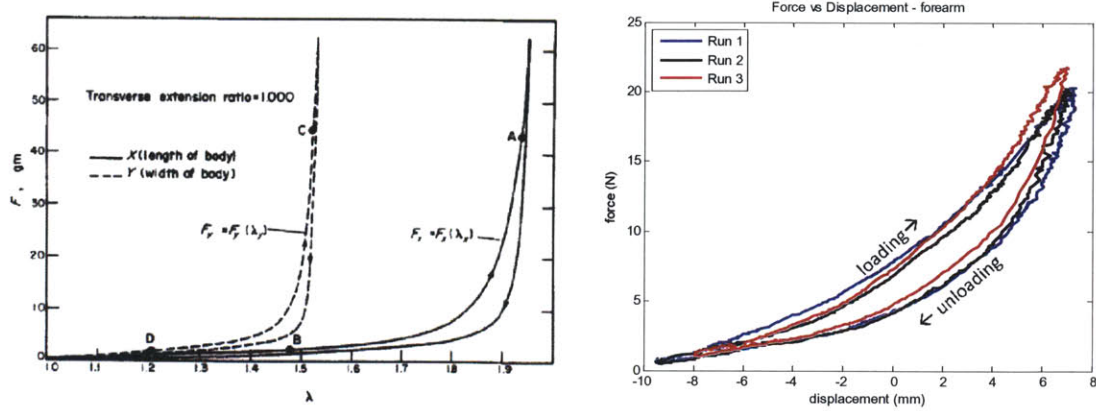


Figure 7-1: Non-linear force-displacement characteristics of human skin (left) [108] and the forearm of a human volunteer, as measured with the dynamic imaging probe (right).

The slope of the force-displacement curve is the tissue stiffness  $k$ , which translates to the elastic modulus  $E$ . The non-linear characteristics of these curves suggest that any estimate of the elastic modulus of tissue should also specify either the pre-load force (or the tissue displacement) at which the measurement was obtained. Said another way, the elastic modulus of the tissue is some nonlinear function of the preload force  $F$ , i.e.,  $E = g(F)$ . Specifying a single value for the elastic modulus, such as  $E = 50\text{ kPa}$ , is simply a single point on the  $E = g(F)$  curve.

This has significant implications for handheld elastography systems, which ascertain the elasticity of tissue via a handheld ultrasound scanner. Since the contact force applied by the hand is not measured and is not repeatable, the elasticity estimate is also not repeatable. For the most diagnostically-informative and repeatable elasticity measurement, the contact force should also be specified.

To investigate the elastic properties of tissue under different preload forces, experiments were conducted upon the quadriceps muscle of a human volunteer with the force-measuring ultrasound probe. A Supersonic Imagine 15-4 probe, which can estimate the elasticity of tissue using shear wave elastography (discussed in Section 7.3), was mounted to the force-measuring probe (Series 2) and the elasticity of a constant region of interest was estimated at preload forces ranging from 1.0 N to 18.0 N. The

results are shown in Fig. 7-2.

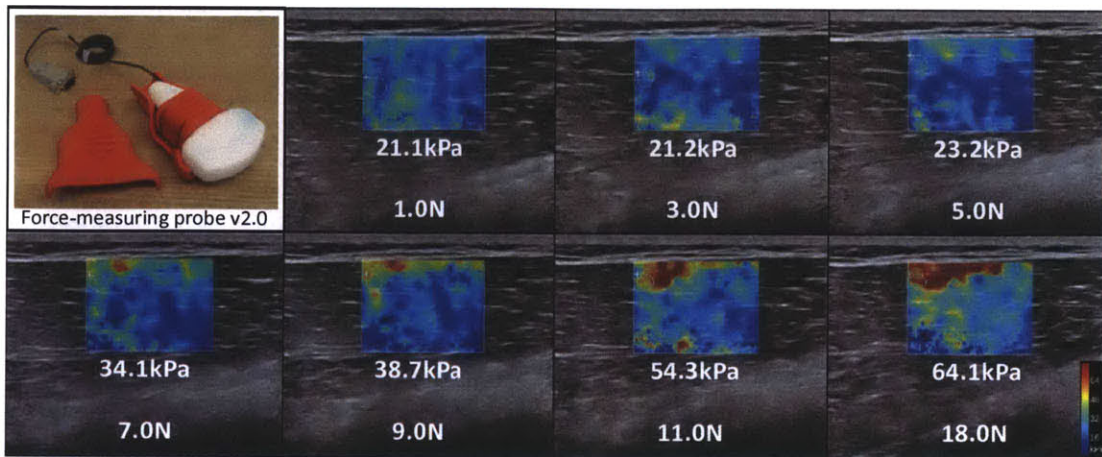


Figure 7-2: Elastic modulus measurements of the quadriceps at different preload forces. Force was recorded with the force-measuring probe; elastic modulus was calculated with the Supersonic Imagine 15-4 probe.

The colored region in the center of each of the seven images indicates the elastic modulus of the tissue (the colormap scale is the same for each image). Qualitatively, we can see that the superficial tissue layers are stiffer at higher forces, as indicated by the red colors at >9.0 N. For quantitative comparison, a common 3 mm diameter region of interest was selected in each image by our clinical collaborator, Manish Dhyani MD, the elastic modulus was estimated, and is recorded in the figure. We can see that the elastic modulus stayed constant at about 22 kPa for forces between 1 — 5 N, and began to stiffen as higher forces were applied. The elastic modulus at 18 N was 64.1 kPa —more than three times stiffer than the elastic modulus at 1 N.

To our knowledge, this is the first quantitative demonstration of the change in tissue elastic modulus as a function of preload force. The question arises: is this a real change in elasticity, or an artificial change due to biases our measurement? Based upon the non-linear stress-strain characteristics observed in ex vivo extension and in vivo indentation tests (Fig. 7-1), we believe this to be a real change in elastic modulus.

## 7.3 Elastography

In the next section, two commonly used elastography methods are discussed: strain based and shear wave-based.

### 7.3.1 Strain-Based Elastography

The simplest form of elastography is strain-based elastography, and is described by Ophir et al [79]. In the most basic implementation of the qualitative form of this technique, the ultrasound transducer is placed in contact with the tissue and a (non-measured) force is applied, causing the tissue to deform. The ultrasound image is captured. Then, a different force is applied and another image is captured. The two images are compared to each other and a strain map is calculated to estimate the relative motion of the tissue between the two frames. It is assumed that the tissue is under uniform stress. Therefore, the elastic modulus of the tissue ( $E$ ) can be calculated from the 3-dimensional form of Hooke's law, using the stress  $\sigma$  and strain  $\epsilon$ :

$$\sigma = E\epsilon \quad (7.1)$$

In the qualitative technique, since the stress is not measured, only the relative elastic modulus can be calculated. Assuming the probe is held in a fixed location, the relative elastic modulus can be estimated with higher accuracy by comparing multiple frames.

This technique is currently implemented in the GE, Philips, and Toshiba commercial ultrasound systems. On the ultrasound screen, the tissue is colored in a spectrum ranging from red ("Hard") to blue ("Soft"). The Philips system relies on natural patient and sonographer motion and does not require the sonographer to consciously vary the force.

### 7.3.2 Shear Wave-Based Elastography

Shear wave elastography (SWE) is a newer technique to quantitatively measure the elasticity of tissue. Pioneered by the Fink et al group at ESPCI Paris [94], [28], [93], SWE, sometimes referred to as “remote palpation,” involves inducing a mechanical vibration in tissue and measuring the speed at which the resulting shear wave propagates. Under several assumptions, the shear wave propagation speed is directly related to the elastic modulus of the tissue.

#### Shear Waves

Any vibration imposed upon a soft material induces both shear waves and compression waves. With compression waves, particle motion is in the direction of wave propagation; with shear waves, the motion is perpendicular to propagation direction. In soft media, such as tissue, compression waves travel at approximately 1540 m/s, nearly 3 orders of magnitude faster than shear waves, which propagate at 1-10 m/s. With a fast enough ultrasound scanner, it is possible to image the propagation of shear waves.

In ultrasound-based shear wave elastography, the ultrasound probe is held normal to the tissue and vibrated in the direction of tissue normality. Compression waves and shear waves are induced. From the perspective of a conventional linear-array ultrasound transducer, which typically has a frame rate of less than 30 frames/sec (the Terason T3000, for example, in abdominal imaging), the movement of the probe will appear as a simultaneous compression of the tissue. All tissue will move closer to the transducer; deeper tissues will move more than superficial tissues.

However, with an ultrafast ultrasound scanning system (i.e., greater than 200 frames/sec), it is possible to image the propagation of the shear wave. Along the edges of the probe-patient contact interface, shear waves are generated, which constructively interfere along the axis of the probe [94]. Therefore, from the perspective of the ultrasound transducer, due the interference of the shear waves and rotational symmetry of the geometry, shear waves will appear to propagate in the same way as a

lower-speed compression wave. I.e., it will appear as though a low-speed compression wave is propagating away from the probe. It is therefore possible to image shear wave propagation with the use of a sufficiently fast ultrasound probe.

### Tissue Modeling

The simplest 1-D tissue mechanical model is the Voigt model, consisting of a parallel spring and damper, as shown in Fig. 7-3.

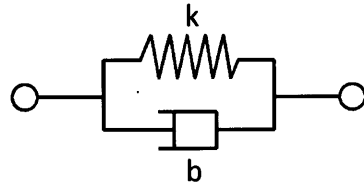


Figure 7-3: The Voigt body, consisting of a simple parallel mass spring system, is the simplest realistic tissue model.

In a continuous medium such as tissue, the stiffness  $k$  translates to elastic modulus  $E$ , and damping  $b$  translates to viscosity  $\eta$ . The field of elastography concerns the measurement of  $E$ . There has been recent work to ascertain tissue viscosity as well and it is hypothesized that tissue health is correlated to viscosity [27],[30],[73],[52], and [116]. For the force-controlled ultrasound probe, we leave this application as the subject of future work.

Shear waves can be induced by mechanically exciting tissue at a frequency  $f_s$  using an indentation system. The mechanical properties of soft media are related to the shear wave propagation speed based upon the following equation [28]:

$$V_s = \sqrt{\frac{2(\mu_1^2 + f_s^2 \mu_2^2)}{\rho (\mu_1 + \sqrt{\mu_1^2 + f_s^2 \mu_2^2})}} \quad (7.2)$$

Where  $V_s$  is the shear wave propagation speed,  $\mu_1$  is the shear modulus,  $\mu_2$  is the shear viscosity,  $f_s$  is the frequency of excitation, and  $\rho$  is the tissue density (typically  $1100 \text{kg/m}^3$  for soft tissue).

If the indentation frequency is sufficiently high, the frequency dependence can be ignored from the shear wave velocity calculation, as shown in Fig. 7-4.

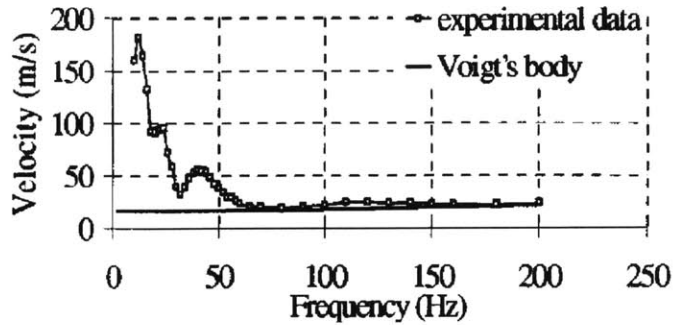


Figure 7-4: Plot from Catheline et al (1999) [28]. Shear wave velocity measurements vs. frequency for beef muscle tissue, demonstrating that velocity levels out above about 60 Hz.

Fig. 7-4 demonstrates that above about 60 Hz, the frequency dependence of the excitation can be ignored. It is worth noting that, while shear waves still propagate at frequencies below 60 Hz, propagation speed is much higher, and requires the use of highly-developed custom ultrasound imaging systems. At frequencies higher than 200 Hz, shear waves are highly attenuated and become difficult to image in deeper tissues [28]. It is therefore advised that, for the sake of imaging and computational simplicity, indentation should be kept between 50 Hz and 200 Hz. A single period of a 50 Hz sinusoid is typically used in the literature [94].

Furthermore, if tissue is assumed to have negligible viscosity (an assumption typically made in the literature [94]), the elastic modulus is directly related to the shear modulus by

$$E = 3\mu_1 \quad (7.3)$$

Combining Equations 7.3 and 7.2 with these assumptions, the elastic modulus can be directly determined from the shear wave propagation speed and density by

$$E = 3\rho V_s^2 \quad (7.4)$$

Therefore, the technique to generate a shear wave is as follows:

1. Place the ultrasound transducer in normal/orthogonal contact with the tissue<sup>1</sup>.

---

<sup>1</sup>It has been shown that transducer diameters less than 4 cm are all approximately equivalent

2. Vibrate the probe with a frequency between 50 Hz and 200 Hz.
3. Image with a speed greater than 500 Hz.

### **Acoustically-generated shear waves**

The previous section described the generation of shear waves due to mechanical vibration of the ultrasound probe. It is worth noting that shear waves can also be generated with acoustic vibration; in this technique, high-intensity focused ultrasound is generated with the ultrasound transducer and directed at the tissue of interest for a short period of time [22]. The tissue vibrates, and the movement of the tissue is recorded with a high-frame rate ultrasound system; the technique is also referred to as “acoustic radiation force imaging” (ARFI)[74]. The appealing aspect of this method is that the ultrasound transducer is used for both shear wave generation and imaging, obviating the need for a mechanical vibration system. This technique is implemented in both the Siemens and Supersonic Imagine ultrasound systems.

However, ARFI imaging systems are considerably more expensive than conventional systems. The appeal of the mechanical-induced vibration approach is that it can be implemented on less-expensive ultrasound systems.

## **7.4 High-speed dynamic imaging probe: mechanical design**

In this section, we describe the design of the high-speed dynamic imaging probe. The overall objective was to develop a handheld force-controlled ultrasound probe with sufficiently high bandwidth, power, and speed capabilities to generate shear waves and also apply constant contact force. The design objectives for the system are listed below.

1. Can generate shear waves

---

with respect to shear wave speed, so nearly all ultrasound transducers will work.

2. Can image shear waves
3. Can apply constant force
4. Handheld

In order to design the device, these qualitative objectives must be converted into a set of quantitative functional requirements. Objectives #1 and 2 can be quantified from a search and analysis of the literature; Objectives 3 and 4 can be quantified based upon the experience of designing the ball screw probe.

1) Ability to generate shear waves:

From the discussion in Section 7.3.2, the typical literature method to mechanically generate shear waves is to apply one period of a 50 Hz sine wave at the surface of the tissue. Typical motion amplitudes are 0.7 mm [94].

The objective of this device is to generate shear waves at different preload forces in order to explore the stress-dependent elastic modulus of tissue. The range of capable preload forces should therefore span a range in which tissue exhibits nonlinear properties. Based upon the results of Fig. 7-2, in which the quadriceps was loaded with forces from 1 N to 18 N and exhibited nonlinear characteristics, we therefore require the high-speed dynamic imaging probe to apply up to 20 N for short durations.

2) Ability to image shear waves:

Due to the fast dynamics of the shear wave, ultrasound imaging systems from the literature operate at rates ranging from 500 Hz [94] to 20,000 Hz [31]. What speed is necessary for our system? Maximum shear wave speed in muscle is about 10 m/s [94], which means that the wave would propagate across 10 cm of tissue (typical maximum depth of an ultrasound probe) in 10 ms. For minimally-acceptable measurement quality, assume that we would like to image the 10 ms propagation with 5 frames, which translates to 2 ms/frame. Therefore, the minimum acceptable frame rate would be 500 frames/sec. Imaging shallower depths would require faster imaging speed; imaging slower shear waves (thus softer tissue) would be better-sampled at this frame rate. Therefore, we place upon the ultrasound imager the functional requirement to image at approximately 500 frames/sec.

### 3) Ability to apply constant force:

The objective to apply a constant force translates into a number of specific functional requirements. Specifically, this influences the necessary range of motion, maximum force capabilities, bandwidth, and power requirements.

Range of motion: During operation, in order to apply constant contact force, the device must stay within its range and away from the travel limits, as discussed in Section 5.9. As described previously, we hypothesize that the necessary stroke length is positively correlated with the characteristic scan length of the device (this is proven later in Section 2.2). In the case of the ball screw probe, which was designed for musculoskeletal imaging, the typical characteristic scan length was approximately 15 cm. In user tests, the range of motion of the device was found to be just sufficient at 50 mm. With the dynamic imaging probe, which will be used primarily for imaging small regions (for example, holding stationary while launching shear waves), we can therefore relax the 50 mm stroke length requirement, and hypothesize that a stroke length of 25 mm will be sufficient in this case.

Bandwidth: To induce shear waves, the system must move with at least  $\pm 1$  mm at 50 Hz. Based upon Fig. 7-4, shear wave speed levels off at about 60 Hz; so, in order to operate with a comfortable safety factor, we require that the system be able to produce measurable motion at 100 Hz.

Power: Perhaps the second most important functional requirement after stroke length, the power requirement helps to inform selection of the actuator, the key component of the system. As with the ball screw probe, the dynamic probe must also supply enough power to overcome both static force and hand tremors, with the additional requirement that it must be able to induce shear waves at 18 N. From Equation 2.11, the necessary maximum power the system must supply is given by the following equations:

$$P = P_{static} + P_{rms} \quad (7.5)$$

$$P = R(KF_{applied})^2 + \frac{m_{eff}A^2\omega^2}{2\sqrt{2}} \quad (7.6)$$

Table 7.1: Functional requirements for the dynamic imaging probe

Parameter	Value
Stroke	>25 mm
Max continuous power	ball screw: >500 W; voice coil: >15 W
Motion	> ±1mm at 50 Hz
Bandwidth	>100 Hz
Imaging rate	>500 frames/sec
Mass	<1 kg
Size	Max length <15 cm; max girth (diameter) <6 cm
Max force	>20 N

Assume, for instance, that the system needs to move a 100 g ultrasound probe with amplitude 1 mm, at a frequency of 100 Hz, while applying a static force of 8 N. By Equation 2.11, a ball screw actuator would need to supply more than 500 W, while a voice coil actuator would only need to supply about 15 W. This already offers some insight into which actuator would be appropriate.

#### 4) Handheld:

The need to be handheld places requirements upon the mass, shape, and size of the device. These requirements were previously explored with the ball screw probe, and are the same for this device.

The functional requirements and quantitative values are shown in Table 7.1.

### 7.4.1 Design parameters: component selection

In this section, the selection of the components based upon the functional requirements is discussed. The important components to select are the actuator, linear motion constraint, position measurement device, and force sensor.

Actuator: Based upon power requirements alone, we can almost immediately determine that the voice coil is the most appropriate actuator.

Linear motion constraint: Based upon a search of the available integrated voice coil actuator/linear bearing products, few are the appropriate factor to be handheld. Therefore, we choose to use our own linear ball bearing to constrain motion in the linear direction.

Table 7.2: The most critical design parameters for the dynamic imaging probe.

Subsystem	Selected component
Actuator	Voice coil
Position measurement	linear potentiometer
Linear motion constraint	linear ball bearing
Force sensor	single-axis load cell
Ultrasound probe	Terason 7L3V

Position measurement: Commonly-used instruments include capacitive sensors, linear potentiometers, and LVDTs. Due to its simplicity and cost-effectiveness, the linear potentiometer is selected.

Force sensor: Options include pressure sensors, and single or multi-axis load cells. The single-axis load cell employed in the ball screw probe performed acceptably, therefore we choose to use it in the dynamic imaging probe.

Ultrasound probe: Choices include a linear array probe or a single-element probe. Based upon early experiments (discussed in Section 7.8), it appeared that the Terason linear array probe would fulfill the >500 frames/sec functional requirement. Therefore, we chose to use the Terason 7L3V probe.

Based upon this discussion, a summary of the important design parameters is shown in Table 7.2.

The next step in the design process is the selection of the specific components to satisfy the functional requirements.

Voice coil: The primary suppliers of linear voice coil motors are Moticon, H2W Technologies, and BEI Kimco; more than 100 voice coil motors from the three companies were considered. A design spreadsheet was created to compare the motors based upon the functional requirements of max continuous power, stroke, mass, size, bandwidth, and maximum force. The Moticon LVCM-038-038-01 was selected because it fulfilled the functional requirements the best.

Linear potentiometer: The Honeywell MLT-F38000201 linear potentiometer, with about 25 mm range of motion, was selected.

Linear bearing: The dynamic probe will primarily be used to scan at a particular location, and is not expected to be used in lateral scanning. Therefore, the pitching,

rolling, and yawing torque requirements from the ball screw probe can be relaxed somewhat. The linear ball bearings available from McMaster were investigated and several possible candidates were considered. Based upon the bearing geometry and the likely positioning of the components, the maximum continuous pitching torque the bearing would have to support was calculated to be approximately 0.6 Nm. With a more than 10x safety factor, to account for possible collisions, the 10 mm-wide #9706K1 was selected.

Single-axis load cell: The load cell must be able to measure up to 20 N. We choose the Futek LSB200 which can measure up to  $\pm 45$  N and withstand up to  $\pm 400$  N.

## 7.5 Dynamic imaging probe: Versions 1 and 2

Two versions of the dynamic imaging probe were created. The first employed the Terason linear array probe; the second, which addressed a number of the limitations of Version 1, employed an Olympus single-element ultrasound probe. Version 1 is discussed first.

### 7.5.1 Version 1

With the important components chosen, the next step in the design of the device was to layout the components to minimize size and ensure that the device fits ergonomically in the hand. The system was designed with SolidWorks. A photo and image of the solid model for Version 1 of the dynamic imaging probe are shown in Fig. 7-5.

Using the 3D scan data for the probe, as described in Section 3.3.2, the probe clamp was printed from ABS plastic, as were all of the other blue components in the figure. Views of the device from different angles are shown in Fig. 7-6.

The device was used in the experiments described in Section 7.9.1, in which the probe was translated, under position control mode, at a certain frequency relative to the imaging frequency. These early experiments uncovered a number of limitations with Version 1 of the device:

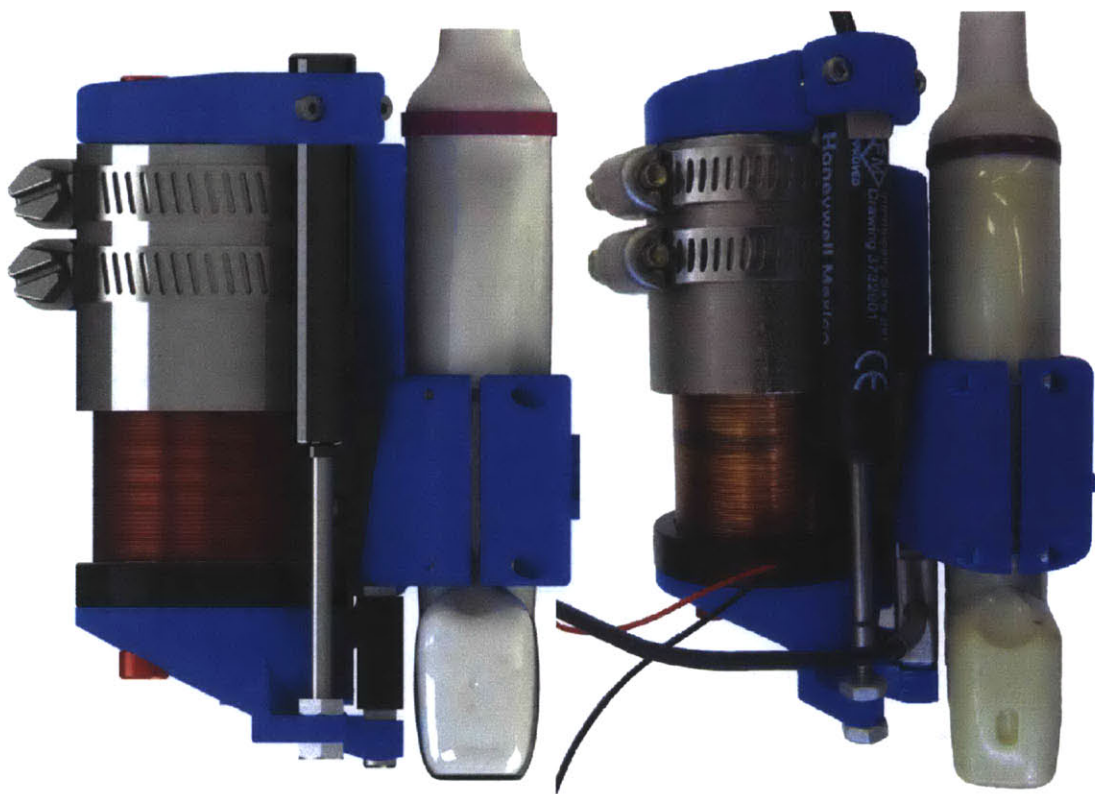


Figure 7-5: The dynamic imaging device, Version 1, which was designed to accommodate the Terason 7L3V linear array probe. Solid model (left) and photo (right). Due to spherical distortion of the camera lens, the photo (right) appears warped compared to the solid model.

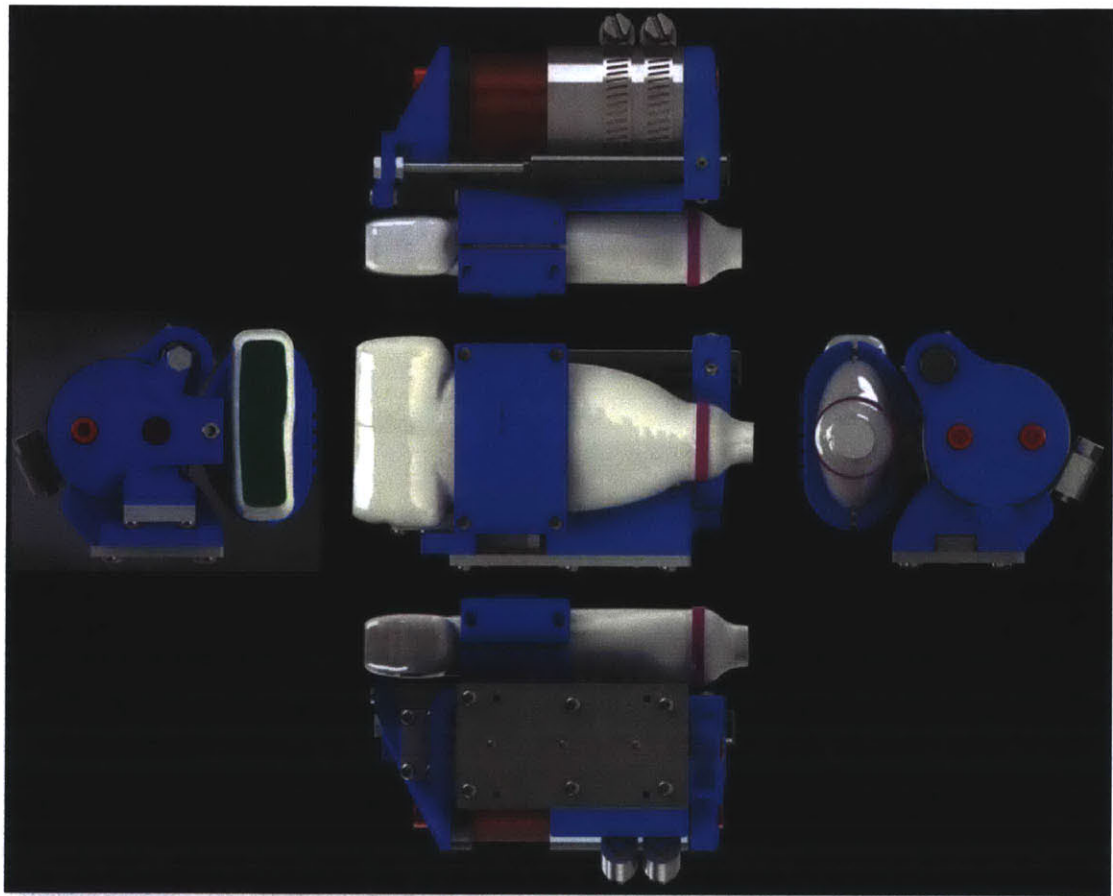


Figure 7-6: Views of Version 1 from the front, sides, top, and bottom.

1. The linear-array probe could not be used to image shear waves (discussed at length in Section 7.8).
2. The linear potentiometer was kinematically-overconstrained, which placed high stresses on the components and significantly increased the motion resistance due to friction.
3. The 3D printed probe mount was not sufficiently stiff. With the mass of the probe and the stiffness of the mount, motion frequencies of around 10 Hz excited a resonance, and the probe would oscillate with high amplitude in the pitching direction. This would also cause the imaging plane to rotate, which, given the need for image consistency, was unacceptable.

### 7.5.2 Version 2

The decision was made to move towards a single-element ultrasound probe, and to address limitations 2 and 3, with the design of a new prototype, referred to as “Version 2.” A photograph and solid model rendering of Version 2 are shown in Fig. 7-7.



Figure 7-7: Solid model rendering (left) and photo (right) of the dynamic imaging probe, Version 2, designed to accommodate a single-element Olympus ultrasonic transducer, and to address the limitations of Version 1.

Views of the device from various directions are shown in Fig. 7-8. An exploded view of the device is depicted in Fig. 7-9. The components annotated in Fig. 7-9 are

discussed in Table 7.3.

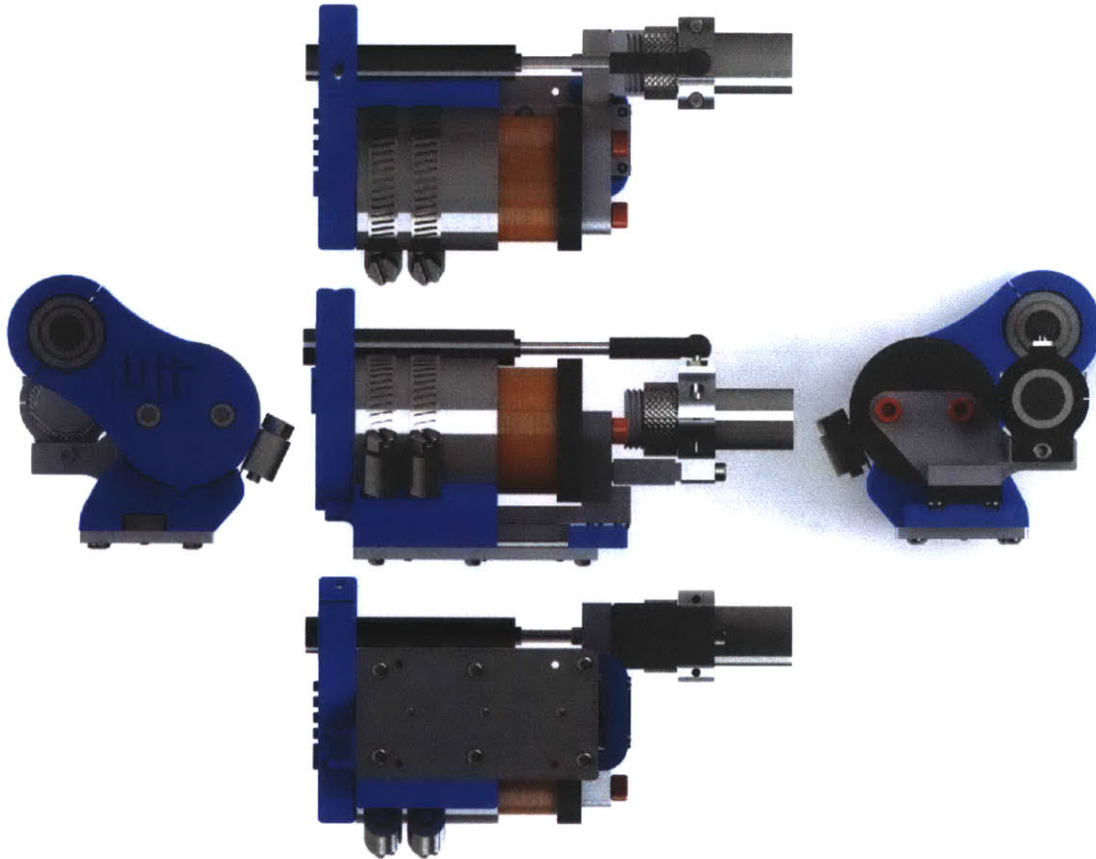


Figure 7-8: Views of Version 2 from the front, top, back, bottom, and sides.

Improvements over Version 1:

1. Adapted the device to accommodate single-element Olympus transducer for high-speed imaging.
2. Provided proper kinematic constraint for the potentiometer. Due to fabrication tolerances, it is not possible to perfectly align the extension/retraction axis of the linear potentiometer with the motion axis of the linear bearing. Therefore, as the potentiometer extends and retracts, both the stationary and moving halves of the potentiometer must be able to move in pitch, yaw, and roll DOFs. The preloaded spherical bearing (2) and the ball/socket joint (preloaded by the clip (12)) permit backlash-free properly-constrained mounting of the linear

Table 7.3: Descriptions of the components of Version 2

Component number	Description	Purpose	Part number
1	Linear potentiometer	Outputs analog voltage proportional to position of probe	Honeywell MLT-F38000201
2	Preloaded spherical bearing	Mounts to one end of linear potentiometer, permits motion in 3 rotational DOFs	McMaster 63195K67
3	Hose clamps	Attach voice coil magnet to cradle (4)	McMaster 5388K26
4	Magnet cradle	Holds voice coil magnet	3D printed
5	Linear bearing rail	Constrains motion in linear direction	McMaster 9706K1
6	Voice coil magnet	Provides resistive/ attractive force to voice coil (7)	LVCM-038-038-01
7	Voice coil	Interacts with magnetic field of permanent magnet (6) to move the stage	LVCM-038-038-01
8	Bumper	Prevents linear bearing from derailing	3D printed
9	Load cell	Converts contact force to an analog voltage	Futek LSB200
10	Linear bearing carriage	Constrains motion in linear direction	McMaster 9706K1
11	Single-element ultrasonic transducer	Images the tissue of interest	Olympus V326-SU
12	Ball/socket preload clip	Provides preload force to linear potentiometer's ball and socket joint, eliminating backlash	Made from a binder clip
13 & 14	Ball & socket	Permits proper kinematic constraint of the linear potentiometer, allows 3DOF rotational motion	Tower hobbies
15	Voice coil to load cell mount	Provides rigid between load cell and voice coil	Machined & waterjetted from aluminum
16	Ultrasound transducer clamp	Rigidly couples the ultrasound probe to the load cell	Machined & waterjetted from aluminum
17	Potentiometer mount	Clamps around spherical bearing, connects it to stationary portion of device	3D printed
18	Mounting base-plate	Connects all stationary components of the device	Machined from aluminum

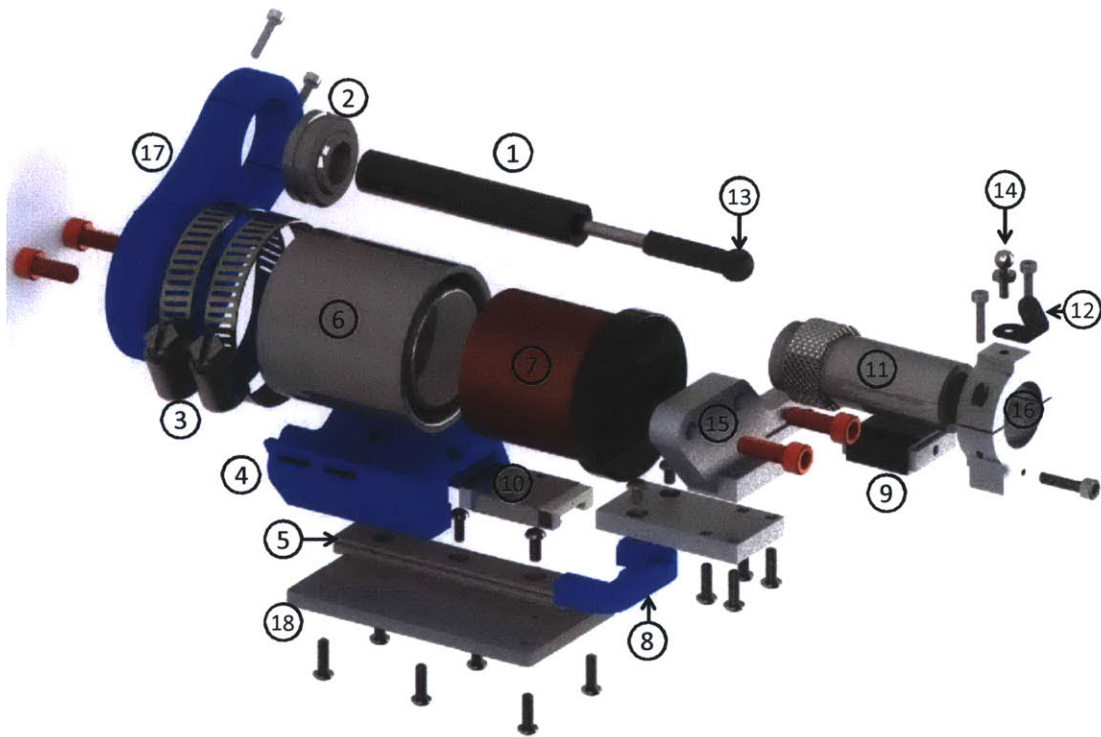


Figure 7-9: Exploded view of Version 2. Labels are discussed in the Table 7.3.

potentiometer. (Note: a suggestion for future work would be to use flexures instead of ball and socket joints in order to simplify the design.)

3. Significantly stiffened force path between the voice coil (point at which effort force is applied) and tissue contact point (at which resistive force is applied) with machined aluminum components. These components do increase the moving mass of the system, but permit sufficient bandwidth for shear wave generation, as discussed in Section 7.9.1.

A comparison between the functional requirements and the actual system specifications is described in Section 7.10.

## 7.6 Dynamic imaging probe: control and modeling

This section discusses the control system implemented to control the motion of the dynamic imaging probe. The second half of this section presents work in modeling

the system, and compares the model with the measured frequency response.

### 7.6.1 Control

The dynamic imaging probe is designed to be used in both position control and force control modes; position is measured with the linear potentiometer while force is measured with the load cell. As discussed with the ball screw-driven probe, since the device has only one DOF, and because force and displacement are coupled when the device is in contact with tissue, it is only possible to control one of these two parameters at a time. When imaging at a specified preload force, force control is operational; when indenting the tissue with a specified position trajectory, position control is active. In both cases, force and displacement can be measured at high speeds because the output voltages from the sensors are both analog.

To control the system, basic PID control was implemented in both force and position control modes. A block diagram of the control loop is shown in Fig. 7-10.

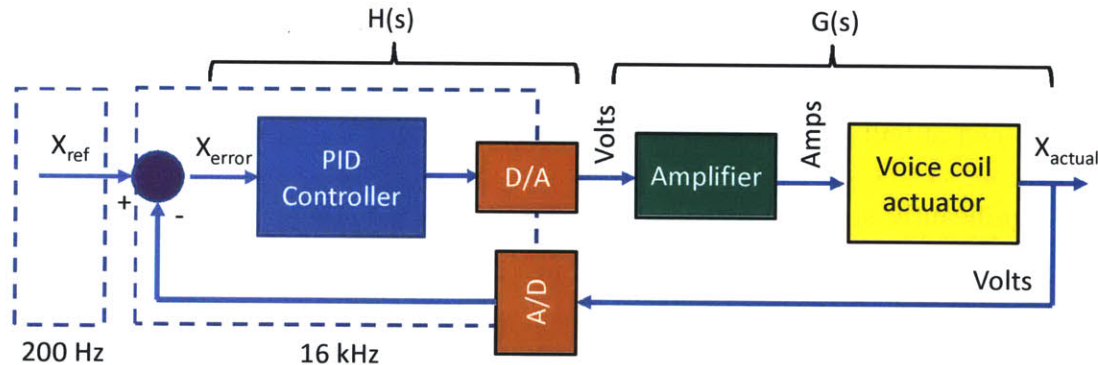


Figure 7-10: Block diagram of the control loop implemented for force and position control modes. In this figure, “X” can represent either position or force.

The target position or force,  $X_{ref}$ , is input on the left side of the diagram; the signal is compared with the actual value  $X_{actual}$  and the resulting error,  $X_{error} = X_{ref} - X_{actual}$ , is sent to the PID controller. The PID controller acts upon  $X_{error}$  to generate a command signal (in counts), which is converted to an analog voltage via the digital-to-analog converter (D/A). The resulting signal is passed to the Copley Controls ADP-090-09 amplifier, which acts as a voltage-controlled current source,

converting the input voltage to an output current. The current is sent to the voice coil, which results in a position or force with voltage  $X_{actual}$ . The signal  $X_{actual}$  is passed through an A/D converter into the digital domain.

As with the ball screw probe, control is implemented on the National Instruments PXI-7358 motion control card, with a loop rate of 16 kHz. Controller parameters, such as the PID gains and the desired position (or force) are input using LabVIEW, with a maximum update rate of about 200 Hz. This control architecture presents a bit of a challenge, because the desired position/force,  $X_{ref}$ , can only be changed at 200 Hz. If the probe must move sinusoidally at a rate of 50 Hz, this means that only 4 points per sinusoidal period can be loaded to the target trajectory, which would result in unacceptably coarse motion. A different control strategy is needed to move the probe at high frequencies. (Alternatively, a more flexible control architecture could be implemented, such as an FPGA, but we leave that as the subject for future work.)

The shortcoming introduced by the 200 Hz  $X_{ref}$  update rate limitation can be overcome by inserting a summing junction into the feedback path that adds a reference voltage  $V_{ref}$  to the feedback voltage, while holding  $X_{ref}$  fixed, as shown in Fig. 7-11. This is analogous to inserting a disturbance input. As long as  $X_{ref}$  is fixed and  $V_{ref}$  is selected with consideration of the A/D gain of  $2^{16}$ cts/volt, this technique is equivalent to varying  $X_{ref}$  alone as in Fig. 7-11.

The physical implementation of this technique consists of constructing a summing op amp circuit, which adds the raw force/position sensor voltage to the voltage output by an HP 33120A function generator. Because the function generator permits total control of the output waveform's characteristics, including frequency, amplitude, phase, burst count, and waveform shape, it allows superior control over the reference voltage for the control loop, and enables evaluation of the frequency response of the system, as described in the next section.

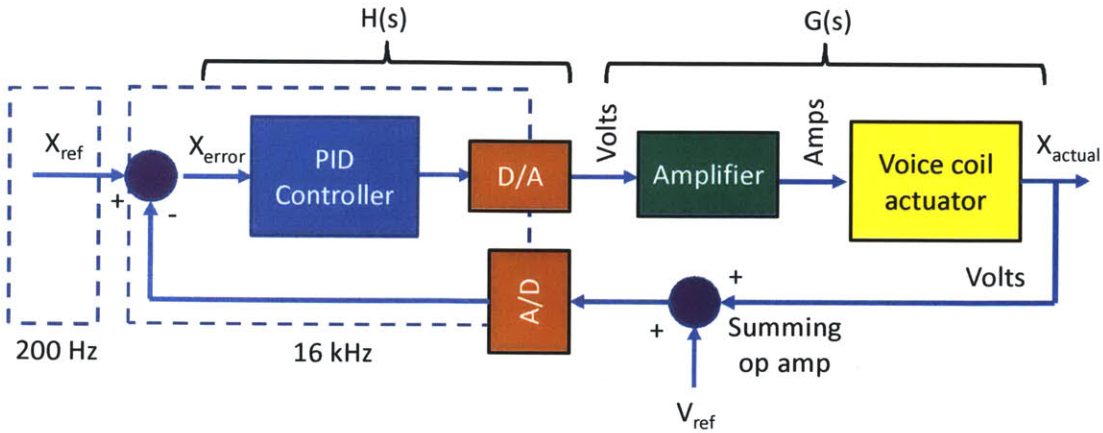


Figure 7-11: The addition of a reference voltage in the feedback path enables superior control over the target position/force and is used to measure the frequency response of the system.

## 7.7 Modeling and Simulation

The dynamics of the system are influenced by both the mechanical and electrical components. The mechanical components of the complete model and reduced-order model are presented in the next section, while the model of the electrical system is discussed in Section 7.7.2. The frequency response of the system operating under position control is presented in the last section, and is compared with the combined electro-mechanical model.

### 7.7.1 Mechanical model

A model of the mechanical components when the device is grasped by the sonographer and placed in contact with the patient is shown in Fig. 7-12.

As with the ball screw probe, the sonographer hand grip, located at position  $x_1$ , consists of stiffness  $k_1$  and damping  $b_1$ , and has the same values presented in Section 5.6.1. The voice coil of mass  $m_c$  (includes total moving mass: voice coil, probe, load cell, mounting hardware, etc.) pushes against the magnetic field of the permanent magnet of mass  $m_m$ , located at position  $x_2$ , with a force  $F_a$ , and is resisted by the reaction force  $F_r$  of the tissue (measured by the load cell), which has stiffness  $k_2$  and damping  $b_2$ . The resulting position of the voice coil is  $x_3$ . The system has

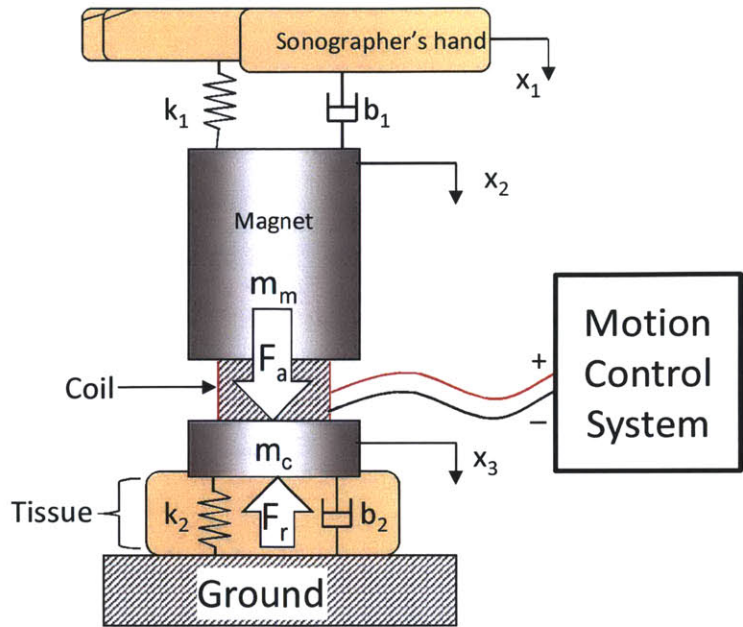


Figure 7-12: Mechanical model of the dynamic imaging probe

three moving masses: sonographer's hand, magnet, and voice coil/moving masses; and has six states: the positions and velocities of each of the three moving masses.

As a first step in evaluating the model, the experiments were performed on a reduced version of the system. In these experiments, the magnet was rigidly affixed to a table, which fixed the position  $x_2$  and eliminated the sonographer grip dynamics. The probe was allowed to vibrate in free air, which eliminated the tissue dynamics. In this reduced system, the only moving mass is  $m_c$ , which is the lumped mass of the voice coil, force sensor, ultrasound probe, and mounting hardware. The system has two states: the position and velocity of the voice coil,  $x_3$  and  $\dot{x}_3$ . The electrical system (discussed in the next section) delivers a voltage and a current to the voice coil, which results in a force  $F_a$ . The interaction of  $F_a$  with the mechanical components is described by the simple Equation 7.7:

$$F_a(t) = m_c \ddot{x}_3(t) \quad (7.7)$$

### 7.7.2 Electrical model

In the literature [58], the voice coil is modeled with inductance  $L$  and resistance  $R$ . The voice coil delivers a back EMF voltage  $V_{BEMF}$  as it moves; the relation is described by:  $V_{BEMF}(t) = K_V \dot{x}_3(t)$ , where  $K_V$  is the back EMF constant (units: volts/(m/s)). The back EMF voltage is represented as a dependent voltage source, and the electrical system model of the voice coil is shown in Fig. 7-13.

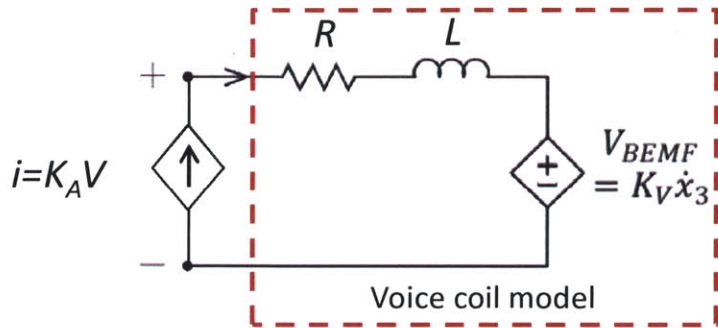


Figure 7-13: Electrical model of the voice coil [58], shown within dotted red line on the right. The Copley amplifier is depicted as the dependent current source on the left.

As described previously, the Copley amplifier acts as a voltage-controlled current source. Internal circuitry provides closed-loop control of the output current; in all of the experiments performed with both the ball screw probe and dynamic probe, the amplifier showed almost perfect match between desired current and actual applied current. Therefore, it is reasonable to neglect the dynamics of the amplifier, and it can be assumed that output current  $i$  is directly proportional to the input voltage  $V$  by the amplifier gain  $K_A$  (units: amps/volt). Because the amplifier delivers the target current to the voice coil regardless of  $V_{BEMF}$ , the resistance and inductance of the voice coil can be ignored. Therefore,

$$I = K_A V \quad (7.8)$$

The force induced upon the voice coil by the current flowing through the wire is determined by Lorentz's force law, which relates the force  $F$  induced upon a wire of

length  $l$  to the current  $I$  that it carries and the magnetic field of strength  $B$ :

$$F = Il \times B \quad (7.9)$$

Since  $l$  and  $B$  are constants inherent to the device, this equation can be simplified to

$$F_a = K_F I \quad (7.10)$$

Where  $F_a$  is the force induced upon the voice coil by the electrical interaction of the coils with the permanent magnet, while  $K_F$  is the force constant, which is specified in the Moticont spec sheet with units of N/A. (Note: just as with an electric motor, it can be shown that the speed constant  $K_V$  equals the force constant  $K_F$  with a balance of electrical and mechanical energy.)

By combining both the mechanical and electrical models, and eliminating  $F_a$  and  $I$ , the equation relating the voltage input into the amplifier  $V(t)$  to the position of the voice coil  $x_3(t)$  is simply

$$K_F K_A V(t) = m_c \ddot{x}_3(t) \quad (7.11)$$

Converting into the frequency domain,

$$G(s) = \frac{x_3(s)}{V(s)} = \frac{K_F K_A}{m_c s^2} \quad (7.12)$$

Where  $G(s)$  is labeled in Fig. 7-11. Note: in these experiments, the device operates under position control; therefore the parameter of interest,  $X$ , is the position of the voice coil,  $x_3$ .

### 7.7.3 Modeling the closed loop system

Assuming that  $X_{ref} = 0$ , the closed loop transfer function  $C(s)$  relating the input voltage  $V_{ref}$  to the output position  $X_{actual}$  is given by

$$C(s) = \frac{V_{ref}(s)}{x_3(s)} = \frac{H(s)G(s)}{1 + H(s)G(s)} \quad (7.13)$$

Where  $H(s)$  is the transfer function for the PID controller, taking into account the A/D and D/A gains. From the voice coil spec sheet, and after measuring the components of the system, the numerical value of  $C(s)$  is approximately

$$C(s) = \frac{25(s + 435)}{s^2 + 25s + 11050} \quad (7.14)$$

In order to evaluate the validity of the model, the dynamic imaging probe was moved (under closed loop position control) by sweeping the reference voltage  $V_{ref}$  from 0.1 Hz to 120 Hz. A comparison of the model and data is shown in Fig. 7-14.

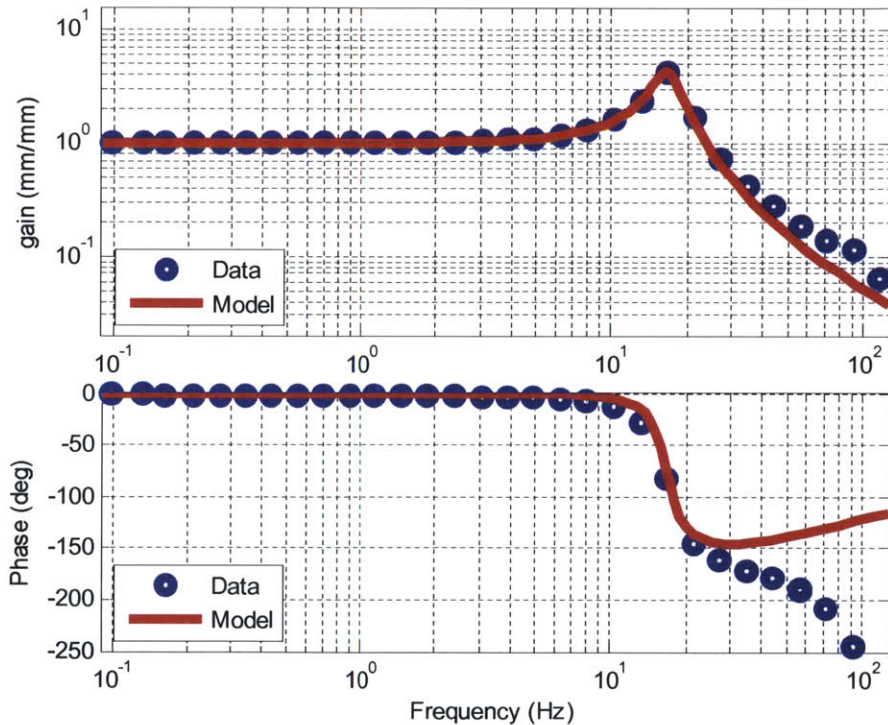


Figure 7-14: Bode magnitude (top) and phase (bottom) plots comparing the model (Equation 7.14) with the actual performance of the dynamic imaging probe, Version 2. The resonant peak occurs around 16.7 Hz. Gain is expressed as the ratio of the effective position commanded by  $V_{ref}$  to the output position  $x_3$  of the voice coil, in units of mm/mm.

From Fig. 7-14, in terms of magnitude, the model and data show good to reason-

able agreement across all frequencies tested; the response is flat below about 5 Hz, indicating that the input exactly follows the output. At 16.7 Hz, we see a resonant peak, with the magnitude decreasing at a slope of approximately -40 db/decade thereafter. The resonant peak occurs because of the mass of the moving components and the effective stiffness arising from the proportional component of the controller. In terms of phase, the model and data show good agreement below 20 Hz, and diverge thereafter. The phase is about 0 degrees below 10 Hz, indicating that the output position is in phase with the input voltage command.

## 7.8 High speed imaging

This section discusses early experiments that were performed to investigate the feasibility of using the Terason linear-array probe to image the propagation of shear waves induced by the dynamic imaging probe. The limitations of this technique are discussed, along with the shift towards the single-element transducer.

The need to acquire ultrasound images at more than 500 frames/sec places challenging constraints upon the system. Conventional linear-array ultrasound scanners image at rates between 10-100 frames/sec depending upon the depth, number of foci, and whether additional functionality, such as color Doppler, is activated. Generally, greater depths, more foci, and more functionality all contribute to a lower frame rates. Unfortunately, even the maximum frame rate of 100 frames/sec does not meet our functional requirement. There exist specialized, commercially-available linear-array systems capable of imaging at higher rates, including Ultrasonix and Supersonic Imagine, but they are generally an order of magnitude more expensive than more conventional systems like those of GE, Philips, Siemens, and Terason.

We investigated the feasibility of achieving higher frame rates with a conventional “low speed” ultrasound imaging system through a combination of repeatable shear wave generation and spatial and temporal aliasing. As discussed in Section 7.3.2, is it possible to generate shear waves with either pulsed excitation (e.g., one period of a 50 Hz sinusoid), or monochromatic excitation (e.g., a continuous 50 Hz sinusoid). Each

time the indentor compresses the tissue, a shear wave is generated. Assuming that each compression of the tissue is identical, each shear wave should also be identical, a regime referred to in the electrical engineering vernacular as “sinusoidal steady state.” A tantalizing possibility arises: what if each image is acquired at a different phase of the shear wave propagation? If the images were stacked together appropriately, it would be possible to reconstruct the full propagation of the shear wave.

As an example, assume the indentation rate of an indentor is  $f_1 = 20$  Hz, for a period of 50 ms. Assume that the ultrasound system is imaging at a rate of  $f_2 = 25$  Hz—a slightly different frequency—and therefore the period is 40 ms (typical of the Terason T3000 system, which we used). Then, the imager would image at a slightly different time (phase) of the compression each instance an image was captured. Specifically, it would capture an image at  $\Delta T = 10$  ms earlier each period. For the 50 ms compression, this means that each image would be captured at a phase of  $360^\circ/5 = 72^\circ$  relative to the previous image. After 4 periods of the 20 Hz compression, the image would repeat; therefore, the resulting sequence of images would repeat with a frequency of  $20\text{ Hz}/4 = 5$  Hz. The relative timings of the indentation and imaging for this example are shown in Figs. 7-15 and 7-16.

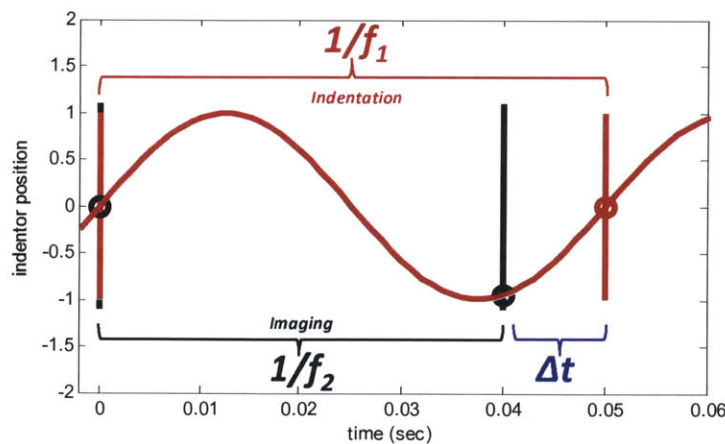


Figure 7-15: Relative timing with 20 Hz indentation (red) and 25 Hz imaging frequency (black).

Thus, under the assumption of sinusoidal steady state, it is possible to use temporal aliasing to capture 5 images/cycle of a 20 Hz indentation using a system imaging

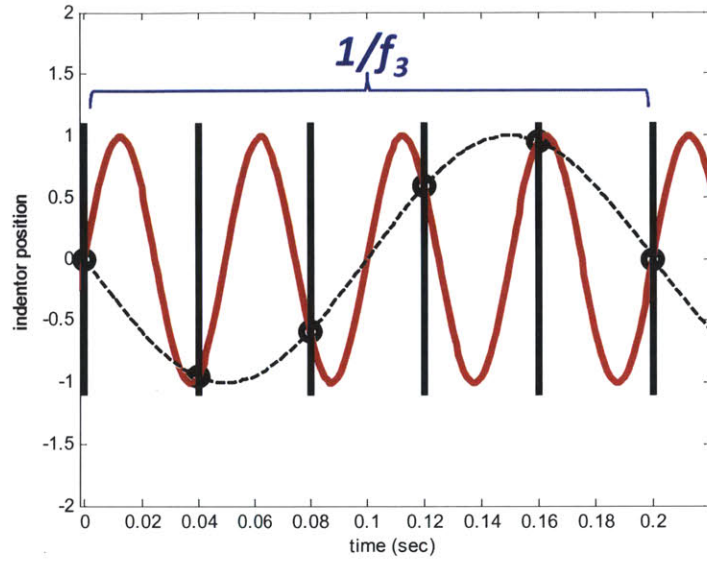


Figure 7-16: As a result, the 20 Hz indentation is sampled 5 times/cycle, for a rate of  $f_3 = 5$  Hz.

at 25 Hz. To extract the most detail from the images, it is desired to sample the compression with the highest speed possible. Next, we turn to theory to estimate the number of images/cycle considering arbitrary indentation and imaging frequencies.

Assume, as in Fig. 7-15, an indentation frequency of  $f_1$  and an imaging frequency of  $f_2$ . The number of times that the indentation will be imaged per cycle,  $N$ , will be approximately equal to the ratio between the indentation period and  $\Delta T$ :

$$N = \frac{1}{f_1/\Delta T} \quad (7.15)$$

where

$$\Delta T = \left| \frac{1}{f_1} - \frac{1}{f_2} \right| \quad (7.16)$$

thus

$$N = \frac{f_2}{|f_1 - f_2|} \quad (7.17)$$

It is desirable to maximize  $N$  in order to maximize the temporal resolution of the

indentation. Maximizing N means maximizing  $f_2$  (which, as mentioned previously, is limited to 100 Hz or so in most conventional imaging systems) or by minimizing  $|f_1 - f_2|$ . Therefore, we want  $f_1 \approx f_2$ . For example, for an indentation frequency of  $f_1 = 29$  Hz,  $f_2 = 30$  Hz gives  $N = 30$ , while  $f_2 = 29.9$  Hz gives  $N = 300$ .

Thus, in theory, by making the indentation frequency close to the imaging frequency, it is possible to use temporal aliasing to achieve high temporal resolution and a high effective frame rate of the transient propagation of a shear wave<sup>2</sup>. The effective frame rate  $f_{eff}$  (units = images/sec) is determined by N (units = images/compression) and  $f_1$  (units = compressions/sec) by the following equation:

$$f_{eff} = N f_1 \quad (7.18)$$

Therefore,

$$f_{eff} = \frac{f_1 f_2}{|f_1 - f_2|} \quad (7.19)$$

Experiments were performed to evaluate the feasibility of technique with the Terason T3000 system. A 5 cm thick phantom was placed upon a flat, rigid plate and the ultrasound probe (attached to the voice coil) was placed in contact with the top of the phantom. The Terason system imaged at 30 Hz while the voice coil vibrated, under position control, at 29 Hz. Sample images capture in this experiment are shown at the top of Fig. 7-17.

Based upon the analysis above, we would expect the compression to be sampled with  $N = 30$  images/period. Since the ultrasound system images at  $f_2 = 30$  images/sec, the expected tissue excitation speed shown on the display is  $f_2/N = 1$  period/sec. Therefore, over the course of one second, the tissue should appear to compress, then relax, once. Indeed, the observed behavior matched the expected behavior, validating the temporal aliasing assumption.

---

<sup>2</sup>It is worth noting that this technique is similar to “crawling wave elastography” [51]. In this technique, two mechanical indentors are placed in contact with tissue and vibrated at slightly different frequencies; a wave resulting from the interference patterns of the shear waves propagates through the tissue, and the propagation speed of the resulting wave is used to estimate the shear wave speed.

This suggests that by carefully controlling the imaging and indentation speeds, very high effective frame rates are possible. In the experiment described in the previous paragraph, the  $f_1 = 29$  compressions/sec indentation is imaged with  $N = 30$  images/compression, giving an effective frame rate of  $f_{eff} = f_1 N = 870$  frames/sec. Subsequent experiments were performed with different imaging and indentation frequencies, and effective frame rates of up to 2,140 frames/sec were achieved.

### 7.8.1 Pixel column synchronization

Unfortunately, other effects come into play that complicate the implementation of this method. Example images from the experiment described above are shown in Fig. 7-17. An unexpected effect is visible in the images: the flat plate (bright white line at about 2/3 depth) appears curved in the ultrasound images. Because the flat, rigid plate was not actually moving, this suggests that some other effects are at work.

One potential explanation for this effect is the fact that ultrasound probe does not sample the entire image simultaneously. The Terason linear probe used in these experiments has 128 piezo elements; our hypothesis is that not all elements are fired and read at the same time. To construct an ultrasound image, probes typically fire 1 to 5 adjacent piezo elements simultaneously, then listen for the reflected signal with the same 1 to 5 piezo elements. The radiofrequency data are then transformed and converted into a single pixel column. Then, the next set of 1-5 piezo elements is scanned and the next pixel column is constructed. When all of the 128 pixel columns have been constructed, they are stacked together and a new image is presented on the computer screen.

Therefore, there is a time (phase) delay between the adjacent pixel columns. For an imaging frequency of 30 Hz and indentation frequency of 29 Hz, for example, the time delay between the 1st column and the 64th column of the 128-column image would be about 17 ms, with a phase delay of approximately  $180^\circ$ . Although this effect would cause adjacent pixel columns to be out of phase, if enough images were captured, it should be possible to appropriately rearrange the pixel columns to reconstruct each image as if all of the columns were captured at the same phase. An

example illustration of this method is shown in Fig. 7-17.

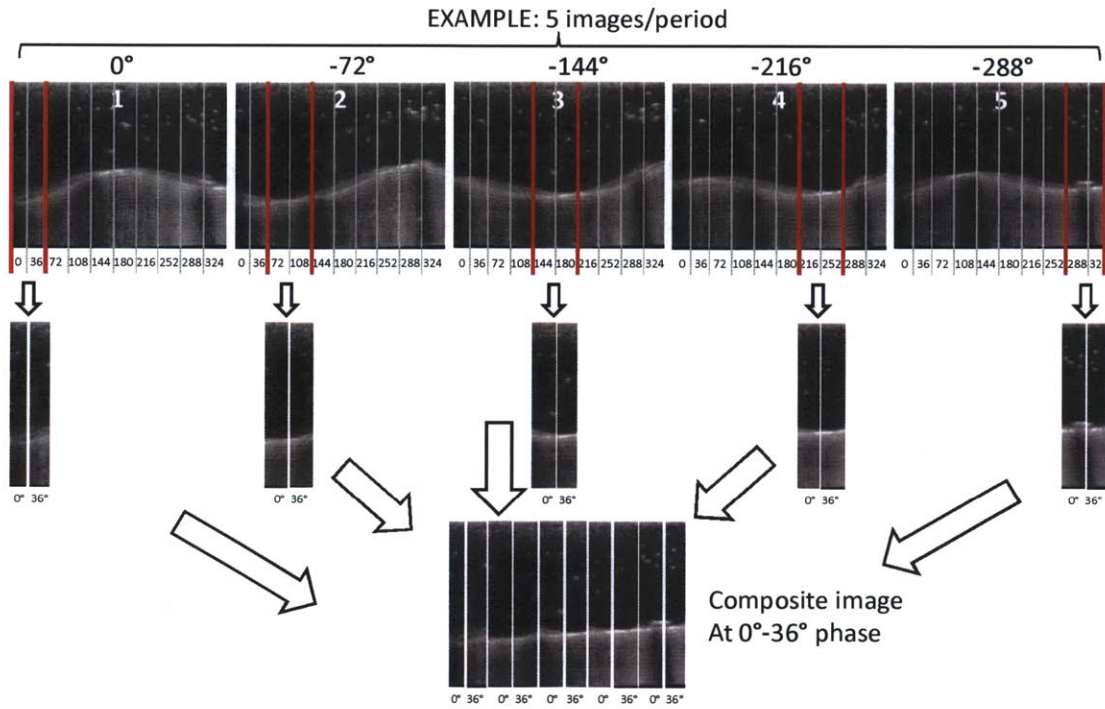


Figure 7-17: An example of stacking together phase-synchronized pixel columns to reconstruct an image of a constant phase.

The example depicted in Fig. 7-17 shows an imaging scenario in which  $N = 5$  images/period. Therefore, corresponding columns from each of the 5 unique images are captured at phases of  $0^\circ$ ,  $72^\circ$ ,  $144^\circ$ ,  $216^\circ$ , and  $288^\circ$  relative to the compression of the tissue. Within each of the five images, as discussed above, adjacent pixel columns are captured at different phases relative to each other. For simplicity, assume that there are 10 pixel columns per image. Thus, if column 1 is at zero phase, column 2 is at  $36^\circ$  relative to column 1, column 3 is at  $72^\circ$  relative to column 1, etc.

It is desired to construct a single image in which all columns are at the same phase. Therefore, the closest approximation would be to extract columns 1 and 2 from raw image 1, columns 3 and 4 from raw image 2, etc., to create the composite image shown at the bottom, in which all phases are between  $0^\circ$  and  $36^\circ$ . A similar procedure is necessary to construct composite image 2; columns 1 and 2 would be extracted from raw image 2, columns 3 and 4 from raw image 3, etc.

An example image of a homogeneous phantom supported by a rigid aluminum plate for  $f_1 = 29$  Hz and  $f_2 = 30$  Hz is shown in Fig. 7-18.

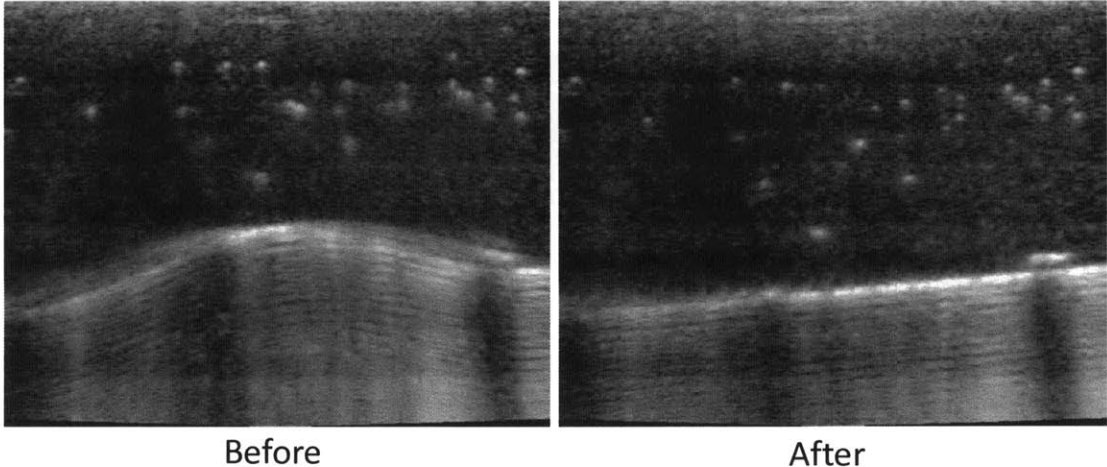


Figure 7-18: Left: example raw image of a flat plate beneath a homogeneous phantom, imaging frequency = 30 Hz, indentation frequency = 29 Hz. Right: image corrected by the pixel column synchronization method.

On the left of Fig. 7-18, the flat plate appears artificially curved due to the phase lag between adjacent ultrasound scan lines. On the right, after pixel column correction has been performed, the plate appears flat, as it would look during static imaging.

### 7.8.2 Limitations of pixel column synchronization

Even after pixel column synchronization, a number of limitations prevent this technique (in its current implementation) from being usable for imaging shear waves. The primary limitation is the presence of a number of image artifacts, which seem to be more significant at greater depths. Based upon the subtlety of shear wave propagation characteristics, it is surmised that the artifacts swamp the tenuous motion induced by the shear waves. During moments in which the phantom is being compressed rapidly, considerable blur is present in the reconstructed images, as shown in Fig. 7-19, right.

This blur is related to the number of pixel columns into which the image is split, which is in turn related to the number of frames per compression,  $N$ . Higher  $N$  results in fewer image artifacts, but also means that the tissue must be imaged for a

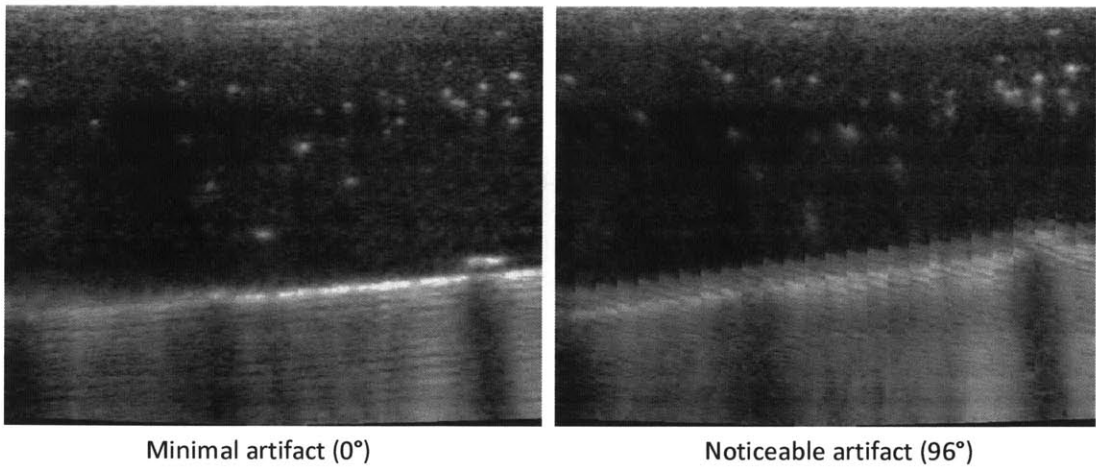


Figure 7-19: Images of a phantom containing a flat plate, reconstructed using pixel column synchronization. More blurring is present when the plate (ultrasound probe) is moving quickly (right).

longer period of time to capture enough images to fully reconstruct one period of the compression. Longer imaging time is acceptable for stationary phantoms, but is less feasible *in vivo*; any motion of the tissue induced by breathing or the pulse during imaging violates the sinusoidal steady state assumption and further degrades image quality.

Another artifact is the presence of a double-line, as shown in Fig. 7-20. The spacing between the lines seems to increase with depth and could suggest that the probe elements are scanned twice before displaying the image.

Due to these artifacts present after the pixel column phase correction, combined with a number of limitations stemming from the Terason systems quantized set of available imaging frequencies, it was not possible to image the propagation of shear waves using the Terason linear-array probe.

## 7.9 Single-element ultrasound transducer

Shear wave imaging systems from the literature employ either a highly-specialized high frame rate imager (such as a Supersonic Imagine or Ultrasonix system) or a single-element transducer. For the dynamic imaging probe, it was decided to move

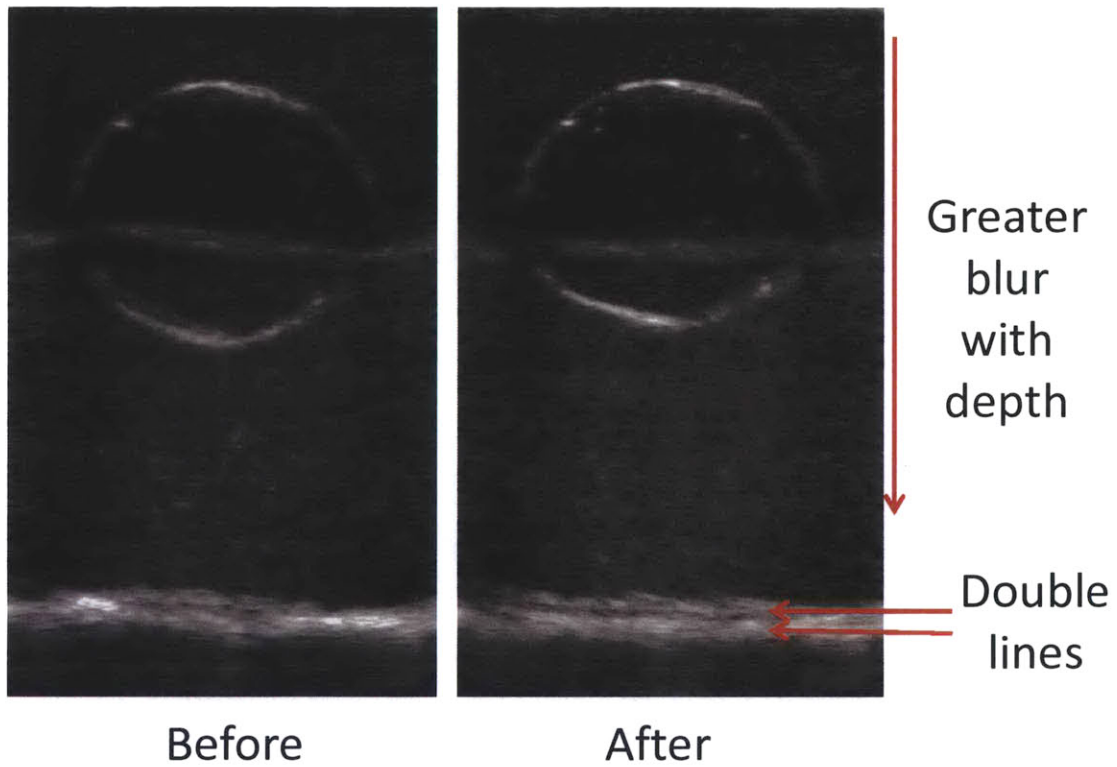


Figure 7-20: Images of a phantom containing a large round inclusion, before and after reconstruction using pixel column synchronization. The presence a double-line artifact is visible, which blurs the image

towards a single-element transducer due to its simplicity and significantly lower cost (\$200 for a single element vs \$10,000 for a linear array probe). Single-element ultrasound transducers are frequently imaged at rates of up to 10 kHz. A 5 MHz Olympus V326-SU 0.375" diameter immersion transducer was chosen for this application.

A comparison of the images generated with a linear-array transducer and a single-element transducer is shown in Fig. 7-21. While a linear-array transducer captures 2D images of tissue, a single-element transducer captures a single column, shown in the red dotted box. To capture an image, the piezo crystal is pulsed with a high voltage, often up to 250 V, and acoustic energy is transmitted into the tissue. As the acoustic energy is reflected back to the transducer, the voltage is measured. Voltage corresponds to tissue echogenicity (tissue that is more ultrasound-reflective reflects more energy back to the transducer), while time corresponds to depth.

The raw voltage versus time plot is referred to as a radiofrequency (RF) line, an example of which is shown in blue. The RF data are typically processed through log compression and envelope detection to accommodate the high dynamic range and to smooth the data, and the result is a single-pixel wide column (shown below with a greater width, for clarity). In the pixel column, visible layers can be compared with the 2D image to determine the structures to which they correspond.

### **7.9.1 Imaging shear wave propagation with the single-element transducer**

In this section, we describe experiments conducted with the voice coil probe and the single-element transducer. The purpose of these experiments was to demonstrate that shear waves could be generated and imaged at different preload forces, and the elasticity of the tissue could be deduced at each preload force.

The experimental setup is shown in the right side of Fig. 7-21. The forearm of a volunteer was rested upon the table and the single-element Olympus probe was placed in contact with the tissue. The ultrasound probe imaged a column of tissue that included the superficial flexor digitorum muscle, as well as the deeper ulna bone.

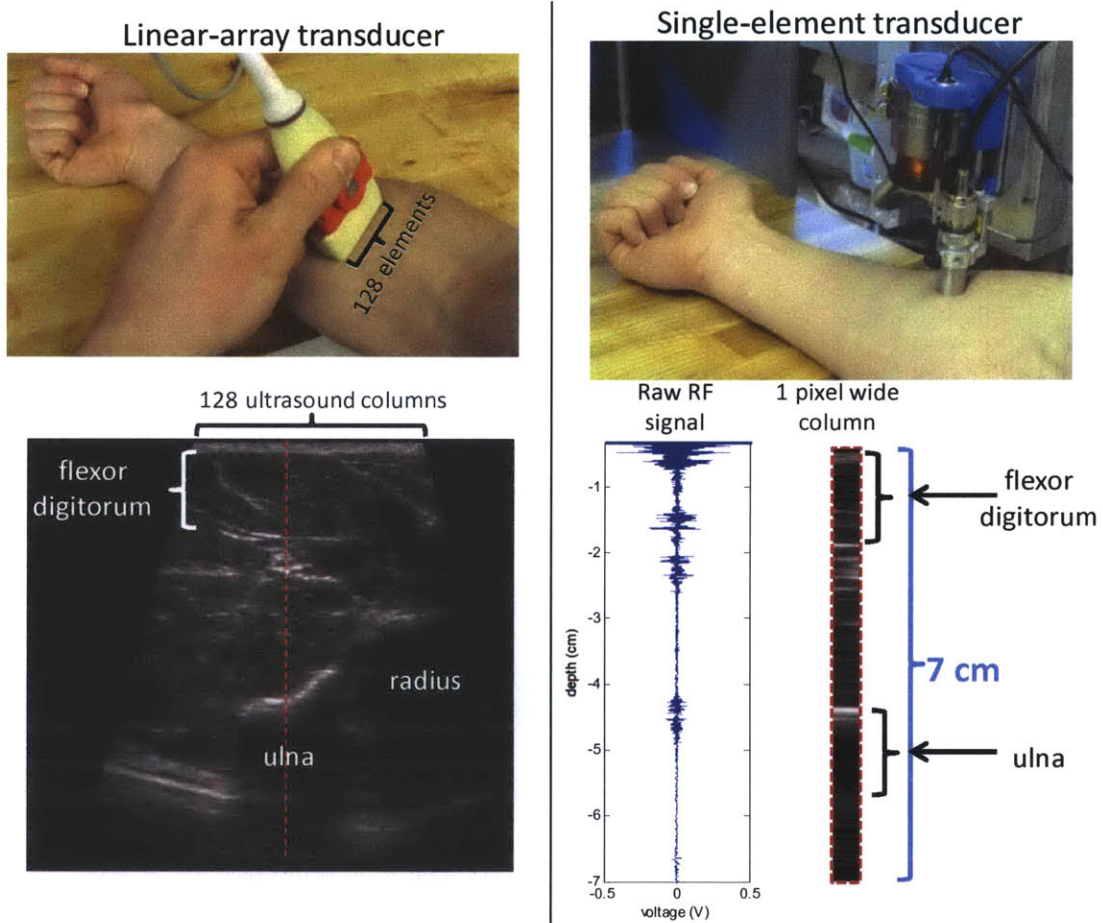


Figure 7-21: A comparison between the images obtained with a linear-array transducer and a single-element transducer.

The ulna provided a motionless reference point in the experiments.

Force control mode was activated and the system was set to apply a constant contact force. The setup of the control system is shown in Fig. 7-11; in this case, the parameter of interest,  $X$ , is the contact force. The HP function generator was setup to apply a single period of a 50 Hz sine wave based upon an external trigger. The trigger source was a digital output on the PXI-7358 motion card, which was controlled by a basic LabVIEW program. Hence, for a majority of the time, a constant, DC bias force is applied. When the function generator was triggered, the force was briefly pulsed up and down by an AC component in order to induce the shear wave. The shear wave propagation was imaged, the propagation speed was measured, and the elastic modulus was calculated based upon Equation 7.3. The procedure was repeated for different preload forces, and an overview of the procedure is shown in Fig. 7-22.

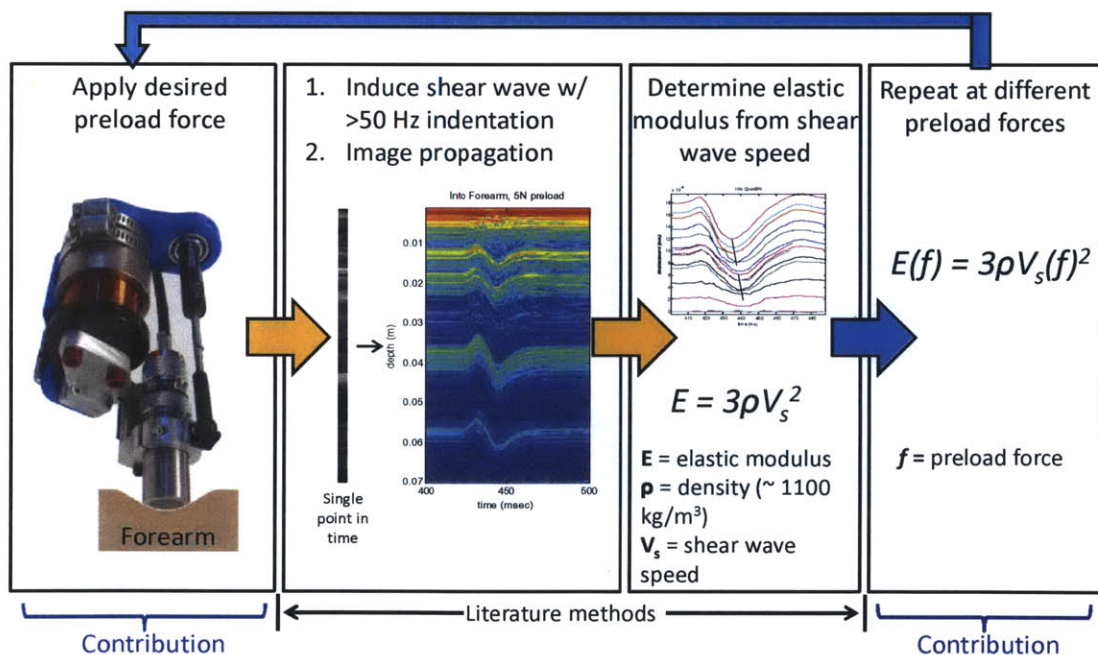


Figure 7-22: Overview of the experiments to evaluate the elasticity of the tissue at different preload forces.

This procedure was conducted for the same range of forces applied in the quadriceps imaging study in Fig. 7-2, with the addition of 14 N: 1, 3, 5, 7, 9, 11, 14, and 18 N. The probe was set to image at a rate of 5 kHz and a depth of 8 cm—greater

than the thickness of the forearm. The data from the experiments are presented in Fig. 7-23 in the form of M-mode images. An M-mode image is created by recording the time-evolution of a single RF scan line (also known as an A-scan), shown as the single pixel column in Fig. 7-21. In M-mode images, which are depicted in color in Fig. 7-23, the Y-axis represents depth while the X-axis represents time (50 ms duration in these experiments).

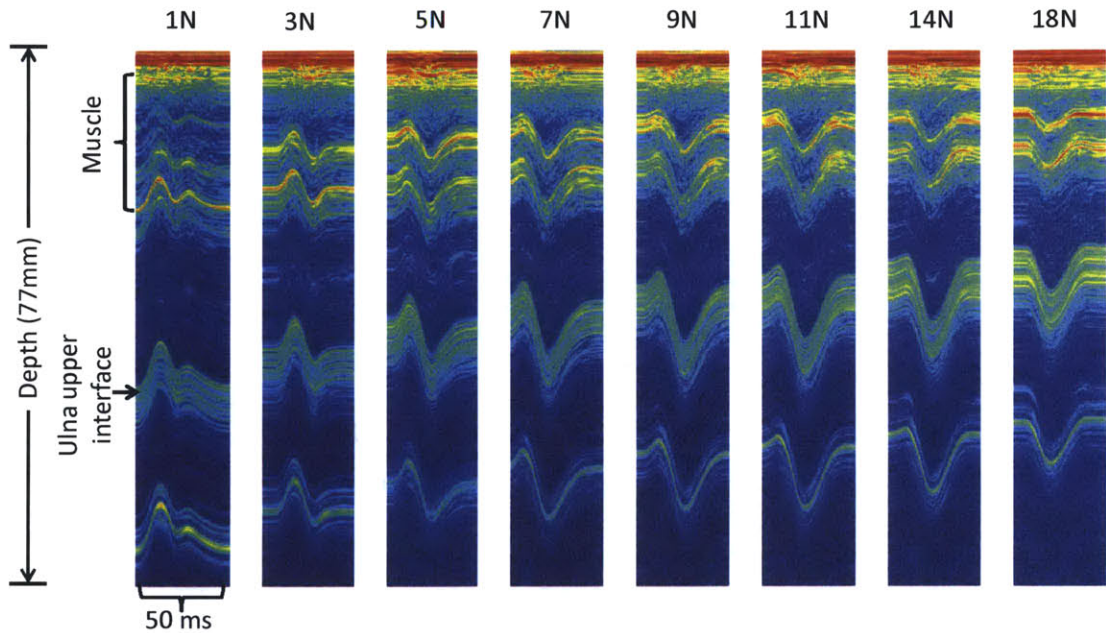


Figure 7-23: M-mode images of the 50 Hz indentation of the tissue at different preload forces. The ultrasound probe is at the top of the image; deeper tissue structures such as the ulna bone are at the bottom of the image.

In each of the M-mode images, the indentation of the tissue is visible. Since the imaging probe is moving while the ulna is stationary, all of the structures appear to move relative to the probe. The superficial tissue structures, because they are close to the probe, show the least motion, while the deep ulna shows the most motion because the full thickness of the tissue is between the bone and the probe. It is analogous to springs in series; the superficial tissue layers, which are thinner and therefore have greater stiffness, compress less than the full column of tissue, which has lower stiffness. We can see that, due to the preload force, all of the structures appear close to the US probe in the 18 N image as compared to the lower-force images.

To visualize the shear wave, it is necessary to subtract out the motion of the probe. This is possible as long as the position of the probe is known. One technique to measure the probe position would be to measure the voltage of the linear potentiometer. This would require an additional step to synchronize the M-mode images with the position voltage trace. Another strategy, as discussed in [94], is to assume that the ulna bone is a motionless interface. Therefore, the position of the ulna bone encodes the position of the ultrasound probe.

To visualize the shear wave, tissue layers in each image were traced manually using Matlab, and the motion of the probe was subtracted from the motion of each of the layers. The resulting layer-image is shown in Fig. 7-24.

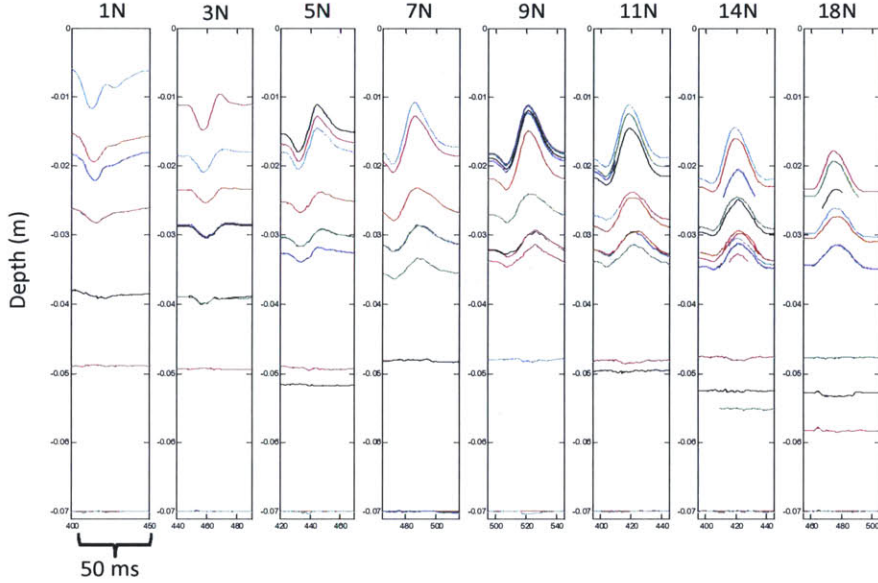


Figure 7-24: Images of the tissue layers at each preload force with the motion of the ultrasound probe removed.

In Fig. 7-24, we notice that the behavior of the tissue differs as the force increases. At low forces, such as 3 N and 5 N, the upper layers of the tissue move with a clear sinusoidal trajectory; first the tissue is compressed, then it is allowed to expand. At higher forces, however, the waveform changes; first, the tissue expands (moves upward), then is compressed back to its initial position. Instead of a sinusoidal compression/expansion, we see only a positive peak.

This suggests that at higher preload forces (i.e., higher levels of compression),

the indentor is less capable of further compressing the tissue. This is reasonable, considering the 200 g moving mass of the actuator and the current limits of the amplifier, which were placed to prevent the coil from overheating and potentially melting the insulation. For reference, at a constant 18 N preload force, the power draw of the voice coil is 40 W. The maximum continuous power recommended for the actuator is only 18 W, which suggests that 18 N is already near the performance limits of the system; additional force on top of this 18 N cannot be sustained for long.

Despite these constraints arising from limitations on the actuator power, it was still possible to image shear wave propagation at each of the frequencies. As discussed in Section 7.3.2, shear waves appear as a 1-10 m/s compression of the tissue originating in the superficial layer and propagating to the deeper layers. Thus, in the M-mode images, we would expect to see superficial tissue disturbed at an earlier point in time than deeper tissue, which should appear as a phase delay (and also potential amplitude reduction due to depth attenuation) as depth increases. An example of this technique from the Catheline et al [28] is show in Fig. 7-25.

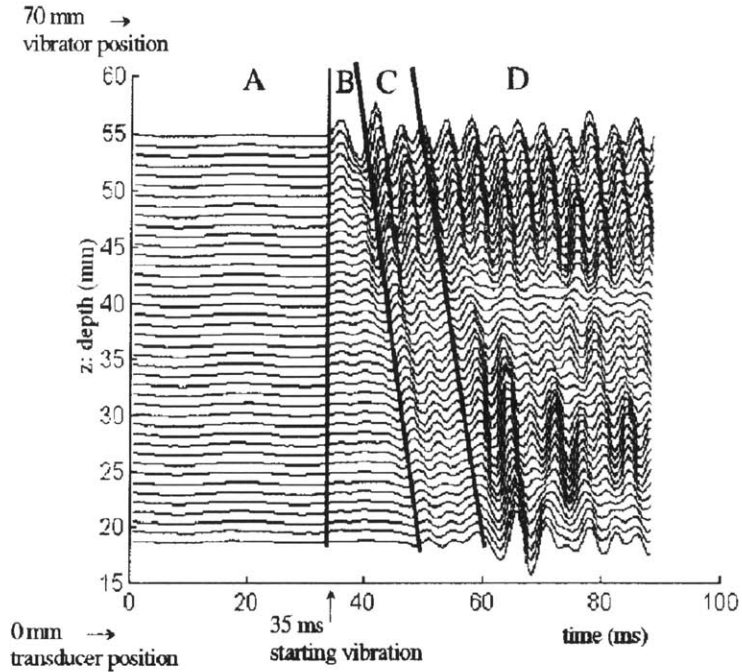


Figure 7-25: Example M-mode imaging of shear wave speed estimation from the Catheline et al [28]. Vertical displacement is exaggerated to enhance shear wave visualization.

Shear wave propagation speed is determined by matching up corresponding features at different depths. In Fig. 7-25, a line is drawn through the different layers at the point in time when the tissue first begins to move. The slope of the line, which has units of m/s, is the shear wave propagation speed. The same technique was applied to the data from the dynamic imaging probe, and an example M-mode image at 11 N is shown in Fig. 7-26.

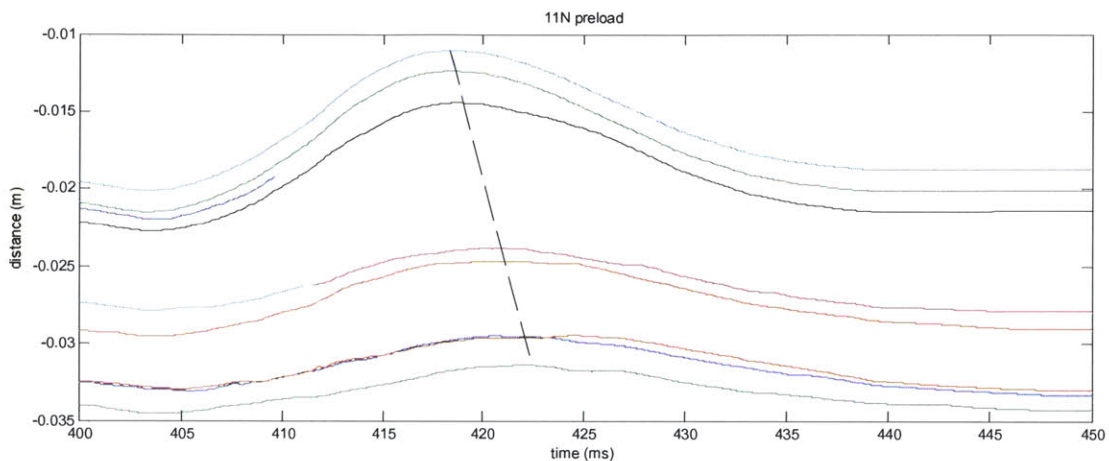


Figure 7-26: Zoomed-in M-mode image of the compression of the tissue at 11 N preload force. The dotted line is drawn through corresponding peaks in the traces at each depth, and has a slope of 4.3 m/s.

The technique outlined in Figs. 7-25 and 7-26 was implemented with the data, and the shear wave propagation speed was calculated at each of the eight different preload forces. Equation 7.3 was used to estimate the elastic modulus based upon the shear wave speed and the assumption that  $\rho = 1100 \text{ kg/m}^3$ . A plot of the elastic modulus versus preload force is shown in Fig. 7-27.

In Fig. 7-27, the experimental data from the dynamic imaging probe, along with the data from the force-measuring Supersonic Imagine Probe (data from Fig. 7-2), are shown on the right. Elastic moduli from example literature studies<sup>3</sup> (all of which are at unknown/unspecified preload forces) are shown on the left.

From Fig. 7-27, we see that the elastic modulus estimates from the dynamic

---

<sup>3</sup>Note: references in the figure correspond to: [Samani 2003] = [92], [Yeh 2002] = [115], [Nordez 2010] = [76], [Sandrin 2002] = [94].

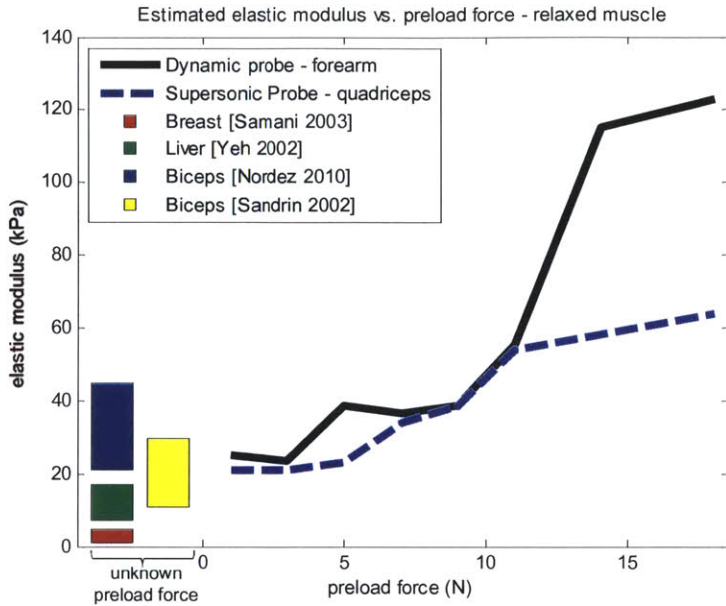


Figure 7-27: Elastic modulus vs. preload force for the dynamic imaging probe and force-measuring Supersonic Probe from Fig. 7-2 (right), compared to the literature (left).

imaging probe and the force-measuring Supersonic Probe both increase with preload force, indicating that tissue becomes stiffer, as expected, as preload force increases. The data from the two studies agree below 11 N, and differ by a factor of 2 at 18 N. The difference could be due to the fact that the forearm was tested with the dynamic probe while the quadriceps was imaged with the force-measuring Supersonic Probe.

Compared with the literature, both methods are within the literature range for the relaxed biceps below about 10 N [94],[76] (literature data for the quadriceps and forearm were not found, but it is assumed that the muscles have similar elasticities), and both methods are higher than the literature values at higher preload forces. For comparison purposes, the elastic moduli of the liver and breast are shown in Fig. 7-27, which are much softer than muscle.

These results are, to our knowledge, the first quantitative demonstration of tissue stiffening with preload force, as measured with shear wave elastography. The primary findings from these experiments were: 1) tissue indeed stiffens with preload force, and 2) stiffening can be quantitatively measured with the dynamic probe.

Table 7.4: Comparison between functional requirements and measured capabilities of the dynamic imaging probe, Version 2.

Parameter	Functional Requirement ( $FR_p$ )	Actual ( $D_p$ )	N	Safety Factor
Stroke	>25 mm	21.5 mm	+1	0.9
Max continuous power	>15 W	18 W	+1	1.2
Motion amplitude at 50 Hz	>1 mm	1 mm	+1	1
Bandwidth	>100 Hz	75 Hz	+1	0.8
Imaging rate	>500 frames/sec	5,000 frames/sec	+1	10
Mass	<1 kg	0.5 kg	-1	2
Size	length <15 cm; girth (diameter) <6 cm	length: 11.5 cm; girth: 6 cm	-1	length: 1.3; girth: 1
Max force	>20 N	45 N	+1	2.3

## 7.10 Dynamic Imaging Probe: Summary

A comparison between the functional requirements ( $FR_p$ ) of the Version 2 and the actual measured capabilities ( $D_p$ ) is shown in Table 7.4. As discussed in Section 6.2,  $N$  is a measure of whether or not high values of the functional requirement are favorable, and is used in calculating the safety factor. If high values of the functional requirement are high (such as bandwidth),  $N = +1$ ; if low values of the functional requirement are favorable (such as mass), then  $N = -1$ .

A graphical comparison of several of the key functional requirements is depicted in the form of a spider plot in Fig. 7-28. As discussed previously, functional requirements with  $N = -1$  are plotted as reciprocals, so that values toward the outside of the “spider web” are favorable.

As discussed in Section 6.2, axes for which the blue curve lies outside of the red curve represent a safety factor greater than 1; conversely, where the blue curve lies inside the red curve indicate safety factors less than 1. From the plot (Fig. 7-28) and Table 7.4, the dynamic probe (Version 2) has safety factors greater than 1 for all of the parameters except the range of motion (21 mm instead of 25 mm) and

### Functional Requirements vs. Device Specs - Dynamic Imaging Probe

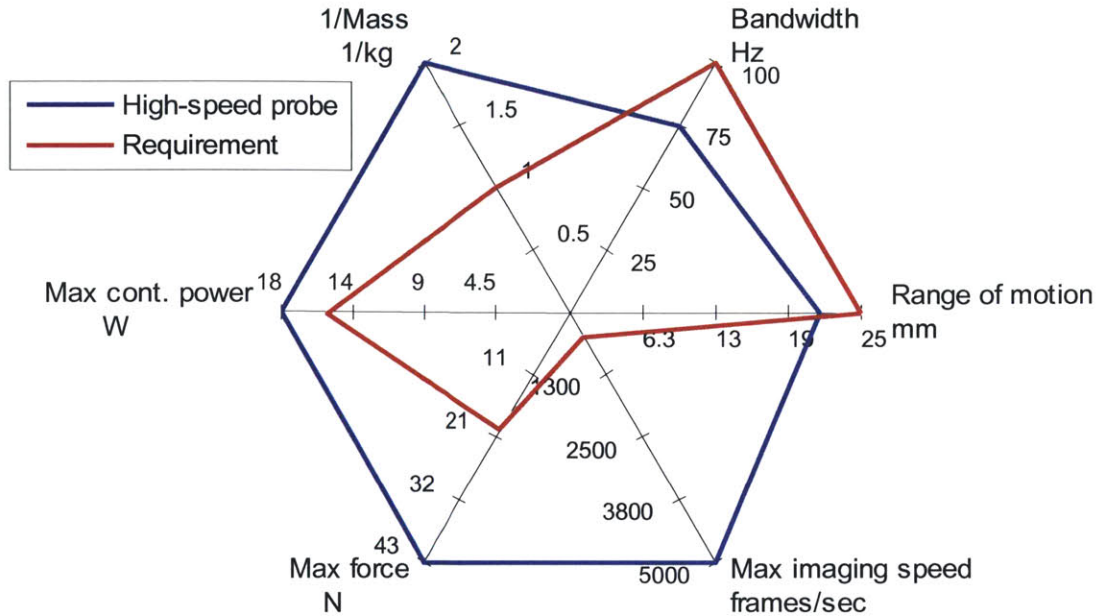


Figure 7-28: Spider plot comparing the functional requirements for the high-speed dynamic imaging probe (red) with the actual performance of Version 2 (blue).

the bandwidth (approximately 75 Hz instead of 100 Hz). The effect of the range of motion limitation was not rigorously evaluated. The bandwidth limitation was likely due to the relatively high moving mass of the probe; a waterproof stainless steel transducer was used. The next design iteration could likely employ a non-waterproof bare transducer in order to reduce moving mass and increase bandwidth. Nevertheless, in spite of the bandwidth limitation, the system was still able to generate shear waves.

## 7.11 Discussion

This chapter presented the design and experimental evaluation of a high-speed dynamic imaging probe that enables 1) high bandwidth constant force imaging, and 2) the ability to measure tissue elastic modulus at different preload forces. The design uses a direct-drive voice coil linear actuator, which can achieve much higher

bandwidth than the ball screw-driven force-controlled probe. Two prototypes of the dynamic imaging probe were constructed; the first incorporated a linear-array ultrasound transducer. A strategy we refer to as “pixel column synchronization” was employed in an effort to achieve a high effective imaging frame rate due to temporal and spatial aliasing effects. However, the method was found to be ineffective for the Terason transducer due to a number of artifacts and unexplained characteristics of the Terason imaging system.

The design was adapted to accommodate a single-element ultrasonic transducer, capable of imaging at much higher speeds. The second prototype, referred to as “Version 2,” is capable of launching shear waves into tissue, through a process called “shear wave elastography.” Shear wave propagation speed correlates directly with tissue elastic modulus, which in turn correlates with tissue health for some tissues. Version 2 was used to measure the elastic properties of the flexor digitorum (forearm muscle) via shear wave imaging at different preload forces. Because biological tissue exhibits stiffening with higher stress, we expected the elastic modulus to be higher at higher preload forces. This was confirmed with data from the Version 2 device, as well as data obtained with a commercial shear-wave elastography probe mounted to the force-measuring probe.

While more experiments are needed to thoroughly-evaluate the capabilities and limitations of the system, the results provide an early demonstration that this device can be used to measure elastic properties at a programmable contact force, which could improve the repeatability of elastography.

# Chapter 8

## Design for All Exams

In this chapter, the suggested device design for all of the various ultrasound exam types is presented. Based upon the framework discussed in Chapter 2, which maps the input variables associated with the exam type, sonographer, and patient, to the device functional requirements, as well as the design parameters for the device, it is possible to suggest the most appropriate device for the range of common ultrasound exam types. In Fig. 8-1, the suggested design of a device to control and/or measure contact force is presented for each of the most commonly-performed ultrasound exams.

For abdominal, external cardiac, musculoskeletal, needle-guidance, and vascular imaging, the ball screw + servo motor is the most appropriate actuator; in these exams, the force-controlled probe, Prototype 3, could be used as long as the suggested modifications to stroke length are performed. The voice coil could be used for the rest of the exam types, again with suggested stroke length modifications for each. The force-measuring probe, since it has no actuated components, could be used in any of the exam types, provided that load cell is appropriately selected for the necessary range and resolution.

### 8.1 Mapping the Design Space

How does this compare to other devices that have been developed within this space?

Let us select two desirable attributes with which to compare the devices with each

Figure 8-1: Suggested design for a force-controlled or force-measuring ultrasound probe in each of the commonly-performed exams, along with the most important functional requirements.

other: bandwidth and range of motion. Higher bandwidth is preferred because it enables the device to compensate for higher-frequency tremors, and better-attenuate sonographer motion. High range of motion is also preferable because it reduces the likelihood that the sonographer will reach a travel limit, guaranteeing that the contact force stays constant. The two attributes, however, are somewhat at odds with each other, because higher range of motion can mean higher moving mass, which would tend to reduce bandwidth.

A plot of bandwidth versus range of motion is shown in Fig. 8-2, with a photo of the literature systems plotted at the appropriate locations. The three systems developed in this thesis are also shown.

In this plot, the most desirable location is the upper-right; this represents a device that has both high range of motion and high bandwidth. A device with range of motion greater than 75 mm would allow constant force scanning in abdominal imaging, the exam type that requires greatest range of motion due to its characteristic scan length. A device with bandwidth greater than 100 Hz would enable shear wave imaging, which could be used to measure the elastic properties of tissue, in addition to attenuating hand tremors. Therefore, the most capable device would lie around the point (75 mm, 100 Hz). It is suggested that some sort of “macro/micro” stage could target this point. Such a device would consist of a “macro stage” which would provide coarse positioning at low bandwidth, along with a “micro stage” which would provide high-bandwidth motion (for launching shear waves or suppressing high-frequency tremors, for example) with low range of motion. Such a stage could consist of a low-range of motion voice coil mounted to a ball screw actuator. Simply mounting the dynamic imaging probe to the force-controlled probe is one possibility; however, the high mass of the voice coil magnet would likely prevent this from being feasible. Using a smaller voice coil with the same bandwidth but lower range of motion would likely be the appropriate alternative.

## Mapping the design space: prior art

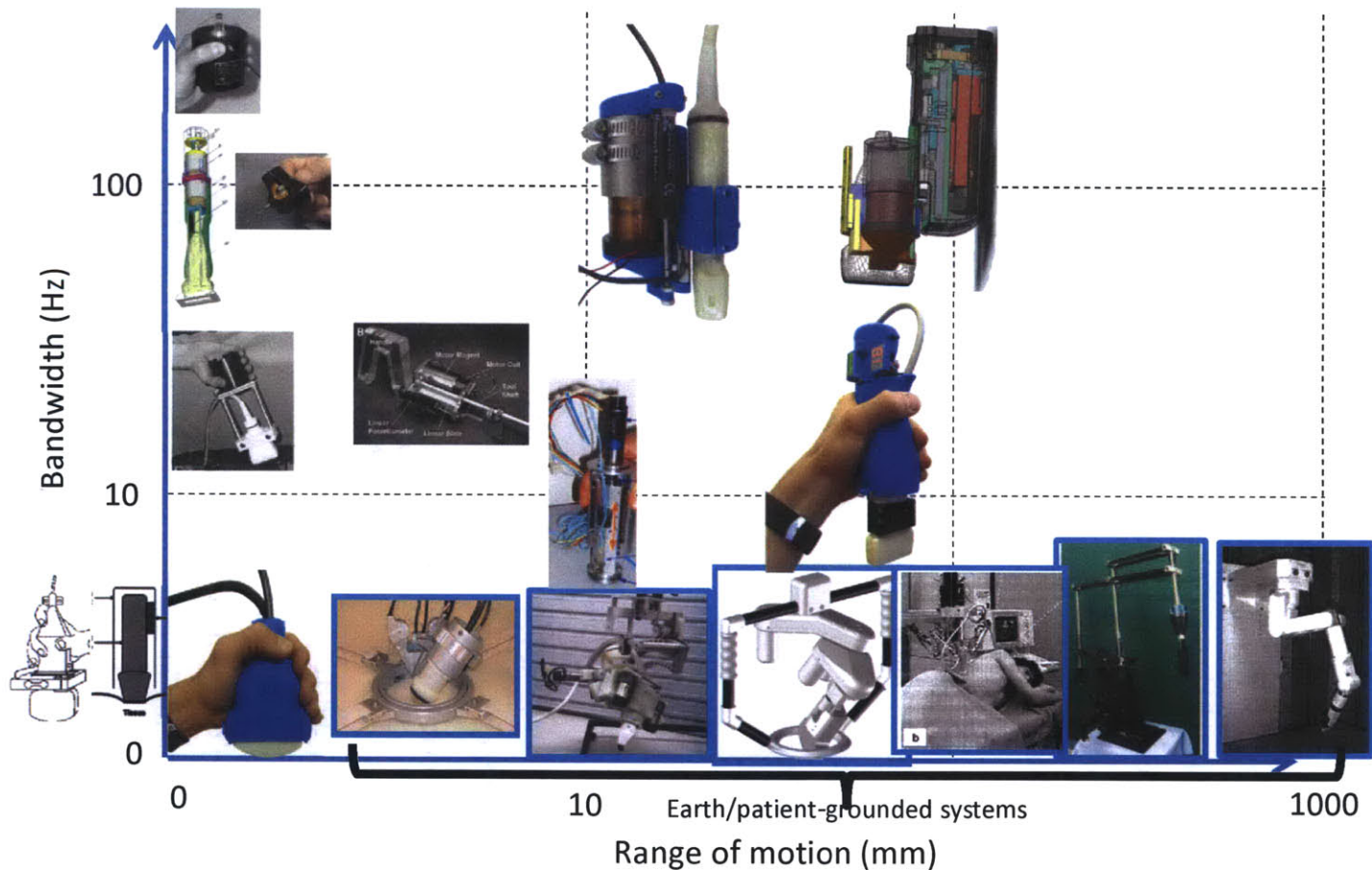


Figure 8-2: Bandwidth versus range of motion of various systems in the literature, along with the devices presented in this thesis. The devices outlined in blue are all earth- or patient/grounded systems, while the rest are handheld. For clarity, two force-measuring devices from the literature are shown to the left of the force-measuring device in this thesis, all of which have zero range of motion.

## **8.2 Conclusion**

In this chapter, device designs were suggested for the spectrum of common exam types, based upon the “meta-design” framework presented in this thesis. The devices presented in this thesis were compared with those in the literature in terms of bandwidth and range of motion, which are both desirable attributes. The design of a “macro/micro stage,” which would combine a high-range of motion actuator with a high-bandwidth actuator, was proposed and the feasibility was discussed.



# Chapter 9

## Contributions and Suggestions for Future Work

### 9.1 Conclusion

This thesis presented three hand-held electromechanical systems that enhance the usability and diagnostic capabilities of ultrasound imaging by measuring and/or controlling ultrasound probe contact force. The first device, which employs a servo-driven ball screw actuator, linearly translates an ultrasound probe in order to apply a constant, programmable contact force between the probe and the patient. The device attenuates hand tremors by a factor of 10, ensuring constant force with low ripple throughout an ultrasound exam. By applying a constant force, the system maintains a constant, repeatable amount of tissue deformation, which results in more repeatable ultrasound images for longitudinal imaging, and requires less operator expertise. In addition to enabling non-experts to obtain repeatable images, the system also helps to reduce the time necessary to obtain a quality image. For example, if the “optimal” contact force for a particular exam is known, the force-controlled probe can be set to apply that optimal force, and the sonographer can conduct a constant-force scan without needing to manually control the force, thereby reducing exam time and thus cost.

The second device passively measures forces and torques in six axes, and fea-

tures a robust, simple mechanical design with no moving parts, that permits rapid attachment and detachment of the ultrasound probe. The device was used in the first rigorous study to quantify contact forces through a study involving 53 abdominal scans, 13 professional sonographers, and 10 healthy volunteers. Correlations were explored between contact force, patient BMI, and years of sonographer experience; higher patient BMI was found to correlate with higher contact force. By measuring probe contact state, the device enables better understanding of the relation between force and sonographer fatigue & injury.

The third device is a direct-drive voice coil-driven stage that enables high-bandwidth constant force ultrasound imaging. By inducing shear waves and measuring propagation speed, the device can be used to measure the elastic modulus of tissue, which correlates with tissue health in some tissues. Combining these two capabilities, the device can also be used to measure tissue elastic modulus at a programmable preload force, which improves the repeatability of the measurement. The device was used to measure elastic modulus of the flexor digitorum (forearm muscle) *in vivo*; the data were found to be in agreement with the expected values.

## 9.2 Workflow Enhancements and Suggested Use

Next, we discuss the suggested use of these device as well as how they fit into the workflow of ultrasound imaging. The use scenarios for these devices can be dichotomized into 1) uses for the current as-is prototypes, and 2) uses for the “ideal” realizations of these prototypes—i.e., uses if the devices were further developed into actual products.

### 9.2.1 Uses: Current Prototypes

*Force-measuring probe:* The force-measuring probe is intended to quantify the forces applied during ultrasound scanning, and can be used to provide feedback to sonographers of the contact force. Although the current device doubles the volume of the ultrasound transducer, during the MGH studies, sonographers qualitatively reported that the device was still comfortable to grasp. Furthermore, in some of the exams

in which multiple subjects were scanned consecutively by the same sonographer, the device was used continuously for approximately 60 minutes with no reports of discomfort caused by the different grasp of the probe. This suggests, anecdotally, that the device can be used during semi-prolonged scanning.

Possible use cases for the current prototype of the force-measuring probe are: 1) further studies to quantify contact forces—i.e., an extension of the MGH study, 2) scenarios in which image repeatability can be improved by manual control of the contact force—i.e., without the use of the force-controlled probe (e.g., the DMD study or longitudinal imaging such as mammography or thyroid nodule imaging), and 3) biofeedback studies to investigate if the risk of injury can be reduced by informing sonographers of their contact force.

*Force-controlled probe:* In its current form, the force-controlled probe is considerably larger than an ultrasound probe, and its shape makes it non-ideal for continuous, prolonged use. The best use for this device would be in occasional imaging of certain tissue structures in which high repeatability is important. For example, in the case of the DMD study, in which ultrasound images are captured over the course of five minutes, the images must have high repeatability, because the images are compared over time to detect change. Another possible use case is mammography; in mammography, if an abnormality is detected, it can be monitored over time to see if the abnormality is growing. In the case of thyroid nodules, the decision of whether or not to perform biopsy is based largely upon the size of the nodule, many of which are benign. The force-controlled probe could be used to image the thyroid at repeatable forces, which would result in repeatable levels of deformation.

*Dynamic imaging probe:* Currently, the dynamic imaging probe is still early in the development process. More work is needed to improve the performance of the system so that it can be used in the studies outlined at the end of this chapter.

### 9.2.2 Uses: Ideal Realizations

*Force-measuring probe:* To realize the full potential of the force-measuring probe, it will be necessary to further miniaturize the system, which will eventually involve

customizing the ultrasound probe itself. We believe that by integrating the load cell into the probe housing, the system can be miniaturized to the point that it is the same size as a conventional probe with almost negligible additional cost or complexity. This means that the device could be used more continuously and more extensively, and would enable much more force data to be collected across the entire spectrum of ultrasound exams. Furthermore, this would make it more feasible to provide force biofeedback to sonographers to help them apply the proper force.

*Force-controlled probe:* The force-controlled could be further miniaturized by providing better integration of the mechanical components. The current system consists mostly of off-the-shelf components: servo motor, coupling, pulleys, linear actuator, load cell, and ultrasound probe. By improving the robustness of the “Soft Limits” strategy, the range of motion could be reduced, shortening the length of device. Using the coupling-free design of Prototype 3, along with a smaller-diameter motor, could further reduce the size of the system. Additional size reductions could be realized by providing better integration between the ultrasound probe and load cell. In the optimal scenario, with much tighter component integration, we believe that the size of the system could be reduced substantially, by a factor of two, perhaps.

A smaller size would enable the system to be used more ergonomically and therefore more continuously. This would expand its use beyond short imaging scenarios such as the DMD study. It could also potentially be used to help train sonographers of the proper force to apply during scanning, or help non-expert sonographers apply the proper force, as discussed later.

*Dynamic imaging probe:* With further development, the size of the dynamic imaging probe could also be reduced. Currently, the voice coil actuator’s permanent magnet is the single largest (and most massive) component in the system. Reducing the mass of the magnet could significantly improve the ergonomics of the device. Eventually, we envision that the device could be a compact, low-cost attachment to a conventional linear array ultrasound probe. With further development of the temporal aliasing technique described in Section 7.8, it could be possible to enable high-speed imaging of repeatable events with conventional, low-speed 2D ultrasound

transducers. Combining the dynamic imaging probe with the image aliasing technique implemented with a conventional linear array transducer, it may be possible to conduct low-cost quantitative elastography imaging at a repeatable preload force. Such a system would enable elastography to be implemented more repeatably and used more extensively. Possible elastography applications to target would be tumor detection, liver fibrosis quantification, and thyroid nodule monitoring.

*Enabling non-expert scanning:* All of the devices could be used to help non-experts (non-sonographers) to acquire diagnostic quality images. If, as discussed later in this chapter, the optimal or “sweet spot” force were known for a particular exam, any of these devices could be used to help the sonographer achieve that contact force. The force-controlled probe and dynamic imaging probe could apply the desired force automatically; with the force-measuring probe, the user would provide the control and actuation of the probe, but the device would provide contact force feedback.

*Longitudinal imaging:* Similarly, all three devices could enhance the quality of longitudinal imaging. In longitudinal imaging, images are acquired of the same tissue at successive points in time and could be days, weeks, months, or even years apart. The images are compared with each other in an effort to detect change. All three systems improve the repeatability of imaging by providing better control over the contact force. As long as the probe is positioned at the same location with respect to the tissue, the contact force can be made more repeatable using any of these three devices, enhancing the diagnostic qualities of longitudinal imaging.

## 9.3 Contributions

The main contributions of this thesis are as follows:

### Overall:

1. Developed three novel electromechanical systems that:
  - (a) Measure and/or control the acquisition state of the ultrasound (US) probe.

- (b) Improve diagnostic quality and repeatability of US imaging (constant force, torque, and angle).
  - (c) Reduce the level of skill necessary to obtain US images (via force control).
  - (d) Improve control of the ultrasound image.
  - (e) Span the design space of force-controlled ultrasound imaging.
2. Evaluated performance of each device in clinical and/or in vivo studies
  3. Control techniques to enable intuitive, ergonomic human-device-human interaction.
  4. Enhanced the understanding of US contact forces (first thorough study of its kind).
    - (a) Explored correlations between force, sonographer experience, and patient BMI.
  5. Developed design guidelines for force-measuring and force-controlling ultrasound systems.

**Force-Controlled Probe:**

1. Developed 3 systems to provide programmable probe contact force during ultrasound scanning.
  - (a) The second prototype attenuates hand tremors 10 times better than conventional US imaging.
2. Developed intuitive-to-use control techniques to keep actuator within range of motion.
  - (a) Validated performance in 190 clinical tests involving 40 young patients.
3. Demonstrated utility of force control in detecting Duchenne Muscular Dystrophy.

### **Force-Measuring Probe:**

1. Developed the first portable, ergonomic device to measure probe contact forces, torques, and angles.
2. Two series:
  - (a) Series 1: 6-axis force/torque measurement.
  - (b) Series 2: 1-axis force measurement, \$1.5k
  - (c) Simple, robust designs; most parts injection-moldable.
  - (d) Quick release: probe attached/detached by hand (no tools) in <20sec.
3. Quantified forces, torques, and angles in 53 clinical exams.
  - (a) Representative range of patients, sonographers.
  - (b) Developed force guidelines based upon patient BMI.
4. Published design details and data.
  - (a) First thorough study/data of contact forces.
  - (b) Data inform the design of future ultrasound-related devices.
5. Demonstrated system to ultrasound community at premier USA ultrasound conference (AIUM).

### **High-Speed Dynamic Imaging Probe:**

1. Developed a high-bandwidth, direct-drive force-controlled ultrasound probe.
  - (a) Appropriate for imaging smaller structures.
  - (b) More compact than the ball screw probe.
2. Can measure tissue elasticity at known preload force.
  - (a) Can make elasticity measurement more repeatable.

## 9.4 Suggestions for Future Work

The following sections provide suggestions for future work:

### 9.4.1 Force-Controlled Probe:

Adapt designs to other ultrasound exam types: The devices developed in this thesis were designed for abdominal and musculoskeletal imaging. As described in Section 8, the suggested designs for other ultrasound exam types, such as ophthalmic, vascular, and neonatal fontanelle, would employ some of the same components as the force-controlled probe or dynamic imaging probes but would differ slightly in terms of range of motion. It would be interesting to create force-controlled probes for other applications in order to further explore the usability and diagnostic improvements afforded by force control.

DMD study data: Further analysis of the DMD study data is of interest. Thus far, it has been demonstrated by Koppaka et al [54], [55] that knowledge of contact force, combined with certain image processing techniques, can be used to enhance automated detection of Duchenne Muscular Dystrophy. The ultimate clinical goal is to not only detect DMD, but to also evaluate disease severity. Therefore, worthwhile future work would involve using force-correlated ultrasound images (and also potentially angle-correlated images, because an angle-sweep is also conducted) to measure the extent of dystrophy.

Ultrasound exam time: Since the device frees the sonographer from needing to concentrate on applying a particular contact force, it is also hypothesized that the device could reduce the time required to conduct an exam. In 1997, Smith et al [100] found a positive correlation between injury and scan time. Potential future work includes investigating average ultrasound exam time with and without this device.

Breast imaging: This device would be particularly applicable for breast imaging. Conventionally, X-ray-based mammography is used to screen for breast cancer, and follow up imaging is performed with ultrasound. In mammography, it is critical to find even the smallest lump, as it could lead to cancer. The radiation dosage caused by

X-rays limits the frequency with which mammography can be performed. However, ultrasound, which is non-ionizing, can be used to image more frequently. Therefore, it would be potentially beneficial to enable ultrasound to expand further unto breast imaging. The force controlled probe could be used to obtain more repeatable scans of the breast. Constant-force ultrasound scans could be performed frequently to more accurately track changes in the sizes of any breast masses without subjecting the patient to radiation.

Control of all six DOFs: As discussed in Section 1.1, any solid body has six degrees of freedom (DOFs). The force-controlled probe controls one DOF: the DOF associated with contact force. Therefore, control over the other five DOFs would enable complete control over the acquisition state of the probe, and would result in the greatest image repeatability. A six-DOF probe tracking system, developed by Sun in our group [107], [105], [106], which consists of a camera mounted to the ultrasound probe, uses pictures taken of the skin surface to measure the relative position and orientation of the probe with respect to the patient's body. By providing feedback to the sonographer to help him/her achieve a desired position and orientation from a previous exam (for example, in longitudinal imaging), and combined with force control, one could attain ultrasound images with all six DOFs repeatable. A photograph illustrating a possible embodiment of this device is shown in Fig. 9-1. Suggested future work includes using this system to achieve more repeatable images, and evaluating the impact of repeatable imaging in diagnostic quality.

Cost reduction: The component cost of the ball screw-driven force-controlled probe is on the order of \$2500, which consists of the ball screw (\$1000), load cell (\$1000), servo motor (\$100), and additional components (\$400). The cost could potentially be reduced by using an OEM-type load cell with lower-cost signal conditioning electronics. Replacing the ball screw with a different type of actuator could also reduce cost significantly. Future work includes investigating the feasibility of using a belt drive linear actuator, which, if properly preloaded, could achieve comparably high-precision motion at a lower cost than the ball screw.

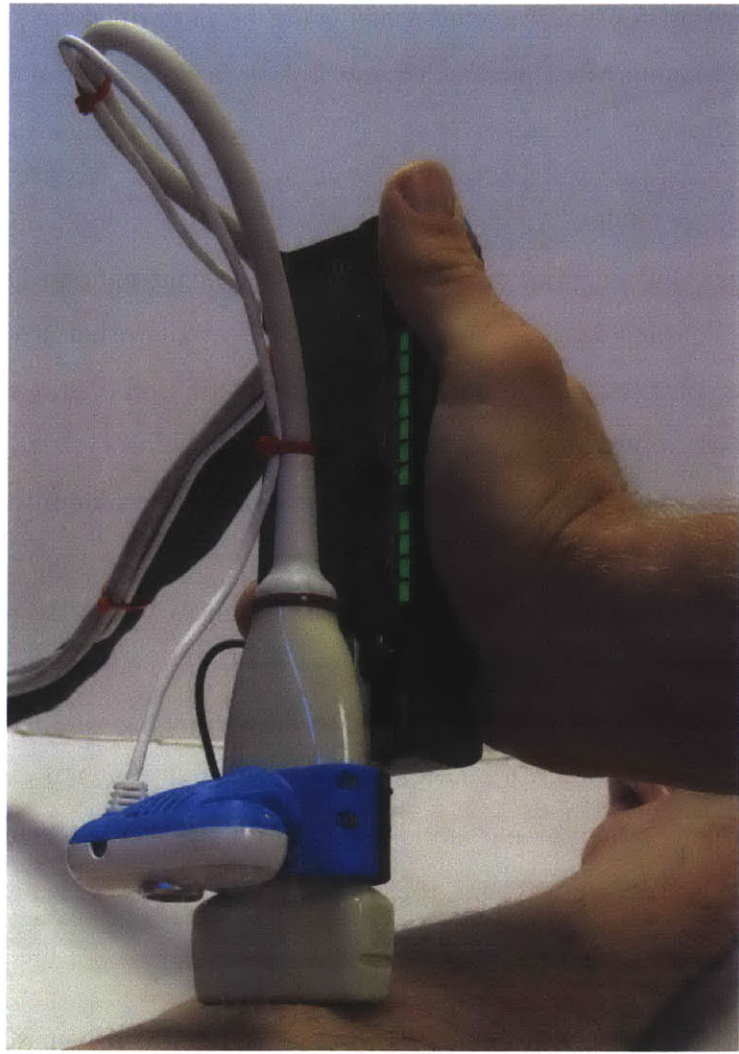


Figure 9-1: A photograph of the force-controlled probe with the 6-DOF probe tracking system by Sun [107], [105], [106]. The device, which has not yet been used in studies, could be used to control the complete 6-DOF contact state of the probe.

#### **9.4.2 Force-Measuring Probe:**

It would be valuable to investigate correlations between contact force and the risk of sonographer injury. So far in this work, the contact forces have been characterized, but no work has yet been performed to reduce the prevalence of injury. One of the major goals of the device is to develop force guidelines, and to provide force feedback for sonographers in order to reduce the risk of injury. The first step has been to quantify the contact forces. The second step, perhaps, would be to conduct a retrospective study to look at the history of injury of the sonographers involved in this study in order to explore correlations between contact force and risk of injury. For example, “sonographer X applies a force of Y, and has an injury history of Z” would be one data point.

Biofeedback study: It may also be valuable to conduct a prospective study to evaluate whether it is possible to influence sonographer behavior based upon contact force. For example, the force-measuring probe could inform the sonographer of his/her contact force in real time. The system could also provide biofeedback to help the sonographer apply the appropriate force. For example, if the force exceeds the recommended limit, the system could beep or vibrate, or a warning could be displayed on the ultrasound screen. The objective of such a hypothetical study would be to see if the risk of injury can be reduced by informing the sonographer of contact force.

It would also be informative to quantify contact state in other types of ultrasound exams. The study presented in this thesis investigated the contact forces, torques, and angles applied during abdominal imaging. To more thoroughly understand and characterize contact forces, it would be informative to use this device in other types of exams, such as those shown in Fig. 2-2.

Another potential avenue to explore would be the concept of an “optimal” or “sweet spot” contact force. The optimization problem would be to determine the contact force that results in highest image quality and lowest risk of injury to the sonographer. To solve this optimization problem, it would be necessary to know the force/image quality correlation in addition to the force/injury correlation (the

latter of which is described above). The force/image quality correlation could be mapped as follows: collect force-correlated images during real clinical scanning, and have an expert/professional, who is blind to the forces, rate the image quality. In the optimization problem, there would potentially need to be some sort of weighting between the relative importances of low injury risk and high image quality.

Structural loop optimization: In conventional ultrasound imaging, one can observe in Fig. 1-1 that the sonographer's body configuration is not particularly ergonomic or comfortable. The sonographer, with his/her head turned towards the screen, reaches his/her arm over the patient and exerts force upon the ultrasound probe. Within the context of the "Structural Loop," discussed in Section 1.3.1, the long force path goes through the sonographer's arm, through his/her body and legs, through the floor, into the patient's bed, and into the patient. It is possible that other structural loops could be more ergonomic. For example, placing the ultrasound screen above the patient could enable the sonographer to see both the screen and the probe at the same time, without requiring him/her to twist his/her neck.

Fig. 9-2, from [70], shows the five imaging tasks that exacerbate symptoms of musculoskeletal injury. The application of force has been implicated as the single most aggravating factor, while different biomechanical configurations, namely trunk twisting and shoulder abduction, constitute the second, third, and fourth most aggravating factors. This suggests that much of the discomfort and injury experienced by sonographers could be alleviated by improving the ergonomics of the biomechanics (i.e., structural loop) and the contact force.

#### **9.4.3 High-Speed Dynamic Imaging Probe:**

Further studies to investigate the preload-dependence of elastic modulus. So far, the device has been used in a study on the forearm to measure elastic modulus versus preload force. The data showed agreement with the literature values and that obtained with an off-the-shelf commercial probe. It would be interesting to repeat the experiment multiple times and in different areas of the body to test repeatability.

Improve performance at higher preload forces. Shear wave generation relies on

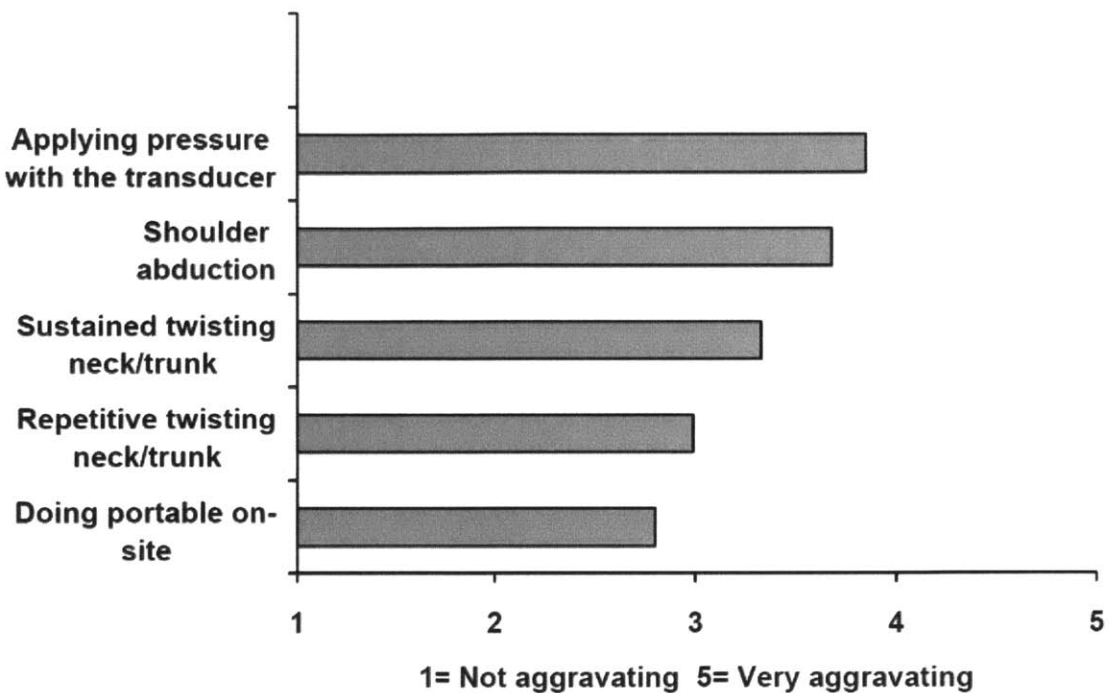


Figure 9-2: Ultrasound imaging tasks that exacerbate musculoskeletal injury symptoms, from a study of 1621 sonographers, reproduced from [70].

one or more periods of a  $>50$  Hz sinusoidal excitation. Currently, the characteristics of the device's waveform differ at 18 N preload force versus 1 N preload force. As the preload force increases, the device is less capable of applying additional force, and the device tends to retract rather than extend into the tissue. Potentially worthwhile future work includes improving the control and mechanical design of the system (e.g., reducing moving mass, choosing a higher-power voice coil) to ensure uniform waveform characteristics at all preload forces, eliminating any possible biases in shear wave generation and propagation speed estimation.



# Bibliography

- [1] "Consensus Conference on Work-Related Musculoskeletal Disorders (WRMSD) in Sonography". May 13, 2003, Dallas, TX.
- [2] "Diagnostic Medical Sonographers and Cardiovascular Technologists and Technicians, Including Vascular Technologists". <http://www.bls.gov/ooh/healthcare/diagnostic-medical-sonographers.htm>, 2004.
- [3] "Mobile Robotics". <http://www.mobile-robotics.com/>, 2004.
- [4] ACR/AIUM/SPR/SRU: "Practice Guideline for the Performance of an Ultrasound Examination of the Abdomen and/or Retroperitoneum". <http://www.acr.org/Quality-Safety/Standards-Guidelines/Practice-Guidelines-by-Modality>, April 2014.
- [5] "Age and Sex Composition: 2010 Census Briefs". <http://www.census.gov/prod/cen2010/briefs/c2010br-03.pdf>, April 2014.
- [6] "Duchenne Muscular Dystrophy". <http://www.nlm.nih.gov/medlineplus/ency/article/000705.htm>, April 2014.
- [7] "Echosens: Fibroscan". <http://www.echosens.com/Public-EN/home-public.html>, April 2014.
- [8] "ESTELE: Tele-Echography Robot". <http://www.robosoft.com/robotic-solutions/healthcare/tele-echography/index.html>, April 2014.
- [9] "How to Case Study: Deep Vein Thrombosis Detection with Ultrasound Part 1 - SonoSite, Inc.". <http://www.youtube.com/watch?v=Sh5cL72kgnU>, April 2014.
- [10] International Journal of Shoulder Surgery. <http://www.internationalshoulderjournal.org>, April 2014.
- [11] "Obesity and Diabetes in New York City, 2002 and 2004". [http://www.cdc.gov/pcd/issues/2008/apr/07\\_0053.htm](http://www.cdc.gov/pcd/issues/2008/apr/07_0053.htm), April 2014.
- [12] "OSHA Testimony - Society of Diagnostic Medical Sonographers". <https://www.sdms.org/msi/osha.asp>, April 2014.

- [13] QED Study. <http://Childrenshospital.org/qedstudy>, March 2014.
- [14] Lama Al Bassit. *Structures mécaniques à modules sphériques optimisées pour un robot médical de télé-échographie mobile*. PhD thesis, Université d'Orléans, 2005.
- [15] Brian Anthony and Matthew Gilbertson. *Handheld Force-Controlled Ultrasound Probe*. In *US Patent Number 8328725*, Dec 2012.
- [16] Brian Anthony and Matthew Gilbertson. *Handheld Force-Controlled Ultrasound Probe*. In *US Patent Number 8333704*, Dec 2012.
- [17] Brian Anthony and Matthew Gilbertson. *Handheld Force-Controlled Ultrasound Probe*. In *US Patent Number 8382671*, Feb 2013.
- [18] Brian W Anthony and Matthew W Gilbertson. *Ultrasound Scanning System*. In *US Patent App. 14/057896*, October 2013.
- [19] Brian W Anthony, Matthew W Gilbertson, and Anthony E Samir. *Sonographer Fatigue Monitoring*. In *US Patent App. 13/494,792*, June 2012.
- [20] Reza Zahiri Azar, Kris Dickie, and Laurent Pelissier. Real-time 1-d/2-d transient elastography on a standard ultrasound scanner using mechanically induced vibration. *Ultrasonics, Ferroelectrics and Frequency Control, IEEE Transactions on*, 59(10), 2012.
- [21] J Bercoff, S Chaffai, M Tanter, L Sandrin, S Catheline, M Fink, JL Gennisson, and M Meunier. In vivo breast tumor detection using transient elastography. *Ultrasound in medicine & biology*, 29(10):1387–1396, 2003.
- [22] Jérémie Bercoff, Mickaël Tanter, and Mathias Fink. Supersonic shear imaging: a new technique for soft tissue elasticity mapping. *Ultrasonics, Ferroelectrics and Frequency Control, IEEE Transactions on*, 51(4):396–409, 2004.
- [23] Emad M Boctor, Gregory Fischer, Michael A Choti, Gabor Fichtinger, and Russell H Taylor. A dual-armed robotic system for intraoperative ultrasound guided hepatic ablative therapy: a prospective study. In *Robotics and Automation, 2004. Proceedings. ICRA'04. 2004 IEEE International Conference on*, volume 3, pages 2517–2522. IEEE, 2004.
- [24] Ivo AMJ Broeders and Jelle Ruurda. Robotics revolutionizing surgery: the intuitive surgical da vinci system. *Industrial Robot: An International Journal*, 28(5):387–392, 2001.
- [25] Michael R. Burcher, J. Alison Noble, Lianghao Han, and Mark Gooding. A system for simultaneously measuring contact force, ultrasound, and position information for use in force-based correction of freehand scanning. *IEEE Transactions on Ultrasonics, Ferroelectrics, and Frequency Control*, 52(8):1330 – 1342, 2005.

- [26] Laurent Castéra, Julien Vergniol, Juliette Foucher, Brigitte Le Bail, Elise Chanteloup, Maud Haaser, Monique Darriet, Patrice Couzigou, and Victor de Lédinghen. Prospective comparison of transient elastography, fibrotest, apri, and liver biopsy for the assessment of fibrosis in chronic hepatitis c. *Gastroenterology*, 128(2):343–350, 2005.
- [27] S Catheline, J-L Gennisson, G Delon, M Fink, R Sinkus, S Abouelkaram, and J Culigoli. Measurement of viscoelastic properties of homogeneous soft solid using transient elastography: An inverse problem approach. *The Journal of the Acoustical Society of America*, 116(6):3734–3741, 2004.
- [28] Stefan Catheline, Jean-Louis Thomas, Francois Wu, and Mathias A Fink. Diffraction field of a low frequency vibrator in soft tissues using transient elastography. *Ultrasonics, Ferroelectrics and Frequency Control, IEEE Transactions on*, 46(4):1013–1019, 1999.
- [29] S Chadli, N Ababou, A Ababou, N Djelal, and N Saadia. A removable device for axial force and orientation measurement on medical ultrasound probe. In *Systems, Signals and Devices (SSD), 2012 9th International Multi-Conference on*, pages 1–4. IEEE, 2012.
- [30] Roger W Chan and Ingo R Titze. Viscoelastic shear properties of human vocal fold mucosa: measurement methodology and empirical results. *The Journal of the Acoustical Society of America*, 106(4):2008–2021, 1999.
- [31] Mathieu Couade, Mathieu Pernot, Claire Prada, Emmanuel Messas, Joseph Emmerich, Patrick Bruneval, Aline Criton, Mathias Fink, and Mickael Tanter. Quantitative assessment of arterial wall biomechanical properties using shear wave imaging. *Ultrasound in medicine & biology*, 36(10):1662–1676, 2010.
- [32] Fabien Courrèges. *Contributions à la conception et commande de robots de télé-échographie*. PhD thesis, Orléans, 2003.
- [33] Brian L Davies, Sunita Chauhan, and Mike JS Lowe. A robotic approach to hifu based neurosurgery. In *Medical Image Computing and Computer-Assisted Intervention MICCAI98*, pages 386–396. Springer, 1998.
- [34] D De Cunha, P Gravez, C Leroy, E Maillard, J Jouan, P Varley, M Jones, M Halliwell, D Hawkes, PNT Wells, et al. The midstep system for ultrasound guided remote telesurgery. In *Engineering in Medicine and Biology Society, 1998. Proceedings of the 20th Annual International Conference of the IEEE*, volume 3, pages 1266–1269. IEEE, 1998.
- [35] Manish Dhyani, Matthew Gilbertson, Arash Anvari, Brian Anthony, and Anthony Samir. Precise quantification of sonographic forces: A first step toward reducing ergonomic injury. American Institute of Ultrasound in Medicine Convention (AIUM), April 2014. Las Vegas, NV.

- [36] Rodger J Elble and James E Randall. Mechanistic components of normal hand tremor. *Electroencephalography and clinical neurophysiology*, 44(1):72–82, 1978.
- [37] Kevin Evans, Shawn Roll, and Joan Baker. Work-related musculoskeletal disorders (wrmsd) among registered diagnostic medical sonographers and vascular technologists a representative sample. *Journal of Diagnostic Medical Sonography*, 25(6):287–299, 2009.
- [38] GT Fallenstein, Verne D Hulce, and John W Melvin. Dynamic mechanical properties of human brain tissue. *Journal of Biomechanics*, 2(3):217–226, 1969.
- [39] Brian S Garra. Tissue elasticity imaging using ultrasound. *Applied Radiology*, 40(4):24, 2011.
- [40] Matthew Gilbertson. Handheld force-controlled ultrasound probe. Master’s thesis, Massachusetts Institute of Technology, 2010.
- [41] Matthew W Gilbertson and Brian W Anthony. A force, image, and position control system for freehand ultrasound (submitted). *Robotics, IEEE Transactions on*.
- [42] Matthew W Gilbertson and Brian W Anthony. Impedance-controlled ultrasound probe. In *SPIE Medical Imaging*, pages 796816–796816. International Society for Optics and Photonics, 2011.
- [43] Matthew W Gilbertson and Brian W Anthony. Ergonomic control strategies for a handheld force-controlled ultrasound probe. In *Intelligent Robots and Systems (IROS), 2012 IEEE/RSJ International Conference on*, pages 1284–1291. IEEE, 2012.
- [44] Matthew W Gilbertson and Brian W Anthony. An ergonomic, instrumented ultrasound probe for 6-axis force/torque measurement. In *Engineering in Medicine and Biology Society (EMBC), 2013 35th Annual International Conference of the IEEE*, pages 140–143. IEEE, 2013.
- [45] Walter D Glanze, Kenneth Anderson, and Lois E Anderson. Mosby’s medical, nursing, and allied health dictionary. 1994.
- [46] Randal P Goldberg, Mazilu Dumitru, Russell H Taylor, and Dan Stoianovici. A modular robotic system for ultrasound image acquisition. In *Medical Image Computing and Computer-Assisted Intervention—MICCAI 2001*, pages 1430–1432. Springer, 2001.
- [47] Alain Gourdon, Ph Poignet, G Poisson, Pierre Vieyres, and P Marché. A new robotic mechanism for medical application. In *Advanced Intelligent Mechatronics, 1999. Proceedings. 1999 IEEE/ASME International Conference on*, pages 33–38. IEEE, 1999.

- [48] Jan DJ Gumprecht, Florian B Geiger, Jens-Uwe Stolzenburg, and Tim C Lueth. Flat-panel ultrasound robot: A novel imaging concept and a novel motorized kinematics for an ultrasound probe during laparoscopic interventions. In *Intelligent Robots and Systems (IROS), 2013 IEEE/RSJ International Conference on*, pages 3564–3569. IEEE, 2013.
- [49] L. Han, J.A. Noble, and M. Burcher. A novel ultrasound indentation system for measuring biomechanical properties in vivo soft tissue. *Ultrasound in Medicine and Biology*, 29(6):813 – 23, 2003/06.
- [50] Neville Hogan. Impedance control: An approach to manipulation, parts i-iii. In *American Control Conference, 1984*, pages 304–313. IEEE, 1984.
- [51] Kenneth Hoyt, Timothy Kneezel, Benjamin Castaneda, and Kevin J Parker. Quantitative sonoelastography for the in vivo assessment of skeletal muscle viscoelasticity. *Physics in medicine and biology*, 53(15):4063, 2008.
- [52] Miklos Z Kiss, Tomy Varghese, and Timothy J Hall. Viscoelastic characterization of in vitro canine tissue. *Physics in medicine and biology*, 49(18):4207, 2004.
- [53] Dieter Klatt, Uwe Hamhaber, Patrick Asbach, Jürgen Braun, and Ingolf Sack. Noninvasive assessment of the rheological behavior of human organs using multifrequency mr elastography: a study of brain and liver viscoelasticity. *Physics in medicine and biology*, 52(24):7281, 2007.
- [54] S. Koppaka, M. Gilbertson, S. Rutkove, and B. Anthony. Evaluating the clinical relevance of force-correlated ultrasound. In *Biomedical Imaging (ISBI), 2014 IEEE 11th International Symposium on*. IEEE, 2014.
- [55] S. Koppaka, M. Gilbertson, J. Wu, S. Rutkove, and B. Anthony. Assessing duchenne muscular dystrophy with force-controlled ultrasound. In *Biomedical Imaging (ISBI), 2014 IEEE 11th International Symposium on*. IEEE, 2014.
- [56] Michael K Kwan and Savio LY Woo. A structural model to describe the non-linear stress-strain behavior for parallel-fibered collagenous tissues. *Journal of biomechanical engineering*, 111(4):361–363, 1989.
- [57] Dale A Lawrence. Stability and transparency in bilateral teleoperation. *Robotics and Automation, IEEE Transactions on*, 9(5):624–637, 1993.
- [58] W Marshall Leach Jr. Loudspeaker voice-coil inductance losses: circuit models, parameter estimation, and effect on frequency response. *Journal of the Audio Engineering Society*, 50(6):442–450, 2002.
- [59] Simon Lessard, Pascal Bigras, and Ilian A Bonev. A new medical parallel robot and its static balancing optimization. *Journal of medical Devices*, 1(4):272–278, 2007.

- [60] Kandice R Levental, Hongmei Yu, Laura Kass, Johnathon N Lakins, Mikala Egeblad, Janine T Erler, Sheri FT Fong, Katalin Csiszar, Amato Giaccia, Wolfgang Weninger, et al. Matrix crosslinking forces tumor progression by enhancing integrin signaling. *Cell*, 139(5):891–906, 2009.
- [61] Jia-Hua Lin, Robert G Radwin, and Terry G Richard. Dynamic biomechanical model of the hand and arm in pistol grip power handtool usage. *Ergonomics*, 44(3):295–312, 2001.
- [62] Robert A MacLachlan, Brian C Becker, Jaime Cuevas Tabares, Gregg W Podnar, Louis A Lobes, and Cameron N Riviere. Micron: an actively stabilized handheld tool for microsurgery. *Robotics, IEEE Transactions on*, 28(1):195–212, 2012.
- [63] M. Marchal and J. Troccaz. A one-DOF freehand haptic device for robotic tele-echography. *Studies in Health Technology and Informatics*, 98:231–233, 2004.
- [64] Kohji Masuda, Eizen Kimura, Norihiko Tateishi, and Ken Ishihara. Three dimensional motion mechanism of ultrasound probe and its application for tele-echography system. In *Intelligent Robots and Systems, 2001. Proceedings. 2001 IEEE/RSJ International Conference on*, volume 2, pages 1112–1116. IEEE, 2001.
- [65] Takeshi Matsumura, Tsuyoshi Mitake, and Tomoyuki Miyazawa. Automated pressing device and ultrasonic diagnosis apparatus using the device, October 2 2012. US Patent 8,277,382.
- [66] P Mirk, N Magnavita, L Masini, M Bazzocchi, and A Fileni. “frequency of musculoskeletal symptoms in diagnostic medical sonographers. results of a pilot survey”. *La Radiologia medica*, 98(4):236–241, 1999.
- [67] Ben Mitchell, John Koo, Iulian Iordachita, Peter Kazanzides, Ankur Kapoor, James Handa, Gregory D Hager, and Russell H Taylor. Development and application of a new steady-hand manipulator for retinal surgery. In *ICRA*, pages 623–629, 2007.
- [68] Mamoru Mitsuishi, Shin’ichi Warisawa, Taishi Tsuda, Takuya Higuchi, Norihiro Koizumi, Hiroyuki Hashizume, and Kazuo Fujiwara. Remote ultrasound diagnostic system. In *Robotics and Automation, 2001. Proceedings 2001 ICRA. IEEE International Conference on*, volume 2, pages 1567–1574. IEEE, 2001.
- [69] Chris R Mol and Paul A Breddels. Ultrasound velocity in muscle. *The Journal of the Acoustical Society of America*, 71(2):455–461, 1982.
- [70] Carmel Murphy, Andre Russo, and Healthcare Benefit Trust. “An Update on Ergonomic Issues in Sonography”. [http://www.soundergonomics.com/pdf/Update\\_on\\_Ergo\\_Issues.pdf](http://www.soundergonomics.com/pdf/Update_on_Ergo_Issues.pdf), July 2000.

- [71] Farshid Najafi. Design and prototype of a robotic system for remote palpation and ultrasound imaging. Master's thesis, Department of Mechanical and Manufacturing Engineering, University of Manitoba, Canada, 2004.
- [72] Farshid Najafi and Nariman Sepehri. Design and prototyping of a force-reflecting hand-controller for ultrasound imaging. *Journal of Mechanisms and Robotics*, 3(2):021002, 2011.
- [73] Simin Nasseri, Lynne E Bilston, and Nhan Phan-Thien. Viscoelastic properties of pig kidney in shear, experimental results and modelling. *Rheologica acta*, 41(1-2):180–192, 2002.
- [74] Kathryn Nightingale, Mary Scott Soo, Roger Nightingale, and Gregg Trahey. Acoustic radiation force impulse imaging: in vivo demonstration of clinical feasibility. *Ultrasound in medicine & biology*, 28(2):227–235, 2002.
- [75] Norman S Nise. *Control Systems Engineering*. John Wiley & Sons, 2007.
- [76] Antoine Nordez and François Hug. Muscle shear elastic modulus measured using supersonic shear imaging is highly related to muscle activity level. *Journal of Applied Physiology*, 108(5):1389–1394, 2010.
- [77] United Kingdom Association of Sonographers. “guidelines for professional working standards: Ultrasound practice”, October 2008.
- [78] Government Accountability Office. “GAO Analysis of Medicare Part B Claims Data for 2005.”, 2005.
- [79] J Ophir, I Cespedes, Hm Ponnekanti, Y Yazdi, and X Li. Elastography: a quantitative method for imaging the elasticity of biological tissues. *Ultrasonic imaging*, 13(2):111–134, 1991.
- [80] World Health Organization. *Obesity: preventing and managing the global epidemic*. Number 894. World Health Organization, 2000.
- [81] Takashi Osaka, Takeshi Matsumura, Tetsuya Hayashi, Mitsuhiro Oshiki, Okinori Yuasa, Naoyuki Murayama, Tsuyoshi Shiina, Satoshi Tamano, and Tsuyoshi Mitake. Ultrasound probe and ultrasound elasticity imaging apparatus, August 30 2011. US Patent 8,007,438.
- [82] J Oudry, C Bastard, V Miette, R Willinger, and L Sandrin. Copolymer-in-oil phantom materials for elastography. *Ultrasound in medicine & biology*, 35(7):1185–1197, 2009.
- [83] F Piccinino, E Sagnelli, G Pasquale, Genzyme Giusti, A Battocchia, M Bernardi, R Bertolazzi, FB Bianchi, E Brunelli, G Budillon, et al. Complications following percutaneous liver biopsy: a multicentre retrospective study on 68 276 biopsies. *Journal of hepatology*, 2(2):165–173, 1986.

- [84] François Pierrot, Etienne Dombre, Eric Dégoulange, Loïc Urbain, Pierre Caron, Sylvie Boudet, Jérôme Gariépy, and Jean-Louis Mégnien. Hippocrate: a safe robot arm for medical applications with force feedback. *Medical Image Analysis*, 3(3):285–300, 1999.
- [85] T Rago, F Santini, M Scutari, A Pinchera, and P Vitti. Elastography: new developments in ultrasound for predicting malignancy in thyroid nodules. *Journal of Clinical Endocrinology & Metabolism*, 92(8):2917–2922, 2007.
- [86] S Rakheja, JZ Wu, RG Dong, AW Schopper, and P-É Boileau. A comparison of biodynamic models of the human hand-arm system for applications to hand-held power tools. *Journal of Sound and Vibration*, 249(1):55–82, 2002.
- [87] William M Rand. Objective criteria for the evaluation of clustering methods. *Journal of the American Statistical association*, 66(336):846–850, 1971.
- [88] Hassan Rivaz and Robert Rohling. An active dynamic vibration absorber for a hand-held vibro-elastography probe. *Journal of Vibration and Acoustics*, 129(1):101–112, 2007.
- [89] Shawn C Roll, Kevin D Evans, Cristina D Hutmire, and Joan P Baker. An analysis of occupational factors related to shoulder discomfort in diagnostic medical sonographers and vascular technologists. *Work: A Journal of Prevention, Assessment and Rehabilitation*, 42(3):355–365, 2012.
- [90] Seward B Rutkove. Electrical impedance myography: background, current state, and future directions. *Muscle & nerve*, 40(6):936–946, 2009.
- [91] S.E. Salcudean, G. Bell, S. Bachmann, W.H. Zhu, P. Abolmaesumi, and P.D. Lawrence. Robot-assisted diagnostic ultrasound - design and feasibility experiments. *Medical Image Computing and Computer-Assisted Intervention - MICCAI'99. Second International Conference. Proceedings (Lecture Notes in Computer Science Vol.1679)*, pages 1062 – 71, 1999.
- [92] Abbas Samani, Jonathan Bishop, Chris Luginbuhl, and Donald B Plewes. Measuring the elastic modulus of ex vivo small tissue samples. *Physics in medicine and biology*, 48(14):2183, 2003.
- [93] Laurent Sandrin, Mickaël Tanter, Stefan Catheline, and Mathias Fink. Shear modulus imaging with 2-d transient elastography. *Ultrasonics, Ferroelectrics and Frequency Control, IEEE Transactions on*, 49(4):426–435, 2002.
- [94] Laurent Sandrin, Mickaël Tanter, J-L Gennisson, Stefan Catheline, and Mathias Fink. Shear elasticity probe for soft tissues with 1-d transient elastography. *Ultrasonics, Ferroelectrics and Frequency Control, IEEE Transactions on*, 49(4):436–446, 2002.

- [95] Jeffrey Schlosser, Kenneth Salisbury, and Dimitre Hristov. Telerobotic system concept for real-time soft-tissue imaging during radiotherapy beam delivery. *Medical physics*, 37(12):6357–6367, 2010.
- [96] Frank C Sciurba and William A Slivka. Six-minute walk testing. In *Seminars in respiratory and critical care medicine*, volume 19, pages 383–392. Copyright© 1998 by Thieme Medical Publishers, Inc., 1998.
- [97] S Shah, Ankur Kapoor, Jienan Ding, Peter Guion, Doru Petrisor, J Karanian, WF Pritchard, Dan Stoianovici, Bradford J Wood, and Kevin Cleary. Robotically assisted needle driver: evaluation of safety release, force profiles, and needle spin in a swine abdominal model. *International Journal of Computer Assisted Radiology and Surgery*, 3(1-2):173–179, 2008.
- [98] Ralph Sinkus, Jeremy Bercoff, Mickaël Tanter, J-L Gennisson, Carl El Khoury, Vincent Servois, Anne Tardivon, and Mathias Fink. Nonlinear viscoelastic properties of tissue assessed by ultrasound. *Ultrasonics, Ferroelectrics and Frequency Control, IEEE Transactions on*, 53(11):2009–2018, 2006.
- [99] Alexander H Slocum. *FUNDAMENTALS of Design*. MIT Mechanical Engineering, 2007.
- [100] Annette C Smith, James G Wolf, Gong-Yuan Xie, and Mikel D Smith. Musculoskeletal pain in cardiac ultrasonographers: results of a random survey. *Journal of the American Society of Echocardiography*, 10(4):357–362, 1997.
- [101] N Smith-Guerin, L Al Bassit, G Poisson, C Delgorge, Ph Arbeille, and P Vieyres. Clinical validation of a mobile patient-expert tele-echography system using isdn lines. In *Information Technology Applications in Biomedicine, 2003. 4th International IEEE EMBS Special Topic Conference on*, pages 23–26. IEEE, 2003.
- [102] John E Speich, Liang Shao, and Michael Goldfarb. Modeling the human hand as it interacts with a telemanipulation system. *Mechatronics*, 15(9):1127–1142, 2005.
- [103] Robert N Stiles. Frequency and displacement amplitude relations for normal hand tremor. *Journal of Applied Physiology*, 40(1):44–54, 1976.
- [104] Dan Stoianovici, Louis L Whitcomb, James H Anderson, Russell H Taylor, and Louis R Kavoussi. A modular surgical robotic system for image guided percutaneous procedures. In *Medical Image Computing and Computer-Assisted Intervention MICCAI98*, pages 404–410. Springer, 1998.
- [105] Shih-Yu Sun, Matthew Gilbertson, and Brian W Anthony. 6-dof probe tracking via skin mapping for freehand 3d ultrasound. In *Biomedical Imaging (ISBI), 2013 IEEE 10th International Symposium on*, pages 780–783. IEEE, 2013.

- [106] Shih-Yu Sun, Matthew Gilbertson, and Brian W Anthony. Computer-guided ultrasound probe realignment by optical tracking. In *Biomedical Imaging (ISBI), 2013 IEEE 10th International Symposium on*, pages 21–24. IEEE, 2013.
- [107] S.Y. Sun, B.A. Anthony, and M.W. Gilbertson. Trajectory-based deformation correction in ultrasound images. In *SPIE Conference on Medical Imaging 2010: Ultrasonic Imaging, Tomography, and Therapy, San Diego, CA, USA*, volume 7629, March 2010.
- [108] Pin Tong and Yuang-Cheng Fung. The stress-strain relationship for the skin. *Journal of Biomechanics*, 9(10):649–657, 1976.
- [109] Takashi Ueta, Yoshiharu Yamaguchi, Yoshihiro Shirakawa, Taiga Nakano, Ryuichi Ieda, Yasuo Noda, Akio Morita, Ryo Mochizuki, Naohiko Sugita, Mamoru Mitsuishi, et al. Robot-assisted vitreoretinal surgery: development of a prototype and feasibility studies in an animal model. *Ophthalmology*, 116(8):1538–1543, 2009.
- [110] A. Vilchis, J. Troccaz, P. Cinquin, K. Masuda, and F. Pellissier. A new robot architecture for tele-echography. *IEEE Transactions on Robotics and Automation*, 19(5):922 – 6, 2003/10/.
- [111] Adriana Vilchis, Jocelyne Troccaz, Philippe Cinquin, Agnes Guerraz, Franck Pellissier, Pierre Thorel, Bertrand Tondu, Fabien Courrèges, Gérard Poisson, Marc Althuser, et al. Experiments with the ter tele-echography robot. In *Medical Image Computing and Computer-Assisted Intervention MICCAI 2002*, pages 138–146. Springer, 2002.
- [112] A. Vilchis-Gonzalez, J.C. Avila-Vilchis, and A. Garcia-Torres. Termi robot. *Electronics, Robotics and Automotive Mechanics Conference, CERMA 2007 - Proceedings*, pages 464 – 469, 2007.
- [113] Joost J Vlassak and WD Nix. Indentation modulus of elastically anisotropic half spaces. *Philosophical Magazine A*, 67(5):1045–1056, 1993.
- [114] LA Wood, CW Suggs, and CF Abrams Jr. Hand-arm vibration part iii: A distributed parameter dynamic model of the human hand-arm system. *Journal of Sound and Vibration*, 57(2):157–169, 1978.
- [115] Wen-Chun Yeh, Pai-Chi Li, Yung-Ming Jeng, Hey-Chi Hsu, Po-Ling Kuo, Meng-Lin Li, Pei-Ming Yang, and Po Huang Lee. Elastic modulus measurements of human liver and correlation with pathology. *Ultrasound in medicine & biology*, 28(4):467–474, 2002.
- [116] Lawrence Yoo, Vijay Gupta, Choongyeop Lee, Pirouz Kavehpore, and Joseph L Demer. Viscoelastic properties of bovine orbital connective tissue and fat: constitutive models. *Biomechanics and modeling in mechanobiology*, 10(6):901–914, 2011.

- [117] Shelten G Yuen, Daniel T Kettler, Paul M Novotny, Richard D Plowes, and Robert D Howe. Robotic motion compensation for beating heart intracardiac surgery. *The International journal of robotics research*, 28(10):1355–1372, 2009.
- [118] Shelten G Yuen, Douglas P Perrin, Nikolay V Vasilyev, Pedro J del Nido, and Robert D Howe. Force tracking with feed-forward motion estimation for beating heart surgery. *Robotics, IEEE Transactions on*, 26(5):888–896, 2010.
- [119] Wen-Hong Zhu, SE Salcudean, Simon Bachmann, and Purang Abolmaesumi. Motion/force/image control of a diagnostic ultrasound robot. In *Robotics and Automation, 2000. Proceedings. ICRA'00. IEEE International Conference on*, volume 2, pages 1580–1585. IEEE, 2000.